Phenomenological Aspects of Supersymmetry with Heavier Scalars

by

Sebastian A. R. Ellis

A dissertation submitted in partial fulfillment
of the requirements for the degree of
Doctor of Philosophy
(Physics)
in the University of Michigan
2017

Doctoral Committee:

Professor Gordon L. Kane, Chair
Professor David J. Baker
Professor Aaron T. Pierce
Professor Thomas A. Schwarz
Professor James D. Wells

Sebastian A. R. Ellis

sarellis@umich.edu

ORCID iD: 0000-0003-3611-2437

Acknowledgements

I would first like to thank my advisor, Gordy Kane. He has encouraged and supported me throughout my graduate career, and my development as a researcher would not have been the same without his invaluable guidance. I would also like to thank James Wells for his advice and support, initially as my advisor, and later as a repeat collaborator.

Additionally, I would like to thank my other collaborators, Bobby Acharya, John Ellis, Rohini Godbole, Shrihari Gopalakrishna, Brent Nelson, Malcolm Perry, Aaron Pierce, Jérémie Quevillon, Veronica Sanz, Tevong You, Zhengkang Zhang, and Bob Zheng for the many stimulating discussions we had while writing papers. They have helped shape my research style and interests, and I have learned different useful skills from each one of them.

I am grateful to Ratindranath Akhoury, Henriette Elvang and Kathryn Zurek for their efforts in teaching me many of the fundamentals of my work.

I thank the other members of the Michigan Centre for Theoretical Physics for providing such a fruitful and encouraging environment.

Special thanks go to my fellow graduate students Anthony Charles, Gino Knodel, Pedro Lisbão, Timothy Olson, Samuel Roland, Zhengkang Zhang and Bob Zheng for being excellent companions on this journey.

The work in this dissertation was in part funded by the U.S. Department of Energy, Office of Science, under grant DE-SC0007859, and in part by a Rackham Graduate Student Research Grant.

Table of Contents

List of Tables

List of Figures

List of Appendices

Abstract

In this dissertation, we will cover aspects of the phenomenology of supersymmetric models, with an emphasis on models with heavier scalar partners of Standard Model fermions. We first introduce the Standard Model, providing explanations for why it should be extended by Supersymmetry. We also provide an introduction to general aspects of supersymmetric models, making use not only of bottom-up phenomenological constraints, but also top-down theoretical insight from String/M-Theory compactifications. In the body of this dissertation, we study in detail the phenomenology of supersymmetric models with heavier scalars at current and future colliders, as well as in low-energy flavor experiments in both the absence and the presence of CP violation. Finally, we discuss general implications of String theory for dark matter in supersymmetric models, as well as the dynamics of Grand Unified Theories in a broad class of models.

Chapter 1

Introduction

This dissertation covers various aspects of the phenomenology associated with low-energy Supersymmetry (SUSY). In particular, we will focus on the phenomenology of supersymmetric models that have heavier scalars, meaning in the few TeV to 10's of TeV range. These models are of interest because they have attractive features like alleviating flavour issues in SUSY, while retaining some of the core motivations for SUSY, such as having a small Higgs Boson mass. In this dissertation we will discuss such models in different contexts. One motivation for such models is from M-Theory (based on pioneering work in [10, 11, 12, 13, 14, 15, 16, 17, 18]). We present the collider [19] and flavour [20] phenomenology of M-Theory derived models in Chapter 2 and Chapter 5 respectively. Independently of M-Theory, we will also consider the phenomenology of simplified models which can be of general interest. In Chapter 3 we will see how these simplified models can be discovered at colliders [21], and in Chapter 4 we will see how CP-conserving flavour observables can constrain or discover their indirect signatures [22]. These first four chapters cover specific phenomenological aspects of supersymmetric models with heavier scalars. In contrast, in Chapters 6 and 7, we will cover general features and concepts which can be applied to all types of supersymmetric models. In particular, we will discuss in Chapter 6, how if Supersymmetry is the low-energy realisation of a compactified String/M-Theory, this can have a profound impact on dark matter in the theory [23]. Finally in Chapter 7, we will discuss generalities of grand unified theories, and apply them to various examples of theories [24].

In this introduction, we will go over some of the aspects of the Standard Model, including the Higgs sector, and therefore motivate why SUSY is an attractive framework for physics beyond the Standard Model (BSM). We will then provide a lightning introduction to SUSY, and then explain why models with heavier scalars are a well-motivated region of the theory-

space. Finally, at the end of the introduction is an outline of the dissertation, where we explain briefly what each chapter covers, and explains some of the results.

1.1 An overview of the Standard Model

The Standard Model of particle physics has been extremely successful for the last 40 years in describing nearly all phenomena observed in low- and high-energy experiments. The discovery of the Higgs Boson in 2012 [25, 26] marked the completion of the puzzle of the Glashow-Weinberg-Salam model (Electroweak part of the Standard Model), and thus the completion of the Standard Model. However, as will be explained in more detail subsequently, it has raised many questions which can only be answered with new physics. Briefly, we will go over the basic mathematical formulation of the Standard Model. We will then discuss the reasons for needing physics beyond the Standard Model.

The theoretical basis of the Standard Model is that it has an $SU(3)_c \times SU(2)_w \times U(1)_Y$ group structure, with the field content and charges under each group written out in table 1.1 below.

The $SU(2)_w \times U(1)_Y$ part of the theory describes weak and electromagnetic interactions. It is a chiral theory, meaning that the left-handed and right-handed fields do not transform in the same way under the symmetries of the theory. In this case, the left-handed fields transform as doublets of $SU(2)_w$, whereas the right-handed fields transform as singlets. The symmetry group undergoes spontaneous symmetry breaking via the Higgs mechanism, as will be described in more detail later, to leave an unbroken $U(1)_{em}$, the electromagnetic force. It therefore has 3 massive bosons (the W's and the Z), and one massless boson (the photon).

Meanwhile the $SU(3)_c$ part of the theory describes the strong interactions. It is an unbroken symmetry, with exactly massless bosons, the gluons. In the same way that the electroweak forces do not distinguish between colours, the strong force does not distinguish between flavours, coupling equally strongly to all species of quarks.

Mathematical formulation of the Standard Model

The Lagrangian of the theory can be written as

$$\mathcal{L}_{SM} = \mathcal{L}_{gauge} + \mathcal{L}_{matter} + \mathcal{L}_{Yukawa} + \mathcal{L}_{Higgs} \ , \tag{1.1}$$

Field	$\mathbf{SU(3)_c}$	$\mathbf{SU(2)_w}$	$\mathbf{U(1)_Y}$	Spin
$H = \begin{pmatrix} H^+ \\ H^0 \end{pmatrix}$	**1**	**2**	$\frac{1}{2}$	0
$W_\mu^{1,2,3}$	**1**	**3**	0	1
B_μ	**1**	**1**	0	1
g_μ^a	**8**	**1**	0	1
$Q_L^i = \begin{pmatrix} u \\ d \end{pmatrix}_L, \begin{pmatrix} c \\ s \end{pmatrix}_L, \begin{pmatrix} t \\ b \end{pmatrix}_L$	**3**	**2**	$\frac{1}{6}$	1/2
$u_R^i = u_R,\ c_R,\ t_R$	**3**	**1**	$\frac{2}{3}$	1/2
$d_R^i = d_R,\ s_R,\ b_R$	**3**	**1**	$-\frac{1}{3}$	1/2
$L_L^i = \begin{pmatrix} \nu_e \\ e \end{pmatrix}_L, \begin{pmatrix} \nu_\mu \\ \mu \end{pmatrix}_L, \begin{pmatrix} \nu_\tau \\ \tau \end{pmatrix}_L$	**1**	**2**	$-\frac{1}{2}$	1/2
$e_R^i = e_R,\ \mu_R,\ \tau_R$	**1**	**1**	-1	1/2

Table 1.1: Field content and charges under the gauge groups of the Standard Model.

where the first term is the gauge sector of the theory, the second is the fermionic sector, the third holds the Yukawa interactions between the fermions and the Higgs field, and the last contains the Higgs sector. The gauge Lagrangian consists of:

$$\mathcal{L}_{gauge} = \sum_{\mathcal{G}} -\frac{1}{4} F_{\mu\nu}^a F^{\mu\nu,a} \ , \tag{1.2}$$

where the sum is done over each of the groups; Greek indices denote Lorentz indices; and the latin index corresponds to the group index. Einstein summation convention for the indices

is assumed here, and in the rest of the text. The field strength tensor $F_\mu\nu$ is defined as

$$F^a_{\mu\nu} = \begin{cases} \partial_\mu B_\nu - \partial_\nu B_\mu & \text{Abelian,} \\ \partial_\mu W^a_\nu - \partial_\nu W^a_\mu + g f^{abc} W^b_\mu W^c_\nu & \text{Non-Abelian,} \end{cases} \tag{1.3}$$

for Abelian and Non-Abelian gauge groups, where g and f^{abc} are the gauge coupling and the structure constant of the group, respectively.

The matter content of the Lagrangian contains the fermionic fields we wrote in table 1.1 above, which by virtue of their spin, obey the Dirac equation, giving rise to the following structure:

$$\mathcal{L}_{matter} = \sum_{i,j} \bar{f}^i_L i \not{D} f^i_L + \bar{f}^j_R i \not{D} f^j_R \ , \tag{1.4}$$

where we have separated out the fermions according to their chirality, with sums over the i left-handed and j right-handed fields. Here, D is the covariant derivative

$$D_\mu = \partial_\mu - \sum_{\mathcal{G}} i g t^a A^a_\mu \ , \tag{1.5}$$

which is contracted with a gamma matrix in Feynman slash notation: $\not{D} = \gamma^\mu D_\mu$. The t^a are the generators of the corresponding group $\mathcal{G}$. The above part of the Lagrangian therefore gives rise to all the fermionic interactions with the spin-1 bosons of the Standard Model.

The Yukawa sector of the Standard Model is required to give masses to the fermions, and has the following form:

$$\mathcal{L}_{Yukawa} = -y^{ij}_u \bar{Q}^i_L \tilde{H} u^j_R - y^{ij}_d \bar{Q}^i_L H d^j_R - y^{ij}_l \bar{L}^i_L H e^j_R \ , \tag{1.6}$$

where the y^{ij} are matrices in flavour-space, and $\tilde{H} = -i\sigma_2 H$, where σ_2 is one of the Pauli matrices. When the Higgs boson acquires a vacuum expectation value, v, the Yukawa Lagrangian will give rise to mass terms for each of the fermions, given by $yv/\sqrt{2}$. These terms also give rise to the Higgs-fermion interactions of the Standard model.

The Higgs sector

The Higgs sector of the Standard Model deserves some more care, as it will lead into one of the primary motivations for considering Supersymmetry as an attractive theory of new physics.

The Higgs Lagrangian is

$$\mathcal{L}_{Higgs} = |D_\mu H|^2 - \mu^2 |H|^2 - \lambda |H|^4 \ , \tag{1.7}$$

which is manifestly symmetric under $SU(2)_w \times U(1)_Y$ by construction. The potential is minimised for $\langle H \rangle = 0$ when $\mu^2 > 0$ and $\lambda > 0$. However, when $\mu^2 < 0$, the potential develops a new minimum at

$$\langle H \rangle = \frac{1}{\sqrt{2}} \begin{pmatrix} 0 \\ v \end{pmatrix}, \qquad v = \sqrt{\frac{-\mu^2}{\lambda}} \ . \tag{1.8}$$

This new minimum does not respect the $SU(2)_w \times U(1)_Y$ symmetry, but rather only has one $U(1)$ symmetry left over, which we identify as that of electromagnetism, $U(1)_{em}$. Since there were initially $3+1$ generators, but the residual symmetry only has 1, there are 3 broken generators, corresponding to massless Goldstone bosons. These Goldstone bosons do not remain massless, however, as they are "eaten" by three of the gauge bosons of the theory, giving them a mass. This can be seen by writing out the kinetic part of $\mathcal{L}_{Higgs}$:

$$\begin{aligned}
|D_\mu H|^2 &= |\left(\partial_\mu \mathbb{I}_2 - i g_Y Y B_\mu \mathbb{I}_2 - i g_2 t^a W_\mu^a\right) H|^2 \\
&= \frac{1}{2} \left| \left(\begin{pmatrix} \partial_\mu & 0 \\ 0 & \partial_\mu \end{pmatrix} - i\frac{g_Y}{2} \begin{pmatrix} B_\mu & 0 \\ 0 & B_\mu \end{pmatrix} - i\frac{g_2}{2} \begin{pmatrix} W_\mu^3 & W_\mu^1 - iW_\mu^2 \\ W_\mu^1 + iW_\mu^2 & -W_\mu^3 \end{pmatrix} \right) \begin{pmatrix} 0 \\ h+v \end{pmatrix} \right|^2 \\
&= \frac{1}{2}(\partial_\mu h)^2 + \frac{g_2^2}{8}(h+v)^2 \left(|W_\mu^1|^2 + |W_\mu^2|^2\right) + \frac{1}{8}(h+v)^2 \left(|-g_Y B_\mu + g_2 W_\mu^3|^2\right) \ ,
\end{aligned}$$

where we denote the $U(1)_Y$ gauge coupling as g_Y, the $SU(2)_w$ gauge coupling as g_2, Y is the hypercharge of the Higgs boson (in this case $1/2$), and h is the physical Higgs boson which remains out of the four initial degrees of freedom of the complex scalar doublet.

We see that there are two mass terms, one for the combination $|W_\mu^1|^2 + |W_\mu^2|^2$, and one for the combination $|-ig_Y B_\mu + ig_2 W_\mu^3|^2$. The first we identify as being $W_\mu^+ W^{\mu,-}$, where

$$W_\mu^+ = \frac{1}{\sqrt{2}} W_\mu^1 - iW_\mu^2 \ , \tag{1.9}$$

with mass

$$m_W^2 = \frac{g_2^2}{4} v^2 \ , \tag{1.10}$$

and the second we identify as the Z boson mass term, with

$$Z_\mu = \frac{g_2 W_\mu^3 - g_Y B_\mu}{\sqrt{g_Y^2 + g_2^2}} \ , \tag{1.11}$$

with mass

$$m_Z^2 = \frac{g_Y^2 + g_2^2}{4} v^2 \ . \tag{1.12}$$

The photon, which is the orthogonal combination of B_μ and W_μ^3 to that of the Z boson,

$$A_\mu = \frac{g_2 W_\mu^3 + g_Y B_\mu}{\sqrt{g_Y^2 + g_2^2}} \ , \tag{1.13}$$

remains massless, in concordance with expectations. The angle which diagonalises W_μ^3 and B_μ is called the electroweak angle, and is defined as

$$\sin\theta_W = \frac{g_Y}{\sqrt{g_Y^2 + g_2^2}} \ , \tag{1.14}$$

such that there is a simple tree-level relation between the masses of the W and Z bosons

$$1 - \frac{m_W^2}{m_Z^2} = \sin^2\theta \ , \tag{1.15}$$

which is a result of a custodial symmetry. This custodial symmetry is broken at the one-loop level, so that the corrections to the above relation are loop-suppressed. For more information on this custodial symmetry, see for example [27].

We now turn our attention to the physical Higgs Boson h. We see from expanding the potential

$$\begin{aligned} V(H) &= \frac{\mu^2}{2}(v+h)^2 + \frac{\lambda}{4}(v+h)^4 \\ &= -\frac{1}{2}\lambda v^2 (v+h)^2 + \frac{\lambda}{4}(v+h)^4 \\ &= \lambda v^2 h^2 + \lambda v h^3 + \frac{\lambda}{4} h^4 \ , \end{aligned} \tag{1.16}$$

where in going from the first to the second line, we have replaced $-\mu^2 = \lambda v^2$. We see that the physical Higgs boson gets a mass,

$$m_h^2 = 2\lambda v^2 = -2\mu^2 \ . \tag{1.17}$$

This last equation contains one of the strongest motivations for physics beyond the Standard Model. In principle, the bare mass μ that we wrote at the start could have taken on any value, since there was no mechanism or symmetry to make it small. However, we have observed a Higgs Boson with a mass of 125 GeV [25, 26, 28], which is much lighter than the cut-off of the theory, which, naively, should be the Planck scale $M_{pl} = 10^{19}$ GeV. This is troubling, because the Higgs Boson mass receives radiative corrections, which are quadratically divergent:

$$\Delta m_h^2 \simeq -\frac{3y_t^2}{8\pi^2}\Lambda^2 \ , \tag{1.18}$$

where y_t is the Top quark Yukawa, which is nearly 1, therefore giving the dominant contribution to the divergence, and Λ is the ultraviolet cut-off of the theory. Therefore, naively, the Higgs Boson mass should be of order $\Lambda \sim M_{pl}$, and not at the electroweak scale. The puzzle of why the Higgs is so light is known as the "hierarchy problem", and is one of the primary motivations for Supersymmetry. How and why Supersymmetry helps alleviate the hierarchy problem will be explained in the next section.

1.2 Introduction to Supersymmetry

The dangerous radiative corrections to the Higgs Boson mass that we saw in the preceding section can be mitigated in a number of ways. One might think that by postulating new physics at some scale Λ to cancel off the divergence in Eq. 1.18, the problem would be solved. However, this new physics must have a very specific structure in order to properly cancel the divergence. For example, introducing some scalar S that couples quadratically to the Higgs gives rise to a correction

$$\Delta m_h^2 \simeq \frac{\kappa}{16\pi^2}(\Lambda^2 - 2m_S^2 \log \Lambda/m_S) \ , \tag{1.19}$$

so for the contributions from both the scalar (above) and the fermion (Eq. (1.18)) to cancel would require exactly tuning the coupling of the scalar to the Higgs, κ. Such a tuning is difficult to justify from a theoretical perspective. However, we point out the useful fact that scalars give contributions to the Higgs mass that carry the opposite sign to that of the top quark, which is a fermion.

Ideally, there would be a symmetry argument that could be used to explain why $\kappa \simeq 6y_t^2$ in order to exactly cancel the large quadratically divergent piece of Eq. (1.18), and this is precisely where Supersymmetry provides an elegant solution.

The Supersymmetry Algebra

Let us now take a step back and consider the symmetries of spacetime. We know from the Coleman-Mandula theorem [29], which was subsequently extended [30], that for an interacting quantum field theory, such as the Standard Model, the number of ways of extending the Poincaré symmetry of spacetime is extremely restricted. However, one of the only allowed extensions is Supersymmetry. The generators of Supersymmetry are spinors, and therefore obey anticommutation relations.

Therefore, in addition the usual Poincaré generators (boosts, rotations, translations), one includes complex spinor generators Q and $Q^\dagger$, which obey the following anticommutation relations:

$$\{Q_\alpha, Q_\beta\} = \{Q^\dagger_{\dot\alpha}, Q^\dagger_{\dot\beta}\} = 0, \qquad \{Q_\alpha, Q^\dagger_{\dot\alpha}\} = 2\sigma^\mu_{\alpha\dot\alpha} P_\mu \ , \tag{1.20}$$

where P_μ is a translation generator (momentum), and $\sigma^\mu_{\alpha\dot\alpha} = (1, \sigma^i)$, where σ^i are the usual Pauli matrices. The Supersymmetry generators commute with translations

$$[P_\mu, Q_\alpha] = [P_\mu, Q^\dagger_{\dot\alpha}] = 0 \ . \tag{1.21}$$

The effect of these generators on various states is to turn a fermion into a boson, and vice versa.

$$Q|\text{fermion}\rangle \to |\text{boson}\rangle, \qquad Q|\text{boson}\rangle \to |\text{fermion}\rangle, \tag{1.22}$$

The irreducible representations of the Supersymmetry algebra are called supermultiplets, which contain both bosons and fermions. Bosons and fermions that reside in the same supermultiplet are referred to as "superpartners". For $\mathcal{N} = 1$ Supersymmetry, defined to be where there is only one Q and one $Q^\dagger$, we can therefore have four different types of supermultiplets (assuming spin ≤ 2):

- Chiral supermultiplet: (spin-0 scalar, spin-1/2 fermion),
- Vector supermultiplet: (spin-1/2 fermion, spin-1 boson),
- Rarita-Schwinger supermultiplet: (spin-1 boson, spin-3/2 fermion),
- Graviton supermultiplet: (spin-3/2 fermion, spin-2 boson),

which we can then use to construct our supersymmetric theory. The third type of supermultiplet we have called "Rarita-Schwinger" because it contains a spin-3/2 fermion which obeys

the Rarita-Schwinger equation. However, it is not to be confused with the "gravitino" which will be referred to hereafter, which is the spin-3/2 fermion in the Graviton supermultiplet.

In the case when the Supersymmetry is unbroken, because $P^\mu P_\mu$ commutes with both Q and $Q^\dagger$, the masses of all particles in a supermultiplet must be the same. This would mean, for example, that if we had an exactly supersymmetric Standard Model, we would expect to see superpartners of Standard Model particles with the exact same mass. Since phenomenologically, this is clearly not the case, it means that Supersymmetry must broken in the vacuum we exist in. We will return to this point later, when discussing Supersymmetry breaking mechanisms.

The Minimal Supersymmetric Extension to the Standard Model (MSSM)

Having briefly explained what Supersymmetry is, and how the various supermultiplets can be constructed, let us now consider what the minimal contents of a supersymmetric Standard Model would look like.

We saw the field content of the Standard Model in Table 1.1, so the obvious first step is to promote all those fields to supermultiplets of some type. For each of the spin-1 bosons of the Standard Model, looking at our list above, we see that there must now be a corresponding vector supermultiplet. Meanwhile for each of the chiral fermion fields, there must be a chiral supermultiplet.

For each 2-component Weyl fermion, there are 2 fermionic degrees of freedom, n_F. Since Supersymmetry requires that $n_F = n_B$ in each supermultiplet, where n_B is the number of bosonic degrees of freedom, for a Weyl fermion we must introduce a complex scalar with $n_B = 2$. The nomenclature for the superpartner of a Standard Model fermion is to add *s-* (for scalar) in front, so an electron's superpartner is a *selectron*, and so on.

For each massless (before symmetry breaking) gauge boson, $n_B = 2$, therefore the superpartner must be a Weyl fermion with $n_F = 2$. Since the gauge bosons reside in the adjoint representation of the gauge group, their superpartners must also reside in the adjoint, and are therefore self-conjugate. The nomenclature for the superpartner of a Standard Model gauge boson is to add *-ino* at the end, so a gluon's superpartner is a *gluino*, and so on.

The Higgs sector of the theory is somewhat more complicated, as promoting the single Standard Model Higgs into a chiral supermultiplet introduces a set of problems. A Higgs supermultiplet with Hypercharge $Y = 1/2$ will couple to up-type quarks only, while a Higgs supermultiplet with Hypercharge $Y = -1/2$ will couple to down-type quarks and leptons only, due to the requirement that the Yukawa terms in a supersymmetric theory be holomor-

phic. Additionally, including only one of the two supermultiplets would lead to anomalies. A requirement of a consistent theory is that gauge anomalies be cancelled (see e.g. [31]), e.g. $\mathrm{Tr}[(t^a)^2 Y] = \mathrm{Tr}[Y^3] = 0$, and the inclusion of only one Higgs supermultiplet with Hypercharge $Y = \pm 1/2$ would result in the traces not evaluating to zero. Therefore, for the minimal supersymmetric version of the Standard Model to be consistent, we must introduce two Higgs supermultiplets, H_u and H_d, with Hypercharge $Y = 1/2$ and $Y = -1/2$ respectively. The overall field content is shown in Table 1.2.

Supermultiplet	$\mathbf{SU(3)_c}$	$\mathbf{SU(2)_w}$	$\mathbf{U(1)_Y}$	Field & Spin
$H_u = \begin{pmatrix} H_u^+, & H_u^0 \end{pmatrix}$	$\mathbf{1}$	$\mathbf{2}$	$\frac{1}{2}$	$(h_u^+, h_u^0) : 0, \quad (\tilde{h}_u^+, \tilde{h}_u^0) : 1/2$
$H_d = \begin{pmatrix} H_d^0, & H_d^- \end{pmatrix}$	$\mathbf{1}$	$\mathbf{2}$	$-\frac{1}{2}$	$(h_d^0, h_d^-) : 0, \quad (\tilde{h}_d^0, \tilde{h}_d^-) : 1/2$
$W^{1,2,3}$	$\mathbf{1}$	$\mathbf{3}$	0	$W_\mu^{1,2,3} : 1, \quad \tilde{W}^{1,2,3} : 1/2$
B	$\mathbf{1}$	$\mathbf{1}$	0	$B_\mu : 1, \quad \tilde{B} : 1/2$
g^a	$\mathbf{8}$	$\mathbf{1}$	0	$g_\mu^a : 1, \quad \tilde{g}^a : 1/2$
Q_i	$\mathbf{3}$	$\mathbf{2}$	$\frac{1}{6}$	$\begin{pmatrix} u, d \end{pmatrix}_L^i : 1/2, \quad \begin{pmatrix} \tilde{u}, \tilde{d} \end{pmatrix}_L^i : 0$
U_i^c	$\bar{\mathbf{3}}$	$\mathbf{1}$	$-\frac{2}{3}$	$u_R^{\dagger,i} : 1/2, \quad \tilde{u}_R^{*,i} : 0$
D_i^c	$\bar{\mathbf{3}}$	$\mathbf{1}$	$\frac{1}{3}$	$d_R^{\dagger,i} : 1/2, \quad \tilde{d}_R^{*,i} : 0$
L^i	$\mathbf{1}$	$\mathbf{2}$	$-\frac{1}{2}$	$\begin{pmatrix} \nu, e \end{pmatrix}_L^i : 1/2, \quad \begin{pmatrix} \tilde{\nu}, \tilde{e} \end{pmatrix}_L^i : 0$
E_i^c	$\mathbf{1}$	$\mathbf{1}$	1	$e_R^{\dagger,i} : 1/2, \quad \tilde{e}_R^{*,i} : 0$

Table 1.2: Supermultiplets and charges under the gauge groups of the Minimal Supersymmetric Standard Model.

With this supermultiplet content, we can then construct "superfields", in order to eventually be able to construct a Lagrangian for the Minimal Supersymmetric Standard Model (for more, see for example [32] and [33]). In order to do this, we use the following coordinate

system:

$$x_\mu, \theta^\alpha, \theta^\dagger_{\dot\alpha} \ , \tag{1.23}$$

where $\theta^\alpha, \theta^\dagger_{\dot\alpha}$ are complex anti-commuting Weyl spinors with mass dimension $-1/2$. This also requires the introduction of derivatives with respect to these anti-commuting coordinates, namely Chiral covariant derivatives:

$$D_\alpha = \frac{\partial}{\partial\theta^\alpha} - i(\sigma^\mu\theta^\dagger)_\alpha\partial_\mu, \quad D^\alpha = -\frac{\partial}{\partial\theta_\alpha} + i(\theta^\dagger\bar\sigma^\mu)^\alpha\partial_\mu, \tag{1.24}$$

$$D^{\dagger\dot\alpha} = \frac{\partial}{\partial\theta^\dagger_{\dot\alpha}} - i(\bar\sigma^\mu\theta)^{\dot\alpha}\partial_\mu, \quad D^\dagger_{\dot\alpha} = -\frac{\partial}{\partial\theta^\dagger_{\dot\alpha}} + i(\theta\sigma^\mu)_{\dot\alpha}\partial_\mu \ , \tag{1.25}$$

In this coordinate system, a general superfield can then be written as

$$\mathcal{F}(x,\theta,\theta^\dagger) = \phi + \theta\psi + \theta^\dagger\chi^\dagger + \theta\theta F + \theta^\dagger\theta^\dagger G + \theta^\dagger\bar\sigma^\mu\theta V_\mu + \theta^\dagger\theta^\dagger\theta\xi + \theta\theta\theta^\dagger\eta^\dagger + \theta\theta\theta^\dagger\theta^\dagger D \ , \tag{1.26}$$

which has 8 bosonic degrees of freedom, ϕ, F, G, D and four in V_μ, and 8 fermionic degrees of freedom in the four 2-component spinors ψ, χ, ξ, η.

A chiral superfield Φ (like the ones we will need for the MSSM), is then obtained by

$$\Phi = D^\dagger D^\dagger \mathcal{F} \ , \tag{1.27}$$

$$\Phi = \phi + i\theta^\dagger\bar\sigma^\mu\theta\partial_\mu\phi + \frac{1}{4}\theta\theta\theta^\dagger\theta^\dagger\partial^2\phi + \sqrt{2}\theta\psi' - \frac{i}{\sqrt{2}}\theta\theta\theta^\dagger\bar\sigma^\mu\partial_\mu\psi' + \theta\theta F \ , \tag{1.28}$$

so that in terms of the components of the general superfield above, $\psi = \sqrt{2}\psi'$, $\chi^\dagger = 0$, $G = 0$, $V_\mu = i\partial_\mu\phi$, $\xi = 0$, $\eta = -\frac{i}{\sqrt{2}}\bar\sigma^\mu\partial_\mu\psi'$. We notice that ϕ is the scalar partner of ψ', and F is an auxiliary field.

A vector superfield V, like the ones we will need for the supermultiplets containing the vector bosons of the MSSM, is obtained by requiring that V be real. Thus $\psi^\dagger = \chi^\dagger$, $G = F^*$, $\xi^\dagger = \eta^\dagger$. In so-called Wess-Zumino gauge, we can eliminate the fields ϕ, ψ, F, this can then be written as

$$V = \theta^\dagger\bar\sigma^\mu\theta V_\mu + \theta^\dagger\theta^\dagger\theta\eta + \theta\theta\theta^\dagger\eta^\dagger + \frac{1}{2}\theta\theta\theta^\dagger\theta^\dagger D \ , \tag{1.29}$$

where we identify V_μ as a gauge boson, with η being the gaugino superpartner, and D being

an auxiliary field. The field strength chiral superfield is then defined as:

$$\mathcal{W}_\alpha = \begin{cases} -\frac{1}{4}D^\dagger D^\dagger D_\alpha V, & \text{Abelian,} \\ -\frac{1}{4}D^\dagger D^\dagger(\exp(-V)D_\alpha \exp V), & \text{non-Abelian.} \end{cases} \tag{1.30}$$

Given these superfields, one can construct what is known as a "superpotential" W, which is a holomorphic function of chiral superfields, is invariant under the gauge symmetries of the theory, and has mass dimension 3. We may also construct what is known as the "Kähler potential" K, which is a function of chiral superfields and, antichiral superfields (Φ^*), and the vector superfield, in a way that is supergauge invariant. From these, we may construct Lagrangians:

$$\begin{aligned} \mathcal{L} = \frac{1}{4}\left(\int d^2\theta\ \mathcal{W}(B)\mathcal{W}(B) + \mathcal{W}_\alpha(W)\mathcal{W}_\alpha(W) + \mathcal{W}_\alpha(g)\mathcal{W}_\alpha(g) + h.c.\right) \\ + \int d^2\theta(W + h.c.) + \int d^2\theta d^2\theta^\dagger K \end{aligned} \tag{1.31}$$

For readers interested in learning more of the mathematical formulation of supersymmetric Lagrangians, please see for example [34, 35, 32].

The Minimal Supersymmetric Standard Model superpotential is written as:

$$W = -U^c \boldsymbol{Y_u} Q H_u - D^c \boldsymbol{Y_d} Q H_d - E^c \boldsymbol{Y_e} L H_d + \mu H_u H_d\ , \tag{1.32}$$

where we have dropped flavour and $SU(2)$ indices i and α. The $\boldsymbol{Y_f}$ are matrices of Yukawa couplings. The superfields in the superpotential are constructed out of the supermultiplets tabulated above in 1.2.

In principle, there are four other terms that we could have written down in the MSSM superpotential, which are gauge invariant and renormalizable, but violate either baryon number B or lepton number L. When included, these terms would result in tree-level proton decay and neutrino masses, and therefore there are strong constraints on the couplings of those terms. However, one can define a symmetry, known as R-parity, under which those terms are not allowed:

$$P_R = (-1)^{3(B-L)+2s}\ , \tag{1.33}$$

where s is the spin of the field. The particles in the same supermultiplet now clearly have different P_R, with Standard Model particles and the two Higgses having $P_R = +1$, and

superpartners having $P_R = -1$. Phenomenological consequences of this are that a) the lightest superparticle in the theory with $P_R = -1$ can not decay further, and is therefore absolutely stable, and b) superpartners can only be produced in even numbers.

We will now briefly discuss Supersymmetry breaking, since it will be important to understanding how one can have supersymmetric models with relatively light gauginos, but heavy scalars.

Lightning Introduction to Supersymmetry Breaking

If our vacuum had unbroken Supersymmetry, this would have fixed the Higgs Boson hierarchy problem by guaranteeing that the quadratic divergences to all scalar masses of the theory would cancel to all orders in perturbation theory. In the Minimal Supersymmetric extension of the Standard Model (MSSM), Supersymmetry dictates that the dimensionless couplings are related in the right way to cancel the quadratic divergences we saw in Eq. (1.18). Taking for example the top quark contribution given in Eq. (1.18), Supersymmetry requires that the coupling κ in Eq. (1.19) should be given by $2 \times N_c y_t^2$, where $N_c = 3$ is the number of colours of the *s*top quark, so that the quadratically divergent parts of Eq. (1.18) and Eq. (1.19) exactly cancel. The factor of two arises due to the fact that for each Standard Model fermion, we had to introduce exactly *two* bosonic degrees of freedom.

However, as discussed briefly, phenomenologically, by the absence of degenerate superpartners, we know that Supersymmetry is broken in our vacuum. We can nevertheless deduce some information about how the breaking comes about by requiring that the breaking does not spoil the relations between the dimensionless couplings that resulted in the cancellation of the quadratic divergences. This leads us to consider what is known as "soft" Supersymmetry breaking, where the MSSM Lagrangian contains two parts, one which is invariant under Supersymmetry, and one which explicitly breaks Supersymmetry, but only contains mass terms and coupling parameters with positive mass dimension:

$$\mathcal{L}_{MSSM} = \mathcal{L}_{SUSY} + \mathcal{L}_{soft\ \cancel{SUSY}} \, . \tag{1.34}$$

The first term contains all the gauge and Yukawa interactions, preserving the relationship between dimensionless couplings, while the second contains the masses of the superpartners

and the trilinears:

$$-\mathcal{L}_{soft\ \not{SUSY}} = \frac{1}{2}\left(\sum_a M_a \tilde{G}_a + h.c.\right) + \left(\mathbf{A}_U^{ij}\tilde{u}_L^i h_u \tilde{u}_R^{*,j} + \mathbf{A}_D^{ij}\tilde{d}_L^i h_d \tilde{d}_R^{*,j} + \mathbf{A}_E^{ij}\tilde{e}_L^i h_d \tilde{e}_R^{*,j} + h.c.\right)$$
$$+ (\tilde{m}_q^2)_j^i \tilde{q}_L^{i,\dagger}\tilde{q}_L^j + (\tilde{m}_u^2)_j^i \tilde{u}_L^{i,T}\tilde{u}_L^{j,*} + (\tilde{m}_d^2)_j^i \tilde{d}_L^{i,T}\tilde{d}_L^{j,*} + (\tilde{m}_\ell^2)_j^i \tilde{l}_L^{i,\dagger}\tilde{l}_L^j + (\tilde{m}_e^2)_j^i \tilde{e}_L^{i,T}\tilde{e}_L^{j,*}$$
$$+ m_{H_u}^2 h_u^\dagger h_u + m_{H_d}^2 h_d^\dagger h_d + (B\mu h_u h_d + h.c.)\ , \tag{1.35}$$

where the M_a, with $a = 1, 2, 3$ are the masses of the Bino, Wino and Gluino respectively, the $\mathbf{A}$ are trilinear couplings which have mass dimension one, the second line gives bare masses to all the scalar partners of Standard Model fermions, and the third line gives the Higgs scalar mass terms. If there was a common mass scale for all the terms in $\mathcal{L}_{soft\ \not{SUSY}}$, which we will denote as $\tilde{m}$, the expected corrections to the Higgs mass would be approximately

$$\Delta m_h^2 \sim \tilde{m}^2 \frac{\lambda}{16\pi^2}\log\frac{\Lambda}{\tilde{m}}\ , \tag{1.36}$$

where λ is some dimensionless coupling (recall from the discussion earlier that the problematic quadratically divergent corrections cancel, but the log-divergent term in Eq. (1.19) does not). This would suggest that in order to not spoil the supersymmetric solution to the hierarchy problem, $\tilde{m}$ should not be very large, and indeed, should not be much larger than the TeV scale. This is one of the strongest motivations for low-energy Supersymmetry.

The exact values of the parameters of the soft Supersymmetry-breaking Lagrangian depend on the precise mechanism for breaking Supersymmetry. In fact, Supersymmetry breaking mechanisms are in and of themselves a rich field of ongoing study. As a result, we will not presume to go into too much detail here, but will instead present a few of the more well-known/motivated options, and an overview of the types of spectrum they would give.

We will use the following notation here, and later on, for the gaugino masses: $m_{1/2}$, and for the scalar masses: m_0. While having universal gaugino and scalar masses will not necessarily always be the case, it is a useful tool for getting a feel for the scales involved.

- **Gravity mediation**: Supersymmetry may be broken in a hidden sector, and is communicated to the visible sector by Planck-suppressed operators [36, 37, 38, 39, 34]. The resulting soft masses are set, in most models, by the value of the gravitino mass, $M_{3/2}$:

$$m_0^2 \sim M_{3/2}^2, \quad m_{1/2} \sim \mathcal{O}(M_{3/2})\ . \tag{1.37}$$

  in most cases, although $m_{1/2} \gg M_{3/2}$ can occur in certain constructions [40]. In M-

Theory with gravity mediation, however, $m_{1/2} \ll M_{3/2}$ is generally expected (see for example [11]).

- **Gauge mediation**: Supersymmetry is again broken in a hidden sector, but is now communicated to the visible sector by "messenger fields", which couple indirectly to the fields of the MSSM via the ordinary gauge interactions [41, 42, 43]. The resulting soft masses are then generated by radiative corrections, and are therefore loop-suppressed relative to the mass scale of the messengers Λ_M:

$$M_a \sim \frac{g_a^2}{16\pi^2}\Lambda_M, \quad m_i^2 \sim \Lambda_M^2 \left(\sum_a \left(\frac{g_a^2}{16\pi^2} \right)^2 C_a(i) \right) \ , \tag{1.38}$$

  where a denotes gauge group, i denotes scalar species, and $C_a(i)$ is the quadratic Casimir invariant.

- **Gaugino mediation**: In an extra-dimensional setup, Supersymmetry may be broken in a hidden sector on a brane that is separated spatially from the visible sector brane along the extra dimension(s). Here, the gauge supermultiplets propagate in the bulk (i.e. between the branes), and therefore feel the Supersymmetry breaking directly, although the effects are suppressed by the size/length of the extra dimension(s) [44, 32, 45, 46]:

$$m_{1/2} \sim \frac{\langle F \rangle}{M_5^2 R_5} \ , \tag{1.39}$$

  in a 5-dimensional setup, where $\langle F \rangle$ is the non-zero vacuum expectation value of an auxiliary field F on the hidden sector brane, and M_5, R_5 are a mass and length scale associated with the fifth dimension. The scalar masses then feel Supersymmetry breaking only at loop level.

- **Anomaly mediation**: again in an extra-dimensional setup (although 4D realisations exist), Supersymmetry is broken on the spatially separated brane, but the transmission to the visible sector brane is not due to the gauge supermultiplets, which do not propagate in the bulk. Instead, the breaking manifests itself due to an anomalous violation of scale invariance, through the non-zero beta functions and anomalous dimensions of the MSSM fields and couplings. The various soft parameters are then [32, 47, 48]:

$$M_a \sim M_{3/2} \frac{b_a^{(1)} g_a^2}{16\pi^2}, \quad (m^2)_j^i \sim M_{3/2}^2 \frac{d}{dt}\gamma_j^i \ , \tag{1.40}$$

where $b_a^{(1)}$ is the one-loop beta function coefficient of the gauge coupling, γ_j^i is the anomalous dimension matrix of the fields, and "..." depends on the beta functions of the gauge and Yukawa couplings.

- **Breaking in the G_2-MSSM**: in this compactified 11-dimensional M-Theory, Supersymmetry is broken by the stabilisation of the moduli fields associated with the compact extra dimensions. The breaking is then communicated to the visible sector gravitationally, leading to [11, 13, 14, 18, 19]:

$$m_{1/2} \sim \alpha_{GUT} M_{3/2}, \quad m_0^2 \sim M_{3/2}^2(1 - C) \ , \tag{1.41}$$

where α_{GUT} is the unified theory coupling, and C is a parameterisation of higher order corrections from the Kähler potential, which can take on values between 0 and 1.

From this brief overview of only a few Supersymmetry breaking mechanisms, there is clearly a wide range of low-energy spectra that can arise. However, since in this dissertation we are mostly concerned with spectra that give heavier scalars, that means we will not be so interested in, for example, spectra arising from pure gauge- or anomaly-mediated Supersymmetry breaking. However, the breaking in the G_2-MSSM, for example, provides a proof of concept of having light gauginos (suppressed by approximately a loop factor) relative to the scalars. This is precisely the type of spectrum we will mostly consider in subsequent chapters.

1.3 Motivation for studying Supersymmetry with heavier scalars

As discussed in the previous section, it is quite possible for the pattern of Supersymmetry breaking from compactified String/M-Theory to give spectra with scalars that are a loop factor *heavier* than the gauginos. Given this sort of spectrum, there are then various phenomenological and theoretical considerations we can apply to reduce the range of possible spectra, which will provide a motivation for studying Supersymmetry with heavier scalars (10-100 TeV).

The first motivation is purely theoretical. In, for example, the G_2-MSSM, the gravitino mass $M_{3/2}$ is entirely fixed by the dynamics of the compactification. As we will see in Chapter 2, we can use certain assumptions about the compactification to fix a range of values for $M_{3/2}$

which are theoretically viable. We will see that there is a benchmark value of $M_{3/2} \sim 35$ TeV, with slight modifications of the compactification yielding a variation around that value of about a factor of 3, so from 10-100 TeV. Thus, we have a working String compactification that suggests we should be studying Supersymmetry with heavier scalars.

The second motivation is phenomenological. If the lightest visible supersymmetric particle (LVSP) is stable (which is not guaranteed, as we will see in Chapter 6), then it could be a dark matter candidate. In order to achieve the correct dark matter relic density, we would expect the mass of the LVSP to then be in the 100-1000 GeV range, if it is a gaugino/higgsino. This suggests that spectra of interest should have relatively light gauginos/higgsinos, but places no requirement on the scalars other than $m_0 \geq m_{1/2},\ \mu$, where μ is the higgsino mass parameter. However, from LHC searches for scalars, we know that they are likely to be heavier than ~ 1 TeV. This therefore hints at a small hierarchy between the gauginos/higgsinos and the scalars.

The third motivation is also phenomenological. The Higgs Boson mass, as discussed, receives radiative corrections to its tree-level mass, as discussed above. As it happens, the observed mass of 125 GeV is easily achievable if in fact there are heavier scalars [49, 50, 51, 52, 53].

1.4 Outline of this dissertation

1.4.1 Chapter 2: Superpartners at LHC and Future Colliders Predictions from Constrained Compactified M-Theory

In this chapter, which is based on [19], written in collaboration with Gordon L. Kane and Bob Zheng, we present a particularly well-motivated supersymmetric theory which predicts heavier SUSY scalars. We make use of both experimental results as well as theoretical tools to constrain this theory both from the bottom-up, and from the top-down. In particular, we require that the theory be consistent with the observed Higgs Boson mass (bottom-up), and understanding of a type of string theory called M-Theory (top-down), to find a class of supersymmetric spectra which can be probed at colliders. We make use of, and expand on, results obtained many years ago [10, 11, 12, 13, 14, 15, 16, 17, 18]. We then study the implications of a benchmark spectra for searches to be conducted at the LHC, and at possible future colliders, including a 100 TeV proton-proton collider. We find that making use of both bottom-up and top-down constraints provides a strong theoretical grounding for

the types of models that will be considered throughout this dissertation.

1.4.2 Chapter 3: Reaching for Squarks and Gauginos at a 100 TeV proton-proton Collider

This chapter is based on [21], written in collaboration with Bob Zheng. In this chapter, we study in more detail the potential for discovering supersymmetric models with heavier scalars at a 100 TeV proton-proton collider. In order to cover a wider range of the parameter space with heavier scalars, we consider a variety of simplified models which are loosely motivated by the benchmark spectrum from Chapter 2. We then analyse the possible reach of a 100 TeV proton-proton collider when the heavy squarks are produced in association with gluinos, winos, higgsinos and binos, in various configurations. For squarks above ~ 20 TeV, associated production becomes the only possible discovery channel, since the squark pair production cross-section is too small. Some of the results from this chapter were included in Chapter 3 of the "Physics at the FCC-hh" Report [54], a report commissioned to investigate the physics prospects of a future 100 TeV proton-proton collider.

1.4.3 Chapter 4: Impact of Future Lepton Flavor Violation Measurements in the Minimal Supersymmetric Standard Model

In this chapter, which is based on [22], written in collaboration with Aaron T. Pierce, we change tack from the previous two chapters, where we studied the phenomenology of supersymmetric models with heavier scalars at colliders. Instead, in this chapter we consider a wide range of supersymmetric models, including some with lighter scalars, and how these can be studied via their effects on low-energy experiments. In particular, we consider the specific situation where there is no new CP violation from the SUSY sector. We then analyse how the constraints from experiments searching for quark flavour-changing neutral currents compare with those searching for lepton flavour violation. These experiments, while incapable of directly discovering supersymmetric particles, can indirectly probe the pattern of Supersymmetry breaking. We show that when the SUSY scalars are heavier, lepton flavour violation experiments will probe large new regions of the parameter space. We also show the constraints on the parameter space for lighter supersymmetric particles, for completeness.

1.4.4 Chapter 5: Theoretical Prediction and Impact of Fundamental Electric Dipole Moments

In this chapter, which is based on [20], written in collaboration with Gordon L. Kane, we again study effects of Supersymmetry which can be tested using low-energy experiments. In this chapter, unlike in chapter 4, we allow CP violation to be present, and therefore study in particular the electric dipole moments of the electron and neutron generated by the supersymmetric particles. Also unlike in chapter 4, in this chapter we study in greater detail the same compactified M-Theory that we studied in Chapter 2. The reason is that the assumption that the M-Theory is correct provides greater control on both the expected amount of CP violation, as well as the spectrum of superparticles. We find that in this M-Theory compactification, while one might have thought that the heavier scalars would mean that the electric dipole moments would be small, this is not the case. In fact, two-loop diagrams, which are of lesser importance for electroweak-scale Supersymmetry, actually dominate when the scalars are heavy. As a result, we find that the particular M-Theory compactification we study predicts an electron electric dipole moment that is in reach of the next generation of experiments, thereby providing a strong test of the theory. As a corollary, we explain why in such a compactified M-Theory, electric dipole moments should be expected to be so small.

1.4.5 Chapter 6: The lightest visible-sector supersymmetric particle is likely to be unstable

This chapter and chapter 7 deviate slightly from the preceding chapters, in that they do not specifically study supersymmetric theories with heavier scalars. Instead, they consist of more general results that apply to all supersymmetric theories, and are therefore relevant to the models with heavier scalars considered in the previous chapters. In this chapter, which is based on [23], written in collaboration with Bobby Acharya, Gordon L. Kane, Brent Nelson and Malcolm Perry, we present an argument based on compactified string/M-Theory, that the lightest visible supersymmetric particle, which is typically assumed to be stable, is in fact unstable. This conclusion can have profound implications for the understanding of dark matter in supersymmetric theories, since the lightest visible-sector supersymmetric particle is usually assumed to be a component, if not all of, the dark matter. By arguing that string/M-Theory indicates that the lightest visible supersymmetric particle is likely to be unstable, we are indicating that it cannot be the dark matter, and therefore motivates a paradigm shift.

We argue a few crucial conditions are met by generic string/M-Theory compactifications, that cause the lightest visible supersymmetric particle to decay into a "hidden sector". This can have observable consequences at colliders, but even more important consequences for supersymmetric model-building, as it requires the serious consideration that dark matter resides in a hidden sector.

1.4.6 Chapter 7: Visualizing gauge unification with high-scale thresholds

In this chapter, which is based on [24], written in collaboration with James D. Wells, we again present more general results, which can be applied to Supersymmetry with heavier scalars. We study in particular how the gauge couplings of a low-energy theory, such as Supersymmetry, can be unified in a Grand Unified Theory (GUT). We present in this chapter a novel way of visualising the evolution of gauge couplings as a function of scale, in terms of the high-scale threshold corrections that would be required to achieve unification. This novel approach has the benefit of presenting the results in an easily interpretable graphical representation. Additionally, it has the benefit of being agnostic of the specifics of the ultraviolet theory, and can therefore be applied to any GUT one wishes to consider. Finally, it is powerful because, unlike usual studies of unified theories, it does not require the definition of a unified gauge coupling. Due to the potential violence from high-scale threshold corrections, defining a unified gauge coupling is not necessarily physically meaningful from the IR perspective. We apply our method to various models, including a supersymmetric model with heavy scalars, thus providing a link to the preceding chapters.

Chapter 2

Superpartners at LHC and Future Colliders Predictions from Constrained Compactified M-Theory

2.1 Introduction

In this chapter, we will discuss how taking a concrete compactification of M-Theory, the G_2-MSSM, will allow us to derive a well-motivated spectrum with heavier supersymmetric scalars, and then study the phenomenology. We use both theoretical and phenomenological motivations to arrive at a benchmark spectrum.

If Supersymmetry (SUSY) is considered as an effective theory of a well-motivated ultraviolet (UV) completion, concrete predictions can be made about the Supersymmetric particle (sparticle) spectrum that is to be expected at the TeV scale. In a top-down approach, the Supersymmetry breaking parameters are set by high-scale dynamics. This leads to concrete, testable predictions for sparticle masses, as opposed to treating sparticle masses as free parameters in a multidimensional parameter space.

In this chapter, we illustrate the power of this top-down approach for a particularly well-motivated UV completion of Supersymmetry: M-theory compactifications on manifolds with G_2 holonomy [55, 56, 57, 58, 59]. We call this framework the G_2-MSSM, following earlier papers which have studied its phenomenological properties [10, 11, 14, 13]. Due to the rigidity of top-down theoretical constraints from moduli stabilization and Supersymmetry breaking, the sparticle spectrum is completely fixed by electroweak symmetry breaking (EWSB), once both the gravitino mass $M_{3/2}$ and the superpotential μ-term are specified. Furthermore, the

measured value of the Higgs mass picks out a particular slice in the $(\mu, M_{3/2})$ plane; thus *all* sparticle masses can be fixed by determining either μ or $M_{3/2}$.

Given minimal assumptions (explained in more detail in Appendix A) regarding the geometry of the compact G_2-manifold, $M_{3/2}$ is approximately calculable once the moduli are stabilized and SUSY is broken. This results in a central value of $M_{3/2} = 35$ TeV. Imposing EWSB and Higgs mass constraints, $M_{3/2} = 35$ TeV corresponds to a gluino mass of 1.5 TeV. The result $M_{3/2} = 35$ TeV can be altered if UV threshold corrections to the non-perturbative superpotential are non-negligible. Allowing a wider range of $20\,\text{TeV} < M_{3/2} < 50\,\text{TeV}$ due to currently unknown UV corrections gives a range of gluino masses, $1\,\text{TeV} < M_{gluino} < 2$ TeV. Thus a gluino mass within this range can be taken as a prediction of the compactified M-theory framework.

For concreteness we will focus on the central value $M_{3/2} = 35$ TeV, which gives a benchmark spectrum with a 1.5 TeV gluino. All sfermion and heavy Higgs masses are of $\mathcal{O}(M_{3/2})$, while the Wino(Bino)-like lighter gauginos have masses of 615 (450) GeV. The hierarchy between gauginos and $M_{3/2}$ follows from the dynamics of moduli stabilization. Specifically, both the hidden sector meson and moduli F-terms contribute to the gravitino mass $M_{3/2}$, while only the moduli F-terms contribute to gaugino masses. The moduli F-terms are suppressed with respect to hidden sector meson F-terms by about $\alpha_{GUT} \approx 1/25$, resulting in $\lesssim$ TeV gaugino masses despite $M_{3/2}$ being tens of TeV [14]. As will be discussed below, this benchmark spectrum is not constrained by LHC-8. Both gluino pair production *and* direct electroweak gaugino production should yield discoveries with $\lesssim 300$ fb $^{-1}$ of LHC-14 data, particularly since electroweak gauginos yield distinctive signatures through $\chi_2^0 \to \chi_1^0 + h$ which has a nearly 100% branching ratio. This bencmark spectrum predicts $\mu \approx 1.4$ TeV, leading to heavy Higgsinos which are out of reach of LHC-14.

We will also discuss implications of the G_2-MSSM for future colliders. Taking the benchmark spectrum, we will show that 1.5 TeV Higgsinos are accessible at both 50 and 100 TeV colliders. Furthermore, the heavier squarks are also accessible at 100 TeV colliders, with hundreds of squark-gluino associated production events expected with $\gtrsim 1000$ fb^{-1} of data. In particular, we point out for the first time (as far as we know) that for a gluino mass of $\sim$ TeV, the cross-section for associated stop-gluino-top production $pp \to \tilde{g} + \tilde{t}_1 + t$, and potentially even sbottom-gluino-bottom $pp \to \tilde{g} + \tilde{b}_1 + b$, can be sizeable at 100 TeV colliders for stops and sbottoms lighter than ~ 20 TeV. This is especially relevant for MSUGRA-like theories with universal scalar masses at the GUT scale, in which third generation squarks are expected to be lighter due to RGE effects.

Thus the benchmark spectrum has the remarkable feature that Higgsinos and squarks are accessible at future colliders, despite the scale of SUSY breaking $M_{3/2}$ being in the tens of TeV range. Furthermore, the constrained relationship between SUSY breaking parameters implies that within the G_2-MSSM, *the discovery of a single sparticle is enough to actually measure* $M_{3/2}$. Given the discovery of a single sparticle, the rest of the G_2-MSSM spectrum is determined uniquely, resulting in a multitude of additional predictions which can be readily confirmed or falsified in ongoing and upcoming collider experiments. This point highlights the potential power of top-down approaches in greatly reducing the naive parameter space of Supersymmetry. We will provide details concerning these points in later work; the results can basically be seen from equations (2.1, 2.2) and Figure 2.1 in Section 2.2 below.

The chapter is organised as follows. Section 2.2 gives a brief overview of the G_2-MSSM framework, and discusses how the benchmark spectrum corresponding to $M_{3/2} = 35$ TeV is obtained. Readers interested only in experimental predictions should skip this section. Section 2.3 provides the sparticle spectrum and relevant branching ratios corresponding to the benchmark spectrum obtained in Section 2.2. Predictions for LHC-14 are given in Section 2.4, while predictions for future colliders are given in Section 2.5. Finally, we summarise the results in Section 5.5.

2.2 Theoretical Framework

We begin by reviewing some features and successes of the compactified M-theory framework. G_2-compactifications of M-theory provide a natural setting for full moduli stabilisation and broken $\mathcal{N} = 1$ Supersymmetry in a deSitter vacuum, while also solving the gauge hierarchy problem [10, 11, 14, 13]. Additionally, EDM [15, 20] and flavour constraints (such as $B_s \to \mu\mu$) [60] are avoided. However, it may not explain $(g-2)_\mu$, while the strong CP problem is solved by the axionic components of moduli fields [61]. The presence of late-decaying moduli results in a non-thermal cosmological history which solves the moduli problem and the gravitino problem [12]. Since the baryon asymmetry and the dark matter both arise from moduli decay (including axions), the ratio of baryonic matter to dark matter is calculable [62]. R-parity conservation is expected [63]; thus consistency with the observed DM relic abundance implies that the visible sector LSP will decay to hidden sector DM particles [64][1]. μ is incorporated into the theory following the proposal of Witten [67] and including effects

[1]For non-thermal cosmologies, a stable Bino-LSP will overclose the universe, while a stable Wino-LSP is in tension with indirect detection contraints [65, 66].

of moduli stabilisation [17]. Calculations in this framework anticipated the mass and decay branching ratios of the Higgs boson observed at the LHC [50].

A key result of the aforementioned references is that once moduli stabilization breaks Supersymmetry and cancels the vacuum energy at tree level, the relationship between SUSY breaking parameters becomes very constrained. Upon moduli stabilization and SUSY breaking, the soft breaking parameters at the renormalization scale $Q \sim M_{GUT}$ are given by [13]:

$$\begin{aligned} & m_0^2 \approx M_{3/2}^2 (1 - C) , \quad A_0 \approx 1.5 M_{3/2} (1 - C) , \\ & M_a \approx [-0.032\eta + \alpha_{GUT} (0.034 (3C_a - C_a') + 0.079 C_a' (1 - C))] \times M_{3/2} \end{aligned} \tag{2.1}$$

where $C_a = (0, 2, 3)$ and $C_a' = (33/5, 7, 6)$. m_0 and A_0 are universal soft scalar masses and trilinears, and "C" parameterizes higher order Kähler potential corrections arising from higher dimensional operators as defined in Appendix A. The quantity η parameterizes KK-threshold corrections to the unified gauge coupling; we will argue in Section 2.2.2 that $\eta \sim 1$, unless the geometry of the G_2 manifold becomes incredibly complicated. A review of moduli stabilization and SUSY breaking along with the derivation of (2.1) is presented in Appendix A. The hierarchy between gaugino masses and $M_{3/2}$ arises because $M_{3/2}$ feels contributions from both hidden sector meson and moduli F-terms, while M_a feels contrbutions from only the moduli F-terms which are suppressed by approximately $\alpha_{GUT} \approx 1/25$ with respect to the meson F-terms. A more detailed discussion of this point is deferred to Appendix A.

Thus the *entire* sparticle spectrum is essentially fixed once $M_{3/2}$, μ and C are specified. We will show in Section 2.2.1 that imposing consistent EWSB along with the measured value of the Higgs mass $M_h = 125.2 \pm 0.4$ GeV [28, 68] reduces the 3D space of allowed $(M_{3/2}, \mu, C)$ values to an approximately one-dimensional space. As a result, the entire sparticle spectrum is completely determined for a given value of $M_{3/2}$. In Section 2.2.2 we will use additional top-down considerations to approximately calculate $M_{3/2}$, giving a central value of $M_{3/2} \approx 35$ TeV which we use to obtain the benchmark spectrum considered in Section 2.3 and onwards.

2.2.1 Imposing Constraints: EWSB and the Higgs Mass

In the previous section, we have stated that the sparticle spectrum is essentially determined by three quantities: $M_{3/2}$, μ, C, or equivalently $M_{3/2}, \mu/M_{3/2}, C$. In principle, these quantities are calculable from the full UV theory. In practice however, there are theoretical uncertainties which preclude a full top-down calculation. Instead, we will show in this section how bottom-up constraints of EWSB along with the measured Higgs mass provide two

independent constraints, reducing the naive 3D region to a one-dimensional strip. This illustrates the power of combining top-down calculations with known bottom-up constraints to increase the predictiveness of a particular theory.

A detailed discussion of how the constraints from EWSB and $M_h = 125.2 \pm 0.4$ GeV are imposed is given in Appendix B; the result is shown in Figure 2.1. One can see that EWSB constraints restrict the region to an approximately 2D-slice. Imposing the constraint $M_h = 125.2 \pm 0.4$ reduces this slice to a thin band; the thickness of this band is due primarily to experimental uncertainties on M_h, M_t and α_s [50]. The range $0 < \mu/M_{3/2} \lesssim 0.1$ is motivated by both top-down [17] and little hierarchy [69] arguments; this is discussed in more detail in Appendix B.

Upon imposing these bottom-up constraints, the entire sparticle spectrum becomes an approximately one-dimensional strip in the original 3D space. In the next section, we take the perspective that Figure 2.1 fixes the entire spectrum in terms of $M_{3/2}$, and use equation (A.6) to approximately compute $M_{3/2}$ to be $\approx 35\,\text{TeV}$, and obtain the associated benchmark spectrum.

2.2.2 Obtaining a Benchmark Spectrum

Having established that the entire Supersymmetric particle spectrum is essentially determined for a given value of $M_{3/2}$, we discuss how $M_{3/2}$ can be approximately computed from the UV theory. Upon moduli stabilization and SUSY breaking, the standard Supergravity expression for the gravitino mass gives [13] :

$$M_{3/2} \approx \frac{9 \times 10^5}{V_X^{3/2}} \left(\frac{A_2}{Q}\right) \text{ TeV} \tag{2.2}$$

where Q is the rank of a hidden sector $SU(Q)$ gauge group which undergoes gaugino condensation, and A_2 is the corresponding non-perturbative superpotential coefficient (see Eq. (A.1) in Appendix A). V_X is the volume of the G_2-manifold in 11-D Planck units. We refer interested readers to Appendix A for a more detailed derivation of Eq. (2.2).

In principle, V_X is a function of the moduli fields and is thus calculable once moduli are stabilized. However the particular expression for V_X in terms of moduli fields is not fully known; we can instead fix V_X by ensuring that dimensional reduction to 4D gives the correct

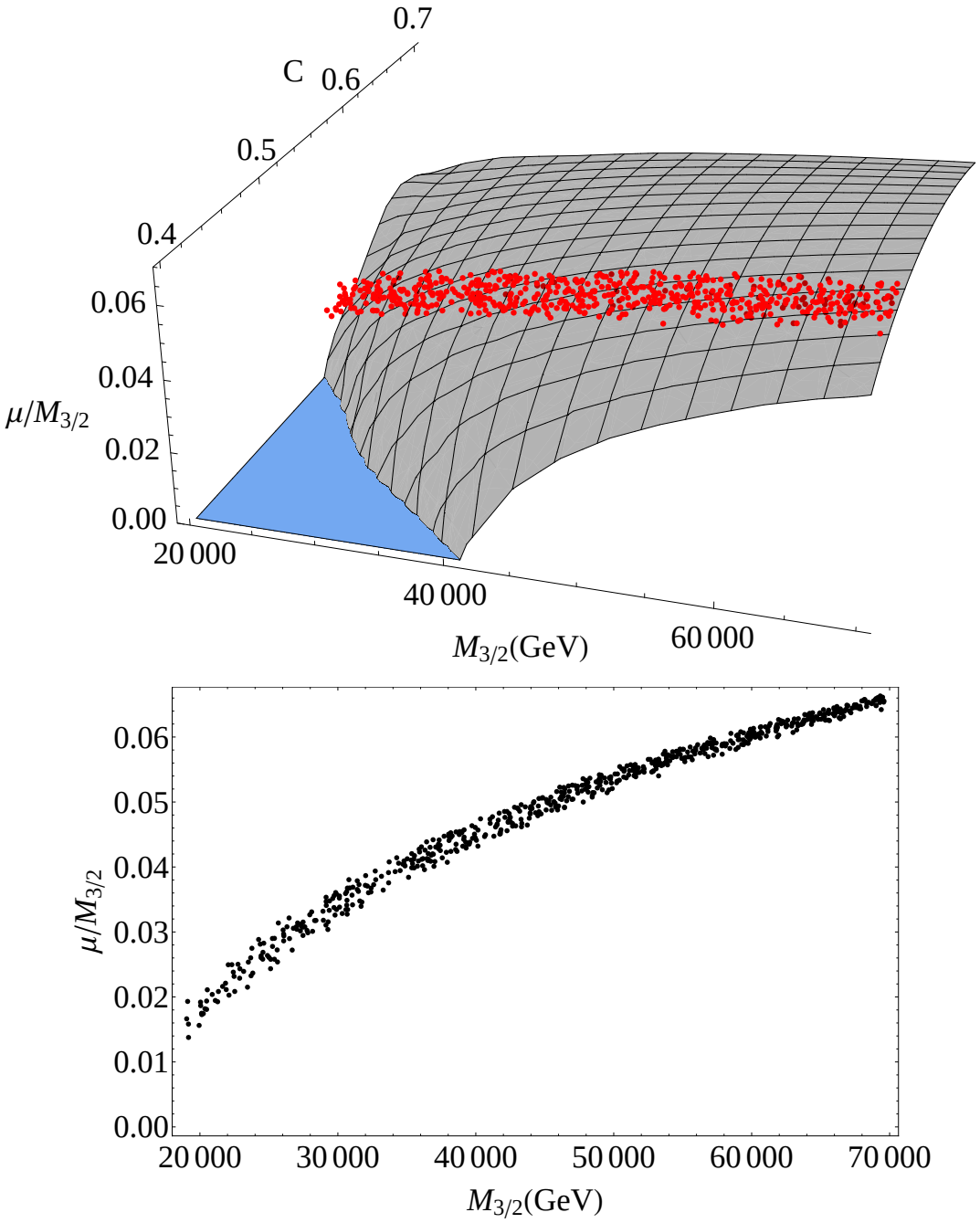

Figure 2.1: **Upper Figure**: The dark gray surface shows the slice of $M_{3/2}, c, \mu/M_{3/2}$ parameter space which satisfies EWSB, while red points also satisfy the Higgs mass constraint $M_h = 125.2 \pm 0.4$ GeV. The blue shaded region corresponds to points which are inconsistent with $\mu/M_{3/2} \lesssim 0.1$; see the Appendix for further discussion. In these plots, μ is defined at the renormalization scale $Q^2 = m_{\tilde{t}_1} m_{\tilde{t}_2}$. The mesh lines are added for perspective, and do not have any physical significance.
Lower Figure: A projection of the upper figure onto the $M_{3/2} - \mu/M_{3/2}$ plane.

value for Newton's constant [70]. This fixes V_X to be [13]:

$$V_X \approx 137.4\, L(\mathcal{Q})^{2/3}, \quad L(\mathcal{Q}) = 4q\, \sin^2\left(\frac{5\pi\omega}{q}\right) \tag{2.3}$$

where $L(\mathcal{Q})$ is a topological invariant which parameterizes threshold corrections from Kaluza-Klein states. This form for $L(\mathcal{Q})$ was computed in [70], assuming that the visible sector $SU(5)$ gauge fields are compactified on a Lens space $\mathcal{Q} \cong S_3/Z_q$ in the presence of a non-trivial Wilson line. For a brief introduction to Wilson lines, see Appendix C. $5\,\omega$ is an integer parameterizing the effect of the Wilson line, as will be discussed below.

To proceed, we briefly review the motivation for considering $SU(5)$ gauge theories compactified on a Lens space $\mathcal{Q}$. In G_2-compactifications of M-theory, non-abelian gauge fields arise from co-dimension 4 ADE singularities and thus propogate on a 7-dimensional manifold $\mathcal{H}$ [56]. In our notation, we take $\mathcal{H} \cong \mathcal{Q} \times M$ where M is our Minkowski spacetime. Starting from an $SU(5)$ GUT theory, the issues of GUT breaking and doublet-triplet splitting must be resolved for a realistic model. As pointed out by Witten, both problems are elegantly solved in the presence of a non-trivial Wilson line background [67], which breaks $SU(5)$ to the SM while admitting a geometric symmetry which solves doublet-triplet splitting.

The resulting symmetry is determined by the fundamental group of $\mathcal{Q}$, which for $\mathcal{Q} \cong S_3/Z_q$ is simply Z_q. The non-trivial Wilson line gives the $\int d^2\theta \mu H_u H_d$ superpotential term charge 5ω under Z_q, while $\int d^2\theta M T_u T_d$ is uncharged. However, realistic phenomenology requires non-zero μ, which implies that Z_q is broken once moduli with charge -5ω obtain *vev*'s [17]. If Z_q is completely broken, higher-dimensional Kähler potential operators will generate dangerous lepton-number violating operators which generically violate neutrino mass bounds [63]. Thus Z_q must be broken to a non-trivial subgroup Z_p, where:

$$p = \mathrm{GCD}(q, 5\omega), \quad p \neq 1 \tag{2.4}$$

The simplest case which satisfies these requirements is therefore the case where $p = 4$ and $5\omega = 2$, corresponding to the Lens space S_3/Z_4 and an unbroken Z_2 symmetry once a non-zero μ term is generated. For our benchmark spectrum, we take these values and obtain from (2.2), (2.3):

$$M_{3/2} \approx 35 \left(\frac{A_2}{Q}\right)\ \text{TeV}. \tag{2.5}$$

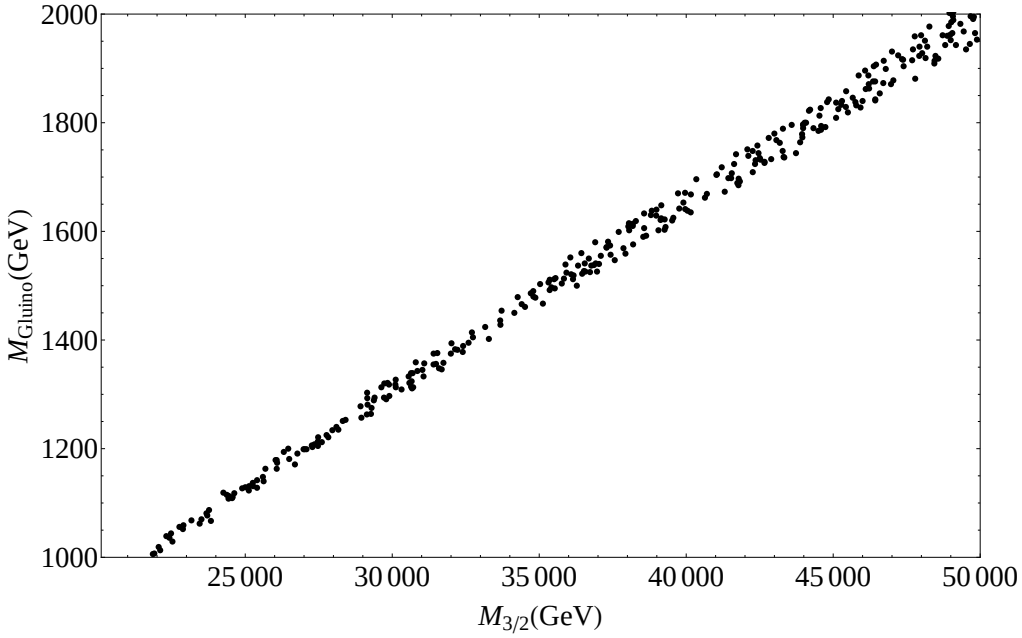

Figure 2.2: Gluino mass vs $M_{3/2}$ for points which satisfy EWSB and Higgs mass constraints, i.e. the red points in Figure 2.1.

Note that this also fixes η in (A.7) [70]:

$$\eta = 1 - \frac{5\alpha_{GUT}}{2\pi} \ln\left(\frac{L(Q)}{q}\right) \approx 0.956 \tag{2.6}$$

We see that $1 - \eta$ is loop suppressed, and can only be $\mathcal{O}(1)$ for $q \gtrsim 100$. This validates our earlier claim that one naturally expects $\eta \sim 1$.

The only remaining undetermined factor in our benchmark spectrum is A_2/Q in (2.5). In the context of Supersymmetric field theories, the precise normalization $A_2 = Q$ [71] in the $\overline{DR}$ scheme was determined by requiring the consistency of various techniques used to study non-perturbative SUSY gauge theories [72]. However, in the present context there may be UV threshold corrections which modify the relation $A_2/Q = 1$. To obtain the benchmark spectrum, we retain $A_2/Q = 1$, which gives $M_{3/2} = 35$ TeV. Imposing constraints from EWSB and M_h for this benchmark value fixes $C \approx 0.52$ and $\mu \approx 1.4$ TeV, resulting in the benchmark spectrum to be discussed in Section 2.3. Figure 2.2 illustrates the effect of relaxing this assumption; the gluino mass is plotted for $0.6 \lesssim A_2/Q \lesssim 1.4$, corresponding to $20\,\text{TeV} \lesssim M_{3/2} \lesssim 50$ TeV. $M_{3/2} = 20$ TeV may barely avoid tension with BBN constraints [16], depending on the particular values of moduli couplings and T_{RH}.

In order to obtain a very approximate lower bound on $M_{\tilde{g}}$, we use the `FastLim` [73]

package. The program currently only implements some of the possible event topologies, and does not yet implement cascade decays such as $\tilde{g} \to qq\chi_2^0 \to qqh\chi_1^0$. Therefore, when using `FastLim` we treat the aforementioned cascade decays as $\tilde{g} \to qq\chi_2^0 \to qq\chi_1^0$, neglecting additional objects from $\chi_2^0 \to \chi_1^0 + h$. This simplification obviously reduces sensitivity to searches involving high (≥ 6) jet multiplicity. Using this method, we obtain the approximate bound $M_{\tilde{g}} \gtrsim 1.1$ TeV in the compactified M-theory framework, though clearly a more precise analysis is desirable. Nonetheless, the benchmark spectrum with a 1.5 TeV gluino mass sits comfortably outside the excluded region, as we will discuss in Section 2.3.

2.3 The spectrum and the branching ratios

In this section we present the benchmark spectrum that results from the theoretical framework presented in Section 2.2. In the compactified M-Theory all scalars are generically of order the gravitino mass, with the universal scalar mass given by $m_0 \sim \mathcal{O}(1)M_{3/2}$. We use the computing package `SOFTSUSY` [8] to do two-loop RGE evolution of the high scale soft parameters to obtain sparticle pole masses.

We compute the branching ratios for the decays of some of the superpartners using `SDECAY` [74], which are given in Table 2.1. We focus in particular on the superpartners that we expect to see at the LHC or at future colliders.

Decay	BR (%)
$\tilde{g} \to \chi_1^+ q_{1,2}\bar{q}_{1,2}$	25
$\tilde{g} \to \chi_1^\pm b\bar{t},\ t\bar{b}$	23
$\tilde{g} \to \chi_1^0 t\bar{t}$	20
$\tilde{g} \to \chi_2^0 q_{1,2}\bar{q}_{1,2}$	12
$\tilde{g} \to \chi_1^0 q_{1,2}\bar{q}_{1,2}$	8
$\tilde{g} \to \chi_2^0 b\bar{b}$	7
$\tilde{g} \to \chi_2^0 t\bar{t}$	4
$\tilde{g} \to \chi_1^0 b\bar{b}$	1

Decay	BR (%)
$\chi_4^0 \to \chi_1^\pm W^\mp$	60
$\chi_4^0 \to \chi_2^0 h$	27
$\chi_4^0 \to \chi_1^0 h$	8
$\chi_4^0 \to \chi_2^0 Z$	4
$\chi_4^0 \to \chi_1^0 Z$	2
$\chi_3^0 \to \chi_1^\pm W^\mp$	60
$\chi_3^0 \to \chi_2^0 Z$	26
$\chi_3^0 \to \chi_1^0 Z$	8
$\chi_3^0 \to \chi_2^0 h$	4
$\chi_3^0 \to \chi_1^0 h$	2
$\chi_2^0 \to \chi_1^0 h$	98
$\chi_2^0 \to \chi_1^0 Z$	2

Decay	BR (%)
$\chi_2^\pm \to \chi_1^\pm h$	31
$\chi_2^\pm \to \chi_1^\pm Z$	30
$\chi_2^\pm \to \chi_2^0 W^\pm$	30
$\chi_2^\pm \to \chi_1^0 W^\pm$	9
$\chi_1^\pm \to \chi_1^0 W^\pm$	100

Table 2.1: Branching ratios of gluino, neutralinos and charginos. The numbers do not add to 100 in the case of the χ_4^0 branching ratios due to rounding errors.

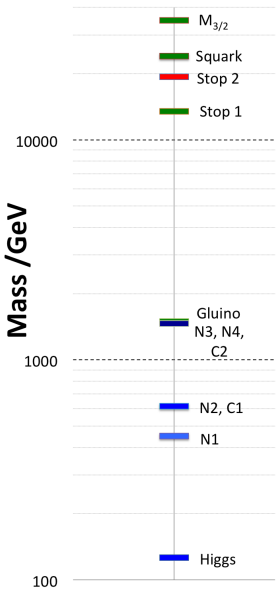

Particle	Mass (GeV)
m_0	24200
$M_{3/2}$	35000
$\tilde{q}_{L,R}$	24000
$\tilde{t}_2$	19300
$\tilde{t}_1$	13500
$\tilde{b}_2$	23900
$\tilde{b}_1$	19300
$\tilde{g}$	1500
χ_1^0	450
χ_2^0	614
χ_3^0	1460
χ_4^0	1460
$\chi_1^\pm$	614
$\chi_2^\pm$	1460
h	125.2[2]

Figure 2.3: Spectrum given GUT scale input values calculated from the theory for the central value $M_{3/2} = 35\,\text{TeV}$. This spectrum has the GUT scale inputs $m_0 \approx 24$ TeV and $A_0 \approx 25$ TeV, where m_0 and A_0 are respectively the universal scalar mass and soft-breaking trilinear. The GUT scale gaugino masses are $M_1 = -1020\,\text{GeV}$, $M_2 = -730\,\text{GeV}$, $M_3 = -590\,\text{GeV}$. Details on how this spectrum was derived are presented in Section 2.2. For the gaugino masses and trilinear, we take the sign convention opposite to that of `SOFTSUSY` [8]. This relative sign affects the 2-loop term in the gaugino mass RGE's which is proportional to A_t.

Since the squark masses are of $\mathcal{O}(M_{3/2})$ at the high scale, they are not detectable at the LHC. RGE running splits the squarks to give the physical spectrum shown in Fig. 2.3. The neutralinos χ_1^0 (χ_2^0) are Bino (Wino)-like, while χ_3^0, χ_4^0 are Higgsino-like. Note that the mixing angles in the neutralino and chargino sectors are small, as $\mu \gg M_W, M_Z$. In previous studies of the G_2-MSSM, the LSP was taken to be Wino-like, as a Wino-LSP serves as a good DM candidate in string-motivated non-thermal cosmologies [75]. However, obtaining a Wino-like as opposed to a Bino-like LSP requires large KK-threshold corrections to GUT scale gaugino masses (see e.g. [76]), which we argued is unnatural in Section 2.2. In this note, we assume that any would-be Bino-like LSP relic abundance decays to a hidden sector DM candidate, but the LSP is sufficiently long-lived to appear stable on collider scales[3].

Of note is the 100 % branching ratio of $\chi_1^\pm \to \chi_1^0 W^\pm$, and the 98.7 % branching ratio of $\chi_2^0 \to \chi_1^0 h$. Note that the $\chi_2^0 \to \chi_1^0 Z$ decay width is subdominant to that of $\chi_2^0 \to \chi_1^0 h$.

[2]For details regarding how the Higgs mass is calculated, we refer the reader to Appendix B.
[3]This occurs for example if χ_1^0 decays to hidden sector DM via kinetic mixing [64, 23].

This can be explained as follows. The $\chi_2^0\chi_1^0 h$ coupling arises from couplings of the form $\tilde{W}^0\tilde{H}h$ and $\tilde{B}^0\tilde{H}h$ in the gauge eigenstate basis. Since χ_1^0 and χ_2^0 are Bino and Wino-like, the $\chi_2^0 \to \chi_1^0 h$ amplitude is suppressed by a single power of gaugino-Higgsino mixing angles, $\mathcal{O}(M_Z/\mu)$. In contrast, in the gauge eigenstate basis only Higgsinos couple directly to Z via couplings of the form $Z_\mu \tilde{H}^\dagger \overline{\sigma}^\mu \tilde{H}$. Thus the $Z_\mu \chi_1^{0\dagger} \overline{\sigma}^\mu \chi_2^0$ coupling is suppressed by two powers of gaugino-Higgsino mixing angles, resulting in a suppresion of the $\chi_2^0 \to \chi_1^0 Z$ amplitude by $\mathcal{O}(M_Z^2/\mu^2)$.

Note that this spectrum with a 1.5 TeV gluino should not have been discovered at LHC-8. In simplified models with decoupled squarks, the strongest limits on the gluino production come from multijet + MET searches [77, 78, 79, 80], which place the bound $M_{\tilde{g}} \gtrsim 1.35$ TeV. When setting limits on simplified models, the gluino is assumed to have a 100% branching ratio into either $qq\chi_1^0$ or $tt\chi_1^0$ final states. For more realistic spectra such as the one considered here, the gluino mass bound will weaken significantly due to branching ratio factors.

2.4 LHC-14 Predictions

In this section, using the spectrum derived and presented above, we discuss the channels we expect to be observable at the LHC. We expect to see three channels, $pp \to \tilde{g}\tilde{g}$, $pp \to \chi_2^0\chi_1^\pm$ and $pp \to \chi_1^\pm\chi_1^\mp$, and only these. The fact that only these three channels would be apparent is a feature of the M-theory construction. The scalars being heavy makes them kinematically inaccessible. The hierarchy between μ and the gaugino masses M_a (and $\mu \gg M_Z$) results in a Bino-like LSP and Wino-like NLSP with heavy Higgsinos, meaning that only two neutralino/chargino direct production channels are accessible at LHC-14.

We computed using the production cross-sections to leading order for the three channels listed above using `MadGraph5` [81] and multiplied them by K factors calculated using `Prospino` [82, 83, 84]. The results, including the expected number of events N given 300 fb^{-1} of data, are tabulated below.

Channel	σ (fb)	N
$pp \to \tilde{g}\tilde{g}$	19	5800
$pp \to \chi_2^0\chi_1^\pm$	19	5800
$pp \to \chi_1^\pm\chi_1^\mp$	10	3000

Given the LSP mass of 450 GeV, a 1.5 TeV gluino is expected to be discoverable at the

5σ level at LHC-14 given 300 fb^{-1} of data [85, 86]. The gluino mass and cross-section allow immediate deduction of the gluino spin [87] and therefore confirmation that the discovery is indeed Supersymmetry. With squarks heavy, that procedure is straightforward. Furthermore, the $\chi_2^0 \to \chi_1^0 h$ decay mode allows for discovery potential in the chargino/neutralino direct production channels. For the benchmark spectrum considered here, direct $\chi_2^0, \chi_1^\pm$ production should be discoverable at LHC-14 with 1000 fb^{-1} of data [88]. We understand that careful background studies need to be done to be sure these processes can be observed. The signatures are distinctive and event numbers large enough so it seems likely signals can be seen, but people more expert than us need to demonstrate the signals are really robust.

2.5 Future Collider Predictions

In this section, we briefly discuss the possible discoveries to be made at future colliders given the spectrum under consideration. We focus in particular on two possible proton-proton colliders, one with $\sqrt{s} = 50\,\text{TeV}$, and the other with $\sqrt{s} = 100\,\text{TeV}$. Prospects for Supersymmetry at such higher energy colliders has been studied recently [86, 89, 90], although not in the context of a top-down, UV complete theory.

Given the spectrum, we find that some crucial new channels are accessible, namely $pp \to t\tilde{t}_1\tilde{g}$, $pp \to b\tilde{b}_1\tilde{g}$, $pp \to \tilde{q}_{1(L,R)}\tilde{g}$, $pp \to \chi_3^0\chi_4^0$, $pp \to \chi_3^0\chi_2^\pm$, $pp \to \chi_4^0\chi_2^\pm$ and $pp \to \chi_2^\pm\chi_2^\mp$.

Unfortunately, scalars are too heavy to be pair-produced [89]. However, we note that associated production of first family squarks with gluinos is accessible. The splitting of the light stop and the heavier first family squark masses, plus the kinematic measurement of the first family squarks, combine to give a precise measurement of the gravitino mass, the fundamental quantity that determines all masses in the theory, and thus deeply probes Supersymmetry breaking!

The associated production of stops and sbottoms can come from gluon splitting, or from the top (bottom) quark being considered as a parton. The question of when the top quark parton distribution function (PDF) becomes important has been studied recently [91], and it has been found that using a top PDF has only a small effect at $\sqrt{s} = 100\,\text{TeV}$. Therefore we simulate the production of stop gluino by looking at diagrams where the gluon splits and emits a top quark also. The bottom PDF is better known, and has a more significant effect at the energies in question, but for the purposes of this calculation, we present results using gluon splitting for the associated production of sbottoms. The dominant Feynman diagram for top stop gluino production is shown in fig. 2.4. The diagram for sbottoms is identical

with $b, \tilde{b}$ swapped for $t, \tilde{t}$. We recognise that careful studies of bottom and top PDFs need to be done to get fully reliable numbers.

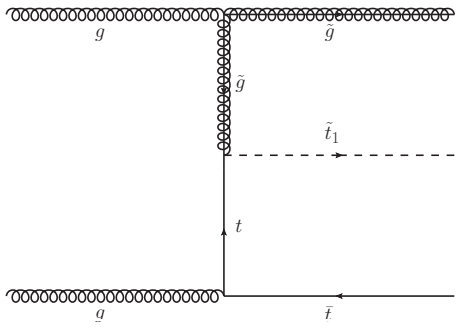

Figure 2.4: Dominant Feynman graph for stop associated production by gluon splitting.

We computed using `MadGraph5` [81] the production cross-sections to leading order for these channels for both $\sqrt{s} = 50$ TeV and 100 TeV. The results are tabulated below, including the number of events N expected given 3000 fb^{-1} of data.

Channel	$\sigma_{50\ \text{TeV}}$ (fb)	$N_{50\ \text{TeV}}$	$\sigma_{100\ \text{TeV}}$ (fb)	$N_{100\ \text{TeV}}$
$pp \to t\tilde{t}_1\tilde{g}$	7.1×10^{-5}	0	1.6×10^{-2}	47
$pp \to b\tilde{b}_1\tilde{g}$	2.6×10^{-6}	0	3.0×10^{-3}	9
$pp \to \tilde{q}_{1(L,R)}\tilde{g}$	3.2×10^{-4}	1	3.0×10^{-1}	900
$pp \to \chi_3^0\chi_4^0$	9.2×10^{-1}	2800	3.4	10200
$pp \to \chi_3^0\chi_2^\pm$	1.8	5400	6.4	19200
$pp \to \chi_4^0\chi_2^\pm$	1.8	5400	6.4	19200
$pp \to \chi_2^\pm\chi_2^\mp$	1.0	3000	3.7	11100

Although the number of stop events is not large, the gluino mass will already be known from LHC, which makes the stop and bottom search significantly simpler. The sbottom production cross-section is expected to be greater given that we make the approximation of gluon splitting rather than using the bottom PDF. We expect 15 or so stop events should already be found given 1000 fb^{-1} of data, as well as 300 first generation squark events. The relatively large number of first family squark associated production events means these should be detectable. Major potential backgrounds for there channels are $t\bar{t}$ and vector boson+jets. We also expect the heavy neutralinos and chargino to be detected, already at a 50 TeV, and certainly at a 100 TeV collider. Note there are other electroweakino production channels e.g. $\chi_2^0\chi_2^\pm$ which have subdominant production cross-sections, two or more orders of magnitude

smaller than those presented here. Because of their small production cross-sections, we do not list those channels here.

2.6 Conclusion

In this chapter, we have examined predictions for Supersymmetric particle masses in the G_2-MSSM, motivated by phenomenogically realistic compactifications of M-theory. By combining top-down constraints from moduli stabilization with bottom-up constraints from EWSB and the measured Higgs mass, the sparticle spectrum is completely determined by $M_{3/2}$. Furthermore, given reasonable assumptions regarding the topology of the G_2 manifold, the gravitino mass is approximately calculable, giving a benchmark value $M_{3/2} = 35$ TeV.

We emphasize that we do not give a pure derivation of $M_{3/2} = 35$ TeV, or of an upper limit of ~ 50 TeV. Rather we use all available top-down information from the UV theory, along with constraints and generic arguments, to find a "natural" value of the gravitino and gluino masses in the G_2-MSSM. If one is agnostic about UV physics, one could by hand fine-tune these quantities away from their natural or generic values that we deduce from the G_2-MSSM plus constraints. The natural and generic values we report are quite different from the "naïve natural" values in the absence of any theory.

The benchmark spectrum corresponding to $M_{3/2} = 35$ TeV is not constrained by LHC-8, and turns out to provide exciting phenomenology for LHC-14 and future colliders. The gluino mass is expected to be about 1.5 TeV for this benchmark spectrum, while the Wino(Bino)-like gaugino mass is about 614(450) GeV. The hierarchy between gaugino masses and $M_{3/2}$ arises because $M_{3/2}$ feels contributions from both the hidden sector meson and moduli F-terms, while gaugino masses only feel contributions from the moduli F-terms which are suppressed by about $\alpha_{GUT} \approx 1/25$ with respect to the meson F-terms. Three and only three production channels should discoverable at LHC-14: $pp \to \tilde{g}\tilde{g}$, $pp \to \chi_2^0\chi_1^\pm$ and $pp \to \chi_1^\pm\chi_1^\pm$ where χ_1^0 and χ_2^0 are respectively Bino and Wino-like. The expected signature of the $\chi_1^\pm\chi_1^\pm$ channel is $\chi^+\chi^- \to W^+W^- + \text{MET}$. The $\chi_2^0\chi_1^\pm$ production channel gives the final state $\chi_2^0\chi_1^\pm \to W^\pm h + \text{MET}$, which should be quite a clear channel at the LHC [88].

We have also investigated the prospects for the discovery of the heavier stops, first family squarks and Higgsinos at future colliders. We find that associated production of gluino stop $pp \to \tilde{g}\tilde{t}_1 t$, gluino sbottom $pp \to \tilde{g}\tilde{b}_1 b$ as well as gluino squark production $pp \to \tilde{g}\tilde{u}, \tilde{d}$ should be seen at a 100 TeV collider, with leading-order production cross-sections of 1×10^{-2}, 3×10^{-3} and 3×10^{-1} fb respectively. This leads to hundreds of gluino-squark events given

3000 fb^{-1} of data; precise knowledge of the gluino mass can help seperate these events from SM background. The heavy Higgsinos should also be detectable at a 50 TeV collider, and produced in relative abundance at a 100 TeV collider. The relevant Higgsino production channels are $pp \to \chi_3^0\chi_4^0$, $pp \to \chi_3^0\chi_2^\pm$, $pp \to \chi_4^0\chi_2^\pm$ and $pp \to \chi_2^\pm\chi_2^\pm$. The relevant production cross sections at 50 (100) TeV are $\sigma \sim 1.8$ (6.4) fb for $pp \to \chi_{3,4}^0\chi_2^\pm$, and $\sigma \sim 1.0$ (3.5) fb for $pp \to \chi_3^0\chi_4^0$ and $pp \to \chi_2^\pm\chi_2^\pm$. Thus given 3000 fb^{-1} of data, we expect of order a few thousand events for each channel at a 50 TeV collider, and of order tens of thousands of events at a 100 TeV collider.

To summarise, we have shown that the G_2-MSSM provides a constrained top-down framework, in which gluinos and some electroweakinos are discovered at LHC-14. The discovery of a single sparticle uniquely determines the remainder of the sparticle spectrum. Thus given a discovery of gauginos at LHC-14, a discovery of squarks and Higgsino at 100 TeV colliders within the predicted mass range would give strong evidence towards Supersymmetry and an UV completion like the compactified M-theory construction presented here.

While in this chapter we studied the precise collider phenomenology of a particular compactified M-Theory, in the next chapter we will consider the collider phenomenology of a general class of models which have similar features to those we considered here.

Chapter 3

Reaching for Squarks and Gauginos at a 100 TeV proton-proton Collider

3.1 Introduction

Current LHC data constrains strongly-interacting superpartner masses to lie near or above a TeV, disfavoring electroweak-scale SUSY in a wide variety of models. Also, as discussed both in Section 1.3 and Chapter 2 above, it is therefore becoming increasingly well motivated to consider the possibility that the superpartner masses lie above ~ 1 TeV, perhaps evading the kinematic reach of LHC-14. This has prompted numerous studies of the SUSY discovery potential of future hadron colliders, which have demonstrated that a $\sqrt{s} = 100$ TeV collider can extend the kinematic reach for superpartners into the multi-TeV range [86, 92, 90, 89, 19, 93, 94, 95, 96, 97]. While in Chapter 2 we studied the spectrum associated with a particular M-Theory compactification, in this chapter we study more general simplified models, which have qualitatively similar spectra to that of Chapter 2.

Previous studies of SUSY at future hadron colliders have focused primarily on pair production, either of colored superpartners [86, 92, 89] or of electroweak-inos [90, 93, 94, 95, 96]. In this chapter, we instead examine the reach of a $\sqrt{s} = 100$ TeV collider for associated production of a heavy squark along with a lighter gaugino. This production channel is particularly noteworthy if the squark masses are $\mathcal{O}(10)$'s of TeV, such that squark pair production is kinematically inaccessible at $\sqrt{s} = 100$ TeV. Spectra where squarks are hierarchically heavier than the gluino/electroweak-inos are predicted in many SUSY breaking models such as anomaly mediation [47, 48] or more general "mini-split"-type scenarios [98, 11, 51]. Moreover, multi-TeV squark masses can naturally accommodate the stop masses required to

achieve a 125 GeV Higgs boson within the MSSM.

In this chapter, we demonstrate that associated squark-gaugino production at a $\sqrt{s} = 100$ TeV proton-proton collider provides a probe of $\gtrsim 10$ TeV squark masses which is complementary to pair production. Our main results are summarized in Figures 3.1-3.5, which show the reach of a $\sqrt{s} = 100$ TeV proton-proton collider with 3 ab^{-1} integrated luminosity for squark-gaugino associated production in various spectra [1].

Squark-gluino production can discover squark masses up to 32 TeV for $\lesssim 4$ TeV gluino masses in spectra with a large gluino-neutralino LSP mass splitting (Fig 3.1). For spectra with a small gluino-neutralino LSP mass splitting, squark masses up to 40 TeV can similarly be discovered (Fig. 3.2). Notably, our analysis finds that the gluino-neutralino DM coannihilation region [100, 101] can be excluded for squark masses $\lesssim 32$ TeV. For squark-Wino (Bino) LSP production, Wino (Bino) masses up to 4 (2) TeV can be discovered for squark masses $\lesssim 9\,(6)$ TeV (Figs. 3.3-3.4). We find a similar reach for squark-Wino NLSP production (Fig 3.5), even without utilizing objects resulting from NLSP $\rightarrow$ LSP decay. Our results indicate that squark-gaugino production represents a SUSY discovery mode at a $\sqrt{s} = 100$ TeV proton-proton collider in a wide variety of models with heavy first- and second-generation squarks.

The remainder of this chapter is organized as follows. Section 3.2 discusses our general methodology and simulation strategies. Section 3.3 presents in detail our analysis of squark-gluino associated production, while Section 3.4 presents our analysis of squark-Wino/Bino associated production. We summarize our results in Section 3.5.

3.2 General Methodology

In this section we briefly discuss the general methodology of the analyses presented below. Event topologies arising from heavy squark - light gaugino associated production are characterized by a hard leading jet and significant $\not{E}_T$. These objects result primarily from the squark decay products, as the associated gaugino is produced at relatively low transverse momentum. The dominant SM background for such events is in the $t\bar{t}+$ jets and vector boson + jets channels [86], which fall off rapidly with increasing leading jet p_T, $\not{E}_T$, and $\not{E}_T/\sqrt{H_T}$ (H_T is defined as the scalar sum of the jet transverse energies).

In the following analyses, we consider the reach of a $\sqrt{s} = 100$ TeV proton-proton collider

[1] Note that a recent study in [99] calls for an integrated luminosity of between 10 and 20 ab^{-1} at a future 100 TeV proton-proton collider. We present here results for 3 ab^{-1} as a conservative estimate, and so as to be directly comparable with the current literature.

given 3 ab^{-1} integrated luminosity. The minimum production cross section yielding $\gtrsim 10$ events is roughly $\sim 10^{-2}$ fb, corresponding to $m_{\tilde{q}} + m_{\tilde{g}} \sim 35$ TeV ($m_{\tilde{q}} + m_{\tilde{W}} \sim 15$ TeV) for squark-gluino (squark-Wino) associated production. For such masses, good background discrimination is achieved with hard leading jet p_T cuts for squark-gluino production, and with hard $\not{E}_T/\sqrt{H_T}$ cuts for squark-Wino/Bino production. Our strategy is as follows: for each analysis we impose a set of baseline cuts catered to a set of spectra. We then scan over leading jet p_T and $\not{E}_T$ cuts (squark-gluino) or $\not{E}_T/\sqrt{H_T}$ cuts (squark-Wino/Bino) to maximize significance σ, defined by

$$\sigma \equiv \frac{S}{\sqrt{1 + B + \lambda^2 B^2 + \gamma^2 S^2}} \ . \tag{3.1}$$

S (B) is the number of signal (background) events passing cuts, and γ (λ) parameterize systematic uncertainties associated with signal (background) normalization. Details of the event generation and collider simulation are given in Appendix D. Like most future collider studies, our simulated σ values are subject to $\mathcal{O}(1)$ uncertainties associated with e.g. the performance of a detector which is yet to be designed. However, this translates to a comparatively mild uncertainty for the predicted reach, due to the rapid decrease of the production cross sections as a function of increasing mass.

Simplified Models

In the analyses presented below, we consider the following SUSY simplified models:

Model	**Particle Content**	**Fig.**
Squark-Gluino	$\tilde{q}$, $\tilde{g}$, $\chi_1^0 = \tilde{B}$	
Non-compressed	$M_1 = 100$ GeV	Fig. 3.1
Compressed	$m_{\tilde{g}} - m_{\chi_1^0} = 15$ GeV	Fig. 3.2
Squark-Wino LSP	$\tilde{q}$, $\chi_1^0 = \tilde{W}$	Fig. 3.3
Squark-Bino LSP	$\tilde{q}$, $\chi_1^0 = \tilde{B}$	Fig. 3.4
Squark-Wino NLSP	$\tilde{q}$, NLSP $= \tilde{W}$, $\chi_1^0 = \tilde{B}/\tilde{H}$	Fig. 3.5
Split	$M_1/\mu = 100$ GeV	
Non-split	$m_{\tilde{W}} - m_{\chi_1^0} = 200$ GeV	

Table 3.1: Simplified models considered in this chapter.

which encompass a wide array of potential event topologies arising from squark-gaugino

production. We take degenerate first and second generation squark masses, and decouple all sparticles not listed in Table 3.1. For the squark-gluino non-compressed model, our results are not sensitive to the choice of $M_1 = 100$ GeV as the LSP is effectively massless for $m_{\chi_1^0} \ll m_{\tilde{g}}$. The squark-gluino compressed model is motivated by the gluino-neutralino coannihilation region [100, 101]. We choose $m_{\tilde{g}} - m_{\chi_1^0} = 15$ GeV as a fiducial value, though the leading jet p_T-based analysis presented below is robust as long as $m_{\tilde{g}} - m_{\chi_1^0} \ll m_{\tilde{g}}$. For the Wino NLSP models, we choose two spectra with differing LSP masses to illustrate the effects of increasing the NLSP-LSP mass splitting. In the "non-split" case, we have chosen an NLSP-LSP mass splitting of 200 GeV so that the NLSP decays to the LSP + on-shell SM bosons.

3.3 Squark-Gluino Associated Production

In this section we discuss squark-gluino associated production. As this process only involves α_s, it can be important at a $\sqrt{s} = 100$ TeV proton-proton collider even if $m_{\tilde{q}} + m_{\tilde{g}} \gtrsim 35$ TeV. If a heavy squark of order tens of TeV is produced in association with a gluino of mass $\lesssim 10$ TeV, the leading jet from the squark decay will be very hard, $p_T \sim m_{\tilde{q}}/2$. Furthermore the neutralino resulting from the decay chain $\tilde{q} \to q\tilde{g} \to 3\,q\chi^0$ will be very boosted, resulting in large $\not{E}_T$. These kinematic features result in a striking collider signature with very low SM background.

We explore the reach in squark-gluino production at a $\sqrt{s} = 100$ TeV proton-proton collider for the two types of squark-gluino spectra listed in Table 3.1. For simplicity we assume the LSP is a Bino, and all other neutralinos/charginos are decoupled. Relaxing this assumption allows squark decays to intermediate neutralinos/charginos, resulting in additional final state objects which can be used for background discrimination.

For both non-compressed and compressed spectra, we impose the following baseline cuts:

$$H_T > 10 \text{ TeV}, \quad \not{E}_T/\sqrt{H_T} > 20 \text{ GeV}^{1/2}$$

while for the non-compressed spectra we impose the additional cut:

$$8 \text{ jets with } p_T > 50 \text{ (150) GeV}$$

The softer cut is optimized for heavier squarks and lighter gluinos, while the harder cut is optimized for lighter squarks and heavier gluinos. Upon imposing these baseline cuts, we

then scan over leading jet p_T and $\not{E}_T$ cuts in order to maximize significance σ as defined in (3.1). We have verified that the optimal cuts render any "background" from gluino pair production subdominant to the SM background.

The results of this analysis are depicted in Figs. 3.1 and 3.2, which show the reach of a $\sqrt{s} = 100$ TeV proton-proton collider with 3 ab^{-1} of integrated luminosity. The solid, long dashed and short dashed lines correspond respectively to systematic uncertainties of 5, 10 and 15% for the signal normalization, while the background systematic uncertainty is fixed to 20%. The projected reach is fairly insensitive to background systematic uncertainties, as the number of background events is quite low due to the hard leading jet p_T and $\not{E}_T$ cuts.

As is evident from Figs. 3.1 and 3.2, a $\sqrt{s} = 100$ TeV collider with 3 ab^{-1} integrated luminosity can begin probing much of the "mini-split" parameter space for sufficiently low gluino masses. Final states in the compressed spectra yield more $\not{E}_T$ compared to the non-compressed spectra, due to the decay of the boosted gluino that arose from the decay of the massive squark, resulting in the greater reach depicted in Figure 3.2. Notably, with 3 ab^{-1} integrated luminosity the entire neutralino-gluino coannihilation region (whose upper endpoint lies at $m_{\tilde{g}} \approx m_{\tilde{\chi}} \approx 8$ TeV [101]) can be excluded if the squark masses are $\lesssim 32$ TeV.

It is worthwhile to compare Figs. 3.1 and 3.2 to projected reaches for gluino pair production. Our results for non-compressed spectra have some overlap with [86][2], which considered both pair production and associated production in similar spectra with squark masses $\lesssim 24$ TeV. The results of [86] indicate that gluino pair production will likely be the discovery channel for colored superpartners for the spectra in Fig. 3.1 provided $m_{\tilde{g}} \lesssim 14$ TeV. On the other hand, if the gluino and the LSP are nearly degenerate, searches for gluino pair production rapidly lose sensitivity [86]. Thus if the gluino and the LSP are nearly degenerate as in the gluino-neutralino coannihilation scenario, squark-gluino associated production would be a potential discovery channel for colored superpartners.

[2]A search optimizing over H_T cuts as opposed to leading jet p_T cuts was done in [86]. For the spectra in Fig. 3.1, the H_T cut based analysis has a 3-5 TeV weaker reach in $m_{\tilde{q}} + m_{\tilde{g}}$ with respect to squark-gluino associated production.

3.4 Squark-Wino and Squark-Bino Associated Production

In this section we discuss squark-Wino and squark-Bino associated production. These channels are particularly important if squark-gluino associated production is inaccessible due to a sufficiently heavy gluino mass[3]. The event topology is qualitatively similar to squark-gluino production, as the squark will decay to a boosted jet and boosted Wino/Bino while the associated Wino/Bino is produced at relatively low p_T. However as noted in Section 3.2, associated squark-Wino/Bino production probes significantly lighter squark masses than squark-gluino production. Consequently, multi-TeV leading jet p_T and $\not{E}_T$ cuts are not as effective for background discrimination in squark-Wino/Bino production. Instead, we find that hard $\not{E}_T/\sqrt{H_T}$ cuts are quite effective at reducing the $t\bar{t}$+ jets and vector boson + jets background without rejecting too many signal events.

In order to determine the projected reach for squark-Wino/Bino production at a $\sqrt{s} =$ 100 TeV pp collider with 3 ab^{-1} integrated luminosity, we impose the following baseline cuts:

$$p_T(j_1) > 2 \text{ TeV}, \quad \not{E}_T > 3 \text{ TeV}, \quad \Delta\phi(j, \not{E}_T) > 0.5$$

where the $\Delta\phi$ cut is imposed only on the two leading jets. We then scan over $\not{E}_T/\sqrt{H_T}$ cuts for each spectrum to maximize σ as defined in (3.1).

Our focus is on spectra listed in Table 3.1 where at most one of the gaugino/Higgsino mass parameters M_1, M_2, μ are $\lesssim$ 1 TeV, such that the gauge eigenstates are approximately aligned with the mass eigenstates in the neutralino/chargino sectors. We omit the "compressed" region $m_{\tilde{q}} - m_{\tilde{\chi}} < 1$ TeV, as in this region the event topology of associated squark-Wino/Bino production is similar to squark pair production, only with a substantially smaller cross section. Assuming a systematic uncertainty of 10% for the signal normalization, the results of the above analysis for the various spectra in Table 3.1 are depicted in Figures 3.3-3.5.

Figure 3.3 shows the reach for squark-Wino production with a pure Wino LSP; the solid, short-dashed, long-dashed lines correspond to background uncertainties of 5%, 10% and 15 %. In Figure 3.4 we show the reach for squark-Bino production with a pure Bino LSP. The solid, short-dashed, long-dashed lines correspond to background systematic uncertainties of 4%, 5% and 6%. Compared to squark-Wino production, the reach for squark-Bino

[3]In the MSSM, a gluino which is hierarchically heavier than the squarks requires fine-tuning of the soft masses. This can be avoided however in a model with Dirac gluinos [102, 103].

associated production is quite sensitive to background uncertainties. This is because the 5σ contours for squark-Bino production correspond to significantly lower masses due to the smaller production cross-section, resulting in lower optimal $\not{E}_T/\sqrt{H_T}$ cuts and thus larger backgrounds.

In Figure 3.5 we show the reach of the $\not{E}_T/\sqrt{H_T}$ based monojet analysis for squark-Wino production with a Wino NLSP, with background uncertainties fixed to be 5%. The green lines correspond to $M_{NLSP} - M_{LSP} = 200$ GeV, while the red lines correspond to $M_{LSP} = 100$ GeV. For comparison, the blue lines show the reach for squark-Wino production when the Wino is the LSP. Away from the $m_{\tilde{q}} \sim m_{\tilde{W}}$ region the sensitivity is lower for a Wino NLSP, as $\not{E}_T$ is being traded for W, Z and higgs bosons arising from the NLSP $\rightarrow$ LSP decay. Note that the analysis considered here does not exploit the additional SM bosons present in the Wino NLSP scenario. Thus the reach for the Wino NLSP scenario depicted in Figure 3.5 applies regardless of whether the LSP is Bino-like or Higgsino-like. Exploiting the additional SM bosons could extend the reach for the Wino NLSP scenario, so the result presented here is a conservative estimate.

We close this section by comparing the results of Figures 3.3-3.5 to studies of pair production at $\sqrt{s} = 100$ TeV. Given 3 ab^{-1} integrated luminosity, squark pair production can discover squark masses up to 2.5 TeV [86] (assuming a conservative 20 % background systematic uncertainty). In the pure Wino case, searches in VBF channels can discover Winos up to 1.1 TeV [96]. Disappearing tracks can also provide a collider probe of pure Wino LSP pair production. Extrapolating the disappearing tracks background from the 8 TeV ATLAS study [104], the projected reach is 2-3 TeV for pure Winos [90]. However, the data-driven disappearing-track background at 100 TeV is difficult to estimate, making this projected reach less reliable than the reach in the VBF channel or the reach depicted in Figure 3.3. Finally, pair production of Wino NLSPs has been considered in [93, 94]. Assuming no systematic uncertainties, for a Higgsino LSP the project discovery reach is 2.3 TeV, while for a Bino LSP the reach is 1-3 TeV depending on the NLSP $\rightarrow Z$ LSP branching ratio. Comparing these reaches to Figures 3.3-3.5, we see that squark-Wino/Bino associated production can provide a SUSY discovery mode provided the squark is not too much heavier than the Wino/Bino.

3.5 Summary

In this chapter, we have examined in this chapter the kinematic reach for squark-gaugino associated production at a 100 TeV proton-proton collider. We studied a variety of simplified models listed in Table 3.1 with heavier scalars, with relatively lighter gauginos, as motivated previously. In models where squark pair production is kinematically inaccessible at a 100 TeV collider, squark-gaugino associated production may be the discovery mode for SUSY in a large portion of parameter space.

For squark-gluino production with $\mathcal{O}$(TeV) gluinos, the discovery reach for first-generation squarks can be up to 40 TeV for compressed spectra, where the LSP is 15 GeV lighter than the gluino, and up to 32 TeV for non-compressed spectra, subject to systematic uncertainties. For squark-Wino LSP production, we have shown that the discovery reach for the Wino slightly exceeds 4 TeV for squarks of ~ 8 TeV, subject to systematic uncertainties. For squark-Wino NLSP production we have analysed two scenarios: one where the NLSP-LSP mass difference is 200 GeV, and one where the LSP mass is ~ 100 GeV. In the first scenario, the Wino discovery reach is just under 4 TeV for squarks of ~ 8 TeV. In the second scenario, the reach extends up to 6 TeV. Our results in the Wino-NLSP scenario are insensitive to the nature of the LSP. For $\lesssim 10$ TeV squark masses, squark-Wino associated production marks a significant increase in the Wino reach compared to pair production channels. We also consider squark-Bino associated production, and find that the kinematic reach for the Bino is up to 2 TeV for squarks of mass ~ 6 TeV, subject to systematic uncertainties.

The results presented here raise the exciting prospect of directly probing a region of parameter space that so far has been the exclusive domain of indirect searches through low-energy FCNC observables. The squark-gaugino associated production channels studied here, coupled with studies of Supersymmetry at 100 TeV colliders already undertaken [86, 92, 90, 89, 19, 93, 94, 95, 96, 97], provide a strong physics case for the construction of such a collider.

This chapter concludes the study of the collider phenomenology of supersymmetric models with heavier scalars. In the next chapter, we will move on to studying low-energy flavor observables of similar models.

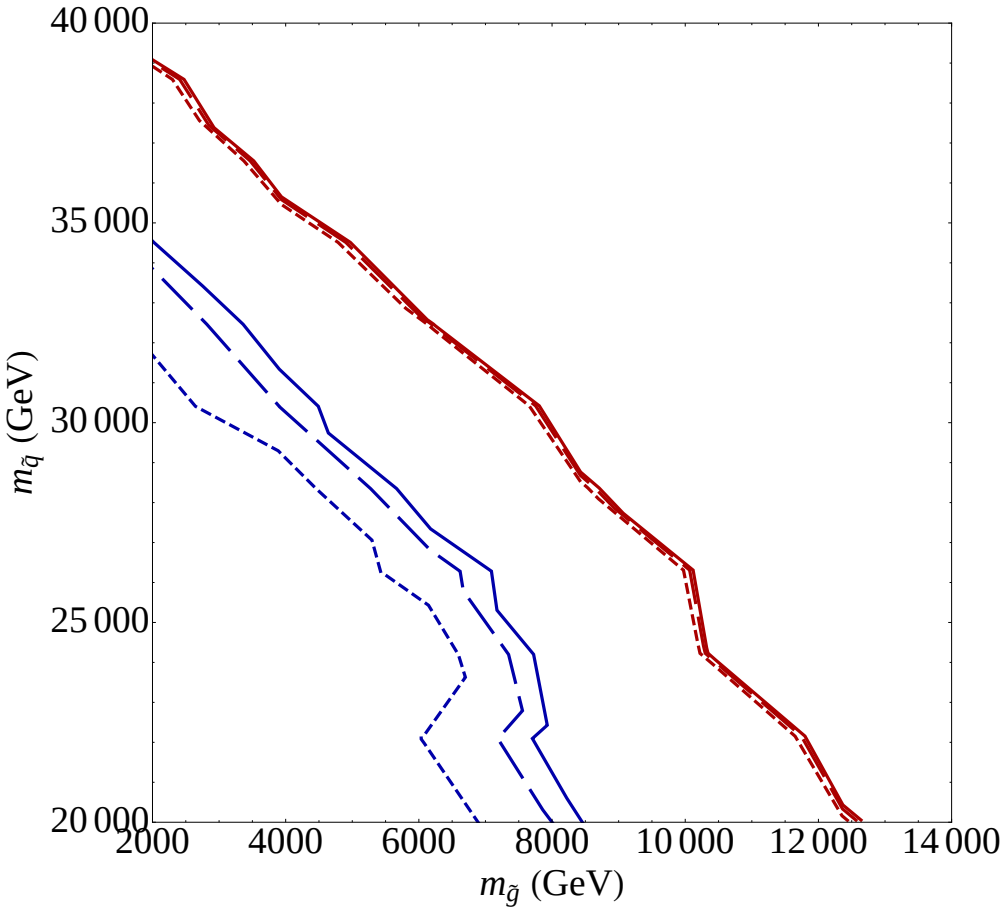

Figure 3.1: Experimental reach for squark-gluino associated production at a 100 TeV proton-proton collider with 3 ab^{-1} integrated luminosity, for spectra with a $\sim$ 100 GeV LSP mass. The solid, long dashed and short dashed lines are for and 5, 10, 15% systematic uncertainty for the signal respectively. Blue lines indicate 5σ discovery reach and red lines indicate 95% exclusion limits. We assume 20% systematic uncertainty in the background. Below 20 TeV in $m_{\tilde{q}}$ is discussed in [86].

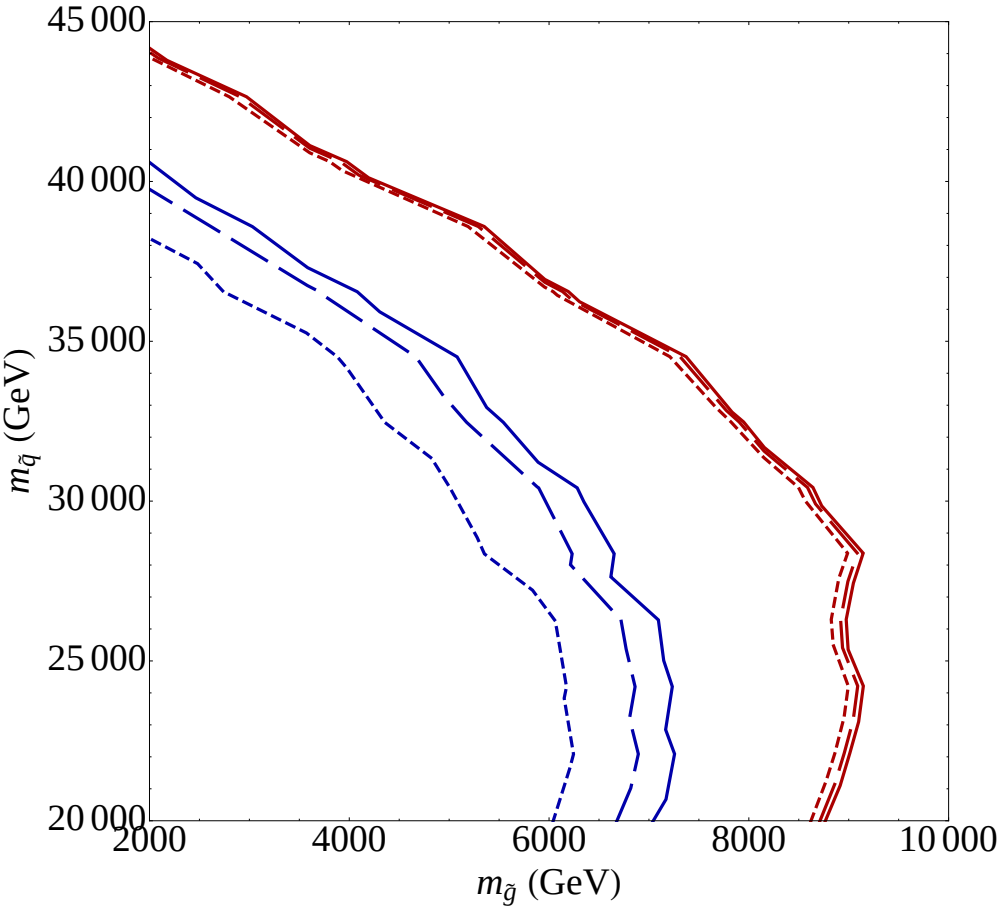

Figure 3.2: Experimental reach for squark-gluino associated production at a 100 TeV proton-proton collider with 3 ab^{-1} integrated luminosity for spectra with $m_{\tilde{g}} - m_{\chi_1^0} = 15$ GeV. The different lines follow the conventions of Fig. 3.1. We assume 20% systematic uncertainty in the background.

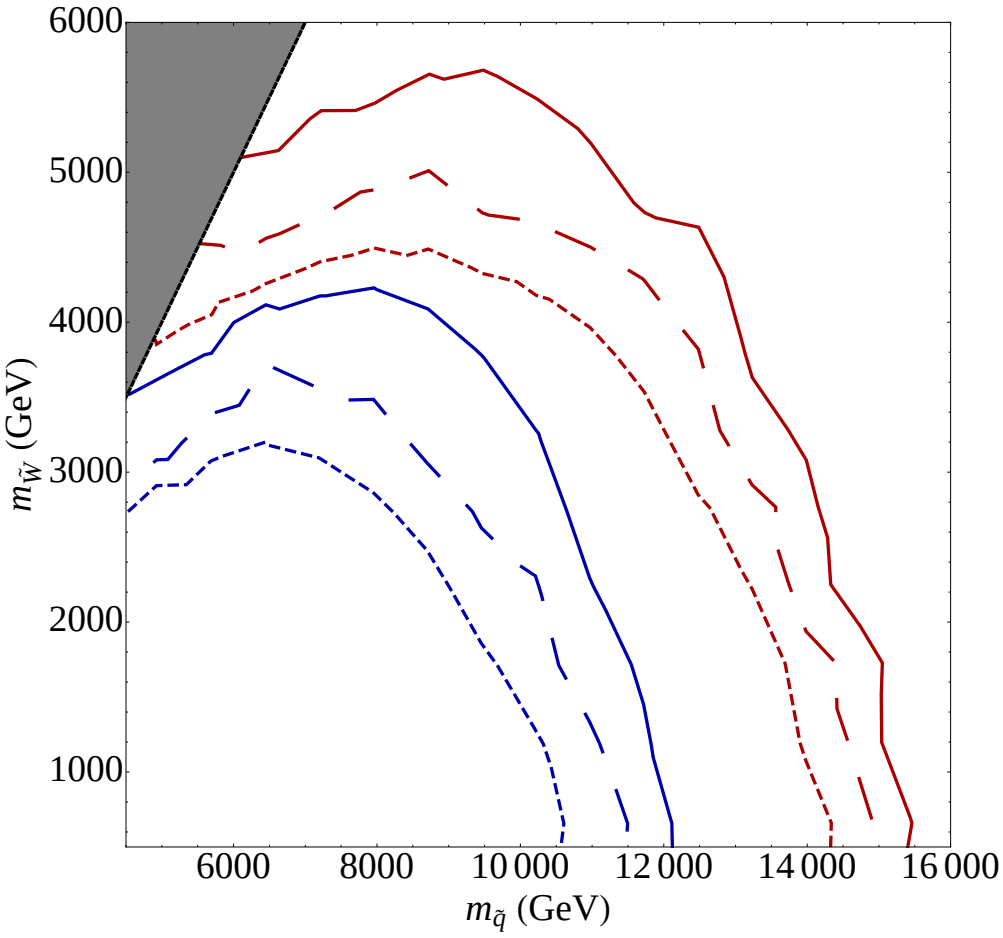

Figure 3.3: Experimental reach for squark-Wino LSP associated production at a 100 TeV proton-proton collider with 3 ab^{-1} integrated luminosity. The solid, long dashed and short dashed lines are for 5, 10, 15% systematic uncertainty for the background respectively. Blue lines indicate 5σ discovery reach and red lines indicate 95% exclusion limits. We do not consider the grey shaded region ($m_{\tilde{q}} - m_{\tilde{W}} < 1$ TeV) for reasons given in the text. We assume 10% systematic uncertainty for the signal.

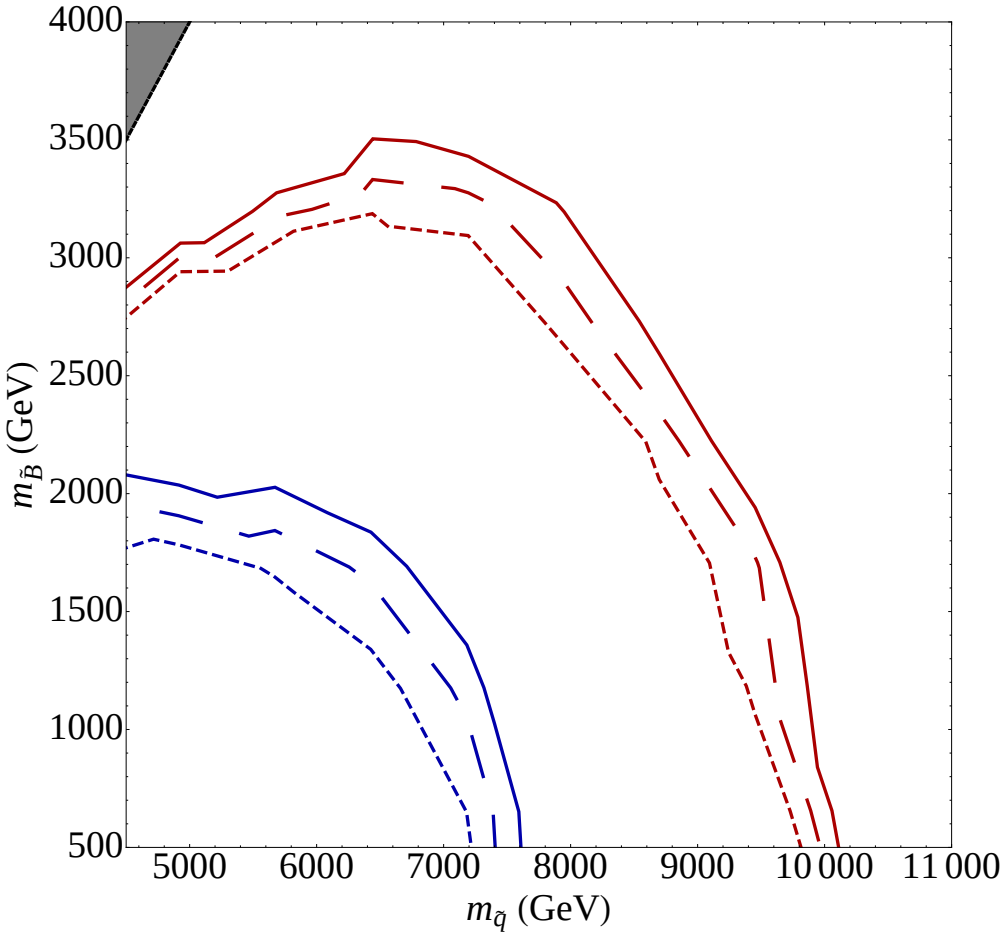

Figure 3.4: Experimental reach for squark-Bino LSP associated production at a 100 TeV proton-proton collider with 3 ab^{-1} integrated luminosity. The solid, long dashed and short dashed lines are for and 4, 5, 6% systematic uncertainty for the background respectively. Blue lines indicate 5σ discovery reach and red lines indicate 95% exclusion limits. We do not consider the grey shaded region ($m_{\tilde{q}} - m_{\tilde{B}} < 1$ TeV) for reasons given in the text. We assume 10% systematic uncertainty in the signal.

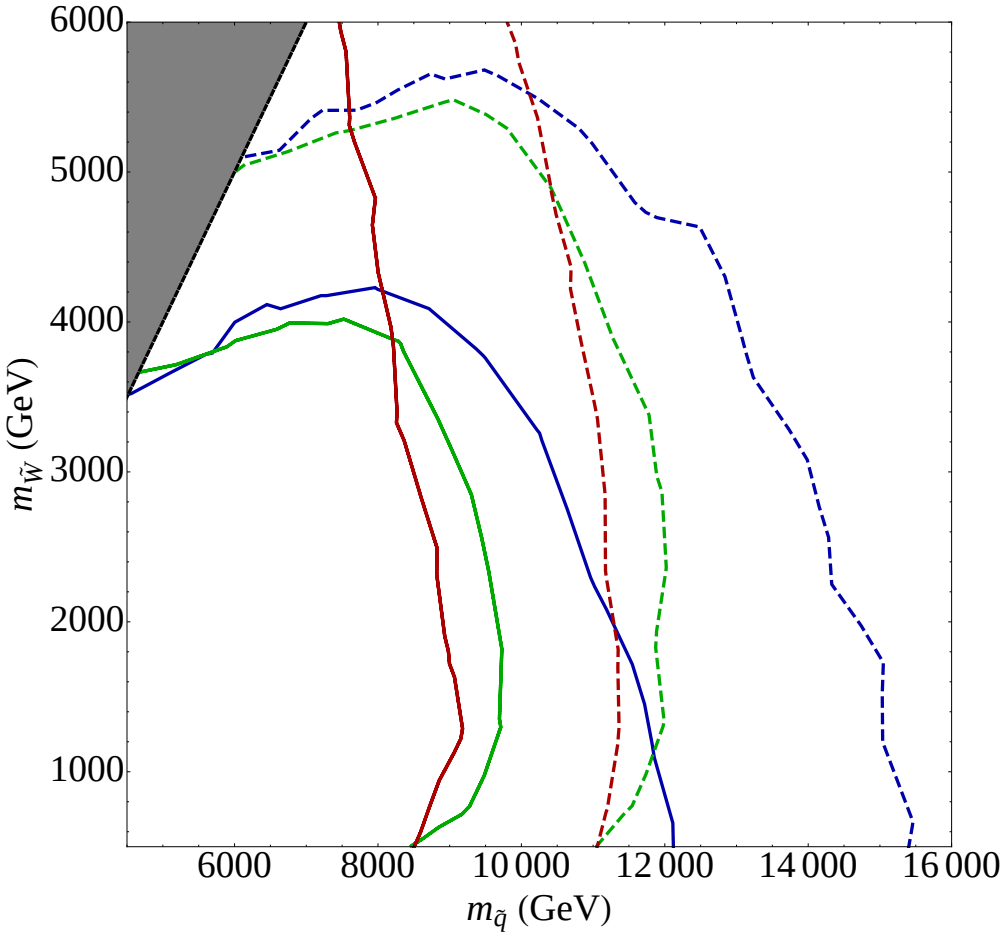

Figure 3.5: Experimental reach for squark-Wino associated production at a 100 TeV proton-proton collider with 3 ab^{-1} integrated luminosity. Solid lines indicate 5σ discovery reach, and dotted lines indicate 95% exclusion limits. Blue curves correspond to a Wino LSP, while the green (red) curves correspond to a Wino NLSP with $M_{\rm NLSP} - M_{\rm LSP} = 200$ GeV ($M_{LSP} \sim 100$ GeV). The results are applicable for both Bino- and Higgsino-like LSP. We do not consider the grey shaded region ($m_{\tilde{q}} - m_{\tilde{W}} < 1$ TeV) for reasons given in the text. We assume 5% systematic uncertainty in the background and 10% in the signal.

Chapter 4

Impact of Future Lepton Flavor Violation Measurements in the Minimal Supersymmetric Standard Model

4.1 Introduction

Lepton flavor violation (LFV) and quark flavor changing neutral currents (FCNCs) are powerful probes of new physics, reaching scales well beyond those accessible at present colliders. A significant effort is underway to improve sensitivity to rare LFV processes such as $\mu \to e\gamma$ and μ to e conversion (see Table 4.1). However, for example, the neutral kaon mass difference places strong bounds on flavor violation in the quark sector, and in some models LFV and quark FCNCs are related to one another. It is interesting to explore under what conditions new LFV experiments will be the most sensitive probe of new physics, superseding limits from the quark sector. We discuss this question in the context of the Minimal Supersymmetric Standard Model (MSSM).

Many studies of flavor violation within the MSSM exist, see e.g. [105, 106, 107, 108, 109, 110, 111, 112, 113, 114, 115] for overviews. Indeed, most of the calculations of the rare processes we explore here have appeared elsewhere in the literature. Our focus will be a comparison between LFV and quark FCNCs, trying to get a feel for the relative power of these constraints.

Supersymmetry (SUSY) breaking scalar masses can receive contributions from operators

of the form

$$K \sim \frac{\kappa_{ij}}{M^2} X_a^\dagger X_a \Phi_i^\dagger \Phi_j \tag{4.1}$$

in the Kähler potential. Here Φ are MSSM superfields with generation indices i, j, and X_a are fields associated with the breaking of SUSY with non-vanishing F_X, and M is associated with the mediation scale of SUSY breaking. Such operators can induce off-diagonal terms in the scalar mass matrices, given by $m_{ij}^2 = \kappa_{ij} \langle F_{X_a} \rangle^2 / M^2$. These terms are a source of flavor violation beyond the Standard Model. The size and form of these off-diagonal contributions depend on the particulars of the UV theory that induces this non-renomalizable operator. It is possible the SUSY breaking respects a Grand Unified Theory (GUT) structure, in which case the quark and lepton flavor violation can be related. However, even in this case quark and lepton superfields residing in different representations may feel SUSY breaking differently. For example, in an $SU(5)$ GUT, since the left-handed (LH) lepton superfields reside in the $\bar{\mathbf{5}}$ while the LH quark superfields reside in the $\mathbf{10}$, this leads to the possibility of a mismatch between contributions to LFV and quark FCNCs. (See for example [116] and discussion in [113].)

It is also possible that off-diagonal mass terms for squarks and sleptons are *a priori* unrelated. Indeed, even if initial flavor violation is related by a symmetry, a mismatch between squark and slepton off-diagonal mass terms may arise once neutrino masses are incorporated into the theory. The inclusion of neutrino Yukawa couplings may lead to sizeable entries in the left-handed slepton mass matrix due to Renormalisation Group Equation (RGE) running from the GUT scale down to the right-handed neutrino scale [117, 118, 119, 120, 121, 122]. Such models naturally lead to non-zero LFV while not contributing to quark FCNCs. This approach has been considered in various contexts, including $SO(10)$ [118, 123] and $SU(5)$ GUT models [117]. The size of these effects are model dependent, but can be large. But even in the case where the quark and lepton flavor violation are decoupled, it is of interest to understand just how different the allowed flavor violation is, consistent with current and upcoming experiments.

New phases in the SUSY breaking parameters would contribute to CP-violating processes, such as ϵ_K. If the phases are $\mathcal{O}(1)$, extremely strong bounds exist, forcing scalars to be in the PeV regime [113]. It is possible that searches for electric dipole moments (EDMs) could eventually provide constraints competitive with those from ϵ_K, a possibility that has been studied recently in, e.g. [137, 4, 3, 138, 139, 113, 20]. However, it is possible a mechanism renders the phases in SUSY breaking parameters small. Moreover, LFV measurements such

Observable	Exp. Measurement	SM prediction
Δm_K	$(3.484 \pm 0.006) \times 10^{-12}$ MeV [124]	$(3.19 \pm 0.41(\text{stat.}) \pm 0.96(\text{sys.})) \times 10^{-12}$ MeV [1]
Δm_{B_d}	$(3.337 \pm 0.033) \times 10^{-10}$ MeV [124]	$(3.48 \pm 0.52) \times 10^{-10}$ MeV [125]
$\sin 2\beta_d$	0.682 ± 0.019 [126]	$0.748^{+0.030}_{-0.032}$ [127]
Δm_{B_s}	$(1.1691 \pm 0.0014) \times 10^{-8}$ MeV [124]	$(1.2 \pm 0.18) \times 10^{-8}$ MeV [125]
$\sin 2\beta_s$	-0.015 ± 0.035 [126]	$-0.03761^{+0.00073}_{-0.00082}$ [127]
Observable	**Current Limit (90% C.L.)**	**Future sensitivity (90% C.L.)**
$\text{BR}(\mu \to e\gamma)$	4.2×10^{-13} [128]	6×10^{-14} [129]
$\text{BR}(\tau \to e\gamma)$	3.3×10^{-8} [130]	10^{-9} [131]
$\text{BR}(\tau \to \mu\gamma)$	4.4×10^{-8} [130]	10^{-9} [131]
$\text{BR}(\mu \to e)_{Au}$	7.0×10^{-13} [132]	
$\text{BR}(\mu \to e)_{Al}$		10^{-16} [133]
$\text{BR}(\mu \to 3e)$	1.0×10^{-12} [134]	10^{-16} [135, 136]

Table 4.1: The experimental measurements and SM predictions for quark observables and the current and future sensitivities of lepton flavor violating processes. Long distance effects in Δm_K are difficult to quantify. The quoted SM Δm_K value is a recent Lattice QCD calculation [1] which uses unphysical values for the pion, kaon and charm quark masses, and as such should not be taken as precise. So, in our numerical work we allow the SUSY contribution to fully saturate the experimental value.

as $\mu \to e\gamma$ are CP-conserving, so a true "apples to apples" comparison is with CP-conserving observables in the quark sector. In this analysis we will restrict ourselves to the assumption that all phases are zero (or at least negligibly small). In the kaon sector, for example, the limits from ΔM_K supersede those from ϵ_K for phases $\lesssim 10^{-2}$.

In this work we consider two scenarios and discuss the interplay between quark FCNCs and LFV in each. In the first, we use the observed Higgs boson mass of 125 GeV as motivation to consider scalar masses that may be (much) heavier than a few TeV, and could fall in the 10's of TeV to even a PeV range [50, 49, 52, 51]. Additionally, having heavy scalars allows for off-diagonal masses to be relatively large, potentially up to $\mathcal{O}(1)$ of the diagonal masses, thus lessening the need for a mechanism to suppress flavor violation. At the same time, the observed abundance of dark matter (DM) indicates either gaugino masses M_i or the Higgsino mass parameter μ should be near the TeV scale (see, for example, [98, 140, 141]). So, in the first scenario, we imagine a modest hierarchy between the fermionic and scalar superpartners. In the second scenario, we consider the possibility that all superpartners lie close to the TeV scale.

In Sections 4.2 and 4.3, we review the structure of the effective Hamiltonians which contribute to quark FCNCs and LFV in the MSSM. In the quark sector, our primary focus is on meson mixing. For LFV we discuss $\ell_j \to \ell_i\gamma$ decays and μ to e conversion. (We comment

briefly on the $b \to s\gamma$ transition in Sec. 4.2.3). We discuss the parametric dependencies of the various operators entering the effective Hamiltonian for each process we consider, and comment on what parameters are most important in what regimes. We discuss the dependence of both quark FCNCs and LFV on Left-Left (LL), Right-Right (RR) and LR mixing. A goal of these sections is to highlight which insertions are most constrained and how this may differ between the quark and lepton sector, an issue which we quantify further in Section 4.5. In Section 4.4 we analyse in more depth how the various gaugino masses M_i and the μ-term impact the strength of quark FCNC constraints relative to LFV bounds. The relative power of LFV and quark FCNCs is summarized in Figs. 4.7 – 4.14, which represent the main results of this chapter. Finally, in Section 4.6 we summarise the results of our analysis, and comment on the implications.

4.2 Anatomy of quark FCNC processes

In this section we review contributions to quark flavor violating observables. In the kaon sector, since we concentrate on CP-conserving new physics, our focus is on ΔM_K. In the B sector, even if new physics contributions are CP-conserving, measurements of CP-violating quantities such as $\sin 2\beta_d$ are relevant. We review our treatment of B-mixing in Sec. 4.2.2. We briefly comment on $\Delta F = 1$ constraints in 4.2.3.

4.2.1 $\Delta F = 2$ transitions

The dominant SUSY contribution to meson oscillations is typically gluino-squark box diagrams.[1] In these processes, one may use the mass insertion approximation for sufficiently small off-diagonal elements in the squark mass matrix, with these insertions appearing on the internal squark lines, shown as crosses in Fig. 4.1 for kaon oscillation. We take the squark mass-squared matrix to be given by

$$\mathcal{M}^2_{\tilde{q}} = \begin{pmatrix} \tilde{m}^2_q(1+\delta^{ij}_{LL}) & \tilde{m}^2_q(\delta^{ij}_{LR}) \\ \tilde{m}^2_q(\delta^{ij}_{RL}) & \tilde{m}^2_q(1+\delta^{ij}_{RR}) \end{pmatrix}, \tag{4.2}$$

where the indices $i, j = 1, 2, 3$ run over generations. An analogous convention is used for sleptons.

[1] For large values of the ratio of the vacuum expectation values of the two Higgs doublets $\tan\beta$, an additional heavy Higgs-mediated contribution to meson oscillations (see, e.g., [111]) may be relevant ($\tan\beta \sim 50$ for $m_A \sim \tilde{m}_q$).

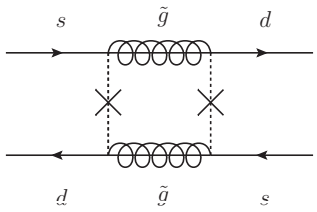

Figure 4.1: Typical kaon mixing diagram induced by SUSY. The crosses represent flavor-violating mass insertions.

The interaction can be described by the corresponding effective Hamiltonian

$$\mathcal{H}_{eff} = \sum_{i=1}^{5} C_i Q_i + \sum_{i=1}^{3} \tilde{C}_i \tilde{Q}_i + h.c. \tag{4.3}$$

where the C_i are the Wilson coefficients for the dimension-6 operators Q_i

$$\begin{gathered} Q_1 = (\bar{d}_L^\alpha \gamma_\mu s_L^\alpha)(\bar{d}_L^\beta \gamma_\mu s_L^\beta), \quad Q_2 = (\bar{d}_R^\alpha s_L^\alpha)(\bar{d}_R^\beta s_L^\beta), \quad Q_3 = (\bar{d}_R^\alpha s_L^\beta)(\bar{d}_R^\beta s_L^\alpha), \\ Q_4 = (\bar{d}_R^\alpha s_L^\alpha)(\bar{d}_L^\beta s_R^\beta), \qquad Q_5 = (\bar{d}_R^\alpha s_L^\beta)(\bar{d}_L^\beta s_R^\alpha) \end{gathered} \tag{4.4}$$

and $\tilde{Q}_i$ given by interchanging $L \leftrightarrow R$ for $i = 1, 2, 3$. For the numerical values of the hadronic matrix elements $\langle \bar{K}_0 | Q_i | K_0 \rangle$ we use the values for the bag factors $B_i(2\text{ GeV})$ from [142], the lattice result for f_K from [143], and the reported kaon mass m_K from [124]. Meanwhile for the B-meson hadronic matrix elements, we use the values for the bag factors $B_i(m_b)$ and the lattice results for $f_B,\ f_{B_s}$ from [144], and the reported B-meson masses from [124]. Expressions for the Wilson coefficients including the Leading Order QCD corrections [145] are reproduced in Appendix E.

In Fig. 4.2, we display the contribution to meson mixing assuming that $\delta_{LL} = \delta_{RR}$. δ_{LR} is set to zero – in any case its contribution is expected to be subdominant, see Eq. (4.6) below. In both the $\frac{m_{\tilde{g}}^2}{\tilde{m}_q^2} \equiv x_{\tilde{g}} \ll 1$ and $x_{\tilde{g}} \simeq 1$ regions, for equal sized insertions, the contribution to $\Delta F = 2$ processes is dominated by the operator Q_4 with coefficient C_4. Notably, this dominant operator depends on the product $\delta_{LL} \times \delta_{RR}$ (rather than δ_{LL}^2 or δ_{RR}^2), so can be varied relative to the others. As we will see, the relative size of δ_{LL} and δ_{RR} will impact the relative strength of of the quark flavor violation and LFV probes.

LR insertions are not expected to be relevant for $\Delta F = 2$ transitions for large ($\gtrsim$ TeV) squark masses. The LR insertions arise due to off-diagonal terms in the scalar trilinear

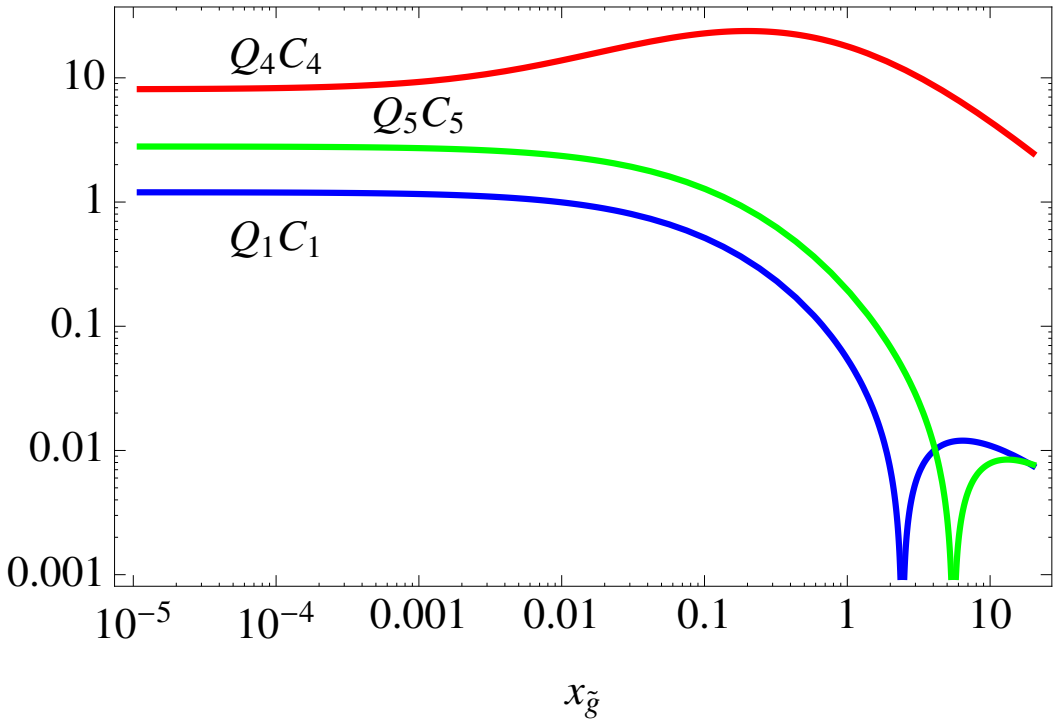

Figure 4.2: The products $C_i(\mu)Q_i$ for kaon oscillations, for insertions $\delta_{LL} = \delta_{RR} = 0.3$, $\delta_{LR} = \delta_{RL} = 0$, and $\tilde{m}_q = 20$ TeV (we set $\mu = m_c$). Shown here are C_1Q_1 (blue), C_4Q_4 (red) and C_5Q_5 (green), demonstrating the domination of C_4Q_4 for all values of $x_{\tilde{g}}$. Not shown are C_2Q_2 and C_3Q_3, which depend only on LR insertions, set to zero here. In any case, these are expected to be subdominant, see text. The numerical values for the Q_i are obtained as described in the text. The relative importance of the C_iQ_i is the same for B-meson oscillations.

couplings A_{ij} and have the form

$$\delta_{LR}^{ij} \sim \frac{m_q A^{ij}}{\tilde{m}_q^2}. \tag{4.5}$$

The result of the quark mass suppression is that A-terms must be very large to affect meson mixing:

$$\frac{A^{12}}{\tilde{m}_q} \gtrsim 170\,\frac{\tilde{m}_q}{\text{TeV}} \qquad \frac{A^{13}}{\tilde{m}_q} \gtrsim 5\,\frac{\tilde{m}_q}{\text{TeV}} \qquad \frac{A^{23}}{\tilde{m}_q} \gtrsim 50\,\frac{\tilde{m}_q}{\text{TeV}}. \tag{4.6}$$

Such large A-terms would not be expected unless the SUSY-breaking spurion were charged under the flavor symmetry, a possibility which we do not consider further.

While LR insertions are unlikely to be relevant for meson mixing as described above, they are potentially relevant for the $\Delta F = 1$ transition of $b \to s\gamma$ (which we discuss later in Section 4.2.3).

4.2.2 Treatment of constraints from B-meson observables

B-meson mixing provides a total of four constraints on the new SUSY contributions. For each of the B_q mesons ($q = d, s$) there are the measured mass difference Δm_{B_q} as well as the measurement of the CP violation in the mixing.

In the B_d sector, the observed CP violation in mixing is given by:

$$\sin 2\phi_d = \frac{\sin 2\beta_d + r_d \sin\theta_d}{C_{B_d}}, \tag{4.7}$$

where $r_d = \frac{|\langle \bar{B}_d | \mathcal{H}_{eff}^{SUSY} | B_d \rangle|}{|\langle \bar{B}_d | \mathcal{H}_{eff}^{SM} | B_d \rangle|}$, θ_d is a potential new CP-violating phase, which we take to vanish, and

$$C_{B_d} = \left(1 + r_d^2 + r_d \cos(2\beta_d - \theta_d)\right)^{1/2}. \tag{4.8}$$

Here, $\sin 2\beta_d$ is the SM prediction, for which we take the latest (Summer 2015) CKMfitter collaboration global fit [127][2] Similarly in the B_s sector, we use the latest value of $\sin 2\beta_s$ from the CKMfitter collaboration global fit, and an expression for $\sin 2\phi_s$ analogous to Eq. (4.7), with the expectation that the SM prediction is $\sin 2\phi_s = \sin 2\beta_s$. We then calculate the χ^2

[2]When constraining the SUSY contribution, we use the global fit as the central value for $S_{\psi K_s}$ rather than the directly experimentally measured value. They agree within 2σ.

values of the combined constraints from the mass difference Δm_{B_q} and $\sin 2\beta_q$ to find the excluded regions in our various plots.

While the experimental precision on both $\sin 2\phi_d$ and $\sin 2\phi_s$ is expected to improve [146], improvements in theoretical precision are less easy to forecast. If the expected experimental improvement is matched by theory, this will result in $\mathcal{O}(1)$ modifications of the bounds on the allowed δ. In our numerical results, we show the expected improvement assuming the theoretical precision increases by a factor of two.

4.2.3 Treatment of $\Delta F = 1$ transitions

The $\Delta F = 1$ decay of $b \to s\gamma$ is known to impose strong constraints on the $2-3$ sector for TeV-scale superpartners (see for example [147, 148, 149, 111]). Particularly when imposing constraints on LR mass insertions, it is necessary to include the results from $b \to s\gamma$ to obtain the constraints on quark $2-3$ transitions. Constraints on LL and RR insertions can also be derived, and are also relevant. Our procedure for calculating the branching ratio is the following: we take the leading contributions to the operators $C_7,\ C_8,\ \tilde{C}_7,\ \tilde{C}_8$ from heavy Higgs boson and gluino diagrams from [111], and use the expression in [150, 151] to calculate the branching ratio for generic new physics contributions to the above listed operators. We assume that the heavy Higgs bosons are degenerate with the squarks and sleptons. We then impose that the branching ratio be within the 90% confidence interval given the latest experimental results [126], and the theoretical estimate for the branching ratio at NNLO in the SM [152, 153]. For simplicity, we assume vanishing flavor violation in the up squark sector (which affects potential chargino diagrams, which are usually subdominant in any case). For heavy Higgs boson masses comparable to squark masses, we find the charged Higgs boson diagram to be smaller than, but not negligibly small compared with the gluino contribution, when δ is near its experimentally allowed value. We note that the sign of the product $M_{\tilde{g}} A^{23}$ which appears in the gluino diagram is physical.

In the future, sensitivity of the High Luminosity LHC to flavor changing top quark decays, $t \to hq$ $(q = u,\ c)$, where h is the Higgs boson, is expected to reach $\mathrm{BR}(t \to hq) \lesssim 2 \times 10^{-4}$ [154, 155] with 3 ab^{-1}. Recent studies (see for example [156] and references therein) indicate that for typical regions of SUSY parameter space, the future sensitivity will be insufficient to probe these rare decays in the MSSM. For this reason we do not compare here the top quark FCNC with the relevant LFV process, $h \to \tau\mu$. This LFV Higgs boson decay has been studied in the context of the MSSM in, for example, [157, 158].

4.3 Anatomy of LFV processes

In this section we review supersymmetric contributions to the processes $\ell_i \to \ell_j \gamma$ and $\mu \to e$ conversion in nuclei. We discuss what contributions dominate in what regimes and comment on the dependence on the gaugino masses and μ.

4.3.1 $\ell_i \to \ell_j \gamma$

The branching ratio of $\ell_i \to \ell_j \gamma$ is

$$\mathrm{BR}(\ell_i \to \ell_j \gamma) = \frac{48\pi^3 \alpha_{em}}{G_F^2} \left(|A_L|^2 + |A_R|^2 \right), \tag{4.9}$$

where the amplitudes $A_{L,R}$ are the coefficients of higher-dimensional operators in the effective Hamiltonian

$$\mathcal{H}_{eff} = e \frac{m_{\ell_i}}{2} \left(A_L \bar{\ell}_j \sigma^{\mu\nu} P_L \ell_i + A_R \bar{\ell}_j \sigma^{\mu\nu} P_R \ell_i \right) F_{\mu\nu}. \tag{4.10}$$

The dominant contribution to A_L arises from Wino loops [113]

$$A_L^{\tilde{W}} = \frac{\alpha_2}{4\pi} \frac{1}{\tilde{m}_\ell^2} \delta_{LL}^{\ell_i \ell_j} \left[-\frac{1}{8} g_1(x_{\tilde{W}}) + g_2(x_{\tilde{W}}, x_\mu) + \mathrm{sgn}(\mu M_2) \sqrt{x_{\tilde{W}} x_\mu}\, t_\beta\, g_3(x_{\tilde{W}}, x_\mu) \right], \tag{4.11}$$

where the g_i are loop functions given in Appendix F, and $x_{\tilde{W}}, (x_\mu) \equiv \frac{m_{\tilde{W}}^2}{\tilde{m}_\ell^2}$, $\left(\frac{\mu^2}{\tilde{m}_\ell^2}\right)$. We have abbreviated $\tan\beta$ as t_β. If the sign of μM_2 is positive (negative), $A_L^{\tilde{W}}$ exhibits destructive (constructive) interference. We will refer to each of these cases in the following analysis.

There are additional contributions to A_L and A_R due to a Bino loop [159, 111]

$$A_L^{\tilde{B}} \supset \frac{\alpha_1}{4\pi} \frac{1}{\tilde{m}_\ell^2} \delta_{LL}^{\ell_i \ell_j} \mathrm{sgn}(\mu M_1) \sqrt{x_{\tilde{B}} x_\mu}\, t_\beta \left[f_{3n}(x_{\tilde{B}}) + \frac{f_{2n}(x_{\tilde{B}}, x_\mu)}{x_\mu - x_{\tilde{B}}} \right], \tag{4.12}$$

$$A_R^{\tilde{B}} \supset \frac{\alpha_1}{4\pi} \frac{1}{\tilde{m}_\ell^2} \delta_{RR}^{\ell_i \ell_j} \mathrm{sgn}(\mu M_1) \sqrt{x_{\tilde{B}} x_\mu}\, t_\beta \left[f_{3n}(x_{\tilde{B}}) - \frac{2 f_{2n}(x_{\tilde{B}}, x_\mu)}{x_\mu - x_{\tilde{B}}} \right], \tag{4.13}$$

with the $f_{2,3n}$ are loop functions given in Appendix F and $x_{\tilde{B}} \equiv \frac{m_{\tilde{B}}^2}{\tilde{m}_\ell^2}$.

While the above contributions to A_R and A_L apply to all $\ell_i \to \ell_j \gamma$ processes, there is an additional diagram which gives an important contribution for $\mu \to e\gamma$ only, arising due to a Bino loop with two flavor changing insertions combined with a flavor-conserving LR

insertion on an internal stau line [159, 113]. The flavor-conserving insertion results in an enhancement of m_τ/m_μ:

$$A_R^{\tilde{B}} \supset \frac{\alpha_1}{4\pi}\left(\frac{m_\tau}{m_\mu}\right)\mathrm{sgn}(\mu M_1)\frac{\sqrt{x_{\tilde{B}}x_\mu}t_\beta}{\tilde{m}_\ell^2} f_{4n}(x_{\tilde{B}})\delta_{LL}^{\mu\tau}\delta_{RR}^{\tau e} \ , \tag{4.14}$$

where $f_{4n}(x_{\tilde{B}})$ is a loop function that can be found in Appendix F. The analogous expression for A_L is found by taking Eq. (4.14) and interchanging the LL and RR insertions. This diagram is of particular interest if a flavor symmetry suppresses $1-2$ insertions, since Eq. (4.14) only depends on $1-3$ and $2-3$ insertions.

In Section 4.2 we saw that meson mixing did not put meaningful constraints on off-diagonal trilinear terms even for TeV scale scalars. In contrast, the LR mixing contributions to LFV may be non-negligible. Consider the contribution to radiative lepton decay arising from a Bino loop, reproduced below [159, 111]

$$A_L^{\tilde{B}} \supset \frac{\alpha_1}{2\pi}\frac{\delta_{RL}^{\ell_i\ell_j}}{\tilde{m}_\ell}\frac{\sqrt{x_{\tilde{B}}}}{m_\mu} f_{2n}(x_{\tilde{B}}) \ , \tag{4.15}$$

with $A_R^{\tilde{B}}$ given by the δ_{LR} insertion. For $x_{\tilde{B}} \sim 1$, we see that this is only suppressed by one power of $\tilde{m}_\ell$. Since δ_{LR}^{ij} arises due to terms of the form

$$\delta_{LR}^{ij} \simeq \frac{m_f A^{ij}}{\tilde{m}_\ell^2} \ , \tag{4.16}$$

we can use these expressions to constrain the ratio of $A^{ij}/\tilde{m}_\ell$ for a given value of $\tilde{m}_\ell$.

In Fig. 4.3 we show the relative contributions to $\mu \to e\gamma$ (arbitrary units) for comparable insertions: $\delta_{LL}^{\mu e} = \delta_{RR}^{\mu e} = \delta_{LL}^{\mu\tau}\delta_{RR}^{\tau e} = 0.3$. The g_i and f_i correspond to the loop functions introduced in Eqs. (4.11)–(4.14). $\tan\beta$ is set to 10. The dominant contributions to $\mu \to e\gamma$ are from the Wino-Higgsino mixing diagrams, denoted by g_2 and g_3, at small x_i. Since both of these only depend on δ_{LL} (see Eqn. (4.11)), at small x_i, $\mu \to e\gamma$ will place constraints on δ_{LL}, but not δ_{RR}. As x_i approaches 1, the Bino contributions porportional to f_{in} can become important. The dominant operator is that with the LR flavor-conserving insertion, as long as $\delta^{\mu\tau}\delta^{\tau e}$ is not too suppressed relative to the single $\delta^{\mu e}$ insertion.

In Fig. 4.3, we see that the largest branching ratio of $\mu \to e\gamma$ is obtained in the small $x_{\tilde{W}}$, x_μ, $x_{\tilde{B}}$ regime. While the figure shown sets $\tan\beta = 10$, since the dominant contributions are proportional to g_3 (small x) and f_{4n} (large x) both of which are also proportional to $\tan\beta$, the scaling is straightforward. The statement was also found to apply for maximising the

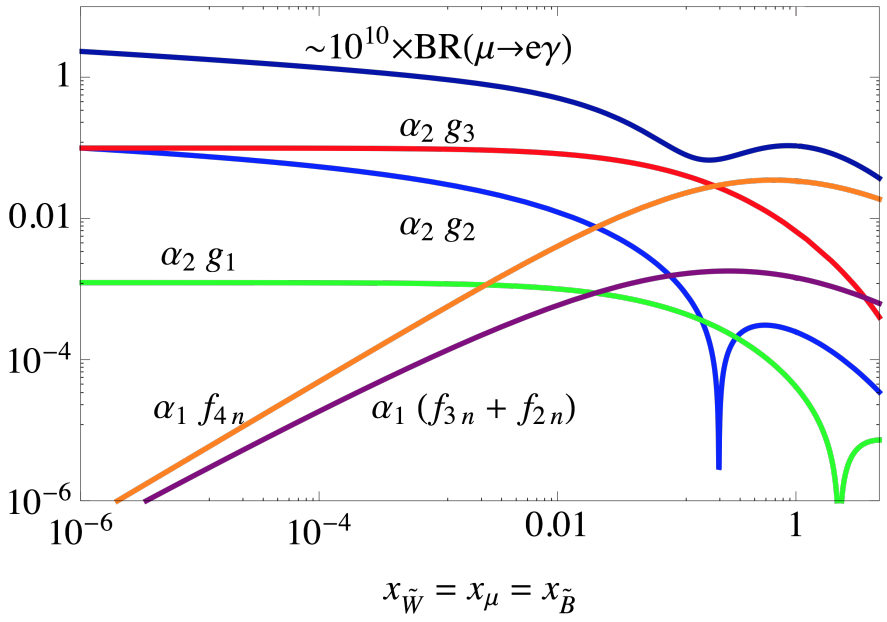

Figure 4.3: The relative importance of various operators to the branching ratio, as well as the total branching ratio scaled up. This shows that for small x (with all being set equal), the loop functions g_2 and g_3 dominate, while for larger values the Bino loop functions f_{2n}, f_{3n}, and f_{4n} become important. We set $\tilde{m}_\ell = 20$ TeV, and we set $\delta^{\mu e}_{LL} = \delta^{\mu e}_{RR} = \delta^{\mu\tau}_{LL}\delta^{\tau e}_{RR} = 0.3$ so that the effective $\delta^{\mu e}$ is the same for each operator. $\tan\beta = 10$.

branching ratios of $\tau \to \mu\gamma$ and $\tau \to e\gamma$. This is to be contrasted with Fig. 4.2 where small x did not enhance the meson mixing. Thus, we expect LFV to be a relatively powerful probe in the small x regime. Given the non-trivial x_i dependence, however, we will give a more detailed study of the dependence on combinations of $x_{\tilde{B}}, x_{\tilde{W}}$ and x_μ in Section 4.4.

4.3.2 $\mu \to e$ conversion in Nuclei

We decompose the contributions to $\mu \to e$ conversion.The branching ratio is given by

$$\begin{aligned}\mathrm{BR}(\mu \to e)_N = \Bigg\{ &\left| \frac{1}{4} e A_L^* D + 2(2g^u_{L,V} + g^d_{L,V})V^{(p)} + 2(g^u_{L,V} + 2g^d_{L,V})V^{(n)} \right|^2 \\ &+ \left| \frac{1}{4} e A_R^* D + 2(2g^u_{R,V} + g^d_{R,V})V^{(p)} + 2(g^u_{R,V} + 2g^d_{R,V})V^{(n)} \right|^2 \Bigg\} \frac{1}{\omega_{capture}}, \end{aligned} \tag{4.17}$$

where $\omega_{capture}$ is the muon capture rate of the nucleus. The $A_{L(R)}$ are the same dipole coefficients that were given in Section 4.3.1, and $g^{u,d}_{L(R),V}$ are the penguin- and box-type Wilson coefficients coupling to up or down-type quarks. The terms D, $V^{(p)}$ and $V^{(n)}$ are overlap integrals calculated in [160] whose values are presented in Appendix G for convenience.

At $x_{\tilde{W}} \sim 1$, the branching ratio for $\mu \to e$ conversion is dominated by the dipole contributions $A_{L,R}$. In this limit there is a simple relation between the $\mu \to e\gamma$ branching ratio and that of $\mu \to e$ conversion, namely:

$$\mathrm{BR}(\mu \to e)_N \simeq \frac{G_F^2 D^2}{192\pi^2 \omega_{capture}} \mathrm{BR}(\mu \to e\gamma) \sim \begin{cases} \frac{\alpha_{em}}{3} \mathrm{BR}(\mu \to e\gamma), & \text{when N is Aluminium,} \\ \frac{\alpha_{em}}{2} \mathrm{BR}(\mu \to e\gamma), & \text{when N is Gold.} \end{cases} \tag{4.18}$$

This will apply to our analysis in the case of TeV scale scalars. Given the future experimental improvements on measuring both $\mu \to e$ conversion and $\mu \to e\gamma$ (see Tab. 4.1), in the case of dipole domination, conversion can impose limits on LFV insertions comparable to those from $\mu \to e\gamma$.

The Wilson coefficients $g^{u,d}_{L(R),V}$ can be decomposed into the box-, γ-penguin and Z-penguin diagram contributions as

$$g^q_{L(R)V} = g^{q,box}_{L(R)V} + g^{q,\gamma}_{L(R)V} + g^{q,Z}_{L(R)V}. \tag{4.19}$$

Wino loops give the dominant contributions to the the g^q_{LV}. Since the operators correspond-

ing to these coefficients become important relative to the dipole contribution at small x_i, we present here the leading contributions in that regime [113].

$$5g_{LV}^{u,box} = g_{LV}^{d,box} = \frac{g_2^4}{(4\pi)^2\tilde{m}_q^2}\delta_{LL}^{\mu e}\frac{5}{4}f\left(\frac{\tilde{m}_\ell^2}{\tilde{m}_q^2}\right), \tag{4.20}$$

$$g_{LV}^{u,\gamma-peng.} = -2g_{LV}^{d,\gamma-peng.} = \frac{-2e^2g_2^2}{3(4\pi)^2\tilde{m}_\ell^2}\delta_{LL}^{\mu e}f_{\gamma,L}(x_{\tilde{W}}) \tag{4.21}$$

$$\simeq \frac{-2e^2g_2^2}{(4\pi)^2\tilde{m}_\ell^2}\delta_{LL}^{\mu e}\left\{\frac{1}{4}+\frac{1}{9}\log\left(x_{\tilde{W}}\right)\right\}, \tag{4.22}$$

where the second line is in the limit of small $x_{\tilde{B}}, x_{\tilde{W}} \ll 1$.

$$\begin{aligned} g_{LV}^{u,Z-peng.} &= \frac{-\left(1-\frac{4}{3}\sin^2\theta_W\right)}{\left(1-\frac{8}{3}\sin^2\theta_W\right)}g_{LV}^{d,Z-peng.} \\ &= \frac{-g_2^4}{(4\pi)^2\tilde{m}_\ell^2}\delta_{LL}^{\mu e}\frac{1}{16}\left(1-\frac{8}{3}\sin^2\theta_W\right) \\ &\times\left\{\cos^2\beta f_1\left(x_{\tilde{W}},x_\mu\right)+\sin^2\beta f_2\left(x_{\tilde{W}},x_\mu\right)+\mathrm{sgn}(\mu M_2)\sqrt{x_{\tilde{W}}x_\mu}\sin\beta\cos\beta f_3\left(x_{\tilde{W}},x_\mu\right)\right\}, \end{aligned} \tag{4.23}$$

where $f(x)$, $f_{\gamma,L}(x)$, $f_1(x)$, $f_2(x)$ and $f_3(x)$ are loop functions given in Appendix G.

The contributions proportional to $\delta_{RR}^{\mu e}$ can also be derived, and are presented here in the mass insertion approximation[3], to our knowledge, for the first time. Here, Bino exchange dominates. In the small x_i limit, the box diagrams give

$$g_{RV}^{u,box} = g_{RV}^{d,box} = \frac{g_1^4}{(4\pi)^2\tilde{m}_q^2}\delta_{RR}^{\mu e}\frac{1}{4}f\left(\frac{\tilde{m}_\ell^2}{\tilde{m}_q^2}\right), \tag{4.24}$$

while the γ-penguin diagrams contribute

$$g_{RV}^{u,\gamma-peng.} = -2g_{RV}^{d,\gamma-peng.} = \frac{-2e^2g_1^2}{3(4\pi)^2\tilde{m}_\ell^2}\delta_{RR}^{\mu e}f_{\gamma,R}(x_{\tilde{B}}) \tag{4.25}$$

$$\simeq \frac{-2e^2g_1^2}{(4\pi)^2\tilde{m}_\ell^2}\delta_{RR}^{\mu e}\left(\frac{1}{4}\right), \tag{4.26}$$

where $f_{\gamma,R}(x)$ is a loop function given in Appendix G. In the final line we have taken the

[3]Complete expressions for both LL and RR contributions in the mass eigenstate basis can be found in [122].

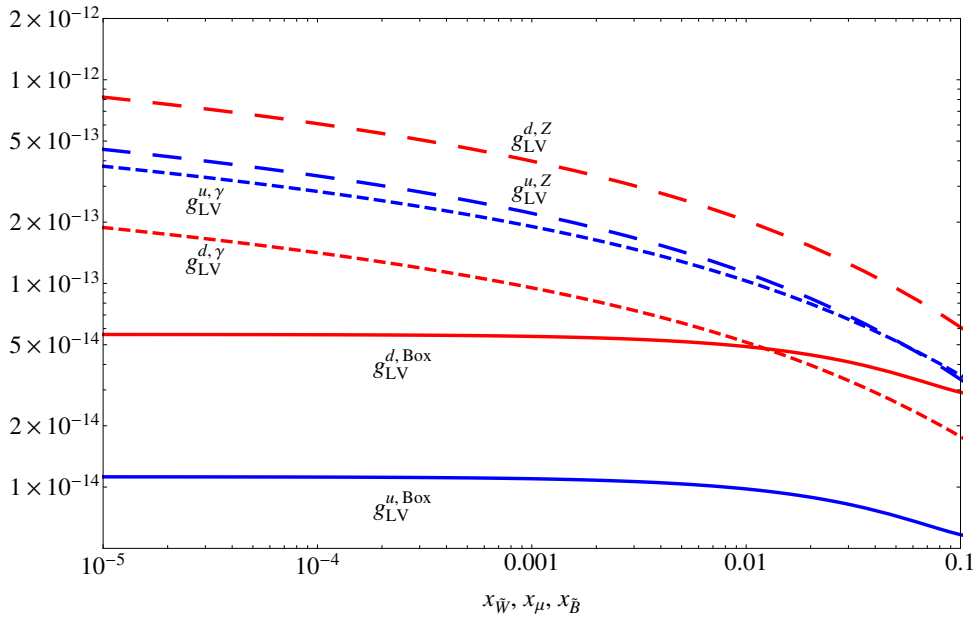

Figure 4.4: The relative importance of various non-dipole operators to the branching ratio as a function of $x_{\tilde{W}},\ x_\mu$. We have taken $\tilde{m}_\ell = \tilde{m}_q = 20$ TeV, $t_\beta = 10$, and $\delta_{LL} = \delta_{RR} = 0.3$. Not shown are the various RH non-dipole operators. They achieve a maximum of 8×10^{-15} for the Bino d-quark Z-penguin diagrams (at $x_i \sim 10^{-5}$) and a maximum of 4×10^{-15} for the Bino u-quark γ-penguin diagrams (at $x_i \sim 0.1$).

$x_{\tilde{B}} \to 0$ limit. The Z-penguin diagrams give

$$g_{RV}^{u,Z-peng.} = \frac{-\left(1-\frac{4}{3}\sin^2\theta_W\right)}{\left(1-\frac{8}{3}\sin^2\theta_W\right)} g_{RV}^{d,Z-peng.} = \frac{-g_1^4}{(4\pi)^2\tilde{m}_\ell^2}\frac{1}{4}\left(1-\frac{8}{3}\sin^2\theta_W\right)\delta_{RR}^{\mu e}\cos 2\beta f_{Z,R}(x_{\tilde{B}}, x_\mu). \tag{4.27}$$

where $f_{Z,R}(x_{\tilde{B}}, x_\mu)$ is a loop function given in Appendix G.

In Fig. 4.4 we show the dependence of non-dipole operators on a common x_i. We see the branching ratio of $\mu \to e$ conversion is dominated by the γ/Z-penguin diagrams for small x_i.

Interference between dipole and non-dipole operators in $\mu \to e$ conversion

We now review interference effects exhibited in $\mu \to e$ conversion. Most importantly, there is interference between the dipole operators and the non-dipole operators listed above. The physical sign $\mathrm{sgn}(\mu M_i)$, where i=1, 2 appears in Eqs. (4.11 – 4.14) in the dipole operators, and in Eq. (4.23) in the non-dipole operators. While in the Wino Z-penguin operator, Eq. (4.23), it has only a small effect on the overall size of the contribution, in the dipole operator of Eqs.

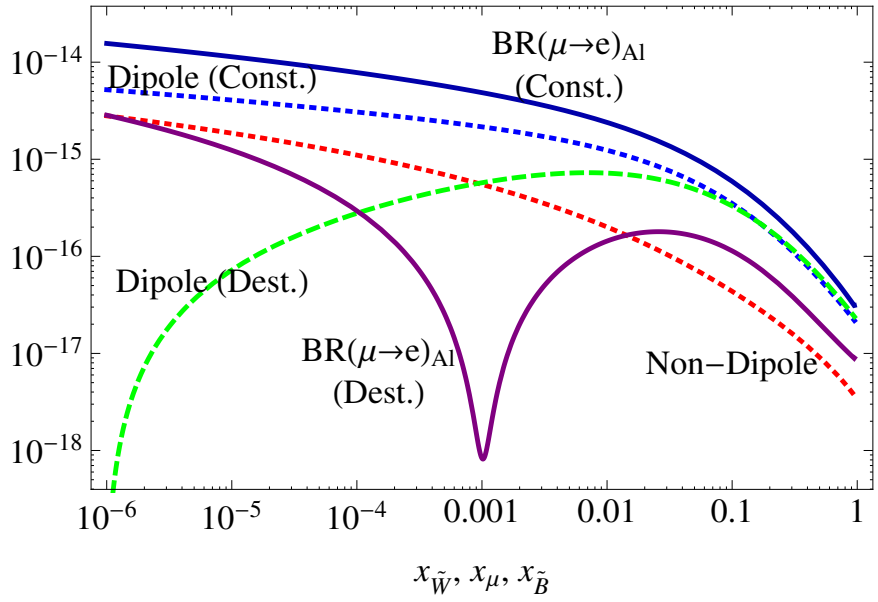

Figure 4.5: The interference of dipole and non-dipole operators as a function of $x_{\tilde{W}}$, x_μ, $x_{\tilde{B}}$. We have taken $\tilde{m}_\ell = \tilde{m}_q = 20$ TeV, $t_\beta = 10$, and $\delta_{LL} = \delta_{RR} = 0.1$. The blue (green) dotted line shows the constructive (destructive) contribution from the dipole operators, while the red dotted line shows the contribution from the non-dipole operators. The dark blue line shows the constructive branching ratio, while the purple line shows the destructive branching ratio.

(4.11 – 4.14) it not only changes the size, but also the sign of these contributions relative to the sum of the non-dipole operators. The result is that if $\mathrm{sgn}(\mu M_i) = -$ (+) the branching ratio of $\mu \to e$ conversion exhibits constructive (destructive) interference.

At large values of x_i the dipole operators dominate, and the interference effects are lessened. At smaller values of x_i however, the dipole and non-dipole operators both contribute, and indeed, there is a region where the LH dipole and LH non-dipole parts cancel exactly. In this case, the branching ratio for $\mu \to e$ conversion is given by the RH contributions, which are themselves dominated by the non-dipole parts in this regime. This is shown in Fig. 4.5 for $\tilde{m}_\ell = 20$ TeV, but a similar cancellation is robust for all values of $\tilde{m}_\ell$.

4.3.3 Rare $\ell_i \to 3\ell_j$ decays

We now examine the operators that contribute to the rare decays of $\ell_i \to 3\ell_j$. In our numerical analysis we restrict ourselves to the decay $\mu \to 3e$, but analytic results apply to rare tau decays as well. We concentrate on $\mu \to 3e$ because of the expected improvement in

sensitivity from the Mu3e experiment [135, 136], which aims to probe $\mathrm{BR}(\mu \to 3e) \lesssim 10^{-16}$. We do not consider $\tau \to 3e(\mu)$ decays in our numerical analysis, as the expected future sensitivity is not much greater than that of $\tau \to e(\mu)\gamma$ [146].

The branching ratio of $\ell_i \to 3\ell_j$ is given by [107, 109] as

$$\begin{aligned}
\mathrm{BR}(\ell_i \to 3\ell_j) \simeq \frac{6\pi^2\alpha_{em}^2}{G_F^2}\Bigg\{ & |A^L_{\gamma-p.}|^2 + |A^R_{\gamma-p.}|^2 - 2\left(A^L_{\gamma-p.}(A^R_{dip.})^* + A^L_{dip.}(A^R_{\gamma-p.})^* + h.c.\right) \\
& + \left(\frac{16}{3}\log\frac{m_\mu}{m_e} - \frac{22}{3}\right)\left(|A^L_{dip.}|^2 + |A^R_{dip.}|^2\right) \\
& + \frac{1}{6}\left(|B^L_1|^2 + |B^R_1|^2\right) + \frac{1}{3}\left(|B^L_2|^2 + |B^R_2|^2\right) \\
& + \frac{1}{24}\left(|B^L_3|^2 + |B^R_3|^2\right) + 6\left(|B^L_4|^2 + |B^R_4|^2\right) \\
& - \frac{1}{2}\left(B^L_3(B^L_4)^* + B^R_3(B^R_4)^* + h.c.\right) \\
& + \frac{1}{3}\left(A^L_{\gamma-p.}(B^L_1)^* + A^R_{\gamma-p.}(B^R_1)^* + A^L_{\gamma-p.}(B^L_2)^* + A^R_{\gamma-p.}(B^L_2)^* + h.c.\right) \\
& - \frac{2}{3}\left(A^R_{dip.}(B^L_1)^* + A^L_{dip.}(B^R_1)^* + A^L_{dip.}(B^R_2)^* + A^R_{dip.}(B^L_2)^* + h.c.\right) \\
& + \frac{1}{3}\Big[2\left(|F_{LL}|^2 + |F_{RR}|^2\right) + |F_{LR}|^2 + |F_{RL}|^2 \\
& + \left(B^L_1(F_{LL})^* + B^R_1(F_{RR})^* + B^L_2(F_{LR})^* + B^R_2(F_{RL})^* + h.c.\right) \\
& + 2\left(A^L_{\gamma-p.}(F_{LL})^* + A^R_{\gamma-p.}(F_{RR})^* + h.c.\right) + \left(A^L_{\gamma-p.}(F_{LR})^* + A^R_{\gamma-p.}(F_{RL})^* + h.c.\right) \\
& - 4\left(A^R_{dip.}(F_{LL})^* + A^L_{dip.}(F_{RR})^* + h.c.\right) - 2\left(A^L_{dip.}(F_{RL})^* + A^L_{dip.}(F_{LR})^* + h.c.\right)\Big]\Bigg\}\,, \quad (4.28)
\end{aligned}$$

where $A^{L,R}_{dip.}$ are the dipole operator coefficients from from Eqs. (4.11) - (4.14) above, $A^{L,R}_{\gamma-p.}$ are the photo-penguin operator coefficients, the $B^{L,R}_i$ are from box-type operators and the $F_{LL,RR,LR,RL}$ are from Z-penguin operators, as defined in [109].

Typically at moderate and low $\tan\beta$, the $\mu \to e\gamma$ dipole operators dominate the $\mu \to 3e$ decay rate [109, 113], in large part due to the appearance of the $\log m_\mu/m_e$ in the second line of Eq. (4.28) above.[4] There exists then a fairly simple relation between the two branching

[4]This logarithm arises due to the phase space integration of the final state fermions– there is a infrared singularity cutoff by the electron mass.

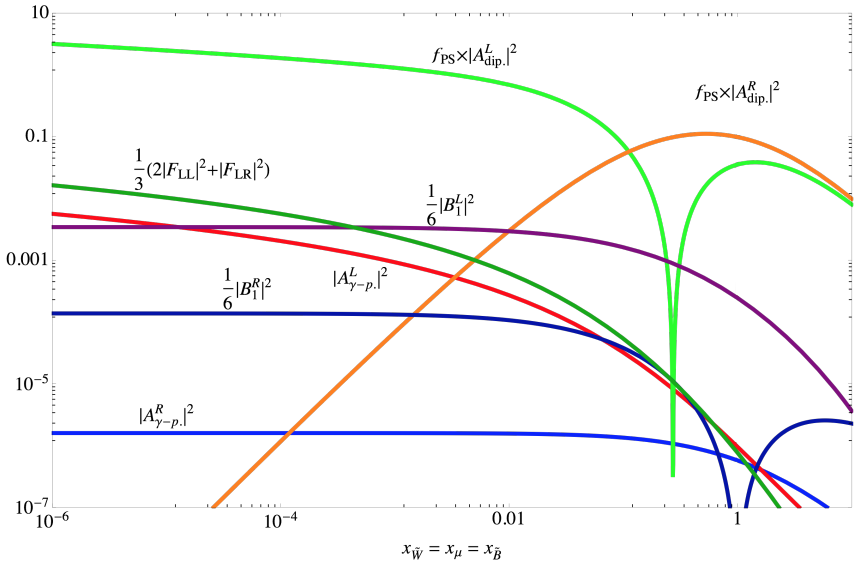

Figure 4.6: The relative importance of various operators to the branching ratio of $\mu \to 3e$, in arbitrary units. We have scaled each one by the appropriate numerical factor ($f_{PS} \equiv \left(\frac{16}{3}\log\frac{m_\mu}{m_e} - \frac{22}{3}\right)$ contains the IR logarithm induced by integration over phase space). This shows that for all values of x (with all being set equal), the dipole coefficents dominate. We set $\tilde{m}_\ell = 20$ TeV, and we set $\delta^{\mu e}_{LL} = \delta^{\mu e}_{RR} = \delta^{\mu\tau}_{LL}\delta^{\tau e}_{RR} = 0.3$ so that the effective $\delta^{\mu e}$ is the same for each operator. $\tan\beta = 10$.

ratios:

$$\frac{\mathrm{BR}(\mu \to 3e)}{\mathrm{BR}(\mu \to e\gamma)} \simeq \frac{\alpha_{em}}{3\pi}\left(2\log\frac{m_\mu}{m_e} - \frac{11}{4}\right) \simeq 6.1\times 10^{-3}\ . \tag{4.29}$$

As can be seen in Fig. 4.6, the dipole operators, enhanced by the phase space factor, greatly dominate over the other operators that contribute to the branching ratio in all regions of x_i parameter space. In our analysis we include the numerical contributions from the other operators, which are given in the mass insertion approximation in Appendix H.

4.4 Dependence on Fermionic Superpartner Masses

In Section 4.3 above, we saw that there is non-trivial dependence of LFV observables on $x_{\tilde{B}}$, $x_{\tilde{W}}$, x_μ and t_β. Additionally, the dependence on $x_{\tilde{g}}$ of quark sector observables was

shown in Fig. 4.2. In this section we examine in detail how the LFV constraints compare with the quark FCNC constraints as a function of various combinations of gaugino masses and μ. With this aim in mind, we show the ratio of squark to slepton mass

$$R_{ij} \equiv \tilde{m}_q / \tilde{m}_\ell, \tag{4.30}$$

for which constraints derived from transitions between generations i and j are equally strong from the quark and lepton sectors. We investigate this ratio as a function of various x_i. Because in this section we set $\delta_{LR} = 0$, the behavior of the various transitions always goes as $\delta/\tilde{m}^2$. Thus, our results in terms of R_{ij} with fixed δ can be reinterpreted as ratios of $\sqrt{\delta_\ell/\delta_q}$ for equal sfermion masses.

Before discussing the relative power of different measurements, we first want to determine what x_i affect our observables most. We first examine the dependence of meson oscillation observables on $x_{\tilde{g}}$. This can be gleaned by studying Fig. 4.2. There is $\mathcal{O}(1)$ variation between small $x_{\tilde{g}}$ and $x_{\tilde{g}} \sim 1$, while for $x_{\tilde{g}} \gg 1$ the variation becomes important. Since we restrict ourselves to either the situation where $x_{\tilde{g}} \ll 1$ or $x_{\tilde{g}} \sim 1$, the relative power of LFV and quark FCNC observables with respect to $x_{\tilde{g}}$ is at most $\mathcal{O}(1)$. In addition, the dependence of the LFV observables on $x_{\tilde{B}}$ in the regions we consider ($x_{\tilde{B}} \ll 1 \to x_{\tilde{B}} \sim 1$) is only slight. Only if one has large $x_\mu \gtrsim 1$ as well as large $x_{\tilde{B}} \gtrsim 1$ does the variation become appreciable. As such, varying $x_{\tilde{B}}$ does not allow one to change the relative power of the LFV and quark FCNC observables much. Therefore, we concentrate on the effect of varying x_μ and $x_{\tilde{W}}$.

We now move to quantify the relative power of quark and LFV constraints by solving for R in several cases. We first specify $x_{\tilde{g}}$. We then find the squark mass which saturates the bound from meson mixing. Similarly, once we fix x_μ, $x_{\tilde{B}}$ and $x_{\tilde{W}}$ we can find the corresponding slepton mass which saturates the current limits on the processes $\mu \to e\gamma$, $\tau \to e\gamma$ and $\tau \to \mu\gamma$. We also consider the combinations which saturate the future sensitivity to $\mu \to e\gamma$, $\mu \to e$ conversion in Aluminium and $\mu \to 3e$. Combining these two results yields R. Results shown in this section assume constructive interference as defined for the LFV processes in Section 4.3. Were we to examine the case of destructive interference, when comparing $\ell_i \to \ell_j\gamma$ with quark FCNCs, we would find qualitatively similar behavior of R_{ij} for values of $x_i \lesssim 1$. R is increased by at most a factor of 2. For large values of x_i, the interference effect is lessened. When comparing $\mu \to e$ conversion however, interference effects can be important, as discussed in Section 4.3.2. If we were to examine destructive interference, R would become very large near $x_i \sim 10^{-3}$.

We study two separate regimes, one where we fix $x_{\tilde{B}} = x_{\tilde{W}} = x_{\tilde{g}} \sim 1$, which corresponds

to TeV-scale physics, and one where we fix $x_{\tilde{B}} = x_{\tilde{W}} = x_{\tilde{g}} \sim 10^{-3}$, corresponding to heavy scalars, but with $\mathcal{O}(\text{TeV})$ gauginos. We then allow only x_μ to vary, primarily because its variation captures most of the important effects. We have already argued that $x_{\tilde{B}}$ and $x_{\tilde{g}}$'s effects are easily understood. In principle, we could have shown the variation with respect to $x_{\tilde{W}}$, but it follows approximately the same pattern as varying x_μ. This can be understood by considering Fig. 4.3. In the small x_i regime, the dominant contribution to the $\mu \to e\gamma$ transition arises due to the LH Wino-Higgsino mixing diagrams with loop functions $g_2(x_{\tilde{W}}, x_\mu)$ and $g_3(x_{\tilde{W}}, x_\mu)$. In the small x_i limit, these functions are approximately

$$g_2(x_{\tilde{W}}, x_\mu) \sim \frac{x_{\tilde{W}} \log x_{\tilde{W}}}{x_\mu - x_{\tilde{W}}} + \frac{x_\mu \log x_\mu}{x_{\tilde{W}} - x_\mu}, \tag{4.31}$$

$$g_3(x_{\tilde{W}}, x_\mu) \sim \frac{\log x_{\tilde{W}}}{x_\mu - x_{\tilde{W}}} + \frac{\log x_\mu}{x_{\tilde{W}} - x_\mu}, \tag{4.32}$$

so that the behavior as a function of x_μ and $x_{\tilde{W}}$ is the same. Therefore varying one while keeping the other fixed is enough to illustrate the general behavior.

In the large $x_i \sim 1$ regime, there is more complicated dependence on various contributions to the $\mu \to e\gamma$ amplitude. We see from both Fig. 4.3 and Fig. 4.7a that the region $0.3 \lesssim x_\mu, x_{\tilde{W}} \lesssim 3$ is where most variation occurs. This is also true for $1-3$ and $2-3$ transitions, as can be seen in Figs. 4.8a and 4.8c. In this regime (the region $0.3 \lesssim x_\mu, x_{\tilde{W}} \lesssim 3$), we find the following functions

$$R_{12} \simeq 7.2 + \sqrt{0.85\, x_{\tilde{W}} x_\mu} + \log x_{\tilde{W}} + \log x_\mu, \tag{4.33}$$

$$R_{13} \simeq 54 + \sqrt{2.5\, x_{\tilde{W}} x_\mu} + 7(\log x_{\tilde{W}} + \log x_\mu), \tag{4.34}$$

$$R_{23} \simeq 2.6 + \sqrt{0.28\, x_{\tilde{W}} x_\mu} + 0.2(\log x_{\tilde{W}} + \log x_\mu), \tag{4.35}$$

capture this behavior accurately to within $\lesssim 6\%$. We choose this particular functional form because it closely matches the functional form of the full expressions (found in Appendix F), with a small number of parameters.

The situation where $x_{\tilde{B}} \sim x_{\tilde{W}} \sim x_{\tilde{g}} \sim 1$ at the low scale could be realized with a GUT-scale boundary condition such that a universal scalar mass m_0 is small compared with high scale gaugino masses $m_{1/2}$. In this case, one arrives at a low-energy spectrum where the slepton masses are dominated by the Wino mass, and the squark masses are dominated by the gluino mass. We find that with these boundary conditions, the low scale squark to slepton mass ratio is fixed, and is approximately $\tilde{m}_q/\tilde{m}_\ell \sim 3$. This is shown by the dotted red line in Fig. 4.7a. Given the constraints from the running on $x_{\tilde{B}},\ x_{\tilde{g}},\ x_{\tilde{W}}$, the only free

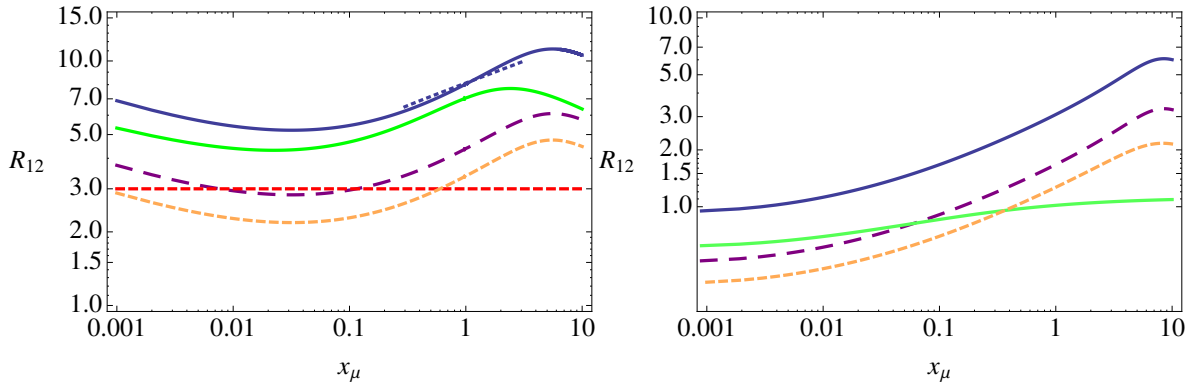

(a) $x_{\tilde{B}} = x_{\tilde{W}} = x_{\tilde{g}} \sim 1$. (b) $x_{\tilde{B}} = x_{\tilde{W}} = x_{\tilde{g}} \sim 10^{-3}$.

Figure 4.7: These figures show x_μ vs. the ratio R_{12} of squark to slepton mass that saturates the experimental bounds from kaon oscillations and rare μ decays. We set $\delta_{LL,RR} = 0.1$, $\delta_{LR} = 0$ and $t_\beta = 10$. In the left figure, $x_{\tilde{B}} = x_{\tilde{W}} = 1$, while in the right figure $x_{\tilde{B}} = x_{\tilde{W}} = 10^{-3}$. The solid blue line is the current $\mu \to e\gamma$ constraint, the dashed purple line is the future $\mu \to e\gamma$ sensitivity, the solid green line is the future sensitivity to $\mu \to e$ conversion in Aluminium, and the dashed orange line corresponds to future $\mu \to 3e$ sensitivity. The dotted blue line corresponds to the function for R_{12} given in Eq. (4.33). The dashed red line is the ratio of $\tilde{m}_q/\tilde{m}_\ell$ obtained by running from the GUT scale to the low scale given initial conditions for a universal gaugino mass $m_{1/2}(M_{GUT}) = 3$ TeV and universal scalar mass $m_0(M_{GUT}) = 0.5$ TeV.

parameters in this case are μ and t_β. We show in Fig. 4.7a how the squark to slepton mass ratio varies as a function of x_μ for the $1-2$ sector, and in Figs. 4.8a and 4.8c for the $1-3$ and $2-3$ sectors respectively.

We show the results for the "heavy scalar case" $x_{\tilde{B}} = x_{\tilde{W}} = x_{\tilde{g}} \sim 10^{-3}$ in Fig. 4.7b for the $1-2$ sector, and in Figs. 4.8b and 4.8d for the $1-3$ and $2-3$ sectors respectively. This situation could arise for example if the boundary conditions at the GUT-scale are such that a universal gaugino mass $m_{1/2}$ is suppressed relative to m_0.

We notice that smaller x_μ increases the relative strength of the LFV probes for all transitions. Moreover, R decreases as a function of increasing t_β, i.e. LFV becomes relatively powerful at large t_β. For the current constraints from $\mu \to e\gamma$, R_{12} decreases from $R_{12} \approx 20$ for $t_\beta = 2$ to $R_{12} \approx 6$ for $t_\beta = 20$ when $x_i \sim 1$, and from $R_{12} \approx 1.6$ for $t_\beta = 2$ to $R_{12} \approx 0.7$ for $t_\beta = 20$ when $x_i \sim 10^{-3}$.

The constraint from $\mu \to e$ conversion shows a decrease from $R_{12} \approx 10$ for $t_\beta = 2$ to $R_{12} \approx 3$ for $t_\beta = 20$ for $x_i \sim 1$, and from $R_{12} \sim 0.7$ for $t_\beta = 2$ to $R_{12} \sim 0.5$ for $t_\beta = 20$ when $x_i \sim 10^{-3}$. For all transitions, being in the small $x_{\tilde{B}}$, $x_{\tilde{W}}$, $x_{\tilde{g}}$ regime results in significant

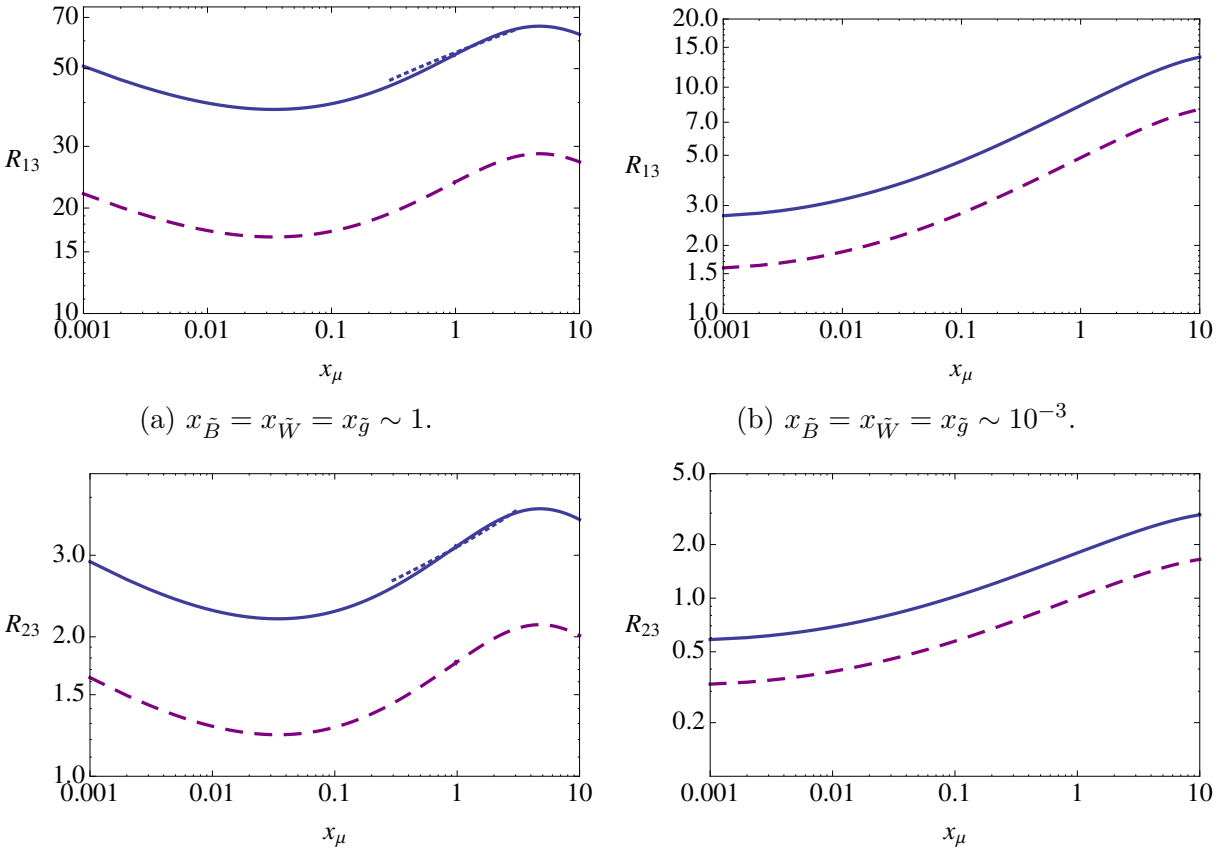

(a) $x_{\tilde{B}} = x_{\tilde{W}} = x_{\tilde{g}} \sim 1$.

(b) $x_{\tilde{B}} = x_{\tilde{W}} = x_{\tilde{g}} \sim 10^{-3}$.

(c) $x_{\tilde{B}} = x_{\tilde{W}} = x_{\tilde{g}} \sim 1$.

(d) $x_{\tilde{B}} = x_{\tilde{W}} = x_{\tilde{g}} \sim 10^{-3}$.

Figure 4.8: The upper (lower) figures show x_μ vs. the ratio R_{13} (R_{23}) of squark to slepton mass that saturates the current experimental bounds from B_d (B_s) meson oscillations and $\tau \to e\gamma$ ($\tau \to \mu\gamma$). We set $\delta_{LL,RR} = 0.1$, $\delta_{LR} = 0$ and $t_\beta = 10$. In the left figure, $x_{\tilde{B}} = x_{\tilde{W}} = 1$, while in the right figure $x_{\tilde{B}} = x_{\tilde{W}} = 10^{-3}$. The solid blue line is calculated using the current $\tau \to e\gamma$ ($\tau \to \mu\gamma$) constraint, while the dashed purple line uses the future $\tau \to e\gamma$ ($\tau \to \mu\gamma$) sensitivity. The dotted blue lines corresponds to the functions for R_{13} (upper left) and R_{23} (lower left) given in Eqs. (4.34) and (4.35) respectively.

increases in the relative strength of LFV observables relative to quark FCNC observables. The increase is a factor of a few for the $1-2$ and $1-3$ transitions, and up to an order of magnitude for the $2-3$ transitions. In the $1-2$ and $2-3$ transitions, we see that at small values of x_i the ratio drops below 1, meaning that the LFV constraints become stronger than those from the meson oscillation observables. In the $1-3$ sector however, the ratio does not drop below 1, a result that is echoed in Section 4.5, where we see that B_d meson oscillations are a stronger constraint than $\tau \to e\gamma$ in much of the δ parameter space also. We also observe that in Fig. 4.7b for small $x_{\tilde{B}},\ x_{\tilde{W}},\ x_{\tilde{g}}$, $\mu \to e$ conversion in the future goes from being a weaker constraint than the future sensitivity of $\mu \to e\gamma$ at small x_μ, to being the stronger constraint for $x_\mu \gtrsim 0.04$.

From our results in this section, we can see that having small x_i results in a relative strengthening of the LFV constraints for all transitions. Nevertheless, varying x_i over 3 orders of magnitude typically only results in variation of R by $\mathcal{O}$(few), and at most an order of magnitude.

4.5 Constraints on δ

In this section we examine constraints on the flavor off-diagonal mass insertions. We show results for $1-2$ transitions (comparing $\mu \to e\gamma$, $\mu \to e$ conversion and $\mu \to 3e$ with Δm_K), and also for $1-3$ and $2-3$ transitions (comparing $\tau \to e(\mu)\gamma$ with $B_{d(s)}$ meson mixing). These analyses summarize the relative sensitivity of quark and lepton flavor violation probes now and into the future.

It is also of interest to connect these results to GUT constructions and or textures. If SUSY breaking respects, e.g., an $SU(5)$ GUT symmetry, particles residing within a $\bar{\mathbf{5}}$ or a $\mathbf{10}$ may share a common soft mass. Inspired by this relation, we define

$$\begin{aligned} \delta^{\tilde{\ell}_i}_{LL} = \delta^{\tilde{d}_i}_{RR} \equiv \delta_{\bar{\mathbf{5}}}, \\ \delta^{\tilde{\ell}_i}_{RR} = \delta^{\tilde{u}_i}_{RR} = \delta^{\tilde{q}_i}_{LL} \equiv \delta_{\mathbf{10}}. \end{aligned} \tag{4.36}$$

We will comment on how our results can be rephrased in this language below.

In subsection 4.5.1 we consider the situation where the LR insertions are zero, and all the mass-squared ratios $x_i \sim \mathcal{O}(10^{-2} - 10^{-3})$, indicative of a significant but modest hierarchy between sfermions and fermionic superpartners. In this region of parameter space we are interested in the possibility that gauginos and the μ parameter are all around the TeV scale,

but sfermions are much heavier, in the tens to hundreds of TeV, akin to models of split or mini-split SUSY [98, 141, 161, 2, 162, 11, 14, 51]. There is strong motivation for such models, and their implications for flavor physics have been considered before [2, 3, 113, 163, 20, 164]. For even smaller x, for fixed sfermion mass, the $\Delta F = 2$ is essentially unchanged. The LFV BRs increase logarithmically as you go to smaller x_i (see Eq. (4.32)). However, too small x_i will result in too small gaugino masses and μ unless the sfermion mass is raised.

In subsection 4.5.2 we consider the case where LR insertions are zero, but the $x_i = 1$. Finally in subsection 4.5.3 we analyse the case where LR insertions are non-zero, and the $x_i = 1$. In the latter two sections with $x_i = 1$, the region of parameter space we consider is one where once again gauginos and the μ parameter are around the TeV scale, motivated both by naturalness and by dark matter considerations. Therefore we set the sfermion masses to also be at the TeV scale.

4.5.1 $\delta_{LR} = 0$, x small

In this subsection we consider $x_i \ll 1$, corresponding to a scenario where there is a hierarchy between scalar and fermionic superpartners. In Figs. 4.9 and 4.10, we display regions excluded by quark and lepton FCNC limits in the δ_{LL}, δ_{RR} plane. Note, meson mixing constraints are symmetric under $\delta_{LL} \leftrightarrow \delta_{RR}$, so these figures can be reinterpreted as $\delta_{RR} \leftrightarrow \delta_{\mathbf{10}}$ and $\delta_{LL} \leftrightarrow \delta_{\bar{\mathbf{5}}}$. In our numerical work, we have set δ's in the up sector to vanish, but flavor violation in the up sector is in any case subdominant for the meson mixing considered here.

In Fig. 4.9, which corresponds to $1-2$ transitions, we have chosen $\tilde{m}_q = \tilde{m}_\ell = 20$ TeV and $x_i = 5 \times 10^{-3}$, while for the $1-3$ (Figs. 4.10a, 4.10b) and $2-3$ transitions (Fig. 4.10c, 4.10d), we have chosen $\tilde{m}_q = \tilde{m}_\ell = 5$ TeV and $x_i = 0.04$. The sfermion masses and value of the common x_i for $1-2$ transitions is chosen so as to avoid falling into the region where the destructive interference in $\mu \to e$ conversion is most important, around $x_i \sim 10^{-3}$ (see Section 4.3.2 for further discussion). The smaller sfermion masses and larger x_i for $1-3$ and $2-3$ transitions are chosen so that useful constraints can be shown, and to comply with limits from Run I of the LHC on gluino masses, respectively. While we have chosen to show plots for particular sfermion mass assignments, the corresponding limits on $\delta_{LL,RR}$ will scale with the masses according to the expressions given in the quark FCNC/LFV anatomy sections 4.2, 4.3 above. We discuss each of these figures now in turn.

In Fig. 4.9, we display limits from Δm_K, $\mu \to e\gamma$, $\mu \to 3e$ and $\mu \to e$ conversion. For muon conversion we use the future experimental sensitivity in Aluminium, shown in Table 4.1 above. We see from Fig. 4.9 a) that in the case of constructive interference for the

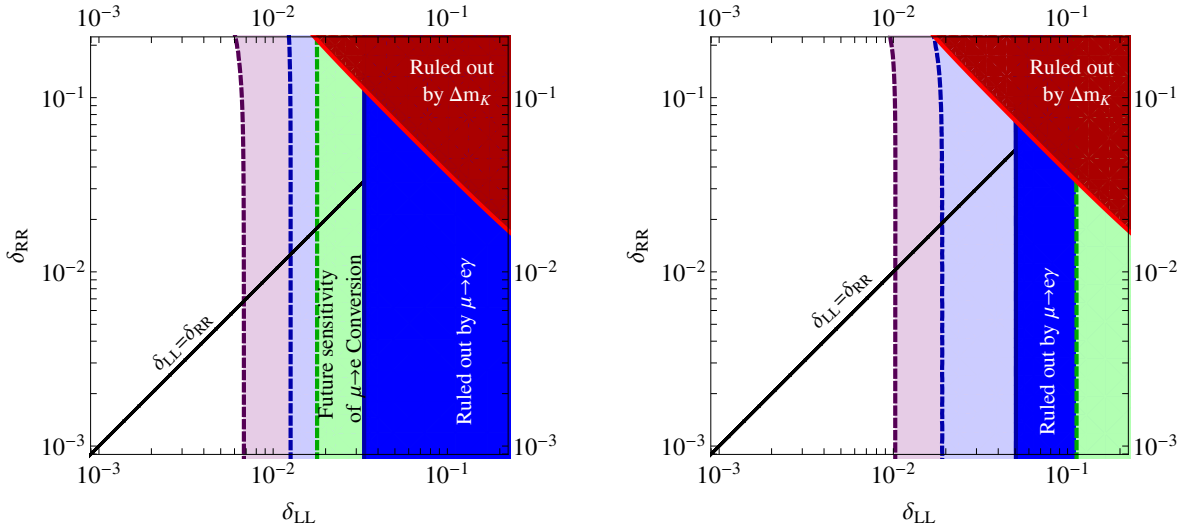

(a) Constructive interference in LFV processes.

(b) Destructive interference in LFV processes.

Figure 4.9: δ_{LL} vs δ_{RR} plots for $1-2$ insertions. These plots compare constraints from Δm_K (red), BR($\mu \to e\gamma$) (current (future) in dark (light) blue), $\mu \to e$ conversion (green) and BR($\mu \to 3e$) (purple). All regions correspond to the measured (projected) limits at 90% C.L. We have set $\tilde{m}_q = \tilde{m}_\ell = 20$ TeV, $x_{\tilde{g}} = x_\mu = x_{\tilde{W}} = x_{\tilde{B}} = 5 \times 10^{-3}$, and $t_\beta = 10$.

LFV processes (see discussion below Eqn. 4.11), $\mu \to e\gamma$ is already a stronger constraint than Δm_K. Also in this case, the future sensitivity of $\mu \to e\gamma$ will be superior to that of $\mu \to e$ conversion. In the case of destructive interference the current constraint from $\mu \to e\gamma$ is stronger than the future sensitivity of $\mu \to e$ conversion (see Fig. 4.9 b)). This is due to $\mu \to e$ conversion experiencing large interference between the dipole and non-dipole operators in the region near $x_i \sim 10^{-3}$, while the interference in $\mu \to e\gamma$, arising only within the dipole operators, is less pronounced. For both constructive and destructive interference, the strongest constraint will be from the improvement on $\mu \to e\gamma$, and eventually from the planned Mu3e experiment.

In Fig. 4.10 we assume δ^{12} is negligibly small, and as such only δ^{13} and δ^{23} processes will be relevant. We choose $x_i = 0.04$ in these plots so that the gauginos and μ are all at 1 TeV. We compare $\tau \to e\gamma$ with Δm_{B_d}, β_d in Figs. 4.10a and 4.10b, and $\tau \to \mu\gamma$ with Δm_{B_s}, β_s in Figs. 4.10c and 4.10d. In both sets of plots we also consider the possibility that $\mu \to e\gamma$ can provide a constraint on $\delta^{13}\delta^{23}$ due to the LR flavor-conserving insertion in the m_τ/m_μ enhanced Bino loop contribution from Section 4.3.1. We compare the possible constraint from $\mu \to e\gamma$ under the assumption that $\delta^{13}_{LL,RR} = \delta^{23}_{RR,LL}$, but $\delta^{12} = 0$. In this case the only operator contributing to $\mu \to e\gamma$ is the LR flavor-conserving Bino operator from section 4.3.

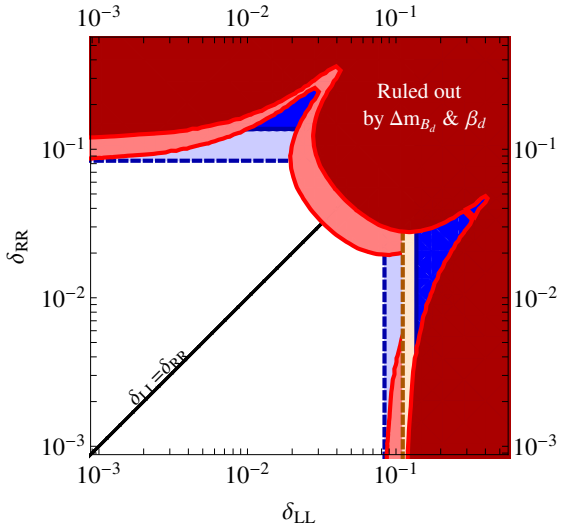

(a) Constructive interference in LFV, $1-3$ transitions

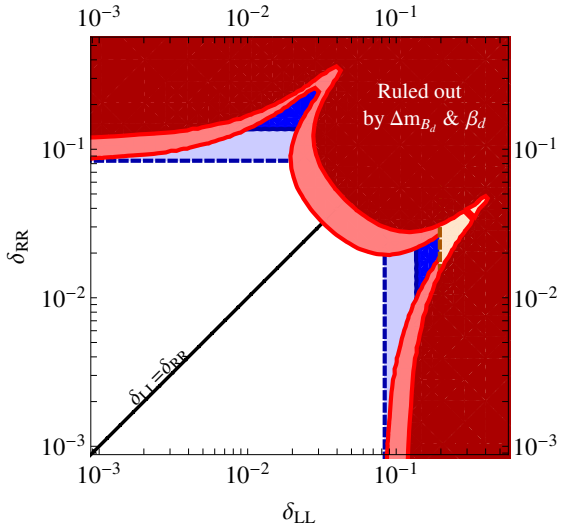

(b) Destructive interference in LFV, $1-3$ transitions

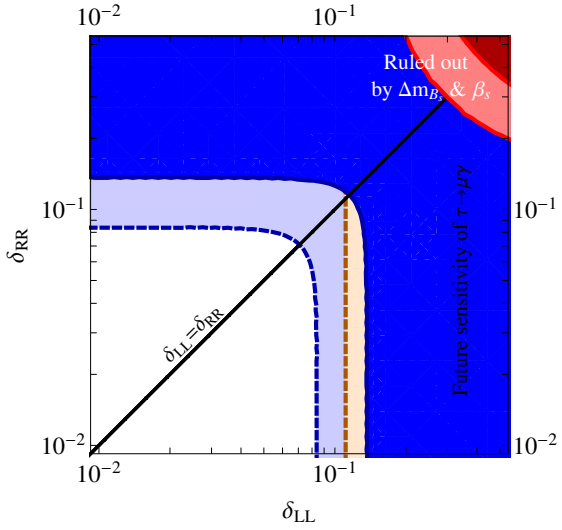

(c) Constructive interference in LFV, $2-3$ transitions

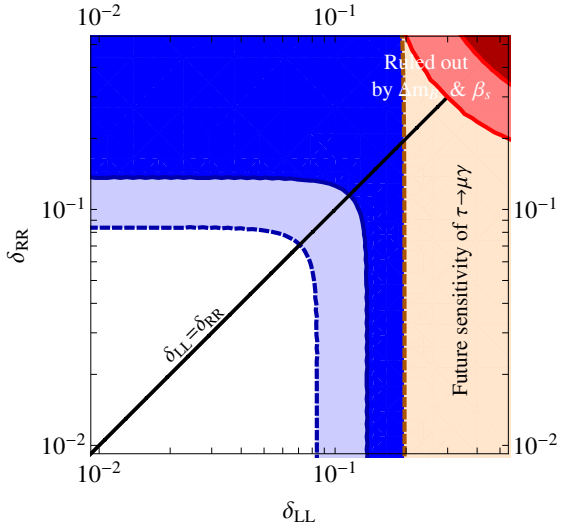

(d) Destructive interference in LFV, $2-3$ transitions

Figure 4.10: δ_{LL} vs δ_{RR} plots for $1-3$ (upper) and $2-3$ (lower) insertions. These plots compare constraints from Δm_{B_d} and β_d, BR$(\tau \to e\gamma)$ for the upper plots, and from Δm_{B_s} and β_s, BR$(\tau \to \mu\gamma)$. The dark red regions are already excluded, and the light red shows the potential future reach with a factor of two improvement. The light orange region shows the future sensitivity of $\tau \to e/\mu\gamma$. We have set $\tilde{m}_q = \tilde{m}_\ell = 5$ TeV, $x_{\tilde{g}} = x_\mu = x_{\tilde{W}} = x_{\tilde{B}} \simeq 0.04$, and $t_\beta = 10$. Also shown is a dark blue region excluded by $\mu \to e\gamma$ making the further assumption that $\delta^{13}_{LL,RR} = \delta^{23}_{RR,LL}$. The light blue is the future sensitivity given the same assumption. All regions shown are excluded at 90% C.L.

Presented are results for both constructive and destructive interference between operators contributing to the rare τ decays.

For the B-meson observables, the central region near $\delta_{LL} = \delta_{RR}$ is dominated by the operator Q_4, as defined in Section 4.2, while the extended regions at small δ_{LL} and δ_{RR} are dominated by the operators Q_1 and $\tilde{Q}_1$ respectively. The two regions where constraints from B_d-mesons are weaker occur due to cancellation between $Q_1/\tilde{Q}_1$ and Q_4.

In Fig. 4.10a we observe that in the future $\tau \to e\gamma$ has the potential to be a stronger constraint (for constructive interference) on δ_{LL} than the current bound from B_d mixing for small $\delta_{RR} \lesssim 2 \times 10^{-2}$. However, if the constraints from B_d mixing improve by a factor of two this will reduce the region where $\tau \to e\gamma$ has the potential to be a stronger constraint to $5 \times 10^{-3} \lesssim \delta_{RR} \lesssim 2 \times 10^{-2}$. If $\delta_{LL} \geq \delta_{RR}$, the constraints from B_d mixing will remain the strongest. In the case of destructive interference, the future $\tau \to e\gamma$ constraint will only be stronger in a small region where the contributions from the quark FCNC operators Q_1 and Q_4 cancel. The current constraints on δ_{LL} from $\mu \to e\gamma$ under the assumptions stipulated above are weaker (stronger) than the future constraints from $\tau \to e\gamma$ in the case of constructive (destructive interference).

Meanwhile from Fig. 4.10c we see that the constraints from B_s mixing are currently stronger than those from LFV in all regions of δ-space. In the future however, the constraints on δ_{LL} from $\tau \to \mu\gamma$ will become stronger for all values of δ_{RR} in the case of constructive interference, and for $\delta_{RR} \lesssim 0.3$ in the case of destructive interference. The constraints on δ_{RR} from $\mu \to e\gamma$ apply only if $\delta^{13}_{LL,RR} = \delta^{23}_{RR,LL}$. Under this assumption, the current constraints from $\mu \to e\gamma$ are always stronger than those from B_s meson mixing, and stronger (weaker) than the future constraints from $\tau \to \mu\gamma$ for constructive (destructive) interference. Additionally, $\mu \to e\gamma$ places constraints on δ^{23}_{RR}. Limints from $\tau \to \mu\gamma$ one this insertion are very weak (not visible on this plot). For both constructive and destructive interference, the future sensitivity of $\mu \to e\gamma$ under the stipulated assumptions is greater than the future sensitivity of $\tau \to \mu\gamma$.

Note that $\mu \to 3e$ can also constrain both $1-3$ and $2-3$ transitions in the same way as $\mu \to e\gamma$, since the same dipole operators dominate both decays. We do not include these constraints in Fig. 4.10, as they can be inferred from the relevant constraints in Fig. 4.9.

To summarize, for small $x_i \ll 1$ (heavy scalars), LFV observables either currently or will provide stronger constraints on left-handed flavor violation than the quark sector for both $1-2$ and $2-3$ transitions. In the case of $1-3$ transitions however, the constraints from B_d meson mixing will remain comparable to or stronger than those from LFV observables

in most of the parameter space. We also wish to re-emphasize the potential of $\mu \to e\gamma$ to provide constraints on $1-3$ and $2-3$ transitions due to the LR flavor conserving operator from section 4.3.1.

4.5.2 $\delta_{LR} = 0$, $x = 1$

In this subsection we consider the situation when $x_i = 1$. We consider a common superpartner mass $M_{SUSY} = 1$ TeV in this section.

In Fig. 4.11 we compare the current and future bounds on δ in the $1-2$ sector from LFV processes and Δm_K. We consider both constructive (a) and destructive (b) interference in the LFV processes. We observe from Fig. 4.11a that $\mu \to e\gamma$ is currently a stronger constraint than Δm_K when there is constructive interference. The future sensitivity of $\mu \to e\gamma$ will be greater than that of $\mu \to e$ conversion for constructive interference. On the other hand, from Fig. 4.11b (destructive interference), we see that Δm_K is currently a stronger constraint than $\mu \to e\gamma$ if $\delta_{LL} = \delta_{RR}$, and $\mu \to 3e$ will become the strongest constraint in the future. The constraints on δ_{RR} currently are strongest from $\mu \to e\gamma$, but in the future will be strongest from $\mu \to 3e$. Currently, $\mu \to e\gamma$ also dominates the constraint on δ_{LL} for constructive interference. For destructive interference δ_{LL} will be most strongly constrained by $\mu \to 3e$, which is slightly stronger than $\mu \to e$ conversion. This is in contrast with the situation at small x_i, where we saw that the constraint from $\mu \to e$ conversion would be weak in the case of destructive interference. As can be understood by examining Fig. 4.5, this is due to the interference at large $x_i \sim 1$ not being as pronounced as at small $x \sim \mathcal{O}(\text{few}) \times 10^{-3}$.

Turning now to $1-3$ transitions, we see from Figs. 4.12a and 4.12b that if $\delta^{12} = 0$, the bound from B_d mixing will remain a stronger constraint than $\tau \to e\gamma$ in a large region of parameter space. This result is largely independent of whether interference in the leptonic observable is constructive or destructive, and in the destructive case $\tau \to e\gamma$ will not improve on the B_d mixing bound at all. As in the previous section, we compare the possible constraint from $\mu \to e\gamma$ under the assumption that $\delta^{13}_{LL,RR} = \delta^{23}_{RR,LL}$. If this assumption is correct, $\mu \to e\gamma$ is already a stronger probe than the future sensitivity of $\tau \to e\gamma$ in all of the parameter space shown, regardless of interference. However, despite improvements in $\mu \to e\gamma$, the sensitivity will not be competitive with the constraints from B_d meson mixing near the line of $\delta_{LL} = \delta_{RR}$.

Finally, we perform the same analysis for $\tau \to \mu\gamma$, comparing with bounds from B_s mixing. From Fig. 4.12c, there is a region where $\tau \to \mu\gamma$ already provides the strongest constraint on $1-3$ mixing in the case of constructive interference. In the future, such a

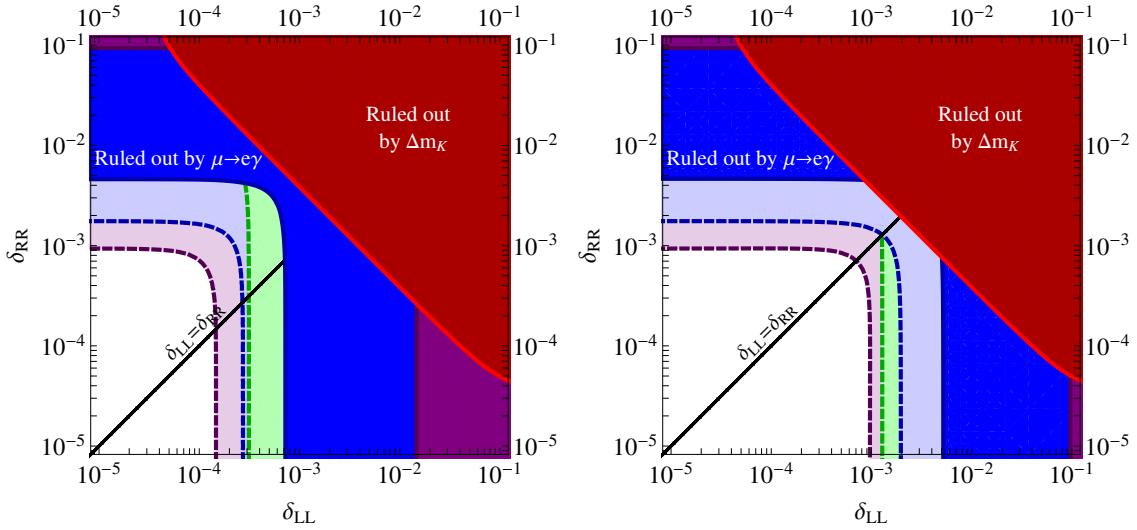

(a) Constructive interference for $\mu \to e\gamma$. (b) Destructive interference for $\mu \to e\gamma$.

Figure 4.11: δ_{LL} vs δ_{RR} plots for $1-2$ insertions. These plots compare the current and future constraints from Δm_K, BR($\mu \to e\gamma$), BR($\mu \to 3e$) and $\mu \to e$ conversion. All regions correspond to the measured (projected) limits at 90% C.L. . We have set $\tilde{m}_q = \tilde{m}_\ell = 1$ TeV, $x_{\tilde{g}} = x_\mu = x_{\tilde{W}} = x_{\tilde{B}} = 1$, and $t_\beta = 10$.

region will exist for destructive interference as well as seen in Fig. 4.12d. Additionally, we note $\mu \to e\gamma$ (again, with the added assumption $\delta^{13}_{LL,RR} = \delta^{23}_{RR,LL}$) is already a stronger probe than both of the other observables in all of the parameter space, and will remain so into the future. If this assumption does not hold, then we note that $b \to s\gamma$, shown by the purple lines, is currently the strongest constraint on δ_{RR} for small δ_{LL} regardless of the sign of the product $M_{\tilde{g}} A^{23}$, which appears in the gluino diagrams contributing to the amplitude. The future sensitivity of $\tau \to \mu\gamma$ will improve on these constraints on δ_{LL} only if there is constructive interference in the τ decay amplitude. It will not however improve on the constraints on δ_{RR}, but rather will have comparable sensitivity.

Note that $\mu \to 3e$ can also constrain both $1-3$ and $2-3$ transitions in the same way as $\mu \to e\gamma$, since the same dipole operators dominate both decays. We do not include these constraints in Fig. 4.12, as they can be inferred from the relevant constraints in Fig. 4.11.

4.5.3 $\delta_{LR} \neq 0$, $x = 1$

For TeV-scale superpartner masses, the factor $m_f/\tilde{m}$ in the LR insertions is small, but not negligibly so. We cannot assume that $\delta_{LR} = 0$ as we had done when the superpartners were of $\mathcal{O}(10)$ TeV. So, in the $x \sim 1$ case, given a particular $\tilde{m}$, using the known SM fermion

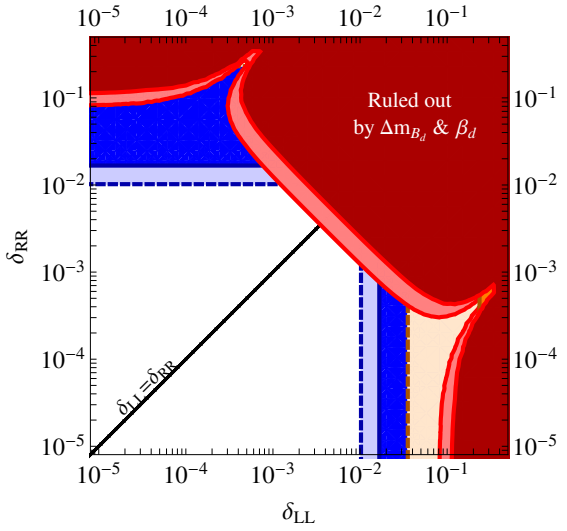

(a) Constructive interference in LFV, $1-3$ transitions.

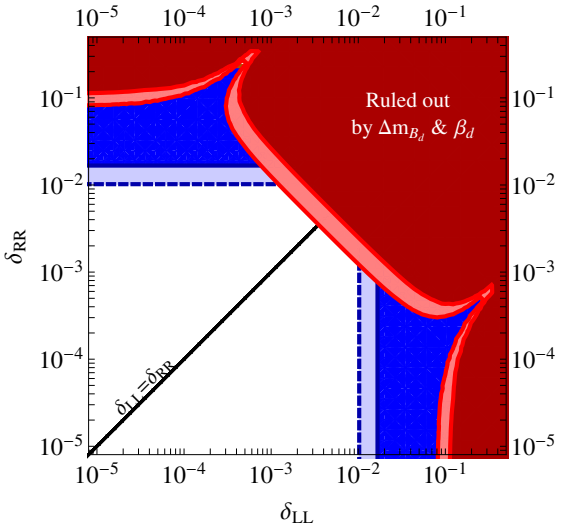

(b) Destructive interference in LFV, $1-3$ transitions.

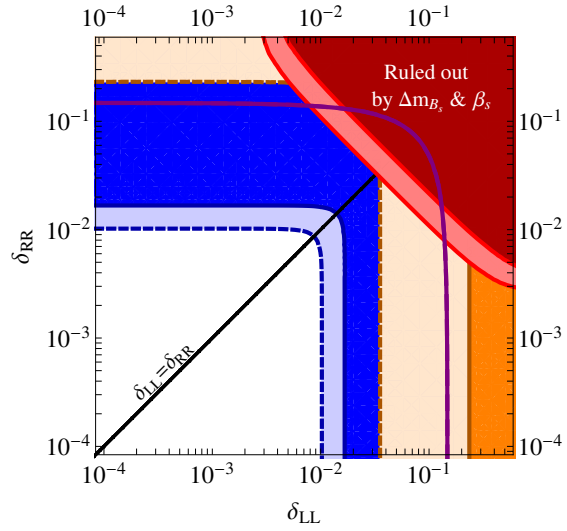

(c) Constructive interference in LFV, $2-3$ transitions.

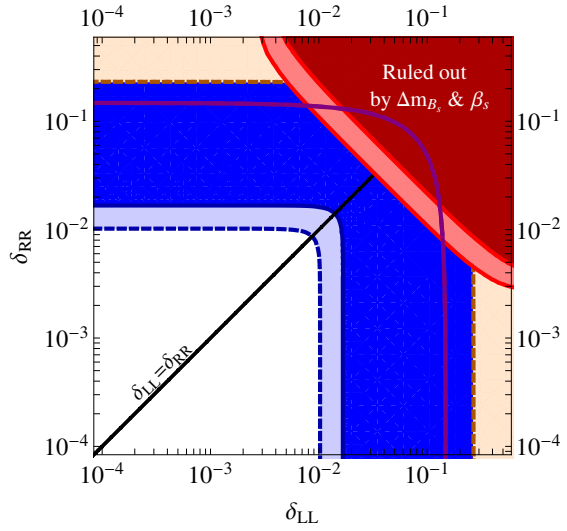

(d) Destructive interference in LFV, $2-3$ transitions.

Figure 4.12: δ_{LL} vs δ_{RR} plots for $1-3$ (upper) and $2-3$ (lower) insertions. The upper plots compare the current constraints from Δm_{B_d}, β_d, $\tau \to e\gamma$ on δ^{13}. The lower plots compare constraints from Δm_{B_s}, β_s, $b \to s\gamma$, $\tau \to \mu\gamma$. The dark red regions are excluded by B meson mixing, the light red is a potential factor of two improvement. The light orange region shows the future sensitivity of $\tau \to \mu\gamma$. The purple line shows the current limits from $b \to s\gamma$. Also shown is a dark blue region excluded by $\mu \to e\gamma$ assuming $\delta^{13}_{LL,RR} = \delta^{23}_{RR,LL}$. The light blue is the future sensitivity given the same assumption. We have set $\tilde{m}_q = \tilde{m}_\ell = 1$ TeV, $x_{\tilde{g}} = x_\mu = x_{\tilde{W}} = x_{\tilde{B}} \simeq 1$, and $t_\beta = 10$.

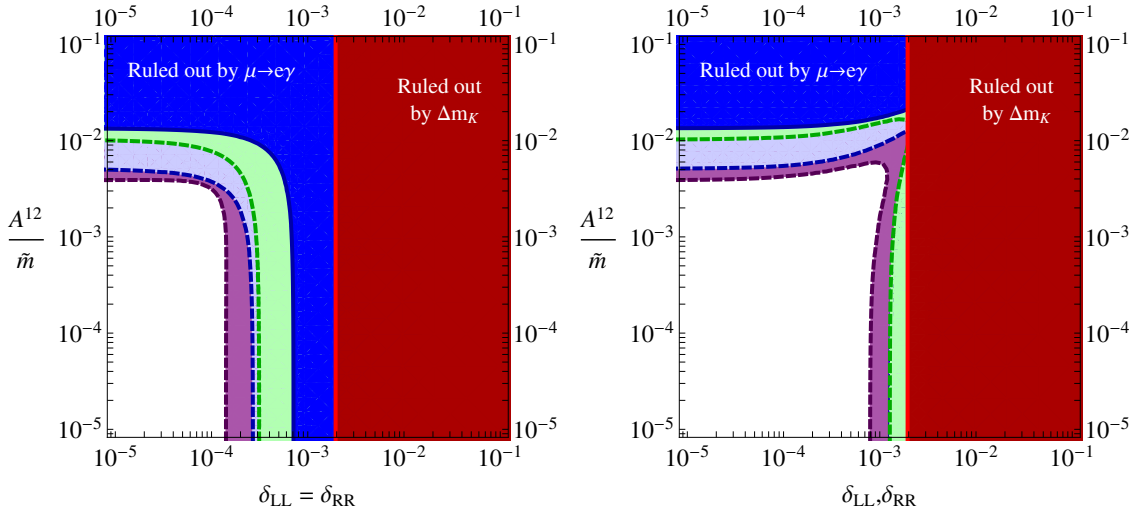

(a) Constructive interference for $\mu \to e\gamma$. (b) Destructive interference for $\mu \to e\gamma$.

Figure 4.13: δ_{LL}, δ_{RR} vs $A^{12}/\tilde{m}$ plots comparing the constraints from Δm_K (red), the current (future) limit on BR($\mu \to e\gamma$) (dark (light) blue), the future sensitivity of $\mu \to e$ conversion (light green) and the future sensitivity of BR($\mu \to 3e$) (purple), all at the 90% C.L.. We have set $\tilde{m}_q = \tilde{m}_\ell = 1$ TeV, $x_{\tilde{g}} = x_\mu = x_{\tilde{W}} = x_{\tilde{B}} = 1$, and $t_\beta = 10$.

mass, we relax the $\delta_{LR} = 0$ assumption. Indeed, we place limits on the ratio $A^{ij}/\tilde{m}$. In this subsection we assume $\delta_{RR} = \delta_{LL} \equiv \delta$.

We see from Fig. 4.13 that in the case of constructive interference $\mu \to e\gamma$ places stronger constraints on the size of $A^{12}/\tilde{m}$ than Δm_K in all regions of parameter space, and large regions if there is destructive interference. Note in the case of constructive interference, $\mu \to e\gamma$ is already constraining $A^{12} \lesssim 10^{-2}\tilde{m}$ for TeV-scale SUSY masses. This is also true when there is destructive interference except for a sliver of parameter space near the $A^{12}/\tilde{m} = \delta_{LL,RR}$ line, where the interference is most pronounced. Eventually, $\mu \to 3e$ will be the strongest constraint on $A^{12}/\tilde{m}$, although only slightly improving on the future $\mu \to e\gamma$ constraint.

In the $1-3$ sector, we find from Figs. 4.14a and 4.14b that B_d mixing imposes a stronger constraint than $\tau \to e\gamma$ in large regions of parameter space. However, for small $\delta_{LL,RR} \lesssim 2 \times 10^{-3}$, we find that $\tau \to e\gamma$, both in the case of constructive and destructive interference, provides a stronger constraint than Δm_{B_d} and $S_{\psi K_s}$ on $A^{13}/\tilde{m}$. We see that while currently the limit is weak: $A^{13} \lesssim 4\tilde{m}$, in the future $\tau \to e\gamma$ will be sensitive up to $A^{13} \lesssim 0.6\tilde{m}$. Additionally we note that under the assumption that $\delta^{13} = \delta^{23}$, $\mu \to e\gamma$ does not improve the constraints on $\delta_{LL,RR}$.

Similarly for the $2-3$ sector, we see from Figs. 4.14c and 4.14d that currently $\tau \to \mu\gamma$

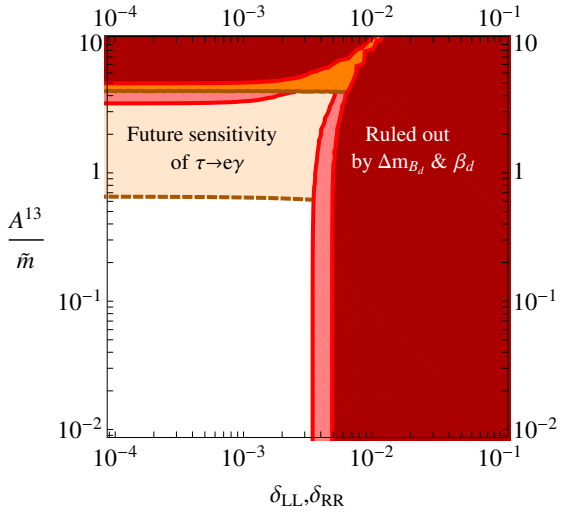

(a) Constructive interference for $\tau \to e\gamma$.

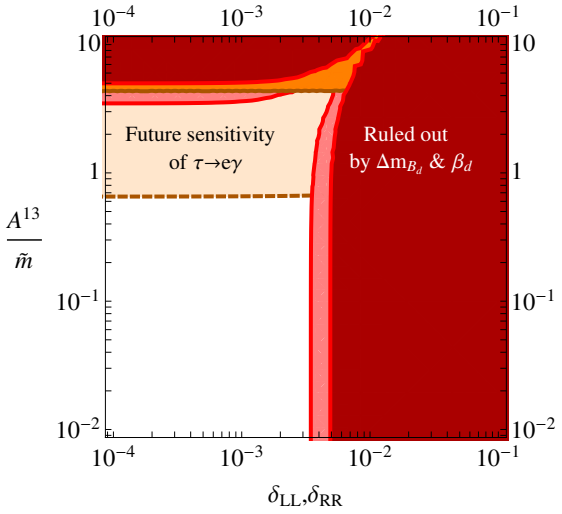

(b) Destructive interference for $\tau \to e\gamma$.

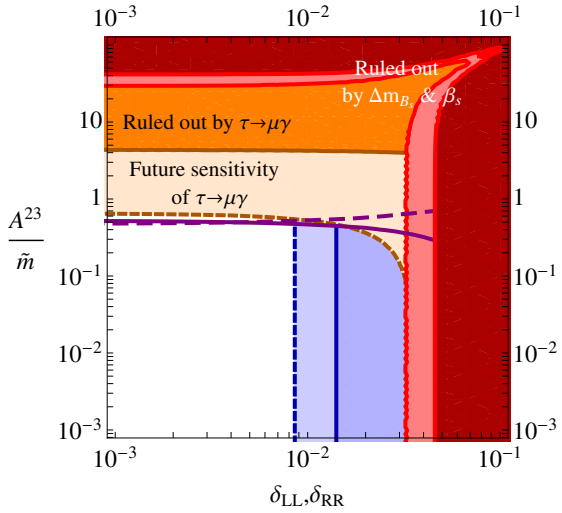

(c) Constructive interference for $\tau \to \mu\gamma$.

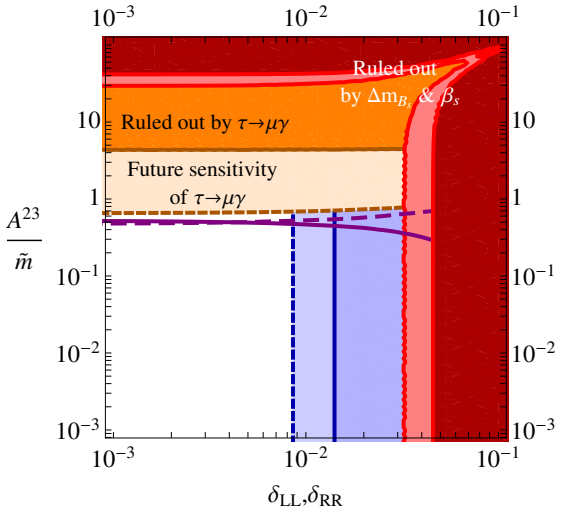

(d) Destructive interference for $\tau \to \mu\gamma$.

Figure 4.14: δ_{LL}, δ_{RR} vs. $A^{13}/\tilde{m}$ (upper) and δ_{LL}, δ_{RR} vs. $A^{23}/\tilde{m}$ (lower) plots. In the upper plots, we compare the current and future constraints from Δm_{B_d}, β_d, $\tau \to e\gamma$. The lower plots compare the current and future constraints from Δm_{B_s}, β_s, $b \to s\gamma$, $\tau \to \mu\gamma$. The dark red region is excluded by meson mixing at 90 % C.L., and the light red assumes a factor of two improvement. The solid (dashed) purple line shows the limit from $b \to s\gamma$ in the case of constructive (destructive) interference. The dark (light) orange region shows the current (future) sensitivity of $\tau \to e\gamma$ (top) and $\tau \to \mu\gamma$ (bottom). We have set $\tilde{m}_q = \tilde{m}_\ell = 1$ TeV, $x_{\tilde{g}} = x_\mu = x_{\tilde{W}} = x_{\tilde{B}} \simeq 1$, and $t_\beta = 10$. In both panels, the dark (light) blue gives a current (future) exclusion from $\mu \to e\gamma$ assuming $\delta^{13} = \delta^{23}$.

imposes a stronger constraint on $A^{23}/\tilde{m}$ than B_s for $\delta_{LL,RR} \lesssim 3 \times 10^{-2}$ only. In this region the current constraint from B_s mixing gives $A^{23}/\tilde{m} \lesssim 50$, improving to $A^{23}/\tilde{m} \lesssim 40$, while the current constraint from $\tau \to \mu\gamma$ yields $A^{23}/\tilde{m} \lesssim 4$ for both constructive and destructive interference. The future sensitivity of $\tau \to \mu\gamma$ will constrain $A^{23}/\tilde{m} \lesssim 0.6$ for $\delta_{LL,RR} \lesssim 10^{-2}$. However, the strongest constraint comes from $b \to s\gamma$, which bounds $A^{23}/\tilde{m} \lesssim 0.5$ for small $\delta_{LL,RR}$, both in the case of constructive ($\mathrm{sgn}(m_{\tilde{g}} A^{23} = +)$ and destructive ($\mathrm{sgn}(m_{\tilde{g}} A^{23} = -)$) interference. As in Figs. 4.12c and 4.12d, we see that for $\delta_{LL} = \delta_{RR}$, if $\delta^{13} = \delta^{23}$, $\mu \to e\gamma$ can provide a stronger constraint than both $\tau \to \mu\gamma$ and B_s mixing.

Again, $\mu \to 3e$ can constrain both $1-3$ and $2-3$ transitions in the same way as $\mu \to e\gamma$. We do not include these constraints in Fig. 4.14, as they can be inferred from the relevant constraints in Fig. 4.13.

4.6 Summary

We have analysed various quark- and lepton-flavor violating processes in the absence of new CP violating phases. While the absence of new CP violating phases is a strong assumption, because LFV measurements are CP conserving, in some ways it provides for the most direct comparison between the two sectors. In general, relaxing this assumption will strengthen – considerably in the case of the $1-2$ sector – the bounds on quark flavor violation.

In the case of heavy scalars, a scenario well motivated by the observed Higgs boson mass, LFV is a particularly powerful probe on LL flavor violation. In the $1-2$ sector, improvements on bounds on $\mu \to e\gamma$, $\mu \to 3e$ and $\mu - e$ conversion will probe new parameter space, even accounting for comparable flavor violation in the quark sector. Similarly, again for δ_{LL}, $\tau \to \mu\gamma$ is a powerful probe. $\tau \to e\gamma$, on the other hand, does not represent as strong a constraint as B_d mixing over much of the parameter space (assuming comparable flavor violation the squark and slepton matrices). In an $SU(5)$ GUT context, these bounds can be interpreted as probes of flavor violation in the $\bar{\mathbf{5}}$ scalar masses.

In the case where all superpartner masses are close to the TeV scale, we obtain similar results on the LL flavor violation. But in this case, LFV has the opportunity to place limits on RR insertions as well. These limits can be reinterpreted as probes of flavor violation in the $\mathbf{10}$ scalar masses in an $SU(5)$ GUT. Moreover, for TeV scalars, LR insertions are likely to give important contributions to LFV observables. Significant bounds already exist on off-diagonal trilinear couplings A_{ij} and these will only strengthen as the experimental sensitivity to LFV improves.

In all, in cases where squark mass matrices are related to slepton mass matrices, quark FCNCs provide a significant constraint. In some areas of parameter space, even improvement of LFV bounds will not make them the most sensitive. However, there are large swathes of parameter space where LFV has the chance to be a discovery tool.

In this chapter, we considered the low-energy flavor observables associated with supersymmetric models, in the absence of CP violation. Since this is a rather strong assumption, in the next chapter, we study low-energy observables in the presence of CP violation, namely electric dipole moments. We will do so in the context of the G_2-MSSM, which we encountered previously in Chapter 2.

Chapter 5

Theoretical Prediction and Impact of Fundamental Electric Dipole Moments

5.1 Introduction

In the previous chapter, we studied Lepton and Quark flavor violating effects in Supersymmetric models in the absence of new sources of CP violation. However, as discussed also in the introduction to that chapter, strong constraints on CP violation originating from physics beyond the Standard Model (BSM) have been imposed by measurements of electric dipole moments (EDMs) of the electron, neutron and heavy atoms. Thus the implication is that new physics should have generic mechanisms for the suppression of EDMs [4].

In Supersymmetric (SUSY) theories, additional sources of CP violation may arise from complex phases in the soft SUSY breaking parameters [34, 35]. If SUSY is only an effective theory for physics at the TeV scale, the phases must be treated as arbitrary, leading to large predictions for EDMs unless the phases are tuned to be small, or there are cancellations. CP violation in SUSY models and the implications for EDM predictions has been studied extensively [165, 166, 167, 168, 169, 170, 137, 171, 138, 172, 173, 163, 139, 113, 174]. If however, we consider SUSY to be the low energy effective theory of an overarching theory such as a compactified string/M-theory, then there must be some underlying mechanism to predict and relate the various phases.

It is well known that the Electroweak scale CP-violating phase of the Standard Model (SM) cannot provide the source of the CP-violation needed for baryogenesis. The compact-

ified M-theory predicts the required phase also does not arise in the softly broken supersymmetric Lagrangian [15]. Baryogenesis can arise via the Affleck-Dine mechanism [175] at high scales, generated with phases generically present in the super partner's composite flat directions and moduli. The magnitudes of both the baryon number and the dark matter then may arise from moduli decay before nucleosynthesis [62]. The associated phases are high scale ones that have no effects on EDMs.

Following on from the results presented in [15] and the body of work behind it [10, 11, 13, 14, 16, 61, 18], we now concentrate on analysing the CP violating phases in the effective four-dimensional theory resulting from $\mathcal{N} = 1$ compactifications of M-theory with chiral matter.

There are two-loop contributions to the EDMs that may be the dominant ones. Even in this case, the phases ultimately arise from the superpotential Yukawas that also give the CKM phase, so we discuss the Yukawa phases first, and turn to the results in Section 5.4. Readers who want to focus on the upper limits can skip Section 5.3 on a first reading.

Since the phases in the theory only arise in the Yukawa sector at the high scale, measurements of EDMs also become a useful testing ground for various textures at said scale. We present here an analysis of a variety of different textures and how future measurements may be used to constrain the set of possible choices.

In Section 5.2 we present a review of the results found in [15] that argue that the dominant CP violating phases are in the superpotential Yukawas. In Section 5.3 we discuss the sources of CP violation in the theory, as well as present the various textures we investigate and their running. We also show how the phases from the Yukawas enter into the computation of EDMs, summarise the current experimental limits, and discuss the Strong CP contribution. In Section 5.4 we present our results, both for two-loop and one-loop contributions to the EDMs. In Section 5.5 we discuss the upper limits and their interpretation.

5.2 Review of Compactified M-Theory prediction of Supersymmetry phases

Here we summarize the arguments from reference [15] that the high-scale soft-breaking Supersymmetry Lagangian from the compactified M-theory leads to the prediction that the dominant CP-violation generating EDMs arises from the phases in the superpotential Yukawas, and thus *has the same source as the CKM phase*.

In reference [15] it is shown that terms in the superpotential align with the same phase,

leaving just one overall phase, which can be rotated away by a global phase transformation. The Kähler potential only depends on the real moduli fields, and the meson condensate $\phi \equiv (\tilde{Q}Q^T)^{1/2}$, so it introduces no explicit phases. This is shown in detail in Section IIB of reference [15]. Basically by removing overall phases one can see that $\partial_J K$ and $\partial_J \bar{W}$ and therefore $F-$ terms are real. It is also argued in [15] that although higher order corrections to the Kähler potential exist, they do not give rise to new CP-violating phases. This is because in the zero flux sector the superpotential only receives non-perturbative corrections from strong gauge dynamics or membrane instantons. The dynamical alignment of phases still works if these additional terms are subdominant, which is required for the consistency of the moduli stabilization. The hidden sector Kähler potential may receive perturbative corrections since there is no non-renormalization theorem for the Kähler potential. But the meson field ϕ is composed of elementary chiral quark fields $Q, \tilde{Q}$ that are charged under the hidden gauge groups, so higher order corrections must be functions of $Q^\dagger Q + \tilde{Q}^\dagger \tilde{Q}$ by gauge invariance, so such corrections are always functions of $\phi^\dagger \phi$ which does not introduce any new phases, since $Q^\dagger Q = \tilde{Q}^T \tilde{Q}^*$. The perturbative corrections to the Kähler potential are always functions of moduli $z_i + \bar{z}_i$ which does not introduce any CP violating phases in the soft terms. The dependence on $z_i + \bar{z}_i$ follows from the shift PQ symmetry of the axion, which is only broken by exponentially suppressed contributions. Thus the result that the CP violating phases in soft parameters are highly suppressed should be quite robust since it only relied on symmetries.

Also, the Kähler potential has an approximately flavor diagonal structure because of the presence of U(1) symmetries under which the chiral matter fields are charged. The conical singularities associated with different flavors do not carry the same charges under the U(1)'s in a given basis, which forbids the existence of off-diagonal terms. Such terms can arise when the symmetries are spontaneously broken, but that should be suppressed. Thus the Kähler metric is expected to be approximately flavor diagonal at the high scale. As we discuss later, renormalization group running will generate small flavor off-diagonal effects at the EW scale.

Finally, when the superpotential contribution to the overall high scale μ parameter vanishes, as it does by the Witten mechanism [67, 17], the μ and B parameters are generated by the Giudice-Masiero mechanism [176]. Then μ and B have a common phase, but this phase is not physical since it can be eliminated by a $U(1)_{PQ}$ rotation.

Since μ vanishes if Supersymmetry is unbroken and if the moduli are not stabilised μ is generically of order $\langle\phi\rangle m_{3/2}/M_{Pl}$, typically an order of magnitude suppressed from $m_{3/2}$ [17]. Including supergravity constraints gives consistency conditions $B = 2m_{3/2}$ and

$2\mu \tan\beta \approx m_{3/2}$.

5.3 CP violation in the Compactified Theory

Given the results of [15], all of the phases in the full Lagrangian originate from the phases of the Yukawa couplings in the underlying superpotential, up to presumably small corrections from the Kähler potential. The Yukawa matrices enter the theory through the matter superpotential

$$W = -U^c \boldsymbol{Y_u} Q H_u - D^c \boldsymbol{Y_d} Q H_d - E^c \boldsymbol{Y_e} L H_d + \mu H_u H_d \tag{5.1}$$

where the $\boldsymbol{Y_i}$ are 3×3 complex matrices in family space. The objects U^c, D^c, Q, E^c, L, H_u and H_d are chiral superfields containing the quark, squark, lepton, slepton and Higgs matter fields. Then, the contributions to CP violation in the compactified M-theory come entirely from the Yukawa sector of the theory.

The Yukawa matrices give rise to the quark and lepton masses by the following interaction Lagrangian

$$\mathcal{L}_{Yukawa} = Y^u_{ij} \bar{Q}_{Li} H_u u_{Rj} + Y^d_{ij} \bar{Q}_{Li} H_d d_{Rj} + Y^e_{ij} \bar{L}_{Li} H_d e_{Rj} + h.c. \tag{5.2}$$

where $Y^\alpha_{ij}, \quad \alpha = u, d, e, \quad i, j = 1, 2, 3$ are the Yukawa matrices, and i, j are family indices. The matter fields here are SM quarks and leptons. When the Higgs boson gains a vacuum expectation value, the sizes of the eigenvalues of the Yukawa matrices dictate the masses of the quarks or leptons. Diagonalisation of the Yukawa matrices is performed by unitary left-(right-)handed $V^{L(R)}_\alpha$ matrices in flavour space in the Standard Model:

$$V^{L\dagger}_\alpha Y^\alpha V^R_\alpha = Y^{diag}_\alpha \propto \begin{pmatrix} m_{\alpha_1} & 0 & 0 \\ 0 & m_{\alpha_2} & 0 \\ 0 & 0 & m_{\alpha_3} \end{pmatrix} \tag{5.3}$$

The CKM matrix is defined as $V_{CKM} = V^{L\dagger}_u V^L_d$, where these are the up and down-type left-handed unitary diagonalisation matrices, so there must be $\mathcal{O}(1)$ phases in the Yukawa matrices in order to explain the experimentally observed phase of the Cabibbo-Kobayashi-Maskawa (CKM) matrix. When the Yukawa matrices are diagonalised, the phases that were in the original 3×3 complex matrices are rotated away by the unitary matrices, so that the eigenvalues are real. Therefore, the left-handed unitary matrices which form the CKM matrix carry the phases that were originally in the Yukawas.

The trilinears that arise in the supersymmetric soft-breaking Lagrangian are defined as $\hat{A}^{\alpha}_{ij} = A^{\alpha}_{ij} Y^{\alpha}_{ij}$, where A^{α}_{ij} is a general 3×3 matrix. Explicitly, the trilinear terms from the soft Lagrangian can then be written as:

$$\mathcal{L}_{soft} \sim A^{u}_{ij} Y^{u}_{ij} \tilde{\bar{Q}}_{Li} H_u \tilde{u}_{Rj} + A^{d}_{ij} Y^{d}_{ij} \tilde{\bar{Q}}_{Li} H_d \tilde{d}_{Rj} + A^{e}_{ij} Y^{e}_{ij} \tilde{\bar{L}}_{Li} H_d \tilde{e}_{Rj} \tag{5.4}$$

where $A^{u,d,e}$ are the trilinear matrices in the gauge eigenstate basis of matter fields, and we are interested in the structure of Y^{α}_{ij}. The matter fields here are the squarks and sleptons.

Rotating to the super-CKM basis is achieved by using the same rotation matrices that diagonalised the Yukawa matrices above, but applying them now to the SUSY squark fields.

$$\hat{A}_{SCKM} \equiv V^{L\dagger}_{\alpha} A^{\alpha} Y^{\alpha} V^{R}_{\alpha} \tag{5.5}$$

where the family indices have been dropped. If the trilinears are not proportional to the Yukawas in the flavour-eigenstate basis, i.e. $A^{\alpha}_{ij} \not\propto \mathbb{1}_{3\times3}$, the rotation to the super-CKM basis can in itself induce CP-violating phases in the diagonal components of the $\hat{A}$s, giving rise to possible contributions to EDMs.

We consider the case where the trilinears $\hat{A}$ are not aligned with the Yukawas as a maximally general treatment of CP violation in the theory.

Additionally, the running of the Yukawas from the high scale to the low scale will mix potential phases in the off-diagonal components into the diagonal elements, thus giving rise to CP-violating phases at the low scale.

5.3.1 Yukawa textures

The crux of the analysis lies in the determination of viable Yukawa textures. They need to satisfy the requirement that they accurately describe the mass hierarchy exhibited in quarks and leptons, and also that they give the correct CKM angles and phases.

In order to better understand the structure of a Yukawa texture, we assume that we may decompose it into $\mathcal{O}(1)$ complex parameters multiplying real parameters giving the relative sizes of the elements of the matrix.

$$Y^{\alpha}_{ij} = \mathcal{O}(1) \cdot \Lambda_{ij} \tag{5.6}$$

where Λ_{ij} is the matrix of powers in some small parameter $\epsilon \sim \alpha^{1/2}_{GUT} \sim 0.2$, set at the high scale, which will give us the correct hierarchy. While this choice of ϵ is not the only possible

one, it implies a connection between flavour structure and grand unification, and is therefore attractive. The multiplying $\mathcal{O}(1)$ is a 3×3 matrix of magnitude one entries containing the various phases.

We consider three types of textures in this analysis, symmetric textures with no zeroes, symmetric textures with zeroes, and asymmetric textures with no zeroes, the reason behind these choices being that this allows us to consider a wide variety of possible texture-dependencies. Although this does not cover all possibilities, we find a maximal prediction, so no further EDMs will arise from additional Yukawas.

Initially we will consider the two possible cases where either the up-type Yukawa matrix, Y_u is diagonal, or the down-type Yukawa matrix, Y_d is diagonal, with the other constrained only by the CKM matrix. We parameterise the CKM matrix in the following manner without loss of generality

$$V_{CKM} = \mathcal{O}(1) \begin{pmatrix} 1 & \epsilon & \epsilon^3 \\ \epsilon & 1 & \epsilon^2 \\ \epsilon^3 & \epsilon^2 & 1 \end{pmatrix} = \mathcal{O}(1) \begin{pmatrix} 1 & 0.2 & 0.008 \\ 0.2 & 1 & 0.04 \\ 0.008 & 0.04 & 1 \end{pmatrix} \tag{5.7}$$

where the $\mathcal{O}(1)$ indicates the presence of a matrix of complex parameters of order 1. This is comparable to the experimentally determined values of the CKM matrix

$$|V_{CKM}| \sim \begin{pmatrix} 0.97 & 0.23 & 0.004 \\ 0.23 & 0.97 & 0.04 \\ 0.008 & 0.04 & 0.99 \end{pmatrix} \tag{5.8}$$

We assume the following hierarchy for the quark masses, as seen in [**?**].

$$m_u : m_c : m_t \equiv (\epsilon^8 : \epsilon^4 : 1) \times v_u \tag{5.9}$$

$$m_d : m_s : m_b \equiv (\epsilon^5 : \epsilon^3 : 1) \times v_d \tag{5.10}$$

$$m_e : m_\mu : m_\tau \equiv (\epsilon^8 : \epsilon^4 : 1) \times v_d \tag{5.11}$$

where $v_u = \langle H_u^0 \rangle$ and $v_d = \langle H_d^0 \rangle$ are the vacuum expectation values (VEVs) of the Higgs fields in equation (5.2), with the SM VEV defined as $v^2 = v_u^2 + v_d^2$. It should be noted here that we use the up-quark hierarchy for the leptons. While this is non-standard, it is done in order to have a better fit to the experimentally measured masses.

Below are ratios between the predicted masses and the observed masses for the choice

of $\epsilon = 0.26$ for the up-type quarks, $\epsilon = 0.27$ for the down-type quarks and $\epsilon = 0.36$ for the leptons. Fixing the masses of the top, bottom and τ to their known values, we find that these choices give

$$\frac{m_u^{th}}{m_u^{exp}} : \frac{m_c^{th}}{m_c^{exp}} : \frac{m_t^{th}}{m_t^{exp}} \equiv 1.21 : 0.61 : 1 \tag{5.12}$$

$$\frac{m_d^{th}}{m_d^{exp}} : \frac{m_s^{th}}{m_s^{exp}} : \frac{m_b^{th}}{m_b^{exp}} \equiv 1.15 : 0.79 : 1 \tag{5.13}$$

$$\frac{m_e^{th}}{m_e^{exp}} : \frac{m_\mu^{th}}{m_\mu^{exp}} : \frac{m_\tau^{th}}{m_\tau^{exp}} \equiv 1.01 : 0.30 : 1 \tag{5.14}$$

All of these are within order one factors of $\alpha_{GUT}^{1/2}$, so this is compatible with the experimentally measured values for entries in the CKM matrix, given our parameterisation of V_{CKM} in terms of ϵ. The deviation from one can be due to the unknown $\mathcal{O}(1)$ factors in our decomposition of the Yukawa matrices described above.

All EDMs will be proportional to some power of ϵ, as will be seen in a later section. Since we are interested in the size of the detectable EDMs, we look for the largest contributions from the Yukawa couplings, which will have the smallest powers of ϵ.

The first set of textures we consider is derived as shown in appendix A, and is of the form

$$Y^u = \begin{pmatrix} \epsilon^8 & \epsilon^5 & \epsilon^3 \\ \epsilon^9 & \epsilon^4 & \epsilon^2 \\ \epsilon^{11} & \epsilon^6 & 1 \end{pmatrix}, \quad Y^d = \begin{pmatrix} \epsilon^5 & 0 & 0 \\ 0 & \epsilon^3 & 0 \\ 0 & 0 & 1 \end{pmatrix} \tag{5.15}$$

where we have taken advantage of being able to perform rotations such that the down-type Yukawa matrix is diagonal.

The same can be repeated where the up-type Yukawa matrix is diagonal, yielding the following textures

$$Y^u = \begin{pmatrix} \epsilon^8 & 0 & 0 \\ 0 & \epsilon^4 & 0 \\ 0 & 0 & 1 \end{pmatrix}, \quad Y^d = \begin{pmatrix} \epsilon^5 & \epsilon^4 & \epsilon^3 \\ \epsilon^6 & \epsilon^3 & \epsilon^2 \\ \epsilon^8 & \epsilon^5 & 1 \end{pmatrix} \tag{5.16}$$

The largest predictions for EDMs, arising from the smallest powers in ϵ, will typically arise from terms such as $Y_{33}^{(u,d)} Y_{32}^{(u,d)^\dagger} Y_{23}^{(u,d)}$ in the running of the diagonal terms from the

high scale, as they involve the $(3,3)$ term which is 1. This will be seen in section (3.2.1).

The second class of textures we consider are those with zeroes. We study in particular the only five textures with five zeroes found in [177] at the high scale, given below

$$Y^u = \begin{pmatrix} 0 & \sqrt{2}\epsilon^6 & 0 \\ \sqrt{2}\epsilon^6 & \epsilon^4 & 0 \\ 0 & 0 & 1 \end{pmatrix}, \quad Y^d = \begin{pmatrix} 0 & 2\epsilon^4 & 0 \\ 2\epsilon^4 & 2\epsilon^3 & 4\epsilon^3 \\ 0 & 4\epsilon^3 & 1 \end{pmatrix} \tag{5.17}$$

$$Y^u = \begin{pmatrix} 0 & \epsilon^6 & 0 \\ \epsilon^6 & 0 & \epsilon^2 \\ 0 & \epsilon^2 & 1 \end{pmatrix}, \quad Y^d = \begin{pmatrix} 0 & 2\epsilon^4 & 0 \\ 2\epsilon^4 & 2\epsilon^3 & 2\epsilon^3 \\ 0 & 2\epsilon^3 & 1 \end{pmatrix} \tag{5.18}$$

$$Y^u = \begin{pmatrix} 0 & 0 & \sqrt{2}\epsilon^4 \\ 0 & \epsilon^4 & 0 \\ \sqrt{2}\epsilon^4 & 0 & 1 \end{pmatrix}, \quad Y^d = \begin{pmatrix} 0 & 2\epsilon^4 & 0 \\ 2\epsilon^4 & 2\epsilon^3 & 4\epsilon^3 \\ 0 & 4\epsilon^3 & 1 \end{pmatrix} \tag{5.19}$$

$$Y^u = \begin{pmatrix} 0 & \sqrt{2}\epsilon^6 & 0 \\ \sqrt{2}\epsilon^6 & \sqrt{3}\epsilon^4 & \epsilon^2 \\ 0 & \epsilon^2 & 1 \end{pmatrix}, \quad Y^d = \begin{pmatrix} 0 & 2\epsilon^4 & 0 \\ 2\epsilon^4 & 2\epsilon^3 & 0 \\ 0 & 0 & 1 \end{pmatrix} \tag{5.20}$$

$$Y^u = \begin{pmatrix} 0 & 0 & \epsilon^4 \\ 0 & \sqrt{2}\epsilon^4 & \epsilon^2/\sqrt{2} \\ \epsilon^4 & \epsilon^2/\sqrt{2} & 1 \end{pmatrix}, \quad Y^d = \begin{pmatrix} 0 & 2\epsilon^4 & 0 \\ 2\epsilon^4 & 2\epsilon^3 & 0 \\ 0 & 0 & 1 \end{pmatrix} \tag{5.21}$$

These have a different hierarchy from that of textures 1 and 2, but all of these textures are consistent with the low-energy fermion masses and the CKM matrix elements. Note that since the matrices are symmetric, pairs of zeroes in the off-diagonal components only count as one zero. Since they are all defined at the high scale, we must turn our attention to their running.

5.3.2 Running of Yukawa textures

In this section we consider the running of the Yukawa textures described in the previous section, and look at how the phases from the off-diagonal terms are rotated into the diagonals by said running. Since we start at the high scale with no phases in the diagonal components, the running of the diagonal elements is crucial to understanding the appearance of phases at the low scale.

The evolution of the up and down Yukawa matrices and the trilinear matrices in the

MSSM is well known [178], and given by,

$$\frac{dY^u}{dt} = \frac{1}{16\pi^2} Y^u \left\{ 3\,\mathrm{Tr}(Y^u Y^{u\dagger}) + 3Y^{u\dagger}Y^u + Y^{d\dagger}Y^d \right\} + \dots \tag{5.22}$$

$$\frac{dY^d}{dt} = \frac{1}{16\pi^2} Y^d \left\{ \mathrm{Tr}(3Y^u Y^{u\dagger} + Y^e Y^{e\dagger}) + 3Y^{d\dagger}Y^d + Y^{u\dagger}Y^u \right\} + \dots \tag{5.23}$$

$$\frac{d\hat{A}^u}{dt} = \frac{1}{16\pi^2} \hat{A}^u \left\{ 3\,\mathrm{Tr}(Y^u Y^{u\dagger}) + 5Y^{u\dagger}Y^u + Y^{d\dagger}Y^d \right\} \tag{5.24}$$

$$+ Y^u \left\{ 6\,\mathrm{Tr}(\hat{A}^u Y^{u\dagger}) + 4Y^{u\dagger}\hat{A}^u + 2Y^{d\dagger}\hat{A}^d \right\} + \dots \tag{5.25}$$

$$\frac{d\hat{A}^d}{dt} = \frac{1}{16\pi^2} \hat{A}^d \left\{ \mathrm{Tr}(3Y^d Y^{d\dagger} + Y^e Y^{e\dagger}) + 5Y^{d\dagger}Y^d + Y^{u\dagger}Y^u \right\} \tag{5.26}$$

$$+ Y^d \left\{ \mathrm{Tr}(6\hat{A}^d Y^{d\dagger} + 2\hat{A}^e Y^{e\dagger}) + 4Y^{d\dagger}\hat{A}^d + 2Y^{u\dagger}\hat{A}^u \right\} + \dots \tag{5.27}$$

where only terms involving the Yukawa matrices are explicitly shown as they are by far the dominant contribution. The trace terms are merely numbers, while the $Y^\dagger Y$ and $Y^\dagger \hat{A}$ terms are matrices that have ϵ dependencies.

When looking at the evolution of the various terms, we consider the leading terms in ϵ that come from the off-diagonal terms, as these will be the ones that multiply the phases that are being rotated into the diagonal components. It should be noted that ϵ is a parameter fixed at the GUT scale that does not run.

Texture specific running

In this section, we look at the leading order contributions in ϵ to the running of the diagonal components of the Yukawa textures from section 2.1 in order to estimate the size of potential phases appearing at the low scale. We consider the running of both the up and down type textures, as each contributes differently.

For the first texture shown in equation (5.15), the dominant terms in the running of the $\hat{A}^u_{ii}$ components are:

$$\frac{d\hat{A}^u_{11}}{dt} \sim \frac{1}{16\pi^2}\left[\hat{A}^u_{13}\left\{5Y^{u\dagger}{}_{33}Y^u_{31}\right\} + Y^u_{13}\left\{4Y^{u\dagger}{}_{33}\hat{A}^u_{31}\right\} + \ldots\right] \sim \frac{27A_0\epsilon^{14}}{16\pi^2} \tag{5.28}$$

$$\frac{d\hat{A}^d_{11}}{dt} \sim \frac{1}{16\pi^2}\left[\hat{A}^d_{11}\left\{Y^{u\dagger}{}_{12}Y^u_{21}\right\} + Y^d_{11}\left\{2Y^{u\dagger}{}_{12}\hat{A}^u_{21}\right\}\right] \sim \frac{3A_0\epsilon^{23}}{16\pi^2} \tag{5.29}$$

$$\frac{d\hat{A}^u_{22}}{dt} \sim \frac{1}{16\pi^2}\left[\hat{A}^u_{23}\left\{5Y^{u\dagger}{}_{33}Y^u_{32}\right\} + Y^u_{23}\left\{4Y^{u\dagger}{}_{33}\hat{A}^u_{32}\right\} + \ldots\right] \sim \frac{18A_0\epsilon^{8}}{16\pi^2} \tag{5.30}$$

$$\frac{d\hat{A}^d_{22}}{dt} \sim \frac{1}{16\pi^2}\left[\hat{A}^d_{22}\left\{Y^{u\dagger}{}_{21}Y^u_{12}\right\} + Y^d_{22}\left\{2Y^{u\dagger}{}_{21}\hat{A}^u_{12}\right\}\right] \sim \frac{3A_0\epsilon^{13}}{16\pi^2} \tag{5.31}$$

$$\frac{d\hat{A}^u_{33}}{dt} \sim \frac{1}{16\pi^2}\left[\hat{A}^u_{33}\left\{5Y^{u\dagger}{}_{32}Y^u_{23}\right\} + Y^u_{33}\left\{4Y^{u\dagger}{}_{32}\hat{A}^u_{23}\right\}\right] \sim \frac{9A_0\epsilon^{4}}{16\pi^2} \tag{5.32}$$

$$\frac{d\hat{A}^d_{33}}{dt} \sim \frac{1}{16\pi^2}\left[\hat{A}^d_{33}\left\{Y^{u\dagger}{}_{32}Y^u_{23}\right\} + Y^d_{33}\left\{2Y^{u\dagger}{}_{32}\hat{A}^u_{23}\right\}\right] \sim \frac{3A_0\epsilon^{4}}{16\pi^2} \tag{5.33}$$

For the texture given in equation (5.16), the leading order terms are:

$$\frac{d\hat{A}^u_{11}}{dt} \sim \frac{1}{16\pi^2}\left[\hat{A}^u_{11}\left\{Y^{d\dagger}{}_{12}Y^d_{21}\right\} + Y^u_{11}\left\{2Y^{d\dagger}{}_{12}\hat{A}^d_{21}\right\}\right] \sim \frac{3A_0\epsilon^{20}}{16\pi^2} \tag{5.34}$$

$$\frac{d\hat{A}^d_{11}}{dt} \sim \frac{1}{16\pi^2}\left[\hat{A}^d_{13}\left\{5Y^{d\dagger}{}_{33}Y^d_{31}\right\} + Y^d_{13}\left\{4Y^{d\dagger}{}_{33}\hat{A}^d_{31}\right\} + \ldots\right] \sim \frac{27A_0\epsilon^{11}}{16\pi^2} \tag{5.35}$$

$$\frac{d\hat{A}^u_{22}}{dt} \sim \frac{1}{16\pi^2}\left[\hat{A}^u_{22}\left\{Y^{d\dagger}{}_{23}Y^d_{32}\right\} + Y^u_{11}\left\{2Y^{d\dagger}{}_{23}\hat{A}^d_{32}\right\}\right] \sim \frac{3A_0\epsilon^{14}}{16\pi^2} \tag{5.36}$$

$$\frac{d\hat{A}^d_{22}}{dt} \sim \frac{1}{16\pi^2}\left[\hat{A}^d_{23}\left\{5Y^{d\dagger}{}_{33}Y^d_{32}\right\} + Y^d_{23}\left\{4Y^{d\dagger}{}_{33}\hat{A}^d_{32}\right\} + \ldots\right] \sim \frac{18A_0\epsilon^{7}}{16\pi^2} \tag{5.37}$$

$$\frac{d\hat{A}^u_{33}}{dt} \sim \frac{1}{16\pi^2}\left[\hat{A}^u_{33}\left\{Y^{d\dagger}{}_{32}Y^d_{23}\right\} + Y^u_{33}\left\{2Y^{d\dagger}{}_{32}\hat{A}^d_{23}\right\}\right] \sim \frac{3A_0\epsilon^{4}}{16\pi^2} \tag{5.38}$$

$$\frac{d\hat{A}^d_{33}}{dt} \sim \frac{1}{16\pi^2}\left[\hat{A}^d_{33}\left\{5Y^{d\dagger}{}_{32}Y^d_{23}\right\} + Y^d_{33}\left\{4Y^{d\dagger}{}_{32}\hat{A}^d_{23}\right\} + \right] \sim \frac{9A_0\epsilon^{4}}{16\pi^2} \tag{5.39}$$

As mentioned earlier, the leading order terms, here of $\mathcal{O}(\epsilon^4)$ for both the textures in equations (5.15) and (5.16), arise from the terms of the form $Y^{(u,d)}_{33}Y^{(u,d)\,\dagger}_{32}Y^{(u,d)}_{23}$. Note that only the leading results for the remaining textures are presented here, and the explicit matrix elements that enter in the running of the other textures are not shown.

For the texture given in equation (5.17), the lowest order terms in ϵ are

$$\frac{d\hat{A}^u_{11}}{dt} \sim \frac{1}{16\pi^2}(12\sqrt{2}A_0\epsilon^{13}) \tag{5.40}$$
$$\frac{d\hat{A}^d_{11}}{dt} \sim \frac{1}{16\pi^2}(72A_0\epsilon^{11}) \tag{5.41}$$
$$\frac{d\hat{A}^u_{22}}{dt} \sim \frac{1}{16\pi^2}(60A_0\epsilon^{10}) \tag{5.42}$$
$$\frac{d\hat{A}^d_{22}}{dt} \sim \frac{1}{16\pi^2}(144A_0\epsilon^{6}) \tag{5.43}$$
$$\frac{d\hat{A}^u_{33}}{dt} \sim \frac{1}{16\pi^2}(48A_0\epsilon^{6}) \tag{5.44}$$
$$\frac{d\hat{A}^d_{33}}{dt} \sim \frac{1}{16\pi^2}(288A_0\epsilon^{6}) \tag{5.45}$$

For the texture given in equation (5.18), the lowest order terms are

$$\frac{d\hat{A}^u_{11}}{dt} \sim \frac{1}{16\pi^2}(12A_0\epsilon^{13}) \tag{5.46}$$
$$\frac{d\hat{A}^d_{11}}{dt} \sim \frac{1}{16\pi^2}(72A_0\epsilon^{11}) \tag{5.47}$$
$$\frac{d\hat{A}^u_{22}}{dt} \sim \frac{1}{16\pi^2}(9A_0\epsilon^{4}) \tag{5.48}$$
$$\frac{d\hat{A}^d_{22}}{dt} \sim \frac{1}{16\pi^2}(6A_0\epsilon^{5}) \tag{5.49}$$
$$\frac{d\hat{A}^u_{33}}{dt} \sim \frac{1}{16\pi^2}(18A_0\epsilon^{4}) \tag{5.50}$$
$$\frac{d\hat{A}^d_{33}}{dt} \sim \frac{1}{16\pi^2}(3A_0\epsilon^{4}) \tag{5.51}$$

For the texture in equation (5.19), the lowest order terms are

$$\frac{d\hat{A}^u_{11}}{dt} \sim \frac{1}{16\pi^2}(18A_0\epsilon^8) \tag{5.52}$$
$$\frac{d\hat{A}^d_{11}}{dt} \sim \frac{1}{16\pi^2}(72A_0\epsilon^{11}) \tag{5.53}$$
$$\frac{d\hat{A}^u_{22}}{dt} \sim \frac{1}{16\pi^2}(60A_0\epsilon^{10}) \tag{5.54}$$
$$\frac{d\hat{A}^d_{22}}{dt} \sim \frac{1}{16\pi^2}(144A_0\epsilon^6) \tag{5.55}$$
$$\frac{d\hat{A}^u_{33}}{dt} \sim \frac{1}{16\pi^2}(48A_0\epsilon^6) \tag{5.56}$$
$$\frac{d\hat{A}^d_{33}}{dt} \sim \frac{1}{16\pi^2}(288A_0\epsilon^6) \tag{5.57}$$

For the texture in equation (5.20), the lowest order terms are

$$\frac{d\hat{A}^u_{11}}{dt} \sim \frac{1}{16\pi^2}(24/\sqrt{2}A_0\epsilon^{13}) \tag{5.58}$$
$$\frac{d\hat{A}^d_{11}}{dt} \sim \frac{1}{16\pi^2}(72A_0\epsilon^{11}) \tag{5.59}$$
$$\frac{d\hat{A}^u_{22}}{dt} \sim \frac{1}{16\pi^2}(9A_0\epsilon^4) \tag{5.60}$$
$$\frac{d\hat{A}^d_{22}}{dt} \sim \frac{1}{16\pi^2}(6A_0\epsilon^7) \tag{5.61}$$
$$\frac{d\hat{A}^u_{33}}{dt} \sim \frac{1}{16\pi^2}(18A_0\epsilon^4) \tag{5.62}$$
$$\frac{d\hat{A}^d_{33}}{dt} \sim \frac{1}{16\pi^2}(3A_0\epsilon^4) \tag{5.63}$$

For the texture in equation (5.21), the lowest order terms are

$$\frac{d\hat{A}^u_{11}}{dt} \sim \frac{1}{16\pi^2}(9A_0\epsilon^8) \tag{5.64}$$
$$\frac{d\hat{A}^d_{11}}{dt} \sim \frac{1}{16\pi^2}(3\sqrt{2}A_0\epsilon^{10}) \tag{5.65}$$
$$\frac{d\hat{A}^u_{22}}{dt} \sim \frac{1}{16\pi^2}(9/2A_0\epsilon^4) \tag{5.66}$$
$$\frac{d\hat{A}^d_{22}}{dt} \sim \frac{1}{16\pi^2}(3A_0\epsilon^7) \tag{5.67}$$
$$\frac{d\hat{A}^u_{33}}{dt} \sim \frac{1}{16\pi^2}(9A_0\epsilon^4) \tag{5.68}$$
$$\frac{d\hat{A}^d_{33}}{dt} \sim \frac{1}{16\pi^2}(3/2A_0\epsilon^4) \tag{5.69}$$

5.3.3 Translating from Yukawas to EDMs

Having described various Yukawa textures and their running, we now concentrate on demonstrating how the phases will enter into a computation of the EDMs.

In the MSSM, the important CP-odd terms in the Lagrangian are

$$\begin{aligned}\mathcal{L}_{CP-odd} \supset & -\sum_{q=u,d,s} m_q\overline{q}(1+i\theta_q\gamma_5)q + \theta_G\frac{\alpha_s}{8\pi}G\tilde{G} \\ & -\frac{i}{2}\sum_{q=u,d,s}(d^E_q\overline{q}F^{\mu\nu}\sigma_{\mu\nu}\gamma_5 q + d^C_q\overline{q}g_sT^aG^{a\mu\nu}\sigma_{\mu\nu}\gamma_5 q) \\ & -\frac{1}{6}d^G_q f_{abc}G_{a\mu\rho}G^{\rho}_{b\nu}G_{c\lambda\sigma}\epsilon^{\mu\nu\lambda\sigma}\end{aligned} \tag{5.70}$$

where θ_G is the QCD θ angle, the second line contains dimension five operators, generated by CP violation in the SUSY breaking sector and evolved down to ~ 1 GeV. The coefficients $d^{E,C}_q$ correspond to the quark electric and chromo-electric dipole moments (EDM, CEDM) respectively. The last line contains the gluonic dimension six Weinberg operator, to which all other purely gluonic P- or T-odd operators are proportional [179]. The CP violating 4-fermion operators [180, 137] are negligible in this mini-split type SUSY spectrum [113].

The explicit expressions for the SUSY contributions to EDMs are given in Appendix B. The phases appear only in the tri-linear $\hat{A}$ parameters in our theory, and after RG evolution and the rotation to the super-CKM basis, they then appear in the off-diagonal elements of

the squark mass matrices.

$$\delta(m^2_{\tilde{q}})^{LR}_{ii} = v_q((\hat{A}^q_{SCKM})_{ii} - \mu^* Y^q_{ii} R_q) \tag{5.71}$$

with $R_q = \cot\beta,\ (\tan\beta)$ for $I_3 = 1/2,\ (-1/2)$ as in Appendix B, and $v_{u(d)} = v\sin\beta(v\cos\beta)$.

The off-diagonal elements of the squark mass matrices enter the expressions for the SUSY EDM contributions as shown in detail in Appendix B. Thus, we find that the EDM contribution $d_i \propto \mathrm{Im}(\hat{A}_{SCKM})$ depends on the phases in the diagonal terms in the trilinears.

5.3.4 Electric Dipole Moments and Current Experimental Limits

We now summarize the experimental results on the electron, neutron and mercury EDMs. In minimal SUSY models, the electron EDM arises from one-loop diagrams with chargino and neutralino exchange, as well as two-loop contributions. Hence we can make the decomposition

$$d^E_e = d^{\chi^\pm}_e + d^{\chi^0}_e + d^{2L}_e \tag{5.72}$$

The current experimental upper bound on the electron EDM is [5]

$$|d^E_e| < 8.7 \times 10^{-29} e\,\mathrm{cm} \tag{5.73}$$

Calculating the neutron EDM requires assumptions about the internal structure, such that there are two possible approaches, the chiral model, and the parton model approach. We will restrict ourselves to the chiral model approach, although a combination could be done in a future study. The neutron EDM can be decomposed by use of the SU(6) coefficients into

$$d_n = \frac{4}{3}d_d - \frac{1}{3}d_u \tag{5.74}$$

which then requires estimation of the quark EDMs, which can be achieved via a naive dimensional analysis, such that

$$d_q = \eta^E d^E_q + \eta^C \frac{e}{4\pi} d^C_q + \eta^G \frac{e\Lambda}{4\pi} d^G \tag{5.75}$$

where $\Lambda \sim 1.19$ GeV is the chiral symmetry breaking scale, and the coefficients are the QCD correction factors, given by $\eta^E = 0.61$, $\eta^C \sim \eta^G \sim 3.4$, as found in [166, 181]. The contributions from SUSY come from 1-loop gluino, chargino and neutralino exchange, as

well as 2-loop contributions, leading to the decomposition

$$d_q^{E,C} = d_q^{\tilde{g}(E,C)} + d_q^{\chi^{\pm}(E,C)} + d_q^{\chi^0(E,C)} + d_q^{2L} \tag{5.76}$$

and two-loop gluino quark squark diagrams which generate d_q^G. The current experimental limit on the neutron EDM is [6]

$$|d_n| < 3 \times 10^{-26} e\,\mathrm{cm} \tag{5.77}$$

The mercury EDM results mostly from T-odd nuclear forces in the mercury nucleus, which induce an interaction of the type $(\boldsymbol{I} \cdot \nabla)\delta(\boldsymbol{r})$ between the electron and the nucleus of spin $\boldsymbol{I}$. The T-odd forces themselves arise due to the effective four-fermion interaction $\bar{p}p\bar{n}i\gamma_5 n$ [169]. The current theoretical estimate is given by

$$d_{Hg} = -7.0 \times 10^{-3} e(d_d^C - d_u^C - 0.012 d_s^C) + 10^{-2} \times d_e \tag{5.78}$$

where the contribution from the strange quark CEDM is included [1] . The experimental bound currently stands at [7]

$$|d_{Hg}| < 3.1 \times 10^{-29}\ e\,\mathrm{cm} \tag{5.79}$$

Strong CP contribution

A possible source of hadronic EDMs in the Standard Model comes from the $\theta-$term of QCD. This contribution is shown in equation (5.70). The limits on the EDMs of the neutron and Mercury can be expressed in terms of this θ parameter as follows

$$\begin{aligned} d_n &\sim 3 \times 10^{-16}\theta\ e\,\mathrm{cm} \\ |d_{Hg}| &\sim \mathcal{O}(10^{-18} - 10^{-19})\theta\ e\,\mathrm{cm} \end{aligned} \tag{5.80}$$

The contribution to the electron EDM, on the other hand, comes from electroweak interactions. Thus, with measurements of the neutron EDM and electron EDM, the strong and weak contributions can hopefully be separated, and θ can also be measured. Our upper

[1] There are uncertainties around the use of Eqns. (5.74) and (5.78), as discussed in [182]. We use in Eq. (5.74) the constituent quark model (CQM), but could have used the parton quark model (PQM), with only slight change in the numerical results. As discussed in detail in Ref. [182], there are differences in the results obtained in the literature for Eq. (5.78) which have yet to be cleared up.

limit on the electron EDM is not affected by the strong CP violation, but for the neutron or Mercury, there could be a strong CP contribution that increases the EW contribution above the EW upper limit. With sufficient data it may be possible to untangle these.

In the SM, a first analysis of the renormalisation of the θ parameter [183] found that the first renormalisation occurs only at $\mathcal{O}(\alpha^2)$, which would give a value of $\theta \sim \mathcal{O}(10^{-16})$. A subsequent detailed analysis yielded a smaller value of $\theta \sim \mathcal{O}(10^{-19})$ [184]. In this case, from equation (5.80), we can see that the strong contribution to the neutron EDM from θ renormalisation would be $\mathcal{O}(10^{-32} - 10^{-35})$. A more recent analysis yields an estimated value of $\theta \sim \mathcal{O}(10^{-17})$, giving a contribution to the neutron EDM of $\mathcal{O}(10^{-33})$ [185].

An estimate of electroweak renormalisation contributions to θ in SUSY is presented in [186], where it is discussed that θ is expected to be small, given that relevant phases are small, and $M_{\tilde{q}} \gg \mathcal{O}(100\,\mathrm{GeV})$. Thus, observation of a neutron or Mercury EDM should likely be interpreted as the Electroweak one we estimate in this chapter, but needs detailed confirmation.

Solutions of the Strong CP problem in string theory have been studied for example in [61, 187]. In this case a combination of the imaginary parts of the moduli fields is the QCD axion and solves the Strong CP problem. However, in the presence of non-perturbative contributions, the minimum of the axion potential need not be zero, and θ can have both strong and electroweak contributions [61, 188].

5.4 Results

Within the framework we are considering of compactified M-Theory, the general structure of SUSY breaking parameters is as follows. The gravitino mass is essentially $\sim F_\phi/M_{Pl}$, which puts it naturally in the range of 25-100 TeV [11]. The F-terms of the moduli are suppressed with respect to F_ϕ, and since the gauge kinetic function for the visible sector depend only on the moduli, it is easy to check that the gaugino masses are suppressed relative to the gravitino mass. Scalar masses, on the other hand, are not suppressed relative to the gravitino mass unless the visible sector is sequestered from the SUSY breaking sector, which is not generic in M-Theory [13]. Thus the scalar masses and trilinears turn out to be of $\mathcal{O}(M_{3/2}) \gtrsim \mathcal{O}(50)$ TeV. Due to the Kähler metric being approximately diagonal in the flavor indices, the scalar mass matrix is roughly diagonal, with suppressed off-diagonal components. In the following, we consider electroweakinos with masses $\lesssim 600$ GeV, scalar masses ~ 50 TeV, with B and trilinear parameters of the same order. The μ parameter is

expected to be suppressed compared to the gravitino mass by an order of magnitude [17].

We estimate the contribution to the EDMs of the electron, neutron and mercury from the operators described in Section 5.3.3 in our chosen M-theory framework.

5.4.1 Dominant two-loop contributions

There exist two-loop diagrams which could give large contributions to EDMs in supersymmetric models [167], [189, 190, 191, 192, 193, 194, 195]. For example, the diagrams considered in [2, 3], one of which is shown in Fig. 5.1, could potentially give large EDMs, as they are not suppressed by the heavy scalar masses, but rather depend on the charginos and neutralinos running in the loops.

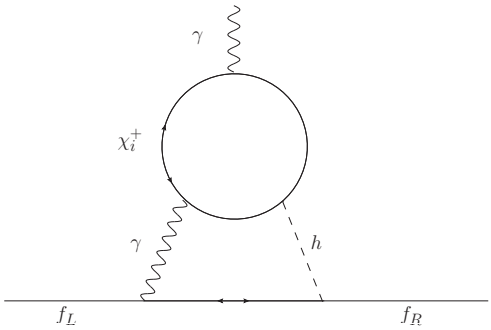

Figure 5.1: An example of a two-loop graph which contributes to fermion EDMs, with charginos running in the inner loop, γ and higgs in the outer loop.

Their contribution to the fermion EDM would be given by

$$d_f = d_f^{\gamma H} + d_f^{ZH} + d_f^{WW} \tag{5.81}$$

where

$$\begin{aligned}
d_f^{\gamma H} &= \frac{eQ_f\alpha^2}{4\sqrt{2}\pi^2 s_W^2}\,\mathrm{Im}(D_{ii}^R)\frac{m_f M_i^+}{M_W m_H^2} f_{\gamma H}(r_{iH}^+) \\
d_f^{ZH} &= \frac{e(T_{3f_L} - 2s_W^2 Q_f)\alpha^2}{16\sqrt{2}\pi^2 c_W^2 s_W^4}\,\mathrm{Im}(D_{ij}^R G_{ji}^R - D_{ij}^L G_{ji}^L)\frac{m_f M_i^+}{M_W m_H^2} f_{ZH}(r_{ZH}, r_{iH}^+, r_{jH}^+) \\
d_f^{WW} &= \frac{eT_{3f_L}\alpha^2}{8\pi^2 s_W^4}\,\mathrm{Im}(C_{ij}^L C_{ij}^{R*})\frac{m_f M_i^+ M_j^0}{M_W^4} f_{WW}(r_{iW}^+, r_{jW}^0)
\end{aligned} \tag{5.82}$$

where

$$
\begin{aligned}
G^L_{ij} &= V_{iW^+} c_{W^+} V^\dagger_{W^+ j} + V_{ih^+_u} c_{h^+_u} V^\dagger_{h^+_u j} \qquad & -G^{R*}_{ij} &= U_{iW^-} c_{W^-} U^\dagger_{W^- j} + U_{ih^-_d} c_{h^-_d} U^\dagger_{h^-_d j} \\
C^L_{ij} &= -V_{iW^+} N^*_{jW_3} + \frac{1}{\sqrt{2}} V_{ih^+_u} N^*_{jh^0_u} & C^R_{ij} &= -U^*_{iW^-} N_{jW_3} - \frac{1}{\sqrt{2}} U^*_{ih^-_d} N_{jh^0_d} \\
D^R_{ij} &= \sin\beta V_{ih^+_u} U_{jW} + \cos\beta V_{iW^+} U_{jh^-_d} & D^L &= (D^R)^\dagger
\end{aligned} \tag{5.83}
$$

A priori, in the framework we are working in, these diagrams would seem not to be important, as the gaugino masses contain no phases at the high scale so the imaginary part of the chargino and neutralino diagonalisation matrices would be zero. However, phases may be introduced by the running of the gaugino masses, given here [178]:

$$
\begin{aligned}
\frac{dM_a}{dt} &= \frac{2g_a^2}{16\pi^2} B^{(1)}_a M_a \\
&\quad + \frac{2g_a^2}{(16\pi^2)^2} \left[\sum_{b=1}^{3} B^{(2)}_{ab} g_b^2 (M_a + M_b) + \sum_{x=u,d,e} C^x_a \left(\mathrm{Tr}[Y^\dagger_x \hat{A}_x] - M_a \,\mathrm{Tr}[Y^\dagger_x Y_x] \right) \right]
\end{aligned} \tag{5.84}
$$

with $B^{(1)}_a, B^{(2)}_{ab}, C^x_a$ being matrices of group coefficients, which are also found in [178].

To 1st loop order there will still be no phases resulting from the running of the gaugino masses as there are no terms that would contain phases. However, at two loop order, phases can be introduced by the trilinear couplings. The term $\mathrm{Tr}[Y^\dagger_x Y_x]$ is manifestly real, and therefore will not contain phases. However, the term $\mathrm{Tr}[Y^\dagger_x \hat{A}_x]$ could well cause a phase to enter the gaugino masses at the low scale in the event where the Yukawa matrices are not aligned with the trilinears. This term would disappear in the case of alignment, as the two matrices would be diagonalised by the same left and right unitary matrices. Then we would have

$$
\mathrm{Tr}[Y^\dagger_x \hat{A}_x] = \mathrm{Tr}[V_R Y^{diag}_x V^\dagger_L V_L \hat{A}^{diag}_x V^\dagger_R] \tag{5.85}
$$

which is also manifestly real.

Since generically in the M-theory framework we expect the trilinears to not be aligned with the Yukawas, we compute how large a phase one could get at the low scale given $\mathcal{O}(1)$ phases in the trilinear via the Yukawa matrix, and therefore how this would enter into the expressions for the EDMs.

For this purpose we parameterise the trilinear matrix $\hat{A}_x = A_x Y_x$ where

$$A_x = \begin{pmatrix} A_0 e^{i\phi_1} & 0 & 0 \\ 0 & A_0 e^{i\phi_2} & 0 \\ 0 & 0 & A_0 e^{i\phi_3} \end{pmatrix} \tag{5.86}$$

To a good approximation, the dominant contribution to the phase in $\mathrm{Tr}[Y_x^\dagger \hat{A}_x]$ will come from the third generation phase, as the others are suppressed by powers of the small parameter ϵ in all the textures we consider here. Consequently the result is largely texture independent in these two-loop diagrams. This is due to the 1 in the $\{3,3\}$ position of the Yukawa matrix being texture-independent, resulting in the dominance of the third generation phase. This is different from the 1-loop results, as in those diagrams, the contribution from the third generation is suppressed relative to the first generation contribution.

Thus we can do a calculation of approximately how big an imaginary part M_a will have at the low scale by considering the running of the imaginary part only. For the purpose of the calculation, we work in a situation where we rotate to a basis where the down-type Yukawa matrix is diagonal, so the phases are contained in the up-type Yukawa matrix.

$$\begin{aligned} \frac{d\,\mathrm{Im}(M_a)}{dt} &\simeq \frac{2g_a^2 C_a^u}{(16\pi^2)^2}\,\mathrm{Im}(\mathrm{Tr}[Y_u^\dagger \hat{A}_u]) \\ &\simeq \frac{2g_a^2 C_a^x}{(16\pi^2)^2} A_0 \sin\phi_3 \end{aligned} \tag{5.87}$$

then we find that

$$\mathrm{Im}(M_a) \simeq \frac{2g_a^2 C_a^x}{(16\pi^2)^2} A_0 \sin\phi_3 \log\left[\frac{M_Q}{M_{GUT}}\right] \tag{5.88}$$

such that

$$\mathrm{Im}(M_2) \simeq -200 \sin\phi_3 \left(\frac{A_0}{75\,\mathrm{TeV}}\right) \mathrm{GeV} \tag{5.89}$$

where we have used

$$C_a^{u,d,e} = \begin{pmatrix} 26/5 & 14/5 & 18/5 \\ 6 & 6 & 4 \\ 4 & 4 & 0 \end{pmatrix} \tag{5.90}$$

as found in [178]. This is closely comparable to the result of doing the full two loop running of the gaugino masses and the gauge couplings using the package RGERun2.0 available for Mathematica.

Knowing how large a phase can appear in the gaugino masses, we turn to computing the diagonalisation matrices for the chargino and neutralino mass matrices, as the phases on said diagonalisation matrices will appear in the expressions for the EDMs.

The chargino mass matrix is known to be

$$X = \begin{pmatrix} M_2 & \sqrt{2}\sin\beta M_W \\ \sqrt{2}\cos\beta M_W & \mu \end{pmatrix} \tag{5.91}$$

where M_2 is complex and the other entries are real. This matrix is diagonalised by the following rotation

$$X^{diag} = U^* X V^{-1} \tag{5.92}$$

where U and V are unitary matrices for which analytic expressions can be obtained. Explicit diagonalisation and the expressions for the matrix elements are given in Appendix I.3.

We can use these matrices to find the imaginary part which enters into the expressions for $d_f^{\gamma H}$ and d_f^{ZH} through the matrices $D^{(L,R)}$ and $G^{(L,R)}$ defined as above in equation (5.83). In order to find the imaginary part of $C^{(L,R)}$ however, we must perform a numerical diagonalisation of the neutralino mass matrix.

We compute the electron EDM first, with

$$d_e = d_e^{\gamma H} + d_e^{ZH} + d_e^{WW} \tag{5.93}$$

and find that this gives us an upper bound from equation (5.82) of

$$|d_e| < 5 \times 10^{-30} e\,\mathrm{cm} \tag{5.94}$$

for $M_{\chi_1^+} \sim M_{\chi_2^0} \sim 274\,\mathrm{GeV}$, $M_{\chi_2^+} \sim M_{\chi_4^0} \sim 5000\,\mathrm{GeV}$ which is well above the estimate from the leading order contributions. The heavier neutralino's mass is dominated by the μ term from the superpotential, which in the M-theory is found to be of order $0.1 m_{3/2} \sim 5000\,\mathrm{GeV}$ [17]. Since this contribution is from a two loop effect, it does not depend on the scalars, but rather on the much lighter neutralinos and charginos.

The neutron EDM upper bound from these diagrams comes from using equations (5.82, 5.74) and is

$$|d_n| < 5 \times 10^{-29} e\,\mathrm{cm} \tag{5.95}$$

for the same values of the chargino and neutralino masses as for the electron. Again, this is well above the estimate from the leading order contributions. The ratio of $d_n/d_e \sim 10$ is

approximately in line with the results in [3]. Our values are about two orders of magnitude lower than their reported results, primarily because we actually compute the phases in the diagram from the high scale, rather than taking it to be some $\mathcal{O}(1)$ factor.

These are upper limits given the predicted values of $m_{3/2}$, M_2 and μ, and therefore could change given different input values. The misalignment of the trilinears and the Yukawas is as yet unknown, so we use $\sin\phi_3 \sim \mathcal{O}(1)$ here. A precise value of $\sin\phi_3$ could in principle be determined for a given Yukawa texture given the known CKM phase and known misalignment.

These are the dominant contributions in the generic case where the trilinears are not aligned with the Yukawas. If this is the case, then they may be accessible in the next round of experiments to measure EDMs. A measurement would of course imply that the relative hierarchy of $\mu \sim 10 \times M_2$ is correct, as for different values of these two parameters, we would get a different result. This can be seen in [3]. Of note is that these results are independent of the choice of texture, due to the third generation dominating. Therefore, a measurement of an EDM would not allow us to learn the high scale structure of the Yukawa textures. If the experiments were to not detect an EDM, this would suggest that either the trilinears are aligned with the Yukawa matrices, or the phases in the trilinears are indeed small. Thus, a non-detection would give us a better understanding of the relation between the full trilinear matrices and the Yukawa matrices, regardless of what texture we are considering.

5.4.2 Sub-dominant one-loop contributions

In the situation where the trilinears are aligned with the Yukawas, the two loop result would be zero, as no phase would enter the gaugino masses, so the diagrams we consider above would not give a contribution to the EDMs. However, the one loop contribution would in principle not be zero, due to the existing CKM and possible PMNS phases. The phases in the Yukawa textures which at the low scale give the CKM and PMNS phases would enter the one-loop contribution to EDMs after running from the GUT scale, calculated in Section 5.3.2. Therefore, we consider here the five-dimensional electric and chromo-electric couplings at one-loop, as seen in Fig. 5.2.

As seen in Appendix J.1, we can express the chromo-EDM for the quarks in terms of the small ratio $r \equiv m_i^2/m_{\tilde{q}}^2$, with $i = \tilde{\chi}^0, \tilde{\chi}^\pm, \tilde{g}$. The gluino loop dominates, as also seen in

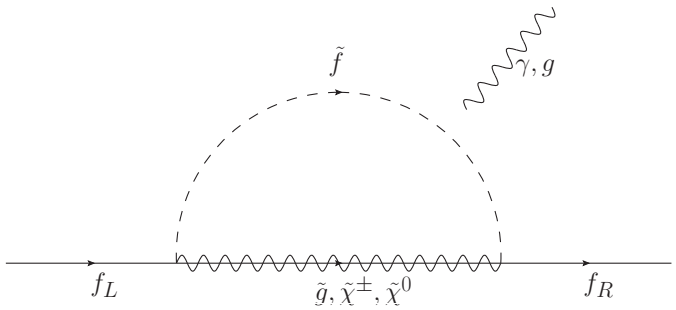

Figure 5.2: One-loop contributions to the fermion EDMs, with scalars running in the loop.

Appendix J.1, so the largest contribution comes from

$$d_q^C \sim \frac{g_s \alpha_s}{4\pi} \frac{\mathrm{Im}(A^q_{SCKM})}{m^3_{\tilde{g}}} r^2 \left[C(r) + rC'(r) \right] \tag{5.96}$$

The quark EDM contributions are small compared with the quark CEDM contributions. The term $\mathrm{Im}(A^q_{SCKM})$ contains the phases that entered the diagonal entries from the running and subsequent diagonalsation to the super-CKM basis. The relevant results for this are given in table 5.1 for each of the textures considered.

Thus, if we make the definition

$$K^\alpha_{ii} \equiv \frac{\mathrm{Im}(A^\alpha_{ii})}{A_0 Y^\alpha_{ii}} \sim \frac{\mathrm{Im}(A^\alpha_{ii})}{m_{\tilde{q}}} \tag{5.97}$$

we can present the results numerically for the various values of ϵ considered. As a reminder, for textures 1 and 2, $\epsilon^u \sim 0.26,\ \epsilon^d \sim 0.27$, and for textures 3-7, $\epsilon^u = \epsilon^d \sim 0.22$.

We rewrite here the expression for d_q^C in such a way as to present our results more clearly for given textures.

$$d_q^C \sim \frac{g_s \alpha_s}{4\pi} \frac{K^q m^3_{\tilde{g}}}{m^3_{\tilde{q}}} \left[C(r) + rC'(r) \right] \tag{5.98}$$

From observing table 5.2, we see that the largest K^α are for the 2nd and 3rd generations. However, the appearance of these in the loop are suppressed, so only the 1st generation need be considered for calculating the upper bound on the quark contribution to the EDM of the neutron.

Thus we present in table 5.3 the upper bounds on the neutron EDM for the various textures, given our results above, and using the relation in equation (5.74).

We see that the maximal prediction is from texture 2, which gives an upper bound for

Texture	$\mathbf{Im}(\boldsymbol{A^u_{11}})$	$\mathbf{Im}(\boldsymbol{A^u_{22}})$	$\mathbf{Im}(\boldsymbol{A^u_{33}})$	$\mathbf{Im}(\boldsymbol{A^d_{11}})$	$\mathbf{Im}(\boldsymbol{A^d_{22}})$	$\mathbf{Im}(\boldsymbol{A^d_{33}})$
1	$27A_0Y^u_{11}\epsilon^6$	$18A_0Y^u_{22}\epsilon^4$	$9A_0Y^u_{33}\epsilon^4$	$3A_0Y^d_{11}\epsilon^{15}$	$3A_0Y^d_{22}\epsilon^{10}$	$3A_0Y^d_{33}\epsilon^4$
2	$3A_0Y^u_{11}\epsilon^{12}$	$3A_0Y^u_{22}\epsilon^{10}$	$3A_0Y^u_{33}\epsilon^4$	$27A_0Y^u_{11}\epsilon^6$	$18A_0Y^u_{22}\epsilon^4$	$9A_0Y^u_{33}\epsilon^4$
3	$12\sqrt{2}A_0Y^u_{11}\epsilon^7$	$60A_0Y^u_{22}\epsilon^6$	$48A_0Y^u_{33}\epsilon^6$	$72A_0Y^d_{11}\epsilon^7$	$144A_0Y^d_{22}\epsilon^3$	$288A_0Y^d_{33}\epsilon^6$
4	$12A_0Y^u_{11}\epsilon^7$	$9A_0Y^u_{22}\epsilon^2$	$18A_0Y^u_{33}\epsilon^4$	$72A_0Y^d_{11}\epsilon^7$	$6A_0Y^d_{22}\epsilon^2$	$3A_0Y^d_{33}\epsilon^4$
5	$18A_0Y^u_{11}\epsilon^4$	$60A_0Y^u_{22}\epsilon^6$	$48A_0Y^u_{33}\epsilon^6$	$36A_0Y^d_{11}\epsilon^7$	$36A_0Y^d_{22}\epsilon^3$	$288A_0Y^d_{33}\epsilon^6$
6	$24/\sqrt{2}A_0Y^u_{11}\epsilon^7$	$9A_0Y^u_{22}\epsilon$	$18A_0Y^u_{33}\epsilon^4$	$36A_0Y^d_{11}\epsilon^7$	$3A_0Y^d_{22}\epsilon^4$	$3A_0Y^d_{33}\epsilon^4$
7	$9A_0Y^u_{11}\epsilon^4$	$9/\sqrt{2}A_0Y^u_{22}\epsilon^2$	$9A_0Y^u_{33}\epsilon^4$	$3/\sqrt{2}A_0Y^d_{11}\epsilon^6$	$3/2A_0Y^d_{22}\epsilon^4$	$3/2A_0Y^d_{33}\epsilon^4$

Table 5.1: The results for the various textures in terms of the diagonal Yukawa matrix elements Y^α_{ii}. The first three columns are for up-type, and the second three are for down-type.

the neutron EDM of

$$|d_n| \sim 8 \times 10^{-31} \cdot \left(\frac{m_{\tilde{g}}}{1\,\mathrm{TeV}}\right) \left(\frac{50\,\mathrm{TeV}}{m_{\tilde{q}}}\right)^3 \left(\frac{\epsilon}{0.26}\right)^6 e\,\mathrm{cm} \tag{5.99}$$

We remark here that this is of order $\sim 100\times$ the expected SM result [196].

The maximal prediction for the mercury EDM can also be seen in table 5.3, and is given by texture 5, with an upper bound of

$$|d_{Hg}| \sim 2 \times 10^{-32} \cdot \left(\frac{m_{\tilde{g}}}{1\,\mathrm{TeV}}\right) \left(\frac{50\,\mathrm{TeV}}{m_{\tilde{q}}}\right)^3 e\,\mathrm{cm} \tag{5.100}$$

We do not give an ϵ dependence for the mercury EDM as it depends on a combination of d_u, d_d and d_s, all of which have different ϵ dependences.

We then turn to the results for the electron EDM. From Appendix J.1, we know that the

Texture	K^u_{11}	K^u_{22}	K^u_{33}	K^d_{11}	K^d_{22}	K^d_{33}
1	8×10^{-3}	0.08	0.04	9×10^{-9}	6×10^{-6}	0.02
2	3×10^{-7}	4×10^{-6}	0.02	0.01	0.1	0.05
3	4×10^{-4}	7×10^{-3}	5×10^{-3}	2×10^{-3}	2	0.03
4	3×10^{-4}	0.4	0.04	2×10^{-3}	0.3	7×10^{-3}
5	0.04	7×10^{-3}	5×10^{-3}	9×10^{-4}	0.4	0.03
6	2×10^{-3}	2	0.04	9×10^{-4}	7×10^{-3}	7×10^{-3}
7	0.02	0.3	0.02	2×10^{-4}	4×10^{-3}	4×10^{-3}

Table 5.2: Numerical results for the various pre-factors K^α. The first three columns are for up-type, and the second three are for down-type.

only diagram that contributes is the neutralino exchange, since if the two-loop contribution is absent, there are no CP violating phases coming from the chargino sector in the theory due to the alignment of the Trilinears with the Yukawa matrices. Thus we have that

$$d_e^E \sim \frac{e\alpha_{EM}}{4\pi \cos\theta_W} \frac{\mathrm{Im}(\hat{A}^e_{SCKM}) m_e}{m^3_{\tilde{B}}} r^2 \left[B(r) + rB'(r)\right] \tag{5.101}$$

where the variable r is defined as $r \equiv \frac{m^2_{\tilde{B}}}{m^2_{\tilde{e}}}$. We recall here that $\mathrm{Im}(\hat{A}^e_{ii}) \sim K^e_{ii} m_{\tilde{e_i}}$, and so this can be rewritten as

$$d_e^E \sim \frac{e\alpha_{EM}}{4\pi \cos\theta_W} m_e m_{\tilde{B}} \frac{K^e}{m^3_{\tilde{e}}} \left[B(r) + rB'(r)\right] \tag{5.102}$$

Our results are summarised in table 5.4.

Texture	**1**	**2**	**3**	**4**	**5**	**6**	**7**
$\boldsymbol{d_u}(\times 10^{-31})$	4	2×10^{-5}	0.2	0.2	20	1	10
$\boldsymbol{d_d}$ $(\times 10^{-31})$	6×10^{-7}	6	1	1	0.5	0.5	0.1
$\boldsymbol{d_s}(\times 10^{-31})$	4×10^{-3}	60	900	200	200	4	2
$\lvert\boldsymbol{d_n}\rvert(\times 10^{-31})$	1	8	1	1	7	0.3	4
$\lvert\boldsymbol{d_{Hg}}\rvert(\times 10^{-31})$	3×10^{-2}	3×10^{-2}	7×10^{-2}	9×10^{-3}	0.2	4×10^{-3}	8×10^{-2}

Table 5.3: Results for the up, down and strange quark EDMs, and the neutron and mercury EDMs for the various textures.

Texture	**1**	**2**	**3**	**4**	**5**	**6**	**7**
$\boldsymbol{d_e}$ $(\times 10^{-34})$	5	2×10^{-3}	0.2	0.2	0.2	0.2	5×10^{-2}

Table 5.4: Results for the electron EDM for the various textures.

We see that the maximal prediction is

$$d_e \sim 5 \times 10^{-34} \left(\frac{m_{\tilde{B}}}{200\,\text{GeV}}\right) \left(\frac{50\,\text{TeV}}{m_{\tilde{q}}}\right)^3 \left(\frac{\epsilon}{0.36}\right)^6 e\,\text{cm} \tag{5.103}$$

as a result of using texture 1. We remark here that this is of order $10^5\times$ the SM prediction [196].

While texture 2 gave the highest neutron EDM, it actually gives the smallest electron EDM. This comes about primarily as a result of two factors. The first is to do with the naive dimensional analysis approach to calculating the EDM, in that the EDM of the down quark contributes $4/3$ whereas the up quark contributes $-1/3$. Thus despite the larger value of K_{11}^u in texture 5, the slightly smaller value of K_{11}^d in texture 2 gives a larger result, albeit marginally. This also explains why texture 7, despite giving the largest d_u, ends up giving a

slightly smaller d_n, as the d_u contribution loses out to the d_d part.

The second reason, which applies to both texture 5 and texture 2, is due to the running. The largest contributions to the EDM arise when the smallest powers of ϵ from running coincide with the largest powers of ϵ in the eigenvalues. In this case, in texture 2, $Y^d_{11} \propto \epsilon^5$, and the running contributed a factor of $27\epsilon^6$. In texture 5, $Y^u_{11} \propto \epsilon^4$, and the running contributed a factor of $18\epsilon^4$. The pre factors from the running of the full trilinears are important because they help counteract the large powers of ϵ.

The electron EDM is suppressed relative to the neutron EDM for a few reasons. Chief among them is that we have factors of α_{EM} rather than α_s, due to the electroweak nature of the diagram. Another suppression arises due to the loop factor in the electron EDM diagram, $B(r)+rB'(r)$ being substantially smaller than the loop factor in the gluino exchange diagram for the quark CEDMs.

It is curious that texture 2, while giving the largest neutron EDM results in the smallest electron EDM. This comes about because in textures 1 and 2, we assume that the Yukawa texture for the leptons is of the same form as that of the up quarks. Therefore when we start in a basis where the up Yukawa texture is diagonal, while it does pick up factors from the running, they are typically large powers of ϵ.

5.5 Conclusion

	M-Theory (2-loop)	**M-Theory** (1-loop)	**Split SUSY** ($\mu \sim 5$ TeV, $M_2 \sim \frac{1}{3}$ TeV)	**Generic SUSY**	**Current Limit**	**SM value**
$\boldsymbol{d_e}$ ($\times 10^{-28}$ e cm)	5×10^{-2}	5×10^{-6}	~ 1	~ 1000	0.87	10^{-10}
$\boldsymbol{d_n}$ ($\times 10^{-28}$ e cm)	0.5	8×10^{-3}	~ 10	~ 1000	300	10^{-4}
$\boldsymbol{d_{Hg}}$ ($\times 10^{-28}$ e cm)	5×10^{-4}	2×10^{-4}	N/A	N/A	0.31	N/A
$\boldsymbol{d_n/d_e}$	~ 10	$\sim 10^3$	~ 9	N/A	N/A	$\sim 10^6$

Table 5.5: Results for the possibly dominant two-loop and 1-loop predictions of EDMs from compactified M-Theory, as compared to the predictions from Split SUSY [2, 3], Generic SUSY models [4], the current limits [5, 6, 7] and the expected SM value [4].

In this chapter we have discussed how the CP-violating phases in compactified M-theory arise only in the Yukawa sector at the high scale, but nevertheless give rise to low scale EDMs via RGE running and the Super-CKM rotation. Therefore there will be a dependence on the Yukawa textures at the high scale. For various textures the running and subsequent diagonalisation of the full trilinear couplings $\hat{A}_{\alpha\beta\gamma}$ to the Super-CKM basis causes them to pick up phases at the low scale.

We have estimated the electron, neutron and mercury EDMs for textures at the high scale, all of which satisfy experimental constraints on quark masses and CKM matrix elements. The dominant source of EDMs in the generic case where the trilinears are not aligned with the Yukawa matrices are from two-loop diagrams involving charginos and neutralinos, and are therefore not suppressed by large scalar masses. These contributions are much larger than the one-loop diagrams as a result. While at the high scale the phase in the gaugino masses is zero, a misalignment between the trilinears and the Yukawas induces a non-zero phase at two-loop order in the running of the masses. Thus there is a non-zero phase at the low scale.

A priori one would think that a phase that arises only at two-loop order, which is then inserted into a two-loop effect, would be smaller than the one-loop contribution. However, several factors contribute to making the two-loop effects large. The phase induced by the running of the gaugino masses depends on the full trilinear, which is large ($\hat{A} \sim \mathcal{O}(75\,\text{TeV})$) in the M-theory compactification, which results in a relatively large phase, despite the two-loop suppression. Further, the two-loop contribution is approximately $d \sim (\alpha^2/\pi^2)(m_f m_{\tilde{\chi}^\pm}/M_{EW}^3)$, as opposed to the $d \sim (\alpha_s^2/\pi)(m_f m_{\tilde{g}}/m_{\tilde{q}}^3)$ for the one-loop contribution. Since $m_{\tilde{q}}^3 \gg m_{EW}^3$, the two-loop contribution turns out to be quite large when the phases are not small.

These two-loop contributions do not depend on the choice of texture, as they arise mainly due to the third generation phase entering the gaugino mass running. Since the third generation coupling is always 1 in the textures we consider here, the texture-dependence is negligible.

We summarise our results and compare with other models in table 5.5. As seen there, the estimated upper bounds we find from the two loop contributions are $|d_n| \lesssim 5 \times 10^{-29} e\,\text{cm}$ and $d_e \lesssim 5 \times 10^{-30} e\,\text{cm}$. These are values that are likely to be accessible in the near future. A detection would confirm a misalignment between the trilinears in the Soft Lagrangian and the Yukawa matrices. Non-detection would imply that they are aligned, or that the phase in the trilinears is indeed small. The results are different from those reported in the Split SUSY scenario [2, 3], as can be seen in table 5.5 and would therefore provide a means of distinguishing between that scenario and the compactified M-theory. Further, the ratio of the EDM predictions from the two-loop diagrams is a strong test of the M_2/μ ratio predicted in the compactified M-theory. These results assume the strong CP contribution is small.

We also compute the sub-dominant one-loop results. The reason being that these would provide the dominant contributions in the case where the trilinears are indeed aligned with

the Yukawas. In this case, the estimated upper bounds turn out to depend strongly on the textures and are all below current experimental limits. We argue that although we only study some textures, the results for EDM upper limits are generic. We find that the Electroweak contribution to the neutron and mercury EDMs is larger than the expected strong contribution in the SM, so any observation of a neutron or mercury EDM may be interpreted as the Electroweak part, but this would require further study. The upper bound we estimate for the electron EDM is well below current experimental limits, so we do not expect experiments in the near future to be able to measure a non-zero EDM.

These results, while done in the context of a compactified M-theory, are likely to be applicable for supersymmetric models which have scalars similar to the M-theory ones (and would scale as the scalar mass cubed), and light gauginos, with CP-violating phases arising only in the Yukawa sector at the high scale.

The upper bounds we find for $d_n \lesssim 8 \times 10^{-31} e\,\mathrm{cm}$, $d_{Hg} \lesssim 2 \times 10^{-32} e\,\mathrm{cm}$ and $d_e \lesssim 5 \times 10^{-34} e\,\mathrm{cm}$ are strong and testable predictions of compactified M-theory. They are much smaller than the sizes expected in supersymmetric and other generic models, but still significantly larger than the SM predictions. Unfortunately, in this case, where the trilinears are aligned with the Yukawas, we expect that non-zero EDMs will not be found until there are major improvements in experimental sensitivity.

The next round of experimental measurements of EDMs will provide valuable insight into the fundamental Yukawa couplings of the quarks and leptons. If non-zero EDMs are measured, it would suggest that there is indeed a misalignment between the full trilinears and the Yukawa couplings, with the dominant EDM contribution arising at two-loop order. If non-zero EDMs are not found, it would suggest that there is alignment between the trilinears and the Yukawas. Further advances in experimental sensitivity might then provide some insight into the structure of the Yukawas at the high scale, given the strong texture dependence of the dominant one-loop contributions.

This chapter concludes the study of low-energy observables associated with supersymmetric models with heavier scalars, both in the absence of (Chapter 4) and in the presence of (this chapter) CP violation. In the next two chapters we will discuss general ideas that apply to a wider class of models, and have profound implications for supersymmetric models.

Chapter 6

The Lightest Visible-sector Supersymmetric Particle is Likely to be Unstable

6.1 Introduction

In the preceding chapters we have considered primarily the collider and low-energy phenomenology of supersymmetric models, with an emphasis on spectra with heavier scalars. However, there are other general aspects of the phenomenology of supersymmetric models which deserve study. In this chapter, we revisit the basic assumption that the lightest visible-sector supersymmetric particle is stable. While not precisely in the context of models with heavier scalars, the results of this chapter have wide-reaching impact on all types of supersymmetric models.

The Standard Model (SM) of particle physics has long been known to lack an adequate candidate for dark matter. An oft-repeated virtue of its minimal supersymmetric extension (the MSSM) is that a conserved matter parity, or R-parity, will imply that the lightest supersymmetric particle is stable, and therefore a natural dark matter candidate [197, 198]. Unfortunately, as we will argue here, when the MSSM is embedded in a ultraviolet (UV) complete theory, such as string or M-theory, the lightest supersymmetric particle will most likely not reside in a visible sector.

Whatever the particular details of any particular string compactification may be, there are certain results that appear to be generic. Of particular importance to this chapter are the existence of hidden sectors. We define a hidden sector as containing states in the low-

energy effective theory that are uncharged at tree-level under the SM gauge symmetries, but can be charged under their own symmetry group G_H. Compactified string/M-theory solutions will generically have hidden sectors, containing, at a minimum, the gauge fields and gauginos associated the various group factors contained in G_H, when the UV solution is supersymmetric [199, 200]. Such sectors have already been used for model-building purposes, in particular for the breaking of Supersymmetry (SUSY), which takes place in a hidden sector and is then mediated to the visible sector.

Hidden sectors will of course interact with our visible sector via gravitational interactions, but can also have other so-called "portals" to the visible sector [201]. We argue that the existence of hidden sectors and portals leads to the conclusion that the lightest supersymmetric particle in the visible sector (LVSP) is likely to be unstable, since there will generically be a lighter particle in one of the many hidden sectors (an LHSP), into which the LVSP will decay via the portal. For this decay to occur, a simple list of conditions is required, and we find that they are all quite typically available, leading to the conclusion that the LVSP decays. The conditions are the following:

1. There exists one or more hidden sectors.

2. There exists a portal connecting the visible sector to the hidden sector.

3. That hidden sector spectrum includes a particle lighter than the LVSP.

We will concentrate on the kinetic mixing portal [202], as we find this to be the most generic portal arising from string theory [199]. The existence of other portals would only serve to strengthen our argument.

6.2 Hidden Sectors in String Theory

A typical feature of the hidden sectors in string/M theory are their multitude and their richness. The presence of hidden sectors is not optional, but often *required* to ensure the mathematical consistency of the theory. While systematic studies remain rare (see the discussion in [64]), the genericity of large hidden sectors, with many small-rank groups, has been demonstrated in several contexts. These include the heterotic string in the free-fermionic approach [203, 204] and in the orbifold limit [205, 206], weakly-coupled Type II string theory [207, 208], and Gepner models [209]. F-theory models are known to produce

similarly rich hidden sectors [210]. Finally, let us consider M-theory compactified on a manifold with G_2 holonomy. Whilst, in this case, we are technically far away from being able to perform systematic surveys of gauge groups, the general picture is expected to be somewhat similar to the F-theory results of [210]. This can also be argued from duality with the heterotic and Type-II string theory. Given that the number of hidden sectors is bounded by the third Betti number, which is typically $\mathcal{O}(100)$ [211, 200], it is expected that having many hidden sectors will also prove generic in M-theory.

It is important to note that the size of the hidden sector gauge group is often much larger than that of the observable sector. We may use the rank of the group G_H (typically a product of non-Abelian and Abelian factors) as a proxy for the richness of the hidden sector. Traditional string model-building has centred upon weakly-coupled heterotic or Type II solutions, which typically give a rank for G_H that is larger than G_{SM}, but roughly comparable in size. In recent years, however, the study of strongly-coupled string theory has been put on a much firmer footing, particularly in the context of F-theory. Here the expectation is for the rank of G_H to be much larger than G_{SM}, perhaps by orders of magnitude[1] (see, for example, the specific case studied in [212]). What is more, the notion of "generic" has become increasingly precise in these contexts [213].

In the next section we will consider the phenomenon of kinetic mixing, which requires the presence of Abelian $U(1)$ factors in the hidden sector. Given the existence of non-Abelian gauge groups in hidden sectors, it is clear that if they are broken, there can be resulting $U(1)$ factors in the hidden sector. The mechanisms for breaking the hidden sector gauge group can be either via Wilson lines, or via radiative breaking at lower energies. The former case is inherently string-theoretic, in that it requires the presence of non-trivial geometry in the compact space. The latter mechanism is familiar from four-dimensional field theory. Furthermore, there can be $U(1)$'s in the four-dimensional effective field theory that do not stem from non-Abelian groups, and have a string-theoretic origin. A well-studied example is the dimensional reduction of Ramond-Ramond (RR) forms on suitable cycles in Type II theory [214].

To be phenomenologically relevant, it is necessary that any such $U(1)$ be non-anomalous, for otherwise the gauge boson would receive a mass of order the string scale through the Green-Schwarz mechanism. In open string theories one typically finds that many of the $U(1)$ factors are anomalous. What is more, many $U(1)$s which are non-anomalous may

[1]Similarly large ranks for G_H have been observed for some time in rational conformal field theory constructions [209].

nevertheless acquire a string-scale mass to satisfy higher-dimensional anomaly cancellation conditions [215, 216]. Yet the effective mass matrix for the collection of $U(1)$s need not have full rank, and indeed generally does not [217, 218, 219]. The same has been observed in heterotic constructions which generalise the structure group of the gauge bundle [220].

Furthermore, there are many circumstances in which one expects massless $U(1)$s to emerge. The most obvious are cases in which the $U(1)$ arises from the breaking of a non-Abelian group via Wilson line breaking, or through parallel splitting of stacks of D-branes. Abelian factors arising from the zero modes of closed string RR-forms are guaranteed to be massless on Calabi-Yau surfaces, and can obtain masses only in non-Kähler backgrounds [221]. Abelian factors supported by $\overline{D3}$-branes cannot participate in the Stückelberg mechanism as the necessary axionic fields are projected out by orientifolding [222]. All of these arguments imply that one generically expects light $U(1)$s in the effective field theory.

6.3 The Kinetic Mixing Portal

The kinetic mixing portal was first considered in the context of four-dimensional field theory [202], in which it arises from the existence, and subsequent integrating out of, heavy bi-fundamental fields, charged under both $U(1)$'s. Such states exist typically in open string theories. For instance, if both $U(1)$'s are supported by D-branes which are separated in the extra dimensions, as is the case for all supersymmetric Type I, Type IIA and Type IIB models, then there will be massive open strings which stretch between the two D-branes, giving rise to massive bi-fundamentals. There are generalisations of this statement in M-theory, F-theory and the heterotic string as well.

These bi-fundamentals will lead to a one-loop mixing of the two $U(1)$ symmetries $U(1)_a$ and $U(1)_b$. In the case of interest let $U(1)_a$ correspond to the visible sector $U(1)_Y$, and $U(1)_b$ correspond to a hidden sector $U(1)$. The Lagrangian of the $U(1)$ kinetic sector then reads

$$\mathcal{L}_{gauge} = -\frac{1}{4}F_a^{\mu\nu}F_{a\mu\nu} - \frac{1}{4}F_b^{\mu\nu}F_{b\mu\nu} + \frac{\epsilon}{2}F_a^{\mu\nu}F_{b\mu\nu} \tag{6.1}$$

where ϵ parameterises the mixing of the two $U(1)$'s each with field strength tensor $F_i^{\mu\nu}$.

Note that in the case of kinetic mixing with $U(1)_Y$ in the visible sector, after spontaneous breaking of the $SU(2)_w \times U(1)_Y$ electroweak symmetry, the photon will still remain massless. Instead of generating a mass term for the photon, kinetic mixing will instead induce a small

shift in the mass of the Z boson.

The expected size of ϵ can be estimated by calculating the two-point polarisation diagram and is given by [202]

$$\epsilon \simeq \frac{g_a g_b}{12\pi^2} Q_a Q_b \log\left(1 + \frac{\Delta m_{ab}^2}{M^2}\right) \tag{6.2}$$

where $g_{a,b}$ ($Q_{a,b}$) are the couplings (charges of bi-fundamentals) of $U(1)_{a,b}$, Δm_{ab} is the mass splitting of the bi-fundamental fields charged under both groups, and M is the bi-fundamental mass scale, such that the bifundamentals have mass $M + \Delta m_{ab}$. Clearly if the $U(1)$'s sit in an unbroken non-Abelian gauge symmetry, $\epsilon = 0$. If the matter spectrum is charged under a non-Abelian gauge symmetry with a $U(1)$ factor then the mass degeneracy of the spectrum would naively cause $\epsilon = 0$ also. However, this degeneracy is not stable against radiative corrections, and mass splittings Δm_{ab} are generated, thus rendering ϵ non-zero.

These bi-fundamentals may have masses $M \sim \frac{R}{l_s^2}$, where R is the separation of two stacks of D_p branes connected by the open string. This suggests that the mass should be $M \sim \mathcal{O}(M_{GUT})$. Depending on the size of Δm_{ab}, ϵ can take on a wide range of possible values. In particular, if the hidden sector gauge group is broken at a scale $M_{G_H} \sim M$ via a Wilson line, ϵ can be of $\mathcal{O}(10^{-3})$ for $\mathcal{O}(1)$ charges Q_a and Q_b and $g_a \sim g_b \sim g_Y$. On the other hand if the hidden sector gauge group is broken radiatively through field theory dynamics at some much smaller scale $M_{G_H} \ll M$, ϵ can be as small as $\mathcal{O}(10^{-26})$ (e.g. if $M_{G_H} \sim 1$ TeV). Crucially however, barring some non-generic external mechanism to prevent ϵ from being generated, it is always non-zero [199]. Since ϵ enters via a dimension-4 operator, it is a priori not suppressed by high mass scales.

Explicit calculations of the kinetic mixing parameter (6.2) in Type II constructions support these arguments. Typical values for the mixing parameter are found to generally lie in the range $10^{-3} \leq \epsilon \leq 10^{-1}$, with values as low as $\epsilon \sim 10^{-6}$ accessible via tuning [223, 224, 225, 226]. Some additional volume suppression in the Type IIB context can be obtained in various LARGE volume scenarios [227], in which the assumption that $g_b \sim g_Y$ is relaxed. In this case, a compact volume which generates an intermediate string scale $M_s \sim 10^{10}\,\text{GeV}$ could produce an effective mixing parameter in the range $10^{-8} \leq \epsilon \leq 10^{-6}$ [228, 229]. It is unclear whether such large volumes are generic, even within the context of flux compactifications of Type IIB string theory, though as we will see below, these values still imply that the LVSP will not be an adequate dark matter candidate.

Finally, we should emphasize that non-vanishing kinetic mixing has also been demon-

strated in heterotic contexts, including heterotic M-theory [230], Calabi-Yau compactifications [231] and in certain heterotic orbifold limits [232]. The genericity of kinetic mixing in string theory, and its typical size ($\epsilon \sim 10^{-3}$) appear to bear out the intuition of Dienes et al. from twenty years ago [199].

6.4 The Decay Mode

Given the existence of a portal, such as the kinetic mixing portal described above, the stability of the LVSP becomes a simple question of kinematics. Note that the usual argument for LVSP stability is based on discrete symmetries, but that requires that the LVSP mass is sufficiently small compared to other particle masses. The LVSP will not decay if it is lighter than all possible combinations of potential hidden sector decay products permitted by gauge invariance alone. One can ask for a sufficient condition for LVSP stability: *why should the LVSP be lighter than all hidden sector particles?* A key point is that this question has no obvious answer, and clearly becomes more and more difficult as one increases the number and complexity of the hidden sectors. If there is no good reason for the LVSP to be light compared to hidden sector particles then, presumably, the LVSP will decay. How does it decay?

With Supersymmetry the hidden sector contains the $U(1)$ gauge boson and the associated gaugino. The sector may also contain matter charged under the hidden $U(1)$. If any of these states are lighter than the LVSP, then the LVSP can decay via the portal, which induces a mixing between the Bino and the hidden $U(1)$-ino in the neutralino mass matrix. Let us assume that the LVSP is a neutralino, as is common within the MSSM. If a kinetic mixing portal exists to a hidden sector in which the LHSP is also a gaugino, then LVSP decay is expected whenever $\delta m = m_{LVSP} - m_{LHSP} > 0$. If $\delta m > m_Z$, the neutralino LVSP undergoes 2-body decay to a Z boson with lifetime

$$\tau_{2-\text{body}}^{\chi_i \to Z\ \chi_j} \sim 10^{-17}\ s \times \left(\frac{10^{-3}}{\epsilon}\right)^2 \left(\frac{0.01}{|N_{i3}N_{j3}^*|}\right)^2 , \tag{6.3}$$

where N_{km} is a neutralino mixing matrix element. We have assumed a mostly Bino or Wino LVSP, and have taken $m_{LVSP} = 1$ TeV and $m_{LHSP} = 100$ GeV for illustrative purposes. Three-body decays can occur if $\delta m < m_Z$, and may dominate [233]. Then the characteristic

lifetime is

$$\tau_{3-\text{body}}^{\chi_i \to Z\ \chi_j} \sim 10^{-9}\ \text{s} \times \left(\frac{10^{-3}}{\epsilon}\right)^2 \left(\frac{0.01}{|N_{i3}N_{j3}^*|}\right)^2 , \tag{6.4}$$

where we have taken $m_{LVSP} = 1$ TeV and $m_{LHSP} = 950$ GeV for illustrative purposes. There are also both two- and three-body decays to a Higgs boson, with $\tau^{\chi_i \to h\ \chi_j} \sim \frac{H_{ij}^2}{|N_{i3}N_{j3}^*|^2} \tau^{\chi_i \to Z\ \chi_j}$, where H_{ij} is the neutralino coupling to higgs bosons. Additionally, if the LVSP is mostly Higgsino, $\tau^{\tilde{H} \to Z\ \chi_j} \sim |N_{i3}N_{j3}^*|\ \tau^{\tilde{B},\tilde{W} \to Z\ \chi_j}$ for both the two- and three-body decays.

There can also be decays into a chiral fermion LHSP which can be much lighter; we will describe the resultant parameter space in a paper in preparation.

6.5 Summary

In this chapter we have put forward arguments that imply that the lightest supersymmetric particle in the visible sector is most likely not, in fact, stable. It may be metastable, though it is far more likely that it undergoes prompt decays into hidden sector states. The components of the argument are simple: (1) there is at least one hidden sector, (2) there is at least one portal connecting it to the visible sector, and (3) there exists matter in that sector which is lighter than the LVSP. We have illustrated these arguments with a kinetic mixing portal, since this appears to be the most generic outcome from string theory, but the presence of additional portals would only strengthen the argument.

Several aspects of our argument have appeared elsewhere in the literature in various forms. Here we have emphasised the generic nature of these components in string/M-theory solutions. Given the multitude of hidden sectors in string compactifications, it is quite likely that there exists at least one sector that satisfies these assumptions. Therefore we conclude that the LVSP will decay. It is the generality of this conclusion that compels us to argue for a paradigm shift in the thinking of phenomenologists when it comes to dark matter. In particular it raises the likelihood that dark matter resides in a hidden sector which might be very difficult to probe.

We conclude by noting that relegating dark matter to some hidden sector has phenomenological consequences. The resulting lifetime may affect collider signatures; we will return to study these in a follow-up paper. The kinetic mixing portal scenario illustrated may be cosmologically perilous, due to long-range forces and millicharged particles, to disruptions in

Big Bang nucleosynthesis, to a relic overabundance that conflicts with the known age of the universe [228, 229, 234, 233]. None of these challenges negate the conclusion that the LVSP is very likely unstable. It is non-generic to avoid sizeable kinetic mixing and light hidden sector states. Instead, it may turn out that the study of dark matter in string theories will illuminate that corner of the string/M-theory landscape in which our world resides.

In this chapter we considered the implications of String/M-Theory for the stability of the LVSP. In the next chapter, we will look at another general aspect of supersymmetric models, namely the details of unification of the gauge couplings into a Grand Unified Theory. The analyses both in this chapter, and in the next, have implications for supersymmetry at all mass scales, including the case where there are heavier scalars.

Chapter 7

Visualizing Gauge Unification with High-scale Thresholds

As in the preceding chapter, in this chapter we will study general aspects of supersymmetric models. Here, we are interested in the high-energy dynamics of the unification of the gauge couplings. The results of this chapter have wide-ranging applications, even to non-supersymmetric models, as we will see in one of the examples we consider.

A common practice in the literature when contemplating gauge coupling unification is to settle upon a weak-scale theory, run the three gauge couplings up to the high scale, and look for theories where the three gauge couplings meet in one place. Famously, the Standard Model (SM) does not unify under that rubric but the Minimal Supersymmetric Standard Model (MSSM) does according to many [235, 236, 237, 238, 239, 240, 241, 242, 243]. However, such statements are too simple. The SM cannot be ruled out as the IR manifestation of a Grand Unified Theory (GUT), nor do the three gauge couplings meet at precisely one point in the MSSM. The key to understanding both claims is that high-scale thresholds are generically expected, which are due to the multiplets at the high scale that get masses by the same mechanism that breaks the GUT symmetry. High-scale threshold corrections kick the infrared couplings further into exact unification if the underlying theory is gauge-coupling unified.

Despite continuing misstatements by a few at times, these facts have been well known by the experts for some time. What is not as widely appreciated is how generically possible unification is in theories without Supersymmetry when expected high scale threshold corrections are contemplated, and how anomalously low the high-scale threshold corrections must be in Supersymmetry to satisfy exact unification compared to generic expectations of a

high-scale unified theory. One of our main goals in this chapter is to argue these two points by making apples to apples comparisons of the renormalized gauge couplings at high scale and expected thresholds.

The second main goal of this work is to transform all the information we have of the low-energy theory into useful data for testing the viability of a high-scale theory of unification. The resulting output also should provide intuitive and immediate meaning to the unification seeker. For example, RGE flow of g_i couplings up to the high scale never achieve exact unification, even within supersymmetric theories. Indeed it should not if there are any high scale thresholds at all. The question then becomes whether the mismatch is too much for a viable unification theory to overcome. Simple data on g_i at an (ambiguously defined) GUT scale is not enough to answer that question even approximately. Further processing of the data is required.

In this chapter we advocate the answer to these requirements are plots of the scale-projected mismatch of couplings vs. the renormalization group running scale: "$\Delta\lambda$ plots". Definitions and details are below. Suffice it to say in the introduction here that these plots encapsulate all the needed information about the infrared thresholds of the theory, unambiguously show what high-scale threshold corrections need to accomplish to achieve exact unification of the couplings, and provide rapid intuition about the generic features that a unified theory must possess to have exact unification (e.g., the approximate size of representations needed). All low-scale theories, including the SM and various forms of low-scale Supersymmetry, need produce only one plot for researchers to use in testing viability of their high-scale unified theories.

The literature contains many examples of grand unified theories and their analyses, building on long-ago studies [235, 236, 237, 238, 244, 239, 240, 241, 242, 243, 245, 246, 247, 248, 9, 249]. Our field continues to pursue grand unification in both supersymmetric contexts and not. Although weak scale supersymmetric grand unified theories are decidedly still viable [250], many recent Supersymmetry studies also consider the salient aspects of very massive superpartners [14, 251, 252, 253, 254, 255]. These theories require somewhat larger threshold corrections at the high scale, which as we will see may be a positive feature due to weak-scale Supersymmetry's requirement of disquietingly small high-scale threshold corrections to achieve exact unification. We demonstrate the utility of this method by applying it to two simple grand unified theories in the literature: The $SO(10)$ SM theory of Lavoura-Wolfenstein [256] and the ϵ-assisted $SU(5)$ supersymmetric theory of Tobe and Wells [257]. Both of these theories are straighforwardly compatible with unification, despite the "run-

ning of the couplings" not meeting exactly at any one scale. The $\Delta\lambda$ plots will be used to demonstrate the results graphically.

7.1 Unification of couplings : preliminaries

Let us begin by reviewing a few basic aspects of unification theory and effective field theory. When discussing the unification of couplings it is of great importance that we make unambiguous statements about what we know from the IR effective theory and what we can calculate from the UV in a particular GUT theory. It is possible to define a unified coupling g_U in an infinite number of ways that are not physically meaningful. For example, we can define it to be the value of the couplings g_1 and g_2 at a scale M_U where $g_1(M_U) = g_2(M_U)$ in some scheme. Or we can definite it to be when $g_2(M_U) = g_3(M_U) = g_U$, or the value of $(g_1+g_2+g_3)/3$ when $(g_1-g_2)^2+(g_1-g_3)^2+(g_2-g_3)^2$ is minimized, or an infinite number of other ways. Although one or more of these definitions can have some utility in some limited circumstances, in careful testing of theories for exact unification it is not useful to define a unified coupling g_U by any procedure from the IR perspective.

Instead, g_U can only be defined from the UV perspective where in the high-energy phase, or GUT phase, of the theory there is a single gauge coupling g_U which is subject to defining boundary conditions to set its value at some scale, and which subsequently runs with scale. At some scale M_* matching is made between the GUT unified theory with gauge coupling g_U and the low-scale theory with gauge couplings g_1, g_2 and g_3. The matching at M_* involves a lot of violence from threshold corrections, and $g_i(M_*)$ can all be quite different than g_U. For that reason there is little utility in trying to define a physically meaningful g_U from the IR perspective. We shall therefore not rely on such artifices below.

7.2 Analytic Definitions and Procedures

Let us continue with some technical remarks on the calculations involved. The hypercharge, weak and strong couplings in the IR are the standard $g_1,\ g_2,\ g_3$, where g_1 has the appropriate GUT normalization. Their values change with scale according to the renormalization group equations (RGEs) of the IR effective theory. From the UV perspective, g_U is defined by our choice of GUT theory. Depending on the choice of UV theory, there may be more than one scale involved depending on the splitting of the gauge boson and scalar masses.

We use the two-loop RGEs for the evolution of the gauge coupling constants in the IR

from the electroweak scale to the high scale. The equations are

$$\frac{dg_i}{dt} = \beta_i^{(1)} + \beta_i^{(2)} = \frac{b_i g_i^3}{16\pi^2} + \frac{g_i^3}{(16\pi^2)^2}\left[\sum_{j=1}^{3} B_{ij} g_j^2 + \sum_{a=u,d,e} C_i^a \,\mathrm{Tr}\left(\boldsymbol{Y}_a^\dagger \boldsymbol{Y}_a\right)\right] \tag{7.1}$$

where b_i, B_{ij} and C_i^a are group coefficients that can be calculated in the Standard Model and its extensions [258, 259, 260, 178].

Rather than pick a particular unification scale, we choose a scale $\mu_* = 10^{16}\,\mathrm{GeV}$ at which to evaluate various quantities. We select this scale since it is closely related to the constraints on the masses of the vector bosons associated with proton decay. We know that at scales near the unification scale, the IR gauge couplings $g_i(\mu_*)$ are related to the unification coupling $g_U(\mu_*)$ by the following relation at one-loop [245, 246]:

$$\left(\frac{1}{g_i^2(\mu_*)}\right)_{\overline{MS}} = \left(\frac{1}{g_U^2(\mu_*)}\right)_{\overline{MS}} - \left(\frac{\lambda_i(\mu_*)}{48\pi^2}\right)_{\overline{MS}} \tag{7.2}$$

where $\lambda_i(\mu_*)$ are the threshold corrections, computed in the $\overline{MS}$ scheme, to each gauge coupling at the scale μ^*. In general, when masses in an irreducible block are identical, $\lambda_i(\mu)$ can be defined as [246]

$$(\lambda_i(\mu))_{\overline{MS}} = l_i^{V_n} - 21\, l_i^{V_n} \ln\frac{M_{V_n}}{\mu} + l_i^{S_n} \ln\frac{M_{S_n}}{\mu} + 8\, l_i^{F_n} \ln\frac{M_{F_n}}{\mu} \tag{7.3}$$

where there is an implicit sum over the n different superheavy particles of a given type (V for vector bosons, S for scalars and F for fermions). It should be understood that only physical scalars contribute. The l_i^X are the weighted Dynkin indices relative to the SM gauge group i. This computation of $\lambda_i(\mu)$ is understood to be accurate only in the region near the scale of unification. The threshold corrections can therefore be determined in the GUT theory of choice.

In the IR, we may use Eq. (7.2) above and define the following relations that are independent of the unification coupling $g_U(\mu_*)$

$$\left(\frac{\Delta\lambda_{ij}(\mu_*)}{48\pi^2}\right)_{\overline{MS},\ \overline{DR}} \equiv \left(\frac{1}{g_i^2(\mu_*)} - \frac{1}{g_j^2(\mu_*)}\right)_{\overline{MS},\ \overline{DR}} = \left(\frac{\lambda_j(\mu_*) - \lambda_i(\mu_*)}{48\pi^2}\right)_{\overline{MS},\ \overline{DR}} \tag{7.4}$$

for $i, j = 1\ , 2,\ 3,\ i \neq j$. Any two $\Delta\lambda_{ij}$ then specify all the threshold corrections up to a constant factor. The subscripts $\overline{MS}$ and $\overline{DR}$ indicate that the threshold corrections and gauge couplings need to be computed in the appropriate renormalization scheme depending

on whether one is dealing with a SUSY theory ($\overline{DR}$) or not ($\overline{MS}$).

From the IR, we only know how to compute $g_i(\mu)$ and run up to some scale μ_*. We may then use Eq. (7.4) to calculate $\Delta\lambda_{ij}$ as a function of μ without requiring knowledge of the UV theory. We may then assume that the UV has some GUT theory description, which would allow us to compute the threshold corrections $\lambda_i(\mu_*)$ and their difference, $\Delta\lambda_{ij}(\mu_*)$ given the spectrum of superheavy particles. If the $\Delta\lambda_{ij}(\mu_*)$ obtained from the IR were to match that obtained from the UV GUT theory for a particular set of GUT masses, unification is possibly achieved. There is an ambiguity due to a shift symmetry since the differences matching may not account for a constant term. Therefore matching the UV and IR calculations of $\Delta\lambda_{ij}$ specifies

$$\frac{1}{g_U^2(\mu_*)} + S \quad \text{and} \quad \frac{\lambda_i(\mu_*)}{48\pi^2} + S \tag{7.5}$$

where S is some constant shift. Thus Eq. (7.2) is satisfied, but with some ambiguity from the IR perspective left over as to the unified coupling constant and the size of the threshold corrections. Of course, from the UV perspective, both are known.

7.3 Numerical Procedure

We compute the running of the gauge couplings in three different cases: (1) the Standard Model (SM); (2) a generic low-scale CMSSM-like SUSY model with weakly (strongly) coupled sparticles at 1 TeV (3 TeV); and, (3) a split Supersymmetry-like model with bino and higgsinos at 1 TeV, winos at 3 TeV, gluinos at 7 TeV and scalar superpartners at 1 PeV. These three cases are all motivated by theory and current experimental constraints from the LHC.

We perform the calculation of the RGE running at two-loop order numerically, with the one-loop coefficients changing depending on the matter content. For the SM, we use the two-loop beta functions derived in [258]. For the supersymmetric cases, we use the two-loop beta functions derived in [178] with the appropriate shifts in the one-loop coefficients as we pass through sparticle thresholds.

Upon applying these spectra to the above formalism we are now able to compute the $\Delta\lambda$ plot of $\Delta\lambda_{13}$ and $\Delta\lambda_{23}$ values from the IR for all three cases as a function of renormalization scale μ. The SM case is provided in Fig. 7.1. This plot is the only data needed when one wishes to check SM compatibility with a favorite unification theory. We will do that later in an $SO(10)$ example.

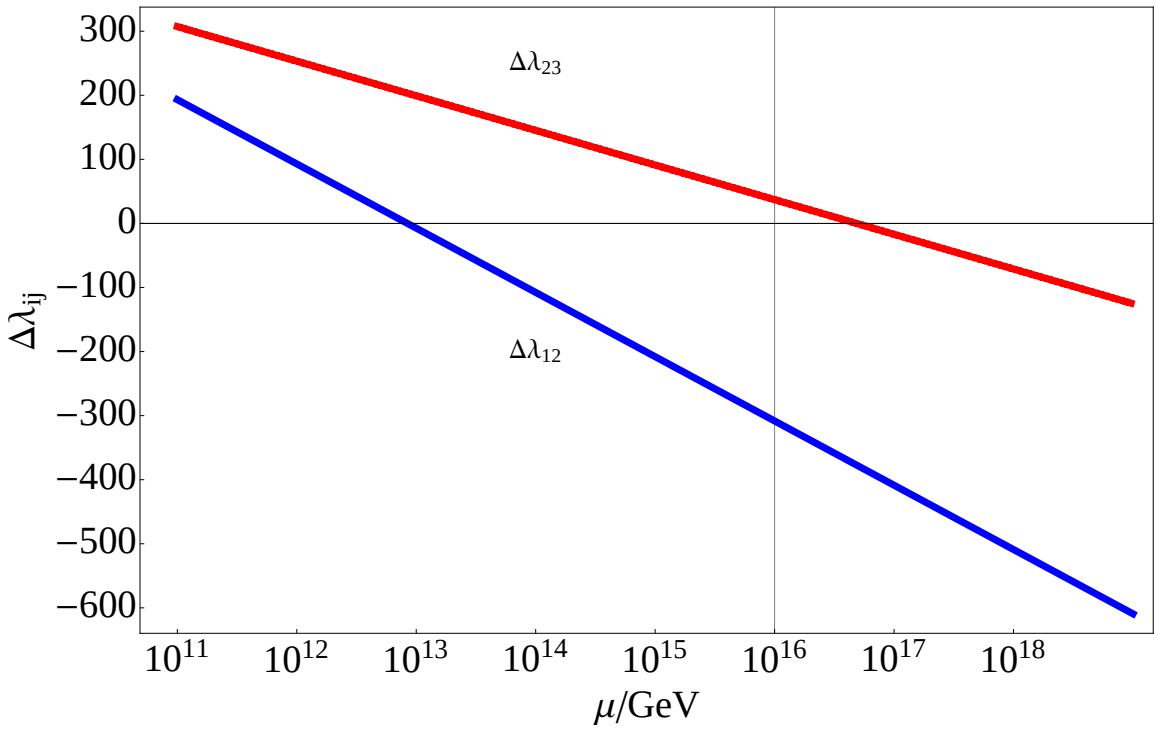

Figure 7.1: Plot of $\Delta\lambda_{23}(\mu)$ (red) and $\Delta\lambda_{12}(\mu)$ (blue) for the Standard Model as a function of scale μ.

Each supersymmetric theory with a well-defined spectrum of superpartners has its own unique $\Delta\lambda$ plot. In our two supersymmetric cases (2) and (3) discussed above, it is straightforward to make a plot of $\Delta\lambda_{13}$ and $\Delta\lambda_{23}$ as a function of μ for each of them as we did for the SM case in Fig. 7.1. However, there is an even simpler representation of the same information that we wish to present. One can plot the correlated values of $\Delta\lambda_{23}$ vs. $\Delta\lambda_{12}$ parametrized by the renormalization scale μ, where the values of μ are labeled on the line. This is done for the SM and the CMSSM-like SUSY model (case 2 above) in Fig. 7.2.

To better aid the vision and intuition of these plots we color code the line into red, orange and green as we cross various thresholds of μ. We suggestively call green "safe" to follow intuitions of simple grand unified groups that thresholds above 10^{14} GeV (at least) are needed to protect the proton from decaying too quickly.

We note in Fig. 7.2 that the supersymmetric line crosses very close to zero for $\mu \simeq 10^{16}$ GeV which is illustrating the famous case for supersymmetric unification. The SM line strays far from the origin of the plot and illustrates the famous case against SM unification. However, what precisely does it mean to "stray far" from the origin? How far is too far? The answer to these questions starts by acknowledging that exact unification at the high scale,

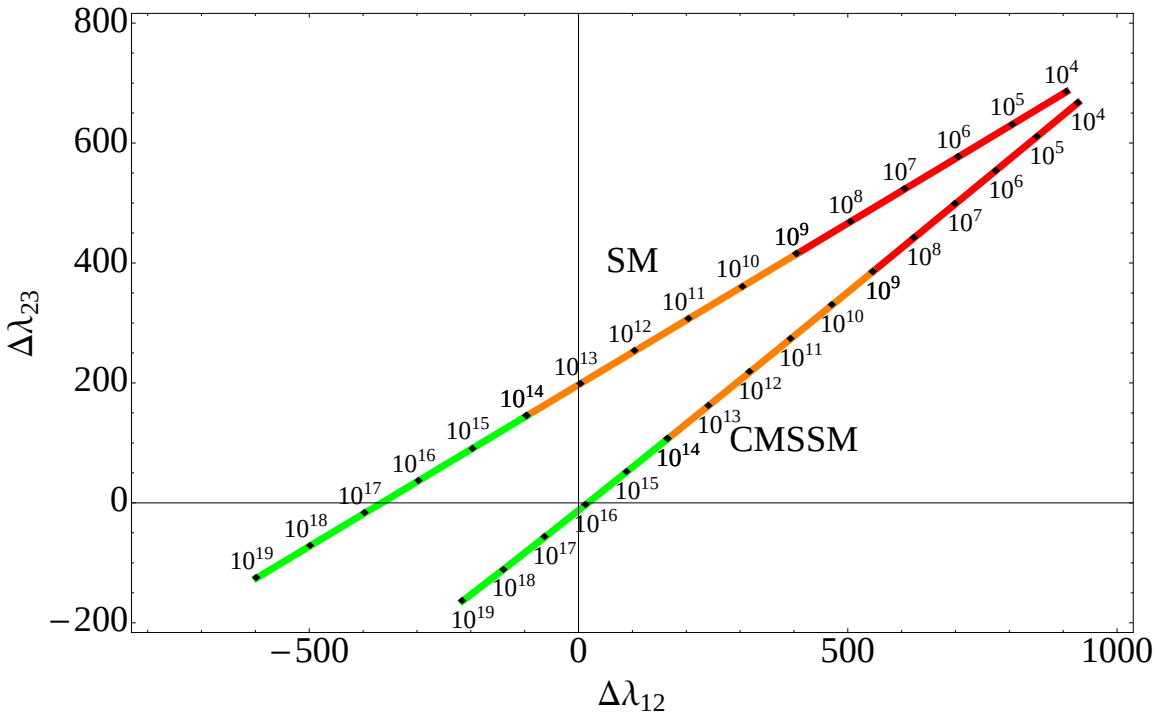

Figure 7.2: This key visualization plot shows $\Delta\lambda_{23}(\mu)$ as a function of $\Delta\lambda_{12}(\mu)$ for the Standard Model and a CMSSM-like SUSY model. Labels on the line indicate the scale μ. Green regions indicate that a unification scale around those values is moderately safe from constraints. Orange indicates relatively unsafe, Red indicates very unsafe.

and a high-scale theory, both require analyzing the high-scale threshold corrections that are generically expected. A line for a theory in the $\Delta\lambda$ plot, such as the SM line in Fig. 7.2, is "too far" away from the origin if we cannot imagine threshold corrections at the high scale shifting the couplings enough to bring it back to the origin.

We will see below that in the case of Supersymmetry, there is never a problem in this regard. In fact, the $\Delta\lambda$'s are arguably too small and threshold corrections have to either not be present for some reason or must have tuned cancellations at the high scale for exact unification to occur. In the case of the SM the corrections are large, and the index of the representations at the high scale must be comparable to the $\Delta\lambda$ values (up to multiplicative logarithms) of up to several hundred. However, the index of representations of grand unified theories based on $SO(10)$ are often in the three digits, such as the **126** representation with index 35 and the **210** representation with index 56 [261]. Indeed, these representations play a key role in our first example of the next section: Lavoura and Wolfenstein's non-supersymmetric $SO(10)$ theory [256].

7.4 Exact Unification Examples

Having described the theoretical framework we use, we give below two examples of grand unified theories that illustrate the viability of SM and supersymmetric GUTs, demonstrate the utility of the $\Delta\lambda$ plots in the search for a precise spectrum that yields exact unification of the couplings. The two examples are Lavoura and Wolfenstein's non-supersymmetric $SO(10)$ theory [256] and Tobe-Wells supersymmetric $SU(5)$ theory [257].

7.4.1 Lavoura-Wolfenstein SO(10) and the Standard Model

The $SO(10)$ GUT of Lavoura and Wolfenstein [256] has a Higgs structure that consists of {**10** and **126**} representations. There is also a **210** which contains heavy scalars that do not condense. The pattern of symmetry breaking is $SO(10) \to SU(2)_L \otimes SU(2)_R \otimes SU(4) \to SU(3)_c \otimes SU(2)_L \otimes U(1)_Y$.

The Lavoura-Wolfenstein Spectrum is shown in table 7.1 below. We label the gauge bosons according to their SM gauge group representations to make clear that the gauge bosons leading to proton decay are all at the common mass M_V, and those not leading to proton decay are all at a different mass M_R. The mass M_R is defined to be $M_R \approx v_R$, where v_R is the VEV of the $(1,3,10)$ of the **126**, which breaks the $SU(2)_L \otimes SU(2)_R \otimes SU(4)$ symmetry. We label the scalars according to their $SU(2)_L \otimes SU(2)_R \otimes SU(4)$ representations. This is done because the simplifying assumption is made that all the SM representations of scalars in a given $SU(2)_L \otimes SU(2)_R \otimes SU(4)$ representation will have the same mass. The $(2,2,1)$ component of the **10** contains the SM Higgs and therefore is not listed, as it will not contribute to the threshold corrections at the unification scale.

The decomposition into the various SM representations for a given $SU(2)_L \otimes SU(2)_R \otimes SU(4)$ can be done. For example, the $(1,1,15)$ of the SO(10) **210** yields under $(SU(2), SU(3))_{U(1)_Y}$ the charges

$$(1,1)_0, \quad (1,3)_{Q'}, \quad (1,\overline{3})_{-Q'}, \quad \text{and} \quad (1,8)_0, \quad \text{where} \quad Q' = \frac{2}{3}\sqrt{\frac{3}{5}}. \tag{7.6}$$

Making the decomposition explicit is unnecessary for the purposes of defining the spectrum of masses, but it must be done in order to compute the contributions that each state will make to the threshold corrections.

The threshold corrections for this particular GUT are obtained by applying the boundary condition equation for the threshold corrections (Eq. (7.2)) for each of the vector bosons

Gauge Bosons			**Scalars**		
$SO(10)$	$SU(2) \otimes SU(3)[U(1)_Y]$	Mass	$SO(10)$	$SU(2)_L \otimes SU(2)_R \otimes SU(4)$	Mass
45	$(1,1)[0]$	M_R	**210**	$(1,1,1)$	N/A
45	$(1,1)[\sqrt{\frac{3}{5}}]$	M_R	**210**	$(2,2,6)$	Goldstone
45	$(1,1)[-\sqrt{\frac{3}{5}}]$	M_R	**210**	$(1,1,15)$	M_1
45	$(1,3)[\frac{2}{3}\sqrt{\frac{3}{5}}]$	M_R	**210**	$(2,2,10)$	M_1
45	$(1,\overline{3})[-\frac{2}{3}\sqrt{\frac{3}{5}}]$	M_R	**210**	$(2,2,\overline{10})$	M_1
45	$(2,3)[\frac{1}{6}\sqrt{\frac{3}{5}}]$	M_V	**210**	$(1,3,15)$	M_4
45	$(2,\overline{3})[-\frac{1}{6}\sqrt{\frac{3}{5}}]$	M_V	**210**	$(3,1,15)$	M_5
45	$(2,3)[-\frac{5}{6}\sqrt{\frac{3}{5}}]$	M_V	**126**	$(1,1,6)$	M_1
45	$(2,\overline{3})[\frac{5}{6}\sqrt{\frac{3}{5}}]$	M_V	**126**	$(2,2,15)$	M_1
			126	$(1,3,10)$	M_2
			126	$(3,1,\overline{10})$	M_3
			10	$(1,1,6)$	M_{H_c}

Table 7.1: Table showing the spectrum of superheavy particles contributing to the threshold corrections in the Lavoura-Wolfenstein SO(10) GUT, with their various masses.

and scalars that has a mass near the unification scale and summing over all heavy fields. Each heavy boson contributes

$$\left(\lambda_i^{V_n}\right)_{\overline{MS}} = l_i^{V_n}\left(1 + 21\ln\frac{\mu_*}{M_V}\right) \tag{7.7}$$

where $l_i^{V_n}$ is the Dynkin index of the n-th vector boson relative to the SM group labelled by i, multiplied by their dimensions relative to the other SM gauge groups. Each scalar contributes

$$\left(\lambda_i^{S_n}\right)_{\overline{MS}} = -l_i^{S_n}\ln\frac{\mu_*}{M_S} \tag{7.8}$$

with the same labels as before, with the Dynkin index for the scalar. Given the content of

the Lavoura-Wolfenstein SO(10) GUT, we obtain

$$\lambda_1^V(\mu_*) = 8 + \frac{294}{5}\log\frac{\mu_*}{M_R} + \frac{546}{5}\log\frac{\mu_*}{M_V} \tag{7.9}$$

$$\lambda_2^V(\mu_*) = 6 + 126\log\frac{\mu_*}{M_V} \tag{7.10}$$

$$\lambda_3^V(\mu_*) = 5 + 21\log\frac{\mu_*}{M_R} + +84\log\frac{\mu_*}{M_V} \tag{7.11}$$

for the contributions from vector bosons, and

$$\lambda_1^S(\mu_*) = -\frac{274}{5}\log\frac{\mu_*}{M_1} - \frac{142}{5}\log\frac{\mu_*}{M_2} - \frac{36}{5}\log\frac{\mu_*}{M_3} - \frac{114}{5}\log\frac{\mu_*}{M_4} - \frac{2}{5}\log\frac{\mu_*}{M_{H_c}} \tag{7.12}$$

$$\lambda_2^S(\mu_*) = -50\log\frac{\mu_*}{M_1} - 40\log\frac{\mu_*}{M_3} - 30\log\frac{\mu_*}{M_5} \tag{7.13}$$

$$\lambda_3^S(\mu_*) = -62\log\frac{\mu_*}{M_1} - 17\log\frac{\mu_*}{M_2} - 18\log\frac{\mu_*}{M_3} - 12\log\frac{\mu_*}{M_4} - 12\log\frac{\mu_*}{M_5} - \log\frac{\mu_*}{M_{H_c}} \tag{7.14}$$

for the contributions from the scalars.

We consider a particular set of high-scale mass ratios, chosen to ensure intersection with the SM $\Delta\lambda_{ij}(\mu_*)$

$$\frac{M_V}{M_R} = 20,\ \frac{M_V}{M_1} = 3,\ \frac{M_V}{M_2} = 7,\ \frac{M_V}{M_3} = 9.2,\ \frac{M_V}{M_4} = 10,\ \frac{M_V}{M_5} = 15,\ \frac{M_V}{M_{H_c}} = \frac{1}{200}. \tag{7.15}$$

as well as ensuring that M_{H_c} is greater than the bound derived in [9]. The choice of the scalar masses M_i can be made by choosing appropriate couplings to the vev which gives rise to the mass.

This enables us to evaluate $\Delta\lambda_{ij}(\mu_*)$ in the Lavoura-Wolfenstein GUT. Since we are interested in what happens if we modify the GUT particle masses, we vary M_V, keeping the ratios fixed. The resultant plot is shown in Fig. 7.3. The point of intersection with the SM $\Delta\lambda_{ij}(\mu_*)$ therefore fixes M_V in the Lavoura-Wolfenstein SO(10).

This example has now demonstrated how to process IR data in the form of the $\Delta\lambda$ plot of Fig. 7.2. Upon choosing a renormalization scale μ^* there is a single point in the $\Delta\lambda_{23} - \Delta\lambda_{12}$ plane that is compatible with exact unification, and it is required that high-scale thresholds must give those values. In Fig. 7.3 we show that indeed those values can be achieved for the spectrum specified in table 7.1, and unification therefore is shown to be viable.

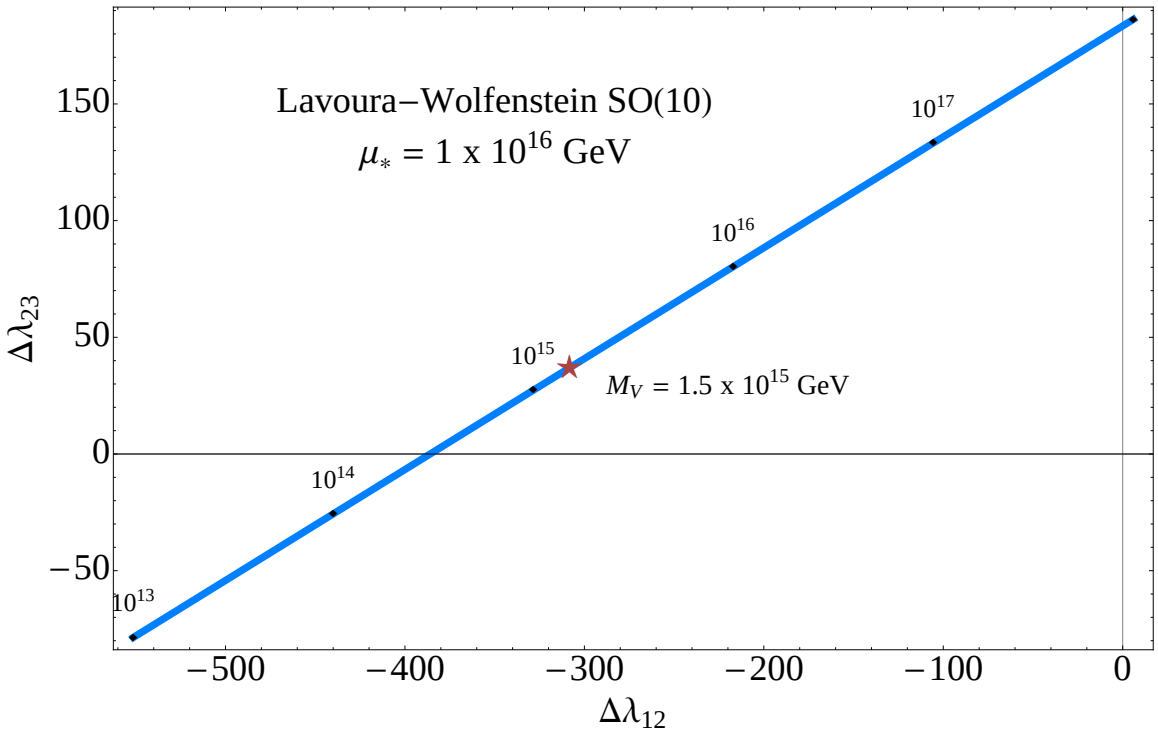

Figure 7.3: Plot of $\Delta\lambda_{23}(\mu)$ as a function of $\Delta\lambda_{12}(\mu)$. Shown is the Lavoura-Wolfenstein SO(10) (blue) with $M_V/M_R = 20$, $M_V/M_1 = 3$, $M_V/M_2 = 7$, $M_V/M_3 = 9.2$, $M_V/M_4 = 10$, $M_V/M_5 = 15$, and $M_V/M_{H_c} = 1/200$, with M_V varying between 10^{13} and 10^{18}. The star corresponds to the required values of $\Delta\lambda_{12}(\mu_*)$ and $\Delta\lambda_{23}(\mu_*)$ in the SM. We find that $M_V = 1.5 \times 10^{15}$ gives the desired $\Delta\lambda_{12}(\mu_*)$ and $\Delta\lambda_{23}(\mu_*)$ in the Lavoura-Wolfenstein SO(10) for the given mass ratios.

7.4.2 Tobe-Wells Supersymmetric SU(5)

We also compare with a SUSY model, taking as an example an SU(5) GUT described by Tobe and Wells [257]. The Higgs structure of this GUT consist of $\{\mathbf{24_H}, \mathbf{5_H}, \overline{\mathbf{5}}_{\mathbf{H}}\}$, and the gauge representation is a $\mathbf{24}$. The spectrum of the superheavy particles in this GUT is shown in Table 7.2.

In this GUT there is an additional non-renormalizable operator connecting the adjoint Higgs representation to the gauge fields. The operator in question arises from the gauge-kinetic function of minimal SU(5) written as

$$\int d^2\theta \left[\frac{S}{8M_{Pl}}\mathcal{W}\mathcal{W} + \frac{y\Sigma}{M_{Pl}}\mathcal{W}\mathcal{W}\right] \tag{7.16}$$

where $\Sigma = \mathbf{24_H}$. The second term gives rise to corrections to the gauge couplings because

Gauge Bosons			Scalars		
$SU(5)$	$SU(2)\otimes SU(3)[U(1)_Y]$	Mass	$SU(5)$	$SU(2)\otimes SU(3)[U(1)_Y]$	Mass
24	$(2,3)[-\frac{5}{6}\sqrt{\frac{3}{5}}]$	M_V	$\mathbf{24}_H$	All	M_Σ
24	$(2,\overline{3})[\frac{5}{6}\sqrt{\frac{3}{5}}]$	M_V	$\mathbf{5}_H+\overline{\mathbf{5}}_H$	$(1,3)[-\frac{1}{3}\sqrt{\frac{3}{5}}]+(1,\overline{3})[\frac{1}{3}\sqrt{\frac{3}{5}}]$	M_{H_c}

Table 7.2: Table showing the spectrum of superheavy particles contributing to the threshold corrections in the Tobe-Wells SU(5) GUT, with their various masses.

the adjoint Higgs must acquire a vacuum expectation value

$$\langle\Sigma\rangle = v_\Sigma \text{ diag}\left(\frac{2}{3},\frac{2}{3},\frac{2}{3},-1,-1\right) \tag{7.17}$$

to break SU(5) to the SM gauge group at the GUT scale. The masses of the X and Y bosons are related to the vev of Σ by

$$M_{X,Y}^2 = \frac{25}{18}g_U^2 v_\Sigma^2. \tag{7.18}$$

The relationship between the g_i and g_U couplings is altered by a term depending on $\epsilon/48\pi^2 \equiv 8yv_\Sigma/M_{Pl}$

$$\left(\frac{1}{g_i^2(\mu_*)}\right)_{\overline{DR}} = \left(\frac{1}{g_U^2(\mu_*)}\right)_{\overline{DR}} - \left(\frac{\lambda_i(\mu_*)-c_i\epsilon}{48\pi^2}\right)_{\overline{DR}} \tag{7.19}$$

where $c_i = \{-2/3, -1,\ 2/3\}$. This allows us to define a further contribution to $\Delta\lambda_{ij}$

$$\Delta\lambda_{ij}^\epsilon = c_i\epsilon - c_j\epsilon \tag{7.20}$$

which can be included along with the contributions from the threshold corrections.

Threshold contributions to $g_i(\mu^*)$ are given in the $\overline{DR}$ scheme by

$$\left(\lambda_i^{Heavy}\right)_{\overline{DR}} = 6\cdot l_{Heavy,i}\ln\frac{\mu_*}{M_{Heavy}} \tag{7.21}$$

where $l_{Heavy,i}$ is the weighted Dynkin index of a heavy particle of mass M_{heavy} for the i-th SM gauge group (the factor of 6 is to obtain the appropriate normalization). We may then write the contributions from the various heavy particles that are not at the unification scale. For the heavy vector bosons, the contributions are

$$\lambda_1^V(\mu_*) = 60\log\frac{\mu_*}{M_V},\quad \lambda_2^V(\mu_*) = 36\log\frac{\mu_*}{M_V},\quad \text{and}\quad \lambda_3^V(\mu_*) = 24\log\frac{\mu_*}{M_V}. \tag{7.22}$$

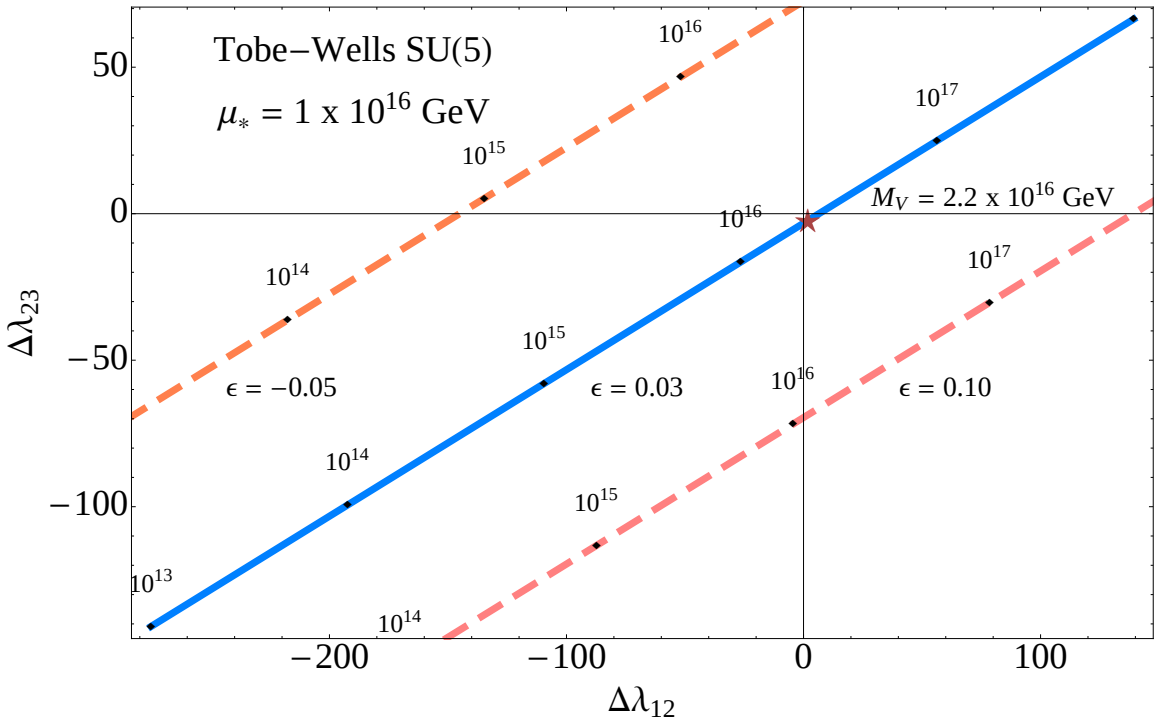

Figure 7.4: Plot of $\Delta\lambda_{23}(\mu_*)$ as a function of $\Delta\lambda_{12}(\mu_*)$ for the CMSSM-like SUSY model. The value of M_{H_c} was fixed to be 3.3×10^{17} GeV, both to ensure coincidence with the CMSSM point, and to ensure avoidance of constraints [9]. Three curves of different ϵ values show the effect of varying that parameter. The ratio M_Σ/M_{H_c} was fixed at 0.1, and then M_V was varied. We find that $M_V = 2.2 \times 10^{16}$ GeV in the Tobe-Wells SU(5) GUT yielded matching of $\Delta\lambda_{ij}(\mu_*)$ to the SM.

Contributions from the heavy colored Higgs H_c are

$$\lambda_1^{H_c}(\mu_*) = -\frac{12}{5}\log\frac{\mu_*}{M_{H_c}}, \quad \lambda_2^{H_c}(\mu_*) = 0, \quad \text{and} \quad \lambda_3^{H_c}(\mu_*) = -6\log\frac{\mu_*}{M_{H_c}}, \tag{7.23}$$

and those from Σ are

$$\lambda_1^{\Sigma}(\mu_*) = 0, \quad \lambda_2^{\Sigma}(\mu_*) = -12\log\frac{\mu_*}{M_\Sigma}, \quad \text{and} \quad \lambda_3^{\Sigma}(\mu_*) = -18\log\frac{\mu_*}{M_\Sigma}. \tag{7.24}$$

The plot for the CMSSM-like SUSY model shown in Fig. 7.4 was made for fixed values of $M_{H_c} = 3.3 \times 10^{17}$ GeV, $M_\Sigma = 0.1 \times M_{H_c}$ and $\epsilon = 0.03$. Then by varying M_V we found the point of intersection of the Tobe-Wells SU(5) $\Delta\lambda_{ij}(\mu_*)$ with the $\Delta\lambda_{ij}(\mu_*)$ from the CMSSM-like IR theory.

The plot for the Split-SUSY-like model shown in Fig. 7.5 was made for fixed values of

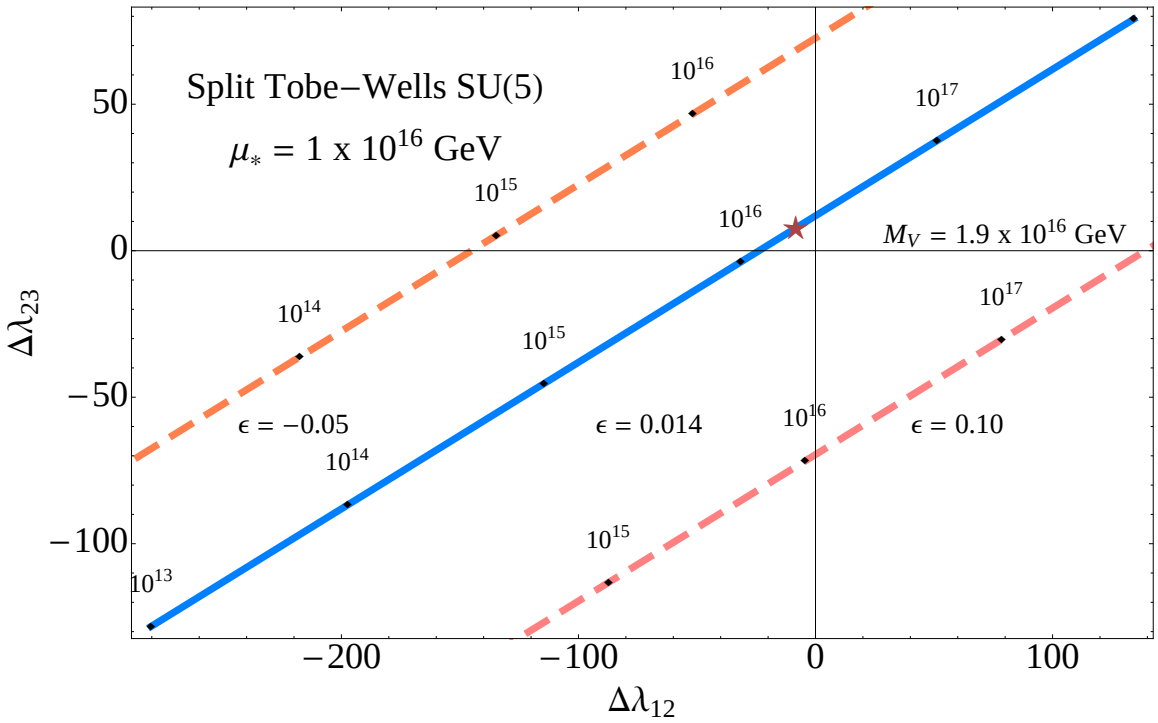

Figure 7.5: Plot of $\Delta\lambda_{23}(\mu_*)$ as a function of $\Delta\lambda_{12}(\mu_*)$ for the Split-SUSY-like model. The value of M_{H_c} was fixed to be 3.3×10^{17} GeV, both to ensure coincidence with the Split-SUSY point, and to ensure avoidance of constraints [9]. Three curves of different ϵ values show the effect of varying that parameter. The ratio M_Σ/M_{H_c} was fixed at 0.1, and then M_V was varied. We find that $M_V = 1.9\times10^{16}$ GeV in the Tobe-Wells SU(5) GUT yielded matching of $\Delta\lambda_{ij}(\mu_*)$ to the SM.

$M_{H_c} = 3.3\times10^{17}$ GeV, $M_\Sigma = 0.1\times M_{H_c}$ and $\epsilon = 0.014$. Then by varying M_V we found the point of intersection of the Tobe-Wells SU(5) $\Delta\lambda_{ij}(\mu_*)$ with the $\Delta\lambda_{ij}(\mu_*)$ from the Split-SUSY-like IR theory. This example again shows how the factorization of the IR data and the UV GUT data can be compared through $\Delta\lambda$ plot visualizations to establish viable exact unification of the gauge couplings.

7.5 Conclusions

In this chapter we have reviewed the technical procedures for determining if a theory is compatible with exact unification of the gauge couplings. For theories with a large desert between the weak scale and the high scale where unification occurs, the problem conveniently factorizes into an analysis of the low-scale theory and the high-scale theory.

We have demonstrated that the data needed from the low-scale theory to make this

assessment is encapsulated well by $\Delta\lambda_{23}$ vs. $\Delta\lambda_{12}$ plots parametrized by the renormalization running scale μ. We have constructed these plots for three different low-scale theories: the SM, a CMSSM-like supersymmetric theory, and a split Supersymmetry theory. The results give us an immediate and intuitive understanding for the scale of gauge coupling unification and the size of corrections (i.e., the indices of high-scale representations) needed to achieve exact unification. They also provide all the information needed technically to perform a careful check of unification.

We have illustrated this approach by matching the data from the SM $\Delta\lambda$ plot to the threshold corrections of the Lavoura-Wolfenstein non-supersymmetric $SO(10)$ theory. It is an example that demonstrates a general result, which is that non-supersymmetric gauge coupling unification is indeed possible without unexpectedly large threshold corrections in grand unified theories based on high-rank gauge group with large representations, such as $SO(10)$.

We also have illustrated the approach by finding a spectrum in the Tobe-Wells $SU(5)$ theory that matches the needed threshold corrections implied by the SM $\Delta\lambda$ plot. This example illustrates the general point that supersymmetric unification requires either very small high-scale threshold corrections, or a partial cancellation of the threshold corrections to achieve exact unification. In the Tobe-Wells case, that cancellation is aided by a non-renormalizable coupling of the Higgs to the gauge kinetic function.

We end by pointing out that any plots of the gauge couplings g_i or $1/g_i$ or even $1/\alpha_i$ are of little value for deciding if a theory is favorable to gauge coupling unification. The $\Delta\lambda$ plot parametrized by the renormalization running scale μ, which can be made for any well defined theory in the IR, is a significantly better way to collect and visualize the necessary data from the low-scale theory to apply to question of high-scale unification. Qualitative understanding of what is required of high-scale thresholds and technical data needed to make the assessment are contained within the $\Delta\lambda$ plot. We also believe that the physically meaningful $\Delta\lambda$ plots also show that when it comes to expected high-scale threshold corrections, unification within a non-supersymmetric theory is just as viable as within a supersymmetric theory. That is to say, unification is attractive in both approaches, and additional considerations are necessary to draw preferences.

In this chapter, we studied a new parameterisation of the unification of gauge couplings into a Grand Unified Theory. We obtained an IR-consistent parameterisation that enables the visualization of gauge coupling unification, which can be applied to a wide range of supersymmetric and non-supersymmetric models.

Chapter 8

Conclusion

In this dissertation, we have studied the phenomenology of supersymmetric models, with an emphasis on models with heavier scalars. We have provided a brief introduction to the Standard Model and Supersymmetry, and shown how the latter is useful for solving numerous unexplained aspects of the former, in Chapter 1. In the same chapter we also motivated why supersymmetric models with heavier scalars were of interest, from taking into account both bottom-up and top-down considerations, such as insight from M-Theory.

We have studied the collider phenomenology of models with heavier scalars in Chapters 2 and 3. In Chapter 2, we have studied the phenomenology of a particular M-Theory compactification on a 7D manifold, and how it would give rise to potential collider signatures at the LHC and a future collider. We found that the relatively light gluinos could potentially be discovered at LHC, but the heavier scalars would be out of reach. In Chapter 3 we studied models with heavier scalars of more general interest, examining how a future 100 TeV proton-proton collider could be used to discover these heavier scalars. We found that a such a collider could discover the valence squarks of spectra similar to the one discussed in Chapter 2. It could also be used to discover heavier electroweakinos in the multi-TeV range.

In Chapters 4 and 5, we studied the flavour and CP phenomenology of various models, and studied the conditions under which low energy experiments could indirectly probe supersymmetric models with slightly heavy scalars. In Chapter 4 we studied CP-conserving models, and found that lepton flavour violation searches can be the strongest probes of supersymmetric models. In Chapter 5 we analysed the same M-Theory compactification as in Chapter 2, and studied how CP violation would show up through non-zero electric dipole moments that are within reach of the next round of experiments.

Finally in Chapters 6 and 7, we analysed more general features of supersymmetric models.

We found that String/M-theory considerations could have important implications for the stability of the lightest visible supersymmetric particle. This finding suggests that Dark Matter may not be in the visible sector, but rather in a hidden sector of a UV theory. In Chapter 7 we studied the conditions for gauge coupling unification to occur in a few different models, including a non-supersymmetric one. We presented a novel way of visualising gauge coupling unification in the presence of threshold corrections near the GUT scale.

Appendix A

Moduli stabilization and SUSY breaking in the G_2-MSSM

In this Appendix, we review the relationship between low energy Supersymmetry and UV dynamics within the G_2-MSSM. This relationship is discussed in [14, 13], and was preceded by a detailed study of dynamical Supersymmetry breaking through moduli stabilization [10, 11]. We will only describe results relevant for our goal of making predictions for Supersymmetric spectra for LHC and future colliders. Interested readers are referred to [18] for a more detailed summary.

In order to stabilize moduli and obtain a de Sitter vacuum, previous studies have assumed the generic presence of an $SU(Q) \times SU(P+1)$ hidden sector, where $SU(Q)$ is pure super Yang-Mills and $SU(P+1)$ is super QCD-like with $N_f = 1$. Non-perturbative effects generate the following superpotential [71, 262] which breaks Supersymmetry and stabilizes all moduli:

$$W = A_1 \phi^{-2/P} \exp ib_1 f_1 + A_2 \exp ib_2 f_2 \tag{A.1}$$

where $2\pi b_1\,(2\pi b_2) = P^{-1}(Q^{-1})$. Here f_1 and f_2 are the gauge kinetic functions of the $SU(Q)$ and $SU(P+1)$ gauge groups, and ϕ is the $SU(P+1)$ meson condensate in Planck units. We assume $f_1 \propto f_2$; otherwise it is difficult to stabilize moduli within the supergravity approximation [11]. For consistency with previous works, we make the simplifying assumption $f_1 = f_2 = f_{vis}$, where f_{vis} is the visible sector gauge kinetic function. We furthermore assume that the visible sector is an $SU(5)$ GUT.

In order to proceed with the moduli stabilization analysis, we use the Kähler potential

derived in [13]:

$$K = -3\log 4\pi^{1/3} V_X + \kappa_{\alpha\beta}\frac{\Phi_\alpha^\dagger \Phi_\beta}{V_X} + \frac{\overline{\phi}\phi}{V_X} + c_{\alpha\beta}\frac{\overline{\phi}\phi}{V_X}\frac{\Phi_\alpha^\dagger \Phi_\beta}{V_X} + ... \tag{A.2}$$

where the volume of the G_2 manifold, V_X, is a homogenous function of the moduli of degree 7/3 [263], Φ, $\Phi^\dagger$ represent visible sector fields, $\kappa_{\alpha\beta}$ is the Kähler metric, and "..." represent higher dimensional operators which are neglected in the analysis.

The term proportional to $c_{\alpha\beta}$ is a higher order correction studied in [13]. It induces flavor changing neutral currents unless the elements of $c_{\alpha\beta}$ are all small, or $c_{\alpha\beta} \sim\propto \kappa_{\alpha\beta}$ up to small corrections. Because scalars are heavy and the tree-level CP phases are rotated away, flavor effects are not expected to cause phenomenogical problems [60]. For simplicity, we assume here that the coefficients of $c_{\alpha\beta}$ are diagonal and universal in the basis where $\kappa_{\alpha\beta}$ is diagonal. Thus we take:

$$c_{\alpha\beta} = \left(\frac{C}{3}\right)\kappa_{\alpha\beta} \tag{A.3}$$

The normalization for C in (A.3) follows that of [13]. We will see that $C \neq 0$ is required for consistent EWSB. Relaxing the assumption taken in (A.3) will induce moderate flavor dependence in the soft breaking parameters, but will not change the gravitino mass or the overall sparticle mass scale.

Given (A.1),(A.2) and (A.3), determining the dynamics of moduli stabilization is straightforward, though rather cumbersome and has been carried out in [13]. The gravitino mass is determined by the standard supergravity relation:

$$M_{3/2} = m_{pl} e^{K/2}\,|W| \approx 0.035\, {V_X}^{-3/2} m_{pl}\,|Q-P|\,\frac{A_2}{Q} e^{-\left(\frac{P_{eff}}{Q-P}\right)}, \quad P_{eff} = \frac{14(3(Q-P)-2)}{3(3(Q-P)-2\sqrt{6(Q-P)})} \tag{A.4}$$

where in the second equality we have fixed moduli at their stabilized values and imposed vanishing vacuum energy [11, 13]. Note that for typical values, $V_X \sim \mathcal{O}(730)$ [13]. Imposing vanishing of the vacuum energy enforces $Q-P \geq 3$, but does not fix $Q-P$ itself. However, from (A.4) we see that for $Q-P \geq 4$, there still exists a large hierarchy between $M_{3/2}$ and the electroweak scale. Thus if a vanishing vacuum energy is imposed, the set of solutions with $Q-P=3$ solves the hierarchy problem. Taking $Q-P=3$ in (A.4) results in:

$$M_{3/2} \approx \frac{9\times 10^5}{V_X^{3/2}}\left(\frac{A_2}{Q}\right)\ \text{TeV}. \tag{A.5}$$

This result was used in Section 2.2.2 to obtain the benchmark value $M_{3/2} \approx 35$ TeV.

Using the standard relations between the Supergravity Lagrangian and soft SUSY breaking parameters [264], it is then straightforward to determine the relation between soft scalar masses, trilinears and $M_{3/2}$, as well as the gaugino masses M_a $(a = 1, 2, 3)$ at the renormalization scale $Q = M_{GUT}$:

$$m_0^2 \approx M_{3/2}^2 \,(1 - C)\,, \;\; A^0 \approx 1.5 M_{3/2}\,(1 - C)\,, \;\; M_a = \frac{e^{K/2} F^i \partial_i f_{vis}}{2i\,\mathrm{Im} f_{vis}} + M_a^{anomaly} \tag{A.6}$$

where m_0 is the universal scalar soft mass, and we haved define trilinears as $\mathcal{L} = -y_{ij} A\, \tilde{Q}_{i,L} H_q \tilde{q}_{j,R}$. We have seperated the tree-level and anomaly-induced [265] contributions to M_a. The tree level contribution to M_a is proportional to the moduli F-terms F_s; moduli stabilization results in $F_s \propto M_{3/2}/V_Q$ where $V_Q \approx 1/\alpha_{GUT}$ is the visible sector 3-cycle volume [14]. Thus, the tree-level gaugino masses are $M_a^{tree} \sim \alpha_{GUT}\; M_{3/2}$, and since the anomaly contribution is loop-suppressed, the two contributions are of comparable size. Such a hierarchy between scalars and gaugino masses has also been observed in other corners of string theory [266, 267], though the physical mechanism may be different.

Including both M_a^{tree} and $M_a^{anomaly}$, the full expression for the gaugino masses upon moduli stabilization is given by [13]:

$$M_a \approx \left[-0.032\eta + \alpha_{GUT}\,(0.034\,(3C_a - C_a') + 0.079 C_a'(1 - C))\right] \times M_{3/2} \tag{A.7}$$

where $C_a = (0, 2, 3)$ and $C_a' = (33/5, 7, 6)$ for $U(1)_Y$, $SU(2)_L$ and $SU(3)_c$ respectively. Here $1 - \eta$ parameterizes threshold corrections to the $SU(5)$ gauge coupling from Kaluza-Klein modes; as discussed in Section 2.2.2, $|1 - \eta| \lesssim 0.1$ is expected for generic compactifications.

Thus taking $\eta \approx 1$, we have shown that top-down constraints from moduli stabilization fix the sparticle spectrum in terms of three almost-calculable constrained quantities: $M_{3/2}$, μ, and C. Note that all SUSY breaking parameters in (A.6), (A.7) are implicitly defined at the renormalisation scale $Q = M_{GUT}$. Given these "high scale" values, one must take into account RG-evolution and other radiative corrections to obtain sparticle pole masses as discussed in Section 2.3.

Appendix B

Constraints from EWSB and M_h

In this appendix, we discuss how both EWSB and with consistency with $M_h = 125.2 \pm 0.4$ GeV are imposed to reduce the dimensionality of the $M_{3/2}, \mu, C$ parameter space. We begin by consider the EWSB conditions, given by:

$$\frac{M_Z^2}{2} = \frac{\overline{m}_{H_d}^2 - \overline{m}_{H_u}^2 \tan^2\beta}{\tan^2\beta - 1} - \mu^2 \tag{B.1}$$

$$B\mu = \frac{1}{2}\sin 2\beta \left(\overline{m}_{H_u}^2 + \overline{m}_{H_d}^2 + 2\mu^2\right) \tag{B.2}$$

where $\overline{m}_{H_u}$ and $\overline{m}_{H_d}$ are the tadpole corrected H_u, H_d soft masses, and all parameters are evaluated at the renormalization scale $Q_{EWSB}^2 = m_{\tilde{t}_1} m_{\tilde{t}_2}$. For the M-theory models we consider, we expect $\mu \lesssim 0.1 M_{3/2}$.

There are two independent arguments for such a suppression of μ with respect to $M_{3/2}$. The first is a top-down argument, which is related to the doublet-triplet splitting mechanism [67] discussed in Section 2.2.2. This mechanism results in a geometric symmetry which forbids the μ term, which is broken by moduli stabilization to generate μ via the Giudice-Masiero mechanism [176]. Thus generically μ is suppressed with respect to $M_{3/2}$ by moduli *vev*'s [17]. This suppression was estimated by [17] to be roughly an order of magnitude, though current theoretical uncertainties preclude a precise estimate. Another argument for $\mu \lesssim 0.1\, M_{3/2}$ is motivated by electroweak naturalness. A measure of fine-tuning in EWSB is the degree to which the two terms on the right hand side of (B.1) are required to cancel in order to obtained the measured value of M_Z. Thus electroweak naturalness favors $\mu^2 \ll M_{3/2}^2$, which mitigates the cancellation in (B.1) required to obtain $M_Z \approx 90$ GeV [69].

In addition to $\mu \lesssim 0.1\, M_{3/2}$, we also expect $0 < \overline{m}_{H_u}^2 \ll \overline{m}_{H_d}^2$, as $m_{H_u}^2$ runs significantly

between $Q = M_{GUT}$ to $Q = Q_{EWSB}$ due to the top Yukawa coupling, while the running of $m^2_{H_d}$ is small for moderate $\tan\beta \lesssim 10$. The lower bound $0 < \overline{m}^2_{H_u}$ is required for consistency with $\mu \lesssim 0.1 M_{3/2}$, as can be seen from (B.1). Taking the $B\mu, \overline{m}^2_{H_d} \gg \mu^2$, $\overline{m}^2_{H_u}$ and $\sin 2\beta \approx 2/\tan\beta$ limit, (B.1) can be written as [69]:

$$\mu^2 \approx \frac{\overline{m}^2_{H_d}}{B^2 - \overline{m}^2_{H_d}} \left(\overline{m}^2_{H_u} + \frac{M_Z^2}{2} \right) \tag{B.3}$$

where $B \approx 2\, M_{3/2}$ at $Q = M_{GUT}$ [14] and $B \approx 1.7 M_{3/2}$ at $Q = Q_{EWSB}$ [69]. Taking $\overline{m}^2_{H_d} \approx m_0^2$ and $\overline{m}^2_{H_u} = M^2_{3/2} f(C)$ where $f(C)$ accounts for the running of m_{H_u} due to the top trilinear A_t, we can recast (B.3) in a more suggestive form:

$$\mu^2 \approx \frac{M^2_{3/2}(1-C)}{B^2 - M^2_{3/2}(1-C)} \left(M^2_{3/2}\, f(C) + \frac{M_Z^2}{2} \right). \tag{B.4}$$

Note that $f(C)$ decreases monotonically as C increases [69]. Thus we have used EWSB conditions to obtain a constraint on the allowed $M_{3/2}, \mu, C$ space; we use one-loop RGE's and one-loop effective potential corrections [268] to compute $f(C)$ for Figure 2.1. In order to minimize large logarithmic corrections, we run α_s and y_t using a 2-step procedure which explicity accounts for the decoupling of squarks at $Q = Q_{EWSB}$.

We now discuss how the constraint on M_h is incoporated in our analysis. The mass of the lightest Higgs boson in the MSSM decoupling limit is given schematically by:

$$M_h^2 = M_Z^2 \cos^2 2\beta + \delta M_h^2 \tag{B.5}$$

where δM_h^2 denotes radiative corrections from both SM and MSSM particles; the value of δM_h^2 is fixed for given values of $M_{3/2}, \mu, C$. We can then use the EWSB condition (B.2) in the $B\mu, \overline{m}^2_{H_d} \gg \mu^2$, $\overline{m}^2_{H_u}$ and $\sin 2\beta \approx 2/\tan\beta$ limit to express $\tan\beta$ in terms $M_{3/2}, C$ and μ:

$$\tan\beta \approx \frac{m_0^2}{B\mu} \approx \frac{M^2_{3/2}(1-C)}{B\mu} \tag{B.6}$$

Thus combining (B.5) and (B.6) with $M_h = 125.2 \pm 0.4$ GeV, we obtain an additional constraint in the $M_{3/2}, \mu, C$ parameter space. To compute M_h for given $M_{3/2}, \mu, C$, we use the "match-and-run" procedure, outlined for example in [49, 50]. Note that some of the authors here made an error in [50] regarding SM radiative corrections to M_h; correcting this error increases M_h by ~ 1.5 GeV. Our calculation here uses 3-loop RGE's and 2-loop

threshold corrections for the matching procedure [52]. From Figure 2.1, we see that the slice of parameter space consistent with $M_h = 125.2 \pm 0.4$ has a non-negligible width. This is due predominantly to experimental uncertanties in M_t, α_s and M_h [50]; more precise measurements of these quantities will sharpen constraints on this parameter space.

Appendix C

Brief introduction to Wilson Lines

In this Appendix, we will briefly introduce the concept of a Wilson Line, and how it applies to symmetry breaking.

A Wilson Line is a quantity defined as the path-ordered exponential of a gauge field:

$$W = \mathrm{Tr}\,\mathcal{P}\mathrm{exp}\left(i \oint A_\mu^a T^a dx^\mu\right) \ , \tag{C.1}$$

where the integral is performed over some closed loop. Those familiar with quantum mechanics will recognise this as being similar to the Ahoronov-Bohm phase [269]:

$$\exp\left(i\frac{e}{\hbar c}\oint \vec{A}\cdot\vec{dx}\right) = \exp\left(i\frac{e\Phi}{\hbar c}\right) \ , \tag{C.2}$$

where Φ is the magnetic flux.

In a theory with a symmetry group G in more than four dimensions, a gauge field in one of the extra dimensions can gain a non-zero expectation value, which breaks the symmetry. In, for example, $SU(5)$ in a 5-dimensional theory, let us consider a gauge field $A_M^a(x_\mu, y)$, where a is the group index, $M = 0, 1, 2, 3, 4, 5$ is the Lorentz index, x_μ is the co-ordinate in the usual four dimensions, and y is the coordinate in the 5th dimension. After decomposition into four dimensions, the fifth component of the gauge field, A_5^a is a 4D scalar that transforms in the adjoint representation.

Let us consider a vacuum configuration which will break the $SU(5)$, where A_5 has a vacuum expectation value along the hypercharge direction. If we take the 5th dimension to be compactified on a circle S_1, then we require periodicity of the gauge transformation on

A_5 under $y \to y + 2\pi R$, where R is the radius of S_1

$$A_5(x_\mu, y) \to A_5(x_\mu, y) + \frac{2n}{R} \ , \quad n \in \mathbb{Z} \tag{C.3}$$

We can make this gauge transformation without changing the boundary conditions on the fields. There are then inequivalent vacua with

$$\langle A_5 \rangle = -\frac{c}{R}, \quad 0 \leq c < 2 \ . \tag{C.4}$$

For $c = 1$, we can evaluate the Wilson line

$$W = \mathrm{diag}(1, 1, 1, -1, -1) \tag{C.5}$$

meaning that the vacuum expectation value of A_5 breaks the $SU(5)$ symmetry down to $SU(3) \times SU(2) \times U(1)$, similarly to in Chapter 7, where the vacuum expectation value of the adjoint Higgs was defined in Eq. 7.17.

Appendix D

Event generation for Chapter 3

Signal events were generated using MADGRAPH5 [81], with showering and hadronization implemented via PYTHIA6.4 [270]. We do not perform MLM for the signal events. We have validated that this is a good approximation by performing MLM with 2 additional jets for a number of benchmark spectra; the cut efficiencies do not significantly differ compared with the unmatched signal events. We use the simulated Snowmass backgrounds [271]. We expect our kinematic cuts to effectively remove any contamination from QCD backgrounds and pileup effects, so we neglect both of these in our analysis. We use the Delphes3.1.2 [272] detector simulator, supplemented by the Snowmass detector card [273] for a $\sqrt{s} = 100$ TeV hadron collider. Production cross sections for squark-gluino associated production are computed at NLO using PROSPINO2 [82]. For squark-Wino/Bino production we use the LO result computed by MADGRAPH5.Event analysis is performed with MadAnalysis5 [274].

Appendix E

Wilson coefficients for $\Delta = 2$ processes

- $x_{\tilde{g}} \simeq 1$

At the SUSY scale defined as $M_{SUSY} = \sqrt{m_{\tilde{g}} \tilde{m}_q}$, the squarks and gluinos are integrated out, and the Wilson coefficients are given by [145]:

$$
\begin{aligned}
C_1(M_{SUSY}) &= \frac{\alpha_s^2(M_{SUSY})}{216\tilde{m}_q^2}\left[(24x f_6(x) + 66\tilde{f}_6(x))\delta_{LL}^2\right], \\
C_2(M_{SUSY}) &= \frac{\alpha_s^2(M_{SUSY})}{216\tilde{m}_q^2}\left[204x f_6(x)\delta_{RL}^2\right], \\
C_3(M_{SUSY}) &= \frac{\alpha_s^2(M_{SUSY})}{216\tilde{m}_q^2}\left[-36\tilde{f}_6(x)\delta_{RL}^2\right], \\
C_4(M_{SUSY}) &= \frac{\alpha_s^2(M_{SUSY})}{216\tilde{m}_q^2}\left[(504x f_6(x) - 72\tilde{f}_6(x))\delta_{LL}\delta_{RR} - 132\tilde{f}_6(x)\delta_{LR}\delta_{RL}\right], \\
C_5(M_{SUSY}) &= \frac{\alpha_s^2(M_{SUSY})}{216\tilde{m}_q^2}\left[(24x f_6(x) + 120\tilde{f}_6(x))\delta_{LL}\delta_{RR} - 180\tilde{f}_6(x)\delta_{LR}\delta_{RL}\right]
\end{aligned}
\tag{E.1}
$$

where the δ_{XY} are mass insertions, and the loop functions $f_6(x)$ and $\tilde{f}_6(s)$ are given by

$$
\begin{aligned}
f_6(x) &= \frac{6(1+3x)\log x + x^3 - 9x^2 - 9x + 17}{6(x-1)^5}, \\
\tilde{f}_6(x) &= \frac{6x(1+x)\log x - x^3 - 9x^2 + 9x + 1}{3(x-1)^5}
\end{aligned}
\tag{E.2}
$$

The $\tilde{C}_i$ are obtained by swapping L $\leftrightarrow$ R everywhere for $i = 1, 2, 3$.

At the hadronic scale, the Wilson coefficients are given by

$$
\begin{aligned}
C_1(\mu_{had}) &= \eta_1 C_1(M_{SUSY}),\\
C_2(\mu_{had}) &= \eta_{22} C_2(M_{SUSY}) + \eta_{23} C_3(M_{SUSY}),\\
C_3(\mu_{had}) &= \eta_{32} C_2(M_{SUSY}) + \eta_{33} C_3(M_{SUSY}),\\
C_4(\mu_{had}) &= \eta_4 C_4(M_{SUSY}) + \frac{1}{3}(\eta_4 - \eta_5) C_5(M_{SUSY}),\\
C_5(\mu_{had}) &= \eta_5 C_5(M_{SUSY})
\end{aligned}
\tag{E.3}
$$

where

$$
\begin{aligned}
\eta_1 &= \left(\frac{\alpha_s(m_c)}{\alpha_s(\mu_{had})}\right)^{6/27} \left(\frac{\alpha_s(m_b)}{\alpha_s(m_c)}\right)^{6/25} \left(\frac{\alpha_s(m_t)}{\alpha_s(m_b)}\right)^{6/23} \left(\frac{\alpha_s(M_{SUSY})}{\alpha_s(m_t)}\right)^{6/21},\\
\eta_{22} &= 0.983\eta_2 + 0.017\eta_3, \quad \eta_{23} = -0.258\eta_2 + 0.258\eta_3,\\
\eta_{32} &= -0.064\eta_2 + 0.064\eta_3, \quad \eta_{33} = 0.017\eta_2 + 0.983\eta_3,\\
\eta_2 &= \eta_1^{-2.42}, \quad \eta_3 = \eta_1^{2.75}, \quad \eta_4 = \eta_1^{-4}, \quad \eta_5 = \eta_1^{1/2}
\end{aligned}
\tag{E.4}
$$

- $x_{\tilde{g}} \ll 1$

In this case one integrates out the squarks at $M_{SUSY} = \tilde{m}_q$, then run down to the gluino mass scale, at which point the gluino is integrated out before running down to the hadronic scale. The Wilson coefficients at the hadronic scale have been computed to be [145]

$$
\begin{aligned}
C_1(\mu_{had}) &= \frac{\alpha_s^2(M_{SUSY})}{216\tilde{m}_q^2}\left[-22\delta_{LL}^2\kappa_1\right],\\
\tilde{C}_1(\mu_{had}) &= \frac{\alpha_s^2(M_{SUSY})}{216\tilde{m}_q^2}\left[-22\delta_{RR}^2\kappa_1\right],\\
C_4(\mu_{had}) &= \frac{\alpha_s^2(M_{SUSY})}{216\tilde{m}_q^2}\left[\delta_{LL}\delta_{RR}\frac{8}{3}(4\kappa_4 + 5\kappa_5) + \delta_{LR}\delta_{RL}(64\kappa_4 - 20\kappa_5)\right],\\
C_5(\mu_{had}) &= \frac{\alpha_s^2(M_{SUSY})}{216\tilde{m}_q^2}\left[\delta_{LL}\delta_{RR}(-40\kappa_5) + \delta_{LR}\delta_{RL}(60\kappa_5)\right]
\end{aligned}
\tag{E.5}
$$

where

$$\kappa_1 = \left(\frac{\alpha_s(m_c)}{\alpha_s(\mu_{had})}\right)^{6/27}\left(\frac{\alpha_s(m_b)}{\alpha_s(m_c)}\right)^{6/25}\left(\frac{\alpha_s(m_t)}{\alpha_s(m_b)}\right)^{6/23}\left(\frac{\alpha_s(m_{\tilde{g}})}{\alpha_s(m_t)}\right)^{6/21}\left(\frac{\alpha_s(\tilde{m}_q)}{\alpha_s(m_{\tilde{g}})}\right)^{6/15},$$
$$\kappa_4 = \kappa_1^{-4}, \quad \kappa_5 = \kappa_1^{1/2} \tag{E.6}$$

Note the power of $\left(\frac{\alpha_s(\tilde{m}_q)}{\alpha_s(m_{\tilde{g}})}\right)$ is 6/15, and not 6/13 as in [145]. This is due to the assumption in [145] that the third generation of squarks would be of a similar mass as the gluino. Removing this assumption changes the beta function coefficient.

- $x_{\tilde{g}} \gg 1$

Contrary to the case where the gluino is considerably lighter than the squarks, in this case the gluino is integrated out first at $m_{\tilde{g}}$, then the squarks are integrated out at $\tilde{m}_q$ before evolving down to the hadronic scale. The Wilson coefficients at the hadronic scale are given by

$$\begin{aligned}
C_1(\mu_{had}) &= \frac{\alpha_s^2(M_{SUSY})}{216\tilde{m}_q^2}\left(4\varepsilon_3^2\eta_1'\right)\delta_{LL}^2,\\
C_2(\mu_{had}) &= \frac{\alpha_s^2(M_{SUSY})}{216\tilde{m}_q^2}\left(\left(\frac{2}{3}(64\varepsilon_1^2-\varepsilon_2^2)-8\varepsilon_3^2\right)\eta_{22}'+(2\varepsilon_2^2-8\varepsilon_3^2)\eta_{23}'\right)\delta_{RL}^2,\\
C_3(\mu_{had}) &= \frac{\alpha_s^2(M_{SUSY})}{216\tilde{m}_q^2}\left(\left(\frac{2}{3}(64\varepsilon_1^2-\varepsilon_2^2)-8\varepsilon_3^2\right)\eta_{32}'+(2\varepsilon_2^2-8\varepsilon_3^2)\eta_{33}'\right)\delta_{RL}^2,\\
C_4(\mu_{had}) &= \frac{\alpha_s^2(M_{SUSY})}{216\tilde{m}_q^2}\left(\frac{4}{3}(64\varepsilon_1^2\eta_4'-\varepsilon_2^2\eta_5')\right)\delta_{LL}\delta_{RR},\\
C_5(\mu_{had}) &= \frac{\alpha_s^2(M_{SUSY})}{216\tilde{m}_q^2}\left(4\varepsilon_2^2\eta_5'\right)\delta_{LL}\delta_{RR}
\end{aligned} \tag{E.7}$$

where η_i' are the same as the η_i in the $x_{\tilde{g}} \simeq 1$ case, and

$$\varepsilon_1 = \left(\frac{\alpha_s(\tilde{m}_q)}{\alpha_s(m_{\tilde{g}})}\right)^{-8/5}, \quad \varepsilon_2 = \varepsilon_1^{7/16}, \quad \varepsilon_3 = \varepsilon_1^{3/8} \tag{E.8}$$

and $\tilde{C}_i$ are given by interchange of L and R for $i = 1, 2, 3$.

Appendix F

Loop functions for $\ell_i \to \ell_j \gamma$

We reproduce here the loop functions for the calculation of the branching ratio of $\ell_i \to \ell_j \gamma$.

$$g_1(x) = \frac{1 + 16x + 7x^2}{(1-x)^4} + \frac{2x(4 + 7x + x^2)}{(1-x)^5} \log x \tag{F.1}$$

$$\begin{aligned} g_2(x,y) = &-\frac{11 + 7(x+y) - 54xy + 11(x^2y + y^2x) + 7x^2y^2}{4(1-x)^3(1-y)^3} \\ &+ \frac{x(2 + 6x + x^2)}{2(1-x)^4(y-x)} \log x + \frac{y(2 + 6y + y^2)}{2(1-y)^4(x-y)} \log y \end{aligned} \tag{F.2}$$

$$\begin{aligned} g_3(x,y) = &-\frac{40 - 33(x+y) + 11(x^2 + y^2) + 7(x^2y + y^2x) - 10xy}{4(1-x)^3(1-y)^3} \\ &+ \frac{2 + 6x + x^2}{2(1-x)^4(y-x)} \log x + \frac{2 + 6y + y^2}{2(1-y)^4(x-y)} \log y \end{aligned} \tag{F.3}$$

$$f_{2n}(x) = \frac{-5x^2 + 4x + 1 + 2x(x+2)\log x}{4(1-x)^4} \tag{F.4}$$

$$f_{2n}(x,y) = f_{2n}(x) - f_{2n}(y) \tag{F.5}$$

$$f_{3n}(x) = \frac{1 + 9x - 9x^2 - x^3 + 6x(x+1)\log x}{3(1-x)^5} \tag{F.6}$$

$$f_{4n}(x) = \frac{-3 - 44x + 36x^2 + 12x^3 - x^4 - 12x(3x+2)\log x}{6(1-x)^6} \tag{F.7}$$

Appendix G

Loop functions and overlap integrals for $\mu \to e$ conversion in nuclei

We reproduce here the loop functions used for the calculation of $\mu \to e$ conversion for convenience:

$$f(x) = \frac{1}{8(1-x)} + \frac{x \log x}{8(1-x)^2}, \tag{G.1}$$

$$\begin{aligned} f_1(x,y) = {} & \frac{x^3(3-9y) + (y-3)y^2 + x^2(3y-1)(1+4y) + xy(y(13-11y)-4)}{2(1-x)^2(1-y)^2(x-y)^2} \\ & + \frac{x(2x^3 + 2y^2 + 3xy(1+y) - x^2(1+9y))}{(1-x)^3(x-y)^3} \log x \\ & + \frac{y^2(y + x(7y-5) - 3x^2)}{(1-y)^3(x-y)^3} \log y, \end{aligned} \tag{G.2}$$

$$\begin{aligned} f_2(x,y) = {} & \frac{x^3(1-3y) + 3(y-3)y^2 + x(y-3)y(y+4) + x^2(y(13-4y)-11)}{2(1-x)^2(1-y)^2(x-y)^2} \\ & + \frac{x(2x^3 + 2y^2 + 3x^2(1+y) - xy(9+y))}{(1-x)^3(y-x)^3} \log x \\ & + \frac{y^2(x^2 + x(7-5y) - 3y)}{(1-y)^3(y-x)^3} \log y, \end{aligned} \tag{G.3}$$

$$\begin{aligned} f_3(x,y) = {} & -\frac{12(x + y + x^2 + y^2 + x^2y + y^2x - 6xy}{(1-x)^2(1-y)^2(x-y)^2} \\ & + \frac{24x(x^2-y)}{(1-x)^3(y-x)^3} \log x + \frac{24y(y^2-x)}{(1-y)^3(x-y)^3} \log y, \end{aligned} \tag{G.4}$$

These loop functions take into account the separation of scale between the gauginos, the $\mu-$term and the scalar masses. Other loop functions used for the calculation of $\mu \to e$ conversion are:

$$f_{\gamma,L}(x) = \frac{1-6x+18x^2-10x^3-3x^4+12x^3\log x}{36(x-1)^5} - \frac{4(7-18x+9x^2+2x^3+(3-9x^2)\log x)}{36(x-1)^5} \tag{G.5}$$

$$f_{\gamma,R}(x) = \frac{1-6x+18x^2-10x^3-3x^4+12x^3\log x}{9(x-1)^5} \tag{G.6}$$

$$\begin{aligned} f_{Z,R}(x,y) = & \frac{x(x(1+2x)+2(x-1)\sqrt{x}\sqrt{y}-(2+x)y)}{(x-1)^3(x-y)^2}\log x \\ & - \frac{y(y(1+2y)+2(y-1)\sqrt{x}\sqrt{y}-(2+y)x)}{(y-1)^3(x-y)^2}\log y \\ & + \frac{y(5+y)+x^2(1+5y)+x(5+y(5y-22))-4\sqrt{x}\sqrt{y}(y-1)(1-x)}{2(x-1)^2(x-y)(y-1)^2} \end{aligned} \tag{G.7}$$

The overlap integrals which appear in Eq. (4.17) were calculated in [160], and are given here for convenience for $^{27}_{13}$Al:

- $D = 0.0357(m_\mu)^{5/2}$,
- $V^{(p)} = 0.0159(m_\mu)^{5/2}$,
- $V^{(n)} = 0.0169(m_\mu)^{5/2}$.

Appendix H

Subdominant operator coefficients and loop functions for $\ell_i \to 3\ell_j$ decays

As discussed in Section 4.3.3, the dipole operators dominate the decay $\ell_i \to 3\ell_j$. Here we list the sub-dominant photo-penguin, box-type and Z-penguin contributions.

The photo-penguin operator coefficients are closely related to those for $\mu \to e$ conversion, and are:

$$A^L_{\gamma-p.} = \frac{-g_2^2}{(4\pi)^2 \tilde{m}_\ell^2} \delta^{\ell_i \ell_j}_{LL} f_{\gamma,L}(x_{\tilde{W}}) \ , \tag{H.1}$$

$$A^R_{\gamma-p.} = \frac{-g_2^2}{(4\pi)^2 \tilde{m}_\ell^2} \delta^{\ell_i \ell_j}_{RR} f_{\gamma,R}(x_{\tilde{B}}) \ , \tag{H.2}$$

where the LH contributions arise dominantly from Wino exchange, while the RH contributions arise from Bino exchange. The loop functions $f_{\gamma,L(R)}$ can be found in Appendix G, and are the same that appeared in the $\mu \to e$ conversion process.

The box-type operator coefficients arise due to neutralino/chargino and slepton exchange, in various configurations. The Higgs-mediated diagrams which contribute to B_2 and B_3 are subdominant in the regime of low to moderate $\tan\beta$ considered here, and thus the dominant coefficients are the $B_1^{L,R}$, given by

$$e^2 B_1^L = \frac{g_2^4}{(4\pi)^2} \delta^{\ell_i \ell_j}_{LL} f_{Box,L}(x_{\tilde{W}}) \ , \tag{H.3}$$

$$e^2 B_1^R = \frac{g_2^4}{(4\pi)^2} \delta^{\ell_i \ell_j}_{RR} f_{Box,R}(x_{\tilde{W}}) \ , \tag{H.4}$$

where the loop functions $f_{Box,L(R)}$ are given below.

The Z-penguin operator coefficients which give rise to $\ell_i \to 3\ell_j$ decays are the following:

$$\begin{aligned} F_{LL} =& \frac{g_2^2}{(4\pi)^2} \frac{1}{4\sin^2\theta_W} \delta_{LL}^{\ell_i\ell_j} \left(-\frac{1}{2} + \sin^2\theta_W \right) \\ & \times \left\{ \cos^2\beta f_1\left(x_{\tilde{W}}, x_\mu\right) + \sin^2\beta f_2\left(x_{\tilde{W}}, x_\mu\right) + \mathrm{sgn}(\mu M_2)\sqrt{x_{\tilde{W}} x_\mu} \sin\beta\cos\beta f_3\left(x_{\tilde{W}}, x_\mu\right) \right\} \ , \end{aligned} \tag{H.5}$$

$$F_{LR} = F_{LL} \times \frac{\sin^2\theta_W}{\left(-\frac{1}{2} + \sin^2\theta_W\right)} \ , \tag{H.6}$$

$$F_{RR} = \frac{g_1^2}{(4\pi)^2 \tilde{m}_\ell^2} \tan^2\theta_W \delta_{RR}^{\ell_i\ell_j} \cos 2\beta f_{Z,R}(x_{\tilde{B}}, x_\mu) \ , \tag{H.7}$$

$$F_{RL} = F_{RR} \times \frac{\left(-\frac{1}{2} + \sin^2\theta_W\right)}{\sin^2\theta_W} \ , \tag{H.8}$$

where the loop functions $f_{1,2,3}$, $f_{Z,R}$ are the same loop functions as in $\mu \to e$ conversion, and are found in Appendix G.

Loop functions which appear in the calculation for $\ell_i \to 3\ell_j$ are:

$$f_{Box,L}(x) = \frac{5 + (4-9x)x + 2x(6+x)\log x}{8(x-1)^3} \tag{H.9}$$

$$f_{Box,R}(x) = \frac{1 + (4-5x)x + 2x(2+x)\log x}{8(x-1)^3} \tag{H.10}$$

Appendix I

Yukawa texture derivations

I.1 Textures where one matrix is diagonal

In the special case where we can rotate to a basis where one of the up or down quark Yukawa matrices is diagonal, the derivation of the other Yukawa matrix is greatly simplified, since $V_{CKM} = (U_u^L)^\dagger U_d^L$ depends on the diagonalisation matrices.

In the case where the down Yukawa matrix is taken to be diagonal, this simplifies to $V_{CKM} = (U_u^L)^\dagger \mathbb{1}_{3\times 3}$. Then since we know that $(U_u^L)^\dagger Y^u (Y^u)^\dagger U_u^L = M_u^2$, where M_u^2 is the diagonal matrix of the quark masses squared, we can solve for Y^u using the expression $Y^u(Y^u)^\dagger = U_u^L M_u^2 (U_u^L)^\dagger$. The expression for this is given below:

$$\begin{aligned} Y^u(Y^u)^\dagger &= \begin{pmatrix} m_u^2 + \epsilon^2 m_c^2 + \epsilon^6 m_t^2 & \epsilon m_u^2 + \epsilon m_c^2 + \epsilon^5 m_t^2 & \epsilon^3 m_u^2 + \epsilon^3 m_c^2 + \epsilon^3 m_t^2 \\ \epsilon m_u^2 + \epsilon m_c^2 + \epsilon^5 m_t^2 & \epsilon^2 m_u^2 + m_c^2 + \epsilon^5 m_t^2 & \epsilon^4 m_u^2 + \epsilon^2 m_c^2 + \epsilon^2 m_t^2 \\ \epsilon^3 m_u^2 + \epsilon^3 m_c^2 + \epsilon^3 m_t^2 & \epsilon^4 m_u^2 + \epsilon^2 m_c^2 + \epsilon^2 m_t^2 & \epsilon^6 m_u^2 + \epsilon^4 m_c^2 + m_t^2 \end{pmatrix} \\ &\approx \begin{pmatrix} \epsilon^{16} + \epsilon^{10} + \epsilon^6 & \epsilon^{17} + \epsilon^9 + \epsilon^5 & \epsilon^{19} + \epsilon^{11} + \epsilon^3 \\ \epsilon^{17} + \epsilon^9 + \epsilon^5 & \epsilon^{18} + \epsilon^8 + \epsilon^4 & \epsilon^{20} + \epsilon^{10} + \epsilon^2 \\ \epsilon^{19} + \epsilon^{11} + \epsilon^3 & \epsilon^{20} + \epsilon^{10} + \epsilon^2 & \epsilon^{22} + \epsilon^{12} + 1 \end{pmatrix} \end{aligned} \tag{I.1}$$

where we have used the approximate hierarchy as described in equation (5.9). We then use the ansatz

$$Y^u = \begin{pmatrix} \epsilon^8 & \epsilon^a & \epsilon^b \\ \epsilon^c & \epsilon^4 & \epsilon^d \\ \epsilon^e & \epsilon^f & 1 \end{pmatrix} \tag{I.2}$$

and solve for $a,\ b,\ c,\ d,\ e,\ f$.

The same analysis can be repeated for the case where the up-type Yukawa matrix is diagonal.

I.2 Minimal matrix derivation

It is of interest to consider what the minimal matrix would be, and whether it is symmetric or not. The only assumption we start with in this derivation is that we know the hierarchy, which is the same as previously, and that the CKM matrix is parameterised by equation (5.7). We know the general structure of the unitary diagonalisation matrices to be

$$U_u^{L,R} = \begin{pmatrix} 1 & \epsilon^i & \epsilon^j \\ \epsilon^i & 1 & \epsilon^k \\ \epsilon^j & \epsilon^k & 1 \end{pmatrix}, \quad U_d^{L,R} = \begin{pmatrix} 1 & \epsilon^x & \epsilon^y \\ \epsilon^x & 1 & \epsilon^z \\ \epsilon^y & \epsilon^z & 1 \end{pmatrix} \tag{I.3}$$

such that

$$V_{CKM} = \begin{pmatrix} 1 & (\epsilon^i + \epsilon^x + \epsilon^{j+z}) & (\epsilon^j + \epsilon^y + \epsilon^{i+z}) \\ (\epsilon^i + \epsilon^x + \epsilon^{j+z}) & 1 & (\epsilon^k + \epsilon^z + \epsilon^{i+y}) \\ (\epsilon^j + \epsilon^y + \epsilon^{i+z}) & (\epsilon^k + \epsilon^z + \epsilon^{i+y}) & 1 \end{pmatrix} \tag{I.4}$$

which leads to the following constraints:

- i, x or $j + z = 1$
- k, z or $i + y = 2$
- j, y or $i + z = 3$

In the subsequent analysis, we assume that the down diagonalisation matrix has the form of the CKM matrix, i.e. $x = 1,\ y = 3,\ z = 2$ in order to have our up type diagonalisation matrix unconstrained, so that to leading order the CKM matrix is satisfied.

We define the following form for the general up type Yukawa matrix

$$Y^u = \begin{pmatrix} \epsilon^8 & \epsilon^l & \epsilon^m \\ \epsilon^n & \epsilon^4 & \epsilon^o \\ \epsilon^p & \epsilon^q & 1 \end{pmatrix} \tag{I.5}$$

such that

$$Y^u Y^{u\dagger} = \begin{pmatrix} (\epsilon^{16} + \epsilon^{2l} + \epsilon^{2m}) & (\epsilon^{4+l} + \epsilon^{8+n} + \epsilon^{m+o}) & (\epsilon^{m} + \epsilon^{8+p} + \epsilon^{l+q}) \\ (\epsilon^{4+l} + \epsilon^{8+n} + \epsilon^{m+o}) & (\epsilon^{8} + \epsilon^{2n} + \epsilon^{2o}) & (\epsilon^{o} + \epsilon^{4+q} + \epsilon^{n+p}) \\ (\epsilon^{m} + \epsilon^{8+p} + \epsilon^{l+q}) & (\epsilon^{o} + \epsilon^{4+q} + \epsilon^{n+p}) & (1 + \epsilon^{2p} + \epsilon^{2q}) \end{pmatrix} \tag{I.6}$$

We derive conditions on the variables by looking at the diagonal components of the diagonalised matrices i) $U_u^{L\dagger} Y^u Y^{u\dagger} U_u^L$, and ii) $U_u^{L\dagger} Y^u U_u^R$. These allow us to determine the minimal up-type Yukawa texture to be:

$$Y^u = \begin{pmatrix} \epsilon^8 & \epsilon^4 & \epsilon^4 \\ \epsilon^4 & \epsilon^4 & \epsilon^2 \\ \epsilon^4 & \epsilon^q & 1 \end{pmatrix} \tag{I.7}$$

with q unconstrained by the diagonalisation and the unitary matrix that diagonalises Y^u is given by

$$U_u^{L,R} = \begin{pmatrix} 1 & \epsilon^4 & \epsilon^4 \\ \epsilon^4 & 1 & \epsilon^4 \\ \epsilon^4 & \epsilon^4 & 1 \end{pmatrix} \tag{I.8}$$

I.3 Explicit chargino diagonalisation expressions

We present here the diagonalisation procedure and results for the Chargino mass matrix with imaginary M_2, but all other entries real.

We do so by solving for V and U given that

$$V X^\dagger X V^{-1} = U^* X X^\dagger U^T = \begin{pmatrix} M_{C_1}^2 & 0 \\ 0 & M_{C_2}^2 \end{pmatrix} \tag{I.9}$$

We parameterise V and U as

$$U, V = \begin{pmatrix} c_{U,V} & t_{U,V} c_{U,V} \\ -t_{U,V}^* c_{U,V} & c_{U,V} \end{pmatrix} \tag{I.10}$$

where $c_i = \cos\theta_i$ and $t_i = \tan\theta_i$, which we solve for.

We give here expressions for $X^\dagger X$ and $X X^\dagger$ in order to simplify our expressions for c_i

and t_i.

$$X^\dagger X \equiv \begin{pmatrix} A_{11} & A_{12} \\ A_{21} & A_{22} \end{pmatrix} = \begin{pmatrix} |M_2|^2 + 2\cos\beta^2 M_W^2 & M_2^* \sqrt{2}\sin\beta M_W + \sqrt{2}\cos\beta M_W \mu \\ M_2\sqrt{2}\sin\beta M_W + \sqrt{2}\cos\beta M_W \mu & 2\sin\beta^2 M_W^2 + \mu^2 \end{pmatrix}$$
$$XX^\dagger \equiv \begin{pmatrix} B_{11} & B_{12} \\ B_{21} & B_{22} \end{pmatrix} = \begin{pmatrix} |M_2|^2 + 2\sin\beta^2 M_W^2 & M_2\sqrt{2}\cos\beta M_W + \sqrt{2}\sin\beta M_W \mu \\ M_2^*\sqrt{2}\cos\beta M_W + \sqrt{2}\sin\beta M_W \mu & 2\cos\beta^2 M_W^2 + \mu^2 \end{pmatrix} \tag{I.11}$$

Then we find that

$$\begin{aligned} t_V &= \frac{(A_{22} - A_{11}) \pm \sqrt{(A_{11} - A_{22})^2 + 4A_{21}A_{12}}}{2A_{21}}, \quad t_V^* = t_{V\, A_{ij} \leftrightarrow A_{ji}} \\ t_U &= \frac{(B_{22} - B_{11}) \pm \sqrt{(B_{11} - B_{22})^2 + 4B_{21}B_{12}}}{2B_{12}}, \quad t_U^* = t_{U\, B_{ij} \leftrightarrow B_{ji}} \end{aligned} \tag{I.12}$$

with $c_i = \frac{1}{\sqrt{1+|t_i|^2}}$. It is noted that $A(B)_{12}$ and $A(B)_{21}$ contain the phase from the trilinears, ϕ_3.

This assignment for the entries of V and U renders X diagonal, with phases in the diagonal components. Since we want our mass eigenvalues to be real, we rotate away the phases, such that our rotation matrices are actually

$$\begin{aligned} U' &= \begin{pmatrix} e^{i\phi_{C1}/2} & 0 \\ 0 & e^{i\phi_{C2}/2} \end{pmatrix} \cdot \begin{pmatrix} c_U & t_U c_U \\ -t_U^* c_U & c_U \end{pmatrix} \\ V' &= \begin{pmatrix} e^{i\phi_{C1}/2} & 0 \\ 0 & e^{i\phi_{C2}/2} \end{pmatrix} \cdot \begin{pmatrix} c_V & t_V c_V \\ -t_V^* c_V & c_V \end{pmatrix} \end{aligned} \tag{I.13}$$

so that $U'^* X V'^{-1} = X^{RD}$ where X^{RD} is real and diagonal.

Appendix J

Contributions to EDMs

J.1 One-loop SUSY contributions to EDMs

In this subsection we present the one-loop SUSY contributions due to the Feynman diagrams in Fig. 5.2. We use the results of Ibrahim and Nath [166].

The electromagnetic contributions to fermion EDMs are as follows

$$
\begin{aligned}
\left(\frac{d_q^{\tilde{g}}}{e}\right)^{(E)} &= \frac{-2\alpha_s}{3\pi}\sum_{k=1}^{2}\mathrm{Im}(\Gamma_q^{1k})\frac{m_{\tilde{g}}}{M^2_{\tilde{q}_k}}Q_{\tilde{q}}\ B\left(\frac{m^2_{\tilde{g}}}{M^2_{\tilde{q}_k}}\right)\\
\left(\frac{d_u^{\chi^\pm}}{e}\right)^{(E)} &= \frac{-\alpha_{EM}}{4\pi\sin^2\theta_W}\sum_{k=1}^{2}\sum_{i=1}^{2}\mathrm{Im}(\Gamma_{uik})\frac{m_{\chi^\pm}}{M^2_{\tilde{d}_k}}\left[Q_{\tilde{d}}\ B\left(\frac{m^2_{\chi^\pm}}{M^2_{\tilde{d}_k}}\right)+(Q_u-Q_{\tilde{d}})\ A\left(\frac{m^2_{\chi^\pm}}{M^2_{\tilde{d}_k}}\right)\right]\\
\left(\frac{d_d^{\chi^\pm}}{e}\right)^{(E)} &= \frac{-\alpha_{EM}}{4\pi\sin^2\theta_W}\sum_{k=1}^{2}\sum_{i=1}^{2}\mathrm{Im}(\Gamma_{dik})\frac{m_{\chi^\pm}}{M^2_{\tilde{u}_k}}\left[Q_{\tilde{u}}\ B\left(\frac{m^2_{\chi^\pm}}{M^2_{\tilde{u}_k}}\right)+(Q_d-Q_{\tilde{u}})\ A\left(\frac{m^2_{\chi^\pm}}{M^2_{\tilde{u}_k}}\right)\right]\\
\left(\frac{d_e^{\chi^\pm}}{e}\right)^{(E)} &= \frac{\alpha_{EM}}{4\pi\sin^2\theta_W}\sum_{i=1}^{2}\mathrm{Im}(\Gamma_{ei})\frac{m_{\chi^\pm}}{m^2_{\tilde{\nu}}}\ A\left(\frac{m^2_{\chi^\pm}}{m^2_{\tilde{\nu}}}\right)\\
\left(\frac{d_f^{\chi^0}}{e}\right)^{(E)} &= \frac{\alpha_{EM}}{4\pi\sin^2\theta_W}\sum_{k=1}^{2}\sum_{i=1}^{4}\mathrm{Im}(\eta_{fik})\frac{m_{\chi^0}}{M^2_{\tilde{f}_k}}Q_{\tilde{f}}\ B\left(\frac{m^2_{\chi^0}}{M^2_{\tilde{f}_k}}\right)
\end{aligned}
\tag{J.1}
$$

where

$$
\Gamma_q^{1k} = e^{-i\phi_3}D_{q2k}D^*_{q1k} \tag{J.2}
$$

with ϕ_3 being the gluino phase, which in our theory can be rotated away, and D_q defined as $D_q^\dagger M_{\tilde{q}}^2 D_q = \mathrm{diag}(M_{\tilde{q}_1}^2, M_{\tilde{q}_2}^2)$. With the sfermion mass matrix $M_{\tilde{f}}^2$ given by

$$M_{\tilde{f}}^2 = \begin{pmatrix} M_L^2 + m_f^2 + M_z^2(\frac{1}{2} - Q_f \sin^2\theta_W)\cos 2\beta & m_f(A_f^* - \mu R_f) \\ m_f(A_f - \mu^* R_f) & M_R^2 + m_f^2 + M_z^2 Q_f \sin^2\theta_W \cos 2\beta \end{pmatrix} \quad \text{(J.3)}$$

where $R_f = \cot\beta$ $(\tan\beta)$ for $I_3 = 1/2$ $(-1/2)$. The chargino vertices are given by

$$\begin{aligned} \Gamma_{uik} &= \kappa_u V_{i2}^* D_{d1k} (U_{i1}^* D_{d1k}^* - \kappa_d U_{i2}^* D_{d2k}^*) \\ \Gamma_{dik} &= \kappa_d U_{i2}^* D_{u1k} (V_{i1}^* D_{u1k}^* - \kappa_u V_{i2}^* D_{u2k}^*) \end{aligned} \quad \text{(J.4)}$$

and

$$\Gamma_{ei} = (\kappa_e U_{i2}^* V_{i1}^*) \quad \text{(J.5)}$$

where in each case κ_f is the Yukawa coupling, defined as $\kappa_u = \frac{m_u}{\sqrt{2} m_W \sin\beta}$ and $\kappa_{d,e} = \frac{m_{d,e}}{\sqrt{2} m_W \cos\beta}$, and U and V are the unitary matrices diagonalizing the chargino mass matrix. The neutralino vertex is defined as

$$\begin{aligned} \eta_{fik} = &\left[-\sqrt{2}\{\tan\theta_W (Q_f - I_{3_f}) X_{1i} + I_{3_f} X_{2i}\} D_{f1k}^* - \kappa_f X_{bi} D_{f2k}^* \right] \\ &\times \left[\sqrt{2} \tan\theta_W Q_f X_{1i} D_{f2k} - \kappa_f X_{bi} D_{f1k} \right] \end{aligned} \quad \text{(J.6)}$$

with $b = 3$ (4) for $I_3 = -1/2$ (1/2), and X being the unitary matrix diagonalizing the neutralino mass matrix. The CEDM contributions are given by

$$\begin{aligned} d_q^{\tilde{g}\ (C)} &= \frac{g_s \alpha_s}{4\pi} \sum_{k=1}^{2} \mathrm{Im}(\Gamma_q^{1k}) \frac{m_{\tilde{g}}}{M_{\tilde{q}_k}^2} C\left(\frac{m_{\tilde{g}}^2}{M_{\tilde{q}_k}^2}\right) \\ d_q^{\tilde{\chi}^\pm\ (C)} &= \frac{-g^2 g_s}{16\pi^2} \sum_{k=1}^{2} \sum_{i=1}^{2} \mathrm{Im}(\Gamma_{qik}) \frac{m_{\tilde{\chi}_i^\pm}}{M_{\tilde{q}_k}^2} B\left(\frac{m_{\tilde{\chi}_i^\pm}^2}{M_{\tilde{q}_k}^2}\right) \\ d_q^{\tilde{\chi}^0\ (C)} &= \frac{g^2 g_s}{16\pi^2} \sum_{k=1}^{2} \sum_{i=1}^{4} \mathrm{Im}(\eta_{qik}) \frac{m_{\tilde{\chi}_i^0}}{M_{\tilde{q}_k}^2} B\left(\frac{m_{\tilde{\chi}_i^0}^2}{M_{\tilde{q}_k}^2}\right) \end{aligned} \quad \text{(J.7)}$$

And the dimension-6 Weinberg operator gives a contribution

$$d^G = -3\alpha_s m_t \left(\frac{g_s}{4\pi}\right)^3 \mathrm{Im}(\Gamma_t^{12}) \frac{z_1 - z_2}{m_{\tilde{g}}^3} H(z_1, z_2, z_3) + (t \to b) \quad \text{(J.8)}$$

with $z_i = \left(\frac{M_{\tilde{t}_i}}{m_{\tilde{g}}}\right)^2$, and $z_t = \left(\frac{m_t}{m_{\tilde{g}}}\right)^2$, with the two-loop function $H(z_1, z_2, z_t)$ being given by

$$H(z_1, z_2, z_t) = \frac{1}{2}\int_0^1 dx \int_0^1 du \int_0^1 dy x(1-x)u\frac{N_1 N_2}{D^4} \tag{J.9}$$

where

$$\begin{aligned} N_1 &= u(1-x) + z_t x(1-x)(1-u) - 2ux[z_1 y + z_2(1-y)] \\ N_2 &= (1-x)^2(1-u)^2 + u^2 - \frac{1}{9}x^2(1-u)^2 \\ D &= u(1-x) + z_t x(1-x)(1-u) + ux[z_1 y + z_2(1-y)] \end{aligned} \tag{J.10}$$

However, for the purpose of this analysis in this framework, the contribution from this two-loop effect is negligible, so it will not be calculated. Thus recording these equations is merely for book-keeping purposes. We consider other two-loop effects which give larger contributions in the text. Another two-loop effect is from the Barr-Zee diagram with scalars in a loop, which is treated in the next subsection.

The functions $A(r),\ B(r)$ and $C(r)$ used in the equations above are the one-loop functions, and are given by

$$\begin{aligned} A(r) &= \frac{1}{2(1-r)^2}\left(3 - r + \frac{2\ln r}{1-r}\right) \\ B(r) &= \frac{1}{2(r-1)^2}\left(1 + r + \frac{2r\ln r}{1-r}\right) \\ C(r) &= \frac{1}{6(r-1)^2}\left(10r - 26 + \frac{2r\ln r}{1-r} - \frac{18\ln r}{1-r}\right) \end{aligned} \tag{J.11}$$

The above equations are rather intractable, and in fact a number of approximations can be utilized to simplify the calculation. For example, for the neutron and mercury, the quark CEDM contributions are much larger than the quark EDM contributions (as seen in [15]), so let us take the example of the dominant gluino contribution, $d_q^{\tilde{g}\ (C)}$. Expanding the relevant line in equation (J.7), and defining $r_i = \frac{m_{\tilde{g}}^2}{m_{\tilde{q}_i}^2}$, we find that

$$d_q^{\tilde{g}\ (C)} = \frac{g_s \alpha_s}{4\pi}\left[\mathrm{Im}(\Gamma_q^{11})\frac{m_{\tilde{g}}}{m_{\tilde{q}_1}^2}C(r_1) - \mathrm{Im}(\Gamma_q^{12})\frac{m_{\tilde{g}}}{m_{\tilde{q}_2}^2}C(r_2)\right] \tag{J.12}$$

But since $\Gamma_q^{11} = -\Gamma_q^{12}$, we can then simplify this further. Also $m_{\tilde{q}_i}^2 = m_{\tilde{q}}^2 \pm \Delta_m$, where $\Delta_m = (m_{\tilde{q}}^2)_{LR}$, i.e. it is the contribution from the off-diagonal components of the squark

mass matrix. We will utilize the assumption that since we are interested in the first generation squarks, the mass splitting is small compared to the squark mass.

This allows us to expand the various factors and functions above and simplify (J.12) to the following form

$$d_q^{\tilde{g}\ (C)} \approx \frac{g_s \alpha_s}{4\pi} \frac{\mathrm{Im}(m_{\tilde{q}}^2)_{LR}}{m_{\tilde{g}}^3} r^2 \left[C(r) + rC^{'}(r) \right] \tag{J.13}$$

as was found in [15].

For the electron EDM, there are a few things we notice which simplify the calculation. The chargino component depends on $\mathrm{Im}(\Gamma_{ei})$, which is zero in the framework considered due to the absence of CP-violating phases in the chargino sector when the trilinears and Yukawas are aligned. Thus only the neutralino diagrams contribute. If we assume no mixing, by a similar analysis to the one performed for the gluino contribution to the quark CEDM, we find that the result for the electron is given by

$$d_e^E \approx \frac{e\alpha_{EM}}{4\pi \cos^2\theta_W} \frac{\mathrm{Im}(m_{\tilde{e}}^2)_{LR}}{m_{\tilde{B}}^3} r^2 \left[B(r_1) + r_1 B^{'}(r_1) \right] \tag{J.14}$$

J.2 Barr-Zee diagram contributions

In general, Barr-Zee type diagrams can involve squarks, charginos or neutralinos in the inner loop, with gauge bosons and or higgs bosons in the outer loop. The two-loop diagrams when the Trilinears are not aligned with the Yukawas are considered above. So here we present the two-loop results when they are aligned. In this case, since the only phases come from the Yukawa sector, we need only consider the diagrams with squarks running in the inner loop. We are particularly interested in diagrams with third generation squarks, $\tilde{t}$ and $\tilde{b}$ running in the inner loop, since they are lighter and are not suppressed by factors of ϵ. The general EDM and CEDM contributions are given by

$$\begin{aligned} \left(\frac{d_f^E}{e}\right) &= Q_f \frac{3\alpha_{em}}{32\pi^3} \frac{R_f m_f}{M_A^2} \sum_{q=t,b} \xi_q Q_q^2 \left[F\left(\frac{M_{\tilde{q}_1}^2}{M_A^2}\right) - F\left(\frac{M_{\tilde{q}_2}^2}{M_A^2}\right) \right] \\ d_f^C &= \frac{g_s \alpha_s}{64\pi^3} \frac{R_f m_f}{M_A^2} \sum_{q=t,b} \xi_q \left[F\left(\frac{M_{\tilde{q}_1}^2}{M_A^2}\right) - F\left(\frac{M_{\tilde{q}_2}^2}{M_A^2}\right) \right] \end{aligned} \tag{J.15}$$

where M_A is the mass of the pseudoscalar Higgs boson A_0, and $R_f = \cot\beta$ $(\tan\beta)$ for $I_3 = 1/2$ $(-1/2)$ and $F(r)$ is the two-loop function defined as

$$F(r) = \int_0^1 dx \frac{x(1-x)}{r - x(1-x)} \ln\left[\frac{x(1-x)}{r}\right] \tag{J.16}$$

The CP-violating couplings are $\xi_{t,b}$, defined as

$$\begin{aligned} \xi_t &= -\frac{\sin 2\theta_{\tilde{t}} m_t \operatorname{Im}(\mu e^{i\delta_t})}{2v^2 \sin^2\beta} \\ \xi_b &= -\frac{\sin 2\theta_{\tilde{b}} m_b \operatorname{Im}(A_b e^{-i\delta_b})}{2v^2 \sin\beta\cos\beta} \end{aligned} \tag{J.17}$$

where one should be careful to note that $v = 246/\sqrt{2}$ GeV, and the minus signs are chosen by convention, differing from [167] and the associated erratum. The variables $\theta_{\tilde{t},\tilde{b}}$ are the stop and sbottom mixing angles, and $\delta_q = \arg(A_q + R_q\mu^*)$. The squark sector mixing angle is defined as

$$\begin{aligned} \tan(2\theta_q) &= -\frac{2m_q|\mu R_q + A_q^*|}{M_{\tilde{Q}}^2 - M_{\tilde{q}}^2 + \cos 2\beta M_Z^2 (T_z^q - 2e_q s_w^2)} \\ &\approx -\frac{2m_q|\mu R_q + A_q^*|}{M_{\tilde{Q}}^2 - M_{\tilde{q}}^2} \end{aligned} \tag{J.18}$$

such that we can rewrite the CP-violating couplings given in (J.17) as

$$\begin{aligned} \xi_t &\approx \frac{y_t^2|A_t^* + \mu\cot\beta|\operatorname{Im}(\mu e^{i\delta_t})}{M_{\tilde{Q}}^2 - M_{\tilde{t}}^2} \\ \xi_b &\approx \cot\beta \frac{y_b^2|A_b^* + \mu\tan\beta|\operatorname{Im}(A_b e^{i\delta_b})}{M_{\tilde{Q}}^2 - M_{\tilde{b}}^2} \end{aligned} \tag{J.19}$$

which can then be used to simplify (J.15) such that it reads

$$\left(\frac{d_f^E}{e}\right) = Q_f \frac{3\alpha_{em}}{32\pi^3}\frac{R_f m_f}{M_A^4}\,\mathrm{Im}\left[\frac{4y_t^2}{9}\mu(A_t+\mu^*\cot\beta)F'\left(\frac{M_{\tilde{q}_1}^2}{M_A^2}\right)+\frac{y_b^2}{9}A_b(A_b^*+\mu\tan\beta)\cot\beta F'\left(\frac{M_{\tilde{q}_2}^2}{M_A^2}\right)\right]$$
$$d_f^C = \frac{g_s\alpha_s}{64\pi^3}\frac{R_f m_f}{M_A^4}\,\mathrm{Im}\left[y_t^2\mu(A_t+\mu^*\cot\beta)F'\left(\frac{M_{\tilde{q}_1}^2}{M_A^2}\right)+y_b^2 A_b(A_b^*+\mu\tan\beta)\cot\beta F'\left(\frac{M_{\tilde{q}_2}^2}{M_A^2}\right)\right] \tag{J.20}$$

where in (J.19) above, $m_{\tilde{t},\tilde{b}}$ are the average masses of the stops and sbottoms respectively. In the above equations, the mass of the CP-odd Higgs mass is given by

$$M_A^2 = m_{H_u}^2 + m_{H_d}^2 + 2|\mu|^2 \tag{J.21}$$

where the first two contributions are considerably larger than that of μ, but we include the μ term for completeness.

Barr-Zee contributions turn out to be very small, and are therefore not included in our final computation of d_e.

Bibliography

[1] Z. Bai, N. H. Christ, T. Izubuchi, C. T. Sachrajda, A. Soni, and J. Yu, "$K_L - K_S$ Mass Difference from Lattice QCD," *Phys. Rev. Lett.*, vol. 113, p. 112003, 2014.

[2] N. Arkani-Hamed, S. Dimopoulos, G. F. Giudice, and A. Romanino, "Aspects of split supersymmetry," *Nucl. Phys.*, vol. B709, pp. 3–46, 2005.

[3] G. F. Giudice and A. Romanino, "Electric dipole moments in split supersymmetry," *Phys. Lett.*, vol. B634, pp. 307–314, 2006.

[4] M. Pospelov and A. Ritz, "Electric dipole moments as probes of new physics," *Annals Phys.*, vol. 318, pp. 119–169, 2005.

[5] J. Baron *et al.*, "Order of Magnitude Smaller Limit on the Electric Dipole Moment of the Electron," *Science*, vol. 343, pp. 269–272, 2014.

[6] C. A. Baker *et al.*, "An Improved experimental limit on the electric dipole moment of the neutron," *Phys. Rev. Lett.*, vol. 97, p. 131801, 2006.

[7] W. C. Griffith, M. D. Swallows, T. H. Loftus, M. V. Romalis, B. R. Heckel, and E. N. Fortson, "Improved Limit on the Permanent Electric Dipole Moment of Hg-199," *Phys. Rev. Lett.*, vol. 102, p. 101601, 2009.

[8] B. C. Allanach, "SOFTSUSY: a program for calculating supersymmetric spectra," *Comput. Phys. Commun.*, vol. 143, pp. 305–331, 2002.

[9] H. Murayama and A. Pierce, "Not even decoupling can save minimal supersymmetric SU(5)," *Phys. Rev.*, vol. D65, p. 055009, 2002.

[10] B. S. Acharya, K. Bobkov, G. Kane, P. Kumar, and D. Vaman, "An M theory Solution to the Hierarchy Problem," *Phys. Rev. Lett.*, vol. 97, p. 191601, 2006.

[11] B. S. Acharya, K. Bobkov, G. L. Kane, P. Kumar, and J. Shao, "Explaining the Electroweak Scale and Stabilizing Moduli in M Theory," *Phys. Rev.*, vol. D76, p. 126010, 2007.

[12] B. S. Acharya, P. Kumar, K. Bobkov, G. Kane, J. Shao, and S. Watson, "Non-thermal Dark Matter and the Moduli Problem in String Frameworks," *JHEP*, vol. 06, p. 064, 2008.

[13] B. S. Acharya and K. Bobkov, "Kahler Independence of the G(2)-MSSM," *JHEP*, vol. 09, p. 001, 2010.

[14] B. S. Acharya, K. Bobkov, G. L. Kane, J. Shao, and P. Kumar, "The G(2)-MSSM: An M Theory motivated model of Particle Physics," *Phys. Rev.*, vol. D78, p. 065038, 2008.

[15] G. Kane, P. Kumar, and J. Shao, "CP-violating Phases in M-theory and Implications for EDMs," *Phys. Rev.*, vol. D82, p. 055005, 2010.

[16] B. S. Acharya, G. Kane, and E. Kuflik, "Bounds on scalar masses in theories of moduli stabilization," *Int. J. Mod. Phys.*, vol. A29, p. 1450073, 2014.

[17] B. S. Acharya, G. Kane, E. Kuflik, and R. Lu, "Theory and Phenomenology of μ in M theory," *JHEP*, vol. 05, p. 033, 2011.

[18] B. S. Acharya, G. Kane, and P. Kumar, "Compactified String Theories – Generic Predictions for Particle Physics," *Int. J. Mod. Phys.*, vol. A27, p. 1230012, 2012.

[19] S. A. R. Ellis, G. L. Kane, and B. Zheng, "Superpartners at LHC and Future Colliders: Predictions from Constrained Compactified M-Theory," *JHEP*, vol. 07, p. 081, 2015.

[20] S. A. R. Ellis and G. L. Kane, "Theoretical Prediction and Impact of Fundamental Electric Dipole Moments," *JHEP*, vol. 01, p. 077, 2016.

[21] S. A. R. Ellis and B. Zheng, "Reaching for squarks and gauginos at a 100 TeV p-p collider," *Phys. Rev.*, vol. D92, no. 7, p. 075034, 2015.

[22] S. A. R. Ellis and A. Pierce, "Impact of Future Lepton Flavor Violation Measurements in the Minimal Supersymmetric Standard Model," *Phys. Rev.*, vol. D94, no. 1, p. 015014, 2016.

[23] B. S. Acharya, S. A. R. Ellis, G. L. Kane, B. D. Nelson, and M. J. Perry, "The lightest visible-sector supersymmetric particle is likely to be unstable," *Phys. Rev. Lett.*, vol. 117, p. 181802, 2016.

[24] S. A. R. Ellis and J. D. Wells, "Visualizing gauge unification with high-scale thresholds," *Phys. Rev.*, vol. D91, no. 7, p. 075016, 2015.

[25] G. Aad *et al.*, "Observation of a new particle in the search for the Standard Model Higgs boson with the ATLAS detector at the LHC," *Phys. Lett.*, vol. B716, pp. 1–29, 2013.

[26] S. Chatrchyan *et al.*, "Observation of a new boson at a mass of 125 GeV with the CMS experiment at the LHC," *Phys. Lett.*, vol. B716, pp. 30–61, 2012.

[27] S. Willenbrock, "Symmetries of the standard model," in *Physics in $D \geq 4$. Proceedings, Theoretical Advanced Study Institute in elementary particle physics, TASI 2004, Boulder, USA, June 6-July 2, 2004*, pp. 3–38, 2004.

[28] G. Aad *et al.*, "Measurement of the Higgs boson mass from the $H \to \gamma\gamma$ and $H \to ZZ^* \to 4\ell$ channels with the ATLAS detector using 25 fb^{-1} of pp collision data," *Phys. Rev.*, vol. D90, no. 5, p. 052004, 2014.

[29] S. R. Coleman and J. Mandula, "All Possible Symmetries of the S Matrix," *Phys. Rev.*, vol. 159, pp. 1251–1256, 1967.

[30] R. Haag, J. T. Lopuszanski, and M. Sohnius, "All Possible Generators of Supersymmetries of the s Matrix," *Nucl. Phys.*, vol. B88, p. 257, 1975.

[31] M. E. Peskin and D. V. Schroeder, *An Introduction to quantum field theory*. 1995.

[32] S. P. Martin, "A Supersymmetry primer," 1997. [Adv. Ser. Direct. High Energy Phys.18,1(1998)].

[33] J. Terning, *Modern supersymmetry: Dynamics and duality*. 2006.

[34] H. P. Nilles, "Supersymmetry, Supergravity and Particle Physics," *Phys. Rept.*, vol. 110, pp. 1–162, 1984.

[35] H. E. Haber and G. L. Kane, "The Search for Supersymmetry: Probing Physics Beyond the Standard Model," *Phys. Rept.*, vol. 117, pp. 75–263, 1985.

[36] A. H. Chamseddine, R. L. Arnowitt, and P. Nath, "Locally Supersymmetric Grand Unification," *Phys. Rev. Lett.*, vol. 49, p. 970, 1982.

[37] L. J. Hall, J. D. Lykken, and S. Weinberg, "Supergravity as the Messenger of Supersymmetry Breaking," *Phys. Rev.*, vol. D27, pp. 2359–2378, 1983.

[38] J. R. Ellis, D. V. Nanopoulos, and K. Tamvakis, "Grand Unification in Simple Supergravity," *Phys. Lett.*, vol. B121, pp. 123–129, 1983.

[39] L. Alvarez-Gaume, J. Polchinski, and M. B. Wise, "Minimal Low-Energy Supergravity," *Nucl. Phys.*, vol. B221, p. 495, 1983.

[40] A. B. Lahanas and D. V. Nanopoulos, "The Road to No Scale Supergravity," *Phys. Rept.*, vol. 145, p. 1, 1987.

[41] M. Dine and W. Fischler, "A Phenomenological Model of Particle Physics Based on Supersymmetry," *Phys. Lett.*, vol. B110, pp. 227–231, 1982.

[42] C. R. Nappi and B. A. Ovrut, "Supersymmetric Extension of the SU(3) x SU(2) x U(1) Model," *Phys. Lett.*, vol. B113, pp. 175–179, 1982.

[43] L. Alvarez-Gaume, M. Claudson, and M. B. Wise, "Low-Energy Supersymmetry," *Nucl. Phys.*, vol. B207, p. 96, 1982.

[44] E. A. Mirabelli and M. E. Peskin, "Transmission of supersymmetry breaking from a four-dimensional boundary," *Phys. Rev.*, vol. D58, p. 065002, 1998.

[45] D. E. Kaplan, G. D. Kribs, and M. Schmaltz, "Supersymmetry breaking through transparent extra dimensions," *Phys. Rev.*, vol. D62, p. 035010, 2000.

[46] Z. Chacko, M. A. Luty, A. E. Nelson, and E. Ponton, "Gaugino mediated supersymmetry breaking," *JHEP*, vol. 01, p. 003, 2000.

[47] L. Randall and R. Sundrum, "Out of this world supersymmetry breaking," *Nucl. Phys.*, vol. B557, pp. 79–118, 1999.

[48] G. F. Giudice, M. A. Luty, H. Murayama, and R. Rattazzi, "Gaugino mass without singlets," *JHEP*, vol. 12, p. 027, 1998.

[49] G. F. Giudice and A. Strumia, "Probing High-Scale and Split Supersymmetry with Higgs Mass Measurements," *Nucl. Phys.*, vol. B858, pp. 63–83, 2012.

[50] G. Kane, P. Kumar, R. Lu, and B. Zheng, "Higgs Mass Prediction for Realistic String/M Theory Vacua," *Phys. Rev.*, vol. D85, p. 075026, 2012.

[51] A. Arvanitaki, N. Craig, S. Dimopoulos, and G. Villadoro, "Mini-Split," *JHEP*, vol. 02, p. 126, 2013.

[52] P. Draper, G. Lee, and C. E. M. Wagner, "Precise estimates of the Higgs mass in heavy supersymmetry," *Phys. Rev.*, vol. D89, no. 5, p. 055023, 2014.

[53] E. Bagnaschi, G. F. Giudice, P. Slavich, and A. Strumia, "Higgs Mass and Unnatural Supersymmetry," *JHEP*, vol. 09, p. 092, 2014.

[54] T. Golling *et al.*, "Physics at a 100 TeV pp collider: beyond the Standard Model phenomena," *Submitted to: Phys. Rept.*, 2016.

[55] G. Papadopoulos and P. K. Townsend, "Compactification of D = 11 supergravity on spaces of exceptional holonomy," *Phys. Lett.*, vol. B357, pp. 300–306, 1995.

[56] B. S. Acharya, "M theory, Joyce orbifolds and superYang-Mills," *Adv. Theor. Math. Phys.*, vol. 3, pp. 227–248, 1999.

[57] B. S. Acharya, "On Realizing N=1 superYang-Mills in M theory," 2000.

[58] M. Atiyah and E. Witten, "M theory dynamics on a manifold of G(2) holonomy," *Adv. Theor. Math. Phys.*, vol. 6, pp. 1–106, 2003.

[59] B. S. Acharya and E. Witten, "Chiral fermions from manifolds of G(2) holonomy," 2001.

[60] K. Kadota, G. Kane, J. Kersten, and L. Velasco-Sevilla, "Flavour Issues for String-Motivated Heavy Scalar Spectra with a low Gluino Mass: the G2-MSSM Case," *Eur. Phys. J.*, vol. C72, p. 2004, 2012.

[61] B. S. Acharya, K. Bobkov, and P. Kumar, "An M Theory Solution to the Strong CP Problem and Constraints on the Axiverse," *JHEP*, vol. 11, p. 105, 2010.

[62] G. Kane, J. Shao, S. Watson, and H.-B. Yu, "The Baryon-Dark Matter Ratio Via Moduli Decay After Affleck-Dine Baryogenesis," *JCAP*, vol. 1111, p. 012, 2011.

[63] B. S. Acharya, G. L. Kane, P. Kumar, R. Lu, and B. Zheng, "R-Parity Conservation from a Top Down Perspective," *JHEP*, vol. 10, p. 1, 2014.

[64] G. L. Kane, P. Kumar, B. D. Nelson, and B. Zheng, "Dark matter production mechanisms with a nonthermal cosmological history: A classification," *Phys. Rev.*, vol. D93, no. 6, p. 063527, 2016.

[65] J. Fan and M. Reece, "In Wino Veritas? Indirect Searches Shed Light on Neutralino Dark Matter," *JHEP*, vol. 10, p. 124, 2013.

[66] T. Cohen, M. Lisanti, A. Pierce, and T. R. Slatyer, "Wino Dark Matter Under Siege," *JCAP*, vol. 1310, p. 061, 2013.

[67] E. Witten, "Deconstruction, G(2) holonomy, and doublet triplet splitting," in *Supersymmetry and unification of fundamental interactions. Proceedings, 10th International Conference, SUSY'02, Hamburg, Germany, June 17-23, 2002*, pp. 472–491, 2001.

[68] C. Collaboration, "Precise determination of the mass of the Higgs boson and studies of the compatibility of its couplings with the standard model," 2014.

[69] D. Feldman, G. Kane, E. Kuflik, and R. Lu, "A new (string motivated) approach to the little hierarchy problem," *Phys. Lett.*, vol. B704, pp. 56–61, 2011.

[70] T. Friedmann and E. Witten, "Unification scale, proton decay, and manifolds of G(2) holonomy," *Adv. Theor. Math. Phys.*, vol. 7, no. 4, pp. 577–617, 2003.

[71] I. Affleck, M. Dine, and N. Seiberg, "Dynamical Supersymmetry Breaking in Supersymmetric QCD," *Nucl. Phys.*, vol. B241, pp. 493–534, 1984.

[72] D. Finnell and P. Pouliot, "Instanton calculations versus exact results in four-dimensional SUSY gauge theories," *Nucl. Phys.*, vol. B453, pp. 225–239, 1995.

[73] M. Papucci, K. Sakurai, A. Weiler, and L. Zeune, "Fastlim: a fast LHC limit calculator," *Eur. Phys. J.*, vol. C74, no. 11, p. 3163, 2014.

[74] M. Muhlleitner, A. Djouadi, and Y. Mambrini, "SDECAY: A Fortran code for the decays of the supersymmetric particles in the MSSM," *Comput. Phys. Commun.*, vol. 168, pp. 46–70, 2005.

[75] T. Moroi and L. Randall, "Wino cold dark matter from anomaly mediated SUSY breaking," *Nucl. Phys.*, vol. B570, pp. 455–472, 2000.

[76] B. S. Acharya, G. Kane, P. Kumar, R. Lu, and B. Zheng, "Mixed Wino-Axion Dark Matter in String/M Theory and the 130 GeV Gamma-line 'Signal'," 2012.

[77] T. A. collaboration, "Search for strong production of supersymmetric particles in final states with missing transverse momentum and at least three b-jets using 20.1 fb1 of pp collisions at sqrt(s) = 8 TeV with the ATLAS Detector.," 2013.

[78] G. Aad *et al.*, "Search for new phenomena in final states with large jet multiplicities and missing transverse momentum at $\sqrt{s}$=8 TeV proton-proton collisions using the ATLAS experiment," *JHEP*, vol. 10, p. 130, 2013. [Erratum: JHEP01,109(2014)].

[79] S. Chatrchyan *et al.*, "Search for new physics in the multijet and missing transverse momentum final state in proton-proton collisions at $\sqrt{s}$= 8 TeV," *JHEP*, vol. 06, p. 055, 2014.

[80] S. Chatrchyan *et al.*, "Search for supersymmetry in pp collisions at $\sqrt{s}$=8 TeV in events with a single lepton, large jet multiplicity, and multiple b jets," *Phys. Lett.*, vol. B733, pp. 328–353, 2014.

[81] J. Alwall, R. Frederix, S. Frixione, V. Hirschi, F. Maltoni, O. Mattelaer, H. S. Shao, T. Stelzer, P. Torrielli, and M. Zaro, "The automated computation of tree-level and next-to-leading order differential cross sections, and their matching to parton shower simulations," *JHEP*, vol. 07, p. 079, 2014.

[82] W. Beenakker, R. Hopker, and M. Spira, "PROSPINO: A Program for the production of supersymmetric particles in next-to-leading order QCD," 1996.

[83] W. Beenakker, R. Hopker, M. Spira, and P. M. Zerwas, "Squark and gluino production at hadron colliders," *Nucl. Phys.*, vol. B492, pp. 51–103, 1997.

[84] W. Beenakker, M. Klasen, M. Kramer, T. Plehn, M. Spira, and P. M. Zerwas, "The Production of charginos / neutralinos and sleptons at hadron colliders," *Phys. Rev. Lett.*, vol. 83, pp. 3780–3783, 1999. [Erratum: Phys. Rev. Lett.100,029901(2008)].

[85] "Projected Performance of an Upgraded CMS Detector at the LHC and HL-LHC: Contribution to the Snowmass Process," in *Proceedings, Community Summer Study 2013: Snowmass on the Mississippi (CSS2013): Minneapolis, MN, USA, July 29-August 6, 2013*, 2013.

[86] T. Cohen, T. Golling, M. Hance, A. Henrichs, K. Howe, J. Loyal, S. Padhi, and J. G. Wacker, "SUSY Simplified Models at 14, 33, and 100 TeV Proton Colliders," *JHEP*, vol. 04, p. 117, 2014.

[87] G. L. Kane, A. A. Petrov, J. Shao, and L.-T. Wang, "Initial determination of the spins of the gluino and squarks at LHC," *J. Phys.*, vol. G37, p. 045004, 2010.

[88] H. Baer, V. Barger, A. Lessa, W. Sreethawong, and X. Tata, "Wh plus missing-E_T signature from gaugino pair production at the LHC," *Phys. Rev.*, vol. D85, p. 055022, 2012.

[89] T. Cohen, R. T. D'Agnolo, M. Hance, H. K. Lou, and J. G. Wacker, "Boosting Stop Searches with a 100 TeV Proton Collider," *JHEP*, vol. 11, p. 021, 2014.

[90] M. Low and L.-T. Wang, "Neutralino dark matter at 14 TeV and 100 TeV," *JHEP*, vol. 08, p. 161, 2014.

[91] S. Dawson, A. Ismail, and I. Low, "Redux on "When is the top quark a parton?"," *Phys. Rev.*, vol. D90, no. 1, p. 014005, 2014.

[92] S. Jung and J. D. Wells, "Gaugino physics of split supersymmetry spectra at the LHC and future proton colliders," *Phys. Rev.*, vol. D89, no. 7, p. 075004, 2014.

[93] B. S. Acharya, K. Bożek, C. Pongkitivanichkul, and K. Sakurai, "Prospects for observing charginos and neutralinos at a 100 TeV proton-proton collider," *JHEP*, vol. 02, p. 181, 2015.

[94] S. Gori, S. Jung, L.-T. Wang, and J. D. Wells, "Prospects for Electroweakino Discovery at a 100 TeV Hadron Collider," *JHEP*, vol. 12, p. 108, 2014.

[95] G. Grilli di Cortona, "Hunting electroweakinos at future hadron colliders and direct detection experiments," *JHEP*, vol. 05, p. 035, 2015.

[96] A. Berlin, T. Lin, M. Low, and L.-T. Wang, "Neutralinos in Vector Boson Fusion at High Energy Colliders," *Phys. Rev.*, vol. D91, no. 11, p. 115002, 2015.

[97] H. Beauchesne, K. Earl, and T. Grégoire, "LHC constraints on Mini-Split anomaly and gauge mediation and prospects for LHC 14 and a future 100 TeV pp collider," *JHEP*, vol. 08, p. 117, 2015.

[98] J. D. Wells, "Implications of supersymmetry breaking with a little hierarchy between gauginos and scalars," in *11th International Conference on Supersymmetry and the Unification of Fundamental Interactions (SUSY 2003) Tucson, Arizona, June 5-10, 2003*, 2003.

[99] I. Hinchliffe, A. Kotwal, M. L. Mangano, C. Quigg, and L.-T. Wang, "Luminosity goals for a 100-TeV pp collider," *Int. J. Mod. Phys.*, vol. A30, no. 23, p. 1544002, 2015.

[100] S. Profumo and C. E. Yaguna, "Gluino coannihilations and heavy bino dark matter," *Phys. Rev.*, vol. D69, p. 115009, 2004.

[101] J. Ellis, F. Luo, and K. A. Olive, "Gluino Coannihilation Revisited," *JHEP*, vol. 09, p. 127, 2015.

[102] P. Fayet, "MASSIVE GLUINOS," *Phys. Lett.*, vol. B78, pp. 417–420, 1978.

[103] P. J. Fox, A. E. Nelson, and N. Weiner, "Dirac gaugino masses and supersoft supersymmetry breaking," *JHEP*, vol. 08, p. 035, 2002.

[104] G. Aad *et al.*, "Search for charginos nearly mass degenerate with the lightest neutralino based on a disappearing-track signature in pp collisions at $\sqrt{(s)}$=8TeV with the ATLAS detector," *Phys. Rev.*, vol. D88, no. 11, p. 112006, 2013.

[105] J. R. Ellis and D. V. Nanopoulos, "Flavor Changing Neutral Interactions in Broken Supersymmetric Theories," *Phys. Lett.*, vol. B110, p. 44, 1982.

[106] F. Gabbiani and A. Masiero, "FCNC in Generalized Supersymmetric Theories," *Nucl. Phys.*, vol. B322, p. 235, 1989.

[107] J. Hisano, T. Moroi, K. Tobe, and M. Yamaguchi, "Lepton flavor violation via right-handed neutrino Yukawa couplings in supersymmetric standard model," *Phys. Rev.*, vol. D53, pp. 2442–2459, 1996.

[108] F. Gabbiani, E. Gabrielli, A. Masiero, and L. Silvestrini, "A Complete analysis of FCNC and CP constraints in general SUSY extensions of the standard model," *Nucl. Phys.*, vol. B477, pp. 321–352, 1996.

[109] E. Arganda and M. J. Herrero, "Testing supersymmetry with lepton flavor violating tau and mu decays," *Phys. Rev.*, vol. D73, p. 055003, 2006.

[110] M. Raidal *et al.*, "Flavour physics of leptons and dipole moments," *Eur. Phys. J.*, vol. C57, pp. 13–182, 2008.

[111] W. Altmannshofer, A. J. Buras, S. Gori, P. Paradisi, and D. M. Straub, "Anatomy and Phenomenology of FCNC and CPV Effects in SUSY Theories," *Nucl. Phys.*, vol. B830, pp. 17–94, 2010.

[112] G. Isidori, Y. Nir, and G. Perez, "Flavor Physics Constraints for Physics Beyond the Standard Model," *Ann. Rev. Nucl. Part. Sci.*, vol. 60, p. 355, 2010.

[113] W. Altmannshofer, R. Harnik, and J. Zupan, "Low Energy Probes of PeV Scale Sfermions," *JHEP*, vol. 11, p. 202, 2013.

[114] M. Arana-Catania, S. Heinemeyer, and M. J. Herrero, "New Constraints on General Slepton Flavor Mixing," *Phys. Rev.*, vol. D88, no. 1, p. 015026, 2013.

[115] M. Arana-Catania, S. Heinemeyer, and M. J. Herrero, "Updated Constraints on General Squark Flavor Mixing," *Phys. Rev.*, vol. D90, no. 7, p. 075003, 2014.

[116] M. Ciuchini, A. Masiero, P. Paradisi, L. Silvestrini, S. K. Vempati, and O. Vives, "Soft SUSY breaking grand unification: Leptons versus quarks on the flavor playground," *Nucl. Phys.*, vol. B783, pp. 112–142, 2007.

[117] J. Hisano, D. Nomura, and T. Yanagida, "Atmospheric neutrino oscillation and large lepton flavor violation in the SUSY SU(5) GUT," *Phys. Lett.*, vol. B437, pp. 351–358, 1998.

[118] J. A. Casas and A. Ibarra, "Oscillating neutrinos and muon —¿ e, gamma," *Nucl. Phys.*, vol. B618, pp. 171–204, 2001.

[119] J. R. Ellis, J. Hisano, S. Lola, and M. Raidal, "CP violation in the minimal supersymmetric seesaw model," *Nucl. Phys.*, vol. B621, pp. 208–234, 2002.

[120] J. R. Ellis, J. Hisano, M. Raidal, and Y. Shimizu, "A New parametrization of the seesaw mechanism and applications in supersymmetric models," *Phys. Rev.*, vol. D66, p. 115013, 2002.

[121] S. Antusch, E. Arganda, M. J. Herrero, and A. M. Teixeira, "Impact of theta(13) on lepton flavour violating processes within SUSY seesaw," *JHEP*, vol. 11, p. 090, 2006.

[122] E. Arganda, M. J. Herrero, and A. M. Teixeira, "mu-e conversion in nuclei within the CMSSM seesaw: Universality versus non-universality," *JHEP*, vol. 10, p. 104, 2007.

[123] R. N. Mohapatra and A. Y. Smirnov, "Neutrino Mass and New Physics," *Ann. Rev. Nucl. Part. Sci.*, vol. 56, pp. 569–628, 2006.

[124] K. A. Olive *et al.*, "Review of Particle Physics," *Chin. Phys.*, vol. C38, p. 090001, 2014.

[125] M. Artuso, G. Borissov, and A. Lenz, "CP Violation in the B_s^0 system," 2015.

[126] Y. Amhis *et al.*, "Averages of b-hadron, c-hadron, and τ-lepton properties as of summer 2014," 2014.

[127] J. Charles, A. Hocker, H. Lacker, S. Laplace, F. R. Le Diberder, J. Malcles, J. Ocariz, M. Pivk, and L. Roos, "CP violation and the CKM matrix: Assessing the impact of the asymmetric B factories," *Eur. Phys. J.*, vol. C41, pp. 1–131, 2005.

[128] A. M. Baldini *et al.*, "Search for the Lepton Flavour Violating Decay $\mu^+ \to e^+\gamma$ with the Full Dataset of the MEG Experiment," 2016.

[129] A. M. Baldini *et al.*, "MEG Upgrade Proposal," 2013.

[130] B. Aubert *et al.*, "Searches for Lepton Flavor Violation in the Decays tau+- —¿ e+- gamma and tau+- —¿ mu+- gamma," *Phys. Rev. Lett.*, vol. 104, p. 021802, 2010.

[131] K. Hayasaka, "Results and prospects on lepton flavor violation at Belle/Belle II," *J. Phys. Conf. Ser.*, vol. 408, p. 012069, 2013.

[132] W. H. Bertl *et al.*, "A Search for muon to electron conversion in muonic gold," *Eur. Phys. J.*, vol. C47, pp. 337–346, 2006.

[133] R. J. Abrams *et al.*, "Mu2e Conceptual Design Report," 2012.

[134] U. Bellgardt *et al.*, "Search for the Decay mu+ —¿ e+ e+ e-," *Nucl. Phys.*, vol. B299, pp. 1–6, 1988.

[135] A. Blondel *et al.*, "Research Proposal for an Experiment to Search for the Decay $\mu \to eee$," 2013.

[136] N. Berger, "The Mu3e Experiment," *Nucl. Phys. Proc. Suppl.*, vol. 248-250, pp. 35–40, 2014.

[137] D. A. Demir, O. Lebedev, K. A. Olive, M. Pospelov, and A. Ritz, "Electric dipole moments in the MSSM at large tan beta," *Nucl. Phys.*, vol. B680, pp. 339–374, 2004.

[138] J. R. Ellis, J. S. Lee, and A. Pilaftsis, "Electric Dipole Moments in the MSSM Reloaded," *JHEP*, vol. 10, p. 049, 2008.

[139] D. McKeen, M. Pospelov, and A. Ritz, "Electric dipole moment signatures of PeV-scale superpartners," *Phys. Rev.*, vol. D87, no. 11, p. 113002, 2013.

[140] A. Pierce, "Dark matter in the finely tuned minimal supersymmetric standard model," *Phys. Rev.*, vol. D70, p. 075006, 2004.

[141] G. F. Giudice and A. Romanino, "Split supersymmetry," *Nucl. Phys.*, vol. B699, pp. 65–89, 2004. [Erratum: Nucl. Phys.B706,65(2005)].

[142] V. Bertone *et al.*, "Kaon Mixing Beyond the SM from N_f=2 tmQCD and model independent constraints from the UTA," *JHEP*, vol. 03, p. 089, 2013. [Erratum: JHEP07,143(2013)].

[143] A. Bazavov *et al.*, "Results for light pseudoscalar mesons," *PoS*, vol. LATTICE2010, p. 074, 2010.

[144] N. Carrasco *et al.*, "B-physics from $N_f = 2$ tmQCD: the Standard Model and beyond," *JHEP*, vol. 03, p. 016, 2014.

[145] J. A. Bagger, K. T. Matchev, and R.-J. Zhang, "QCD corrections to flavor changing neutral currents in the supersymmetric standard model," *Phys. Lett.*, vol. B412, pp. 77–85, 1997.

[146] T. Aushev *et al.*, "Physics at Super B Factory," 2010.

[147] R. Barbieri and G. F. Giudice, "b —¿ s gamma decay and supersymmetry," *Phys. Lett.*, vol. B309, pp. 86–90, 1993.

[148] G. Degrassi, P. Gambino, and G. F. Giudice, "B —¿ X(s gamma) in supersymmetry: Large contributions beyond the leading order," *JHEP*, vol. 12, p. 009, 2000.

[149] M. Carena, D. Garcia, U. Nierste, and C. E. M. Wagner, "b —¿ s gamma and supersymmetry with large tan Beta," *Phys. Lett.*, vol. B499, pp. 141–146, 2001.

[150] A. Freitas and U. Haisch, "Anti-B —¿ X(s) gamma in two universal extra dimensions," *Phys. Rev.*, vol. D77, p. 093008, 2008.

[151] W. Altmannshofer, M. Carena, N. R. Shah, and F. Yu, "Indirect Probes of the MSSM after the Higgs Discovery," *JHEP*, vol. 01, p. 160, 2013.

[152] M. Czakon, P. Fiedler, T. Huber, M. Misiak, T. Schutzmeier, and M. Steinhauser, "The (Q_7 , $Q_{1,\ 2}$) contribution to $\overline{B} \to X_s\gamma$ at $\mathcal{O}\left(\alpha_s^2\right)$," *JHEP*, vol. 04, p. 168, 2015.

[153] M. Misiak *et al.*, "Updated NNLO QCD predictions for the weak radiative B-meson decays," *Phys. Rev. Lett.*, vol. 114, no. 22, p. 221801, 2015.

[154] K. Agashe *et al.*, "Working Group Report: Top Quark," in *Community Summer Study 2013: Snowmass on the Mississippi (CSS2013) Minneapolis, MN, USA, July 29-August 6, 2013*, 2013.

[155] "Sensitivity of ATLAS at HL-LHC to flavour changing neutral currents in top quark decays t cH, with H ," Tech. Rep. ATL-PHYS-PUB-2013-012, CERN, Geneva, Sep 2013.

[156] A. Dedes, M. Paraskevas, J. Rosiek, K. Suxho, and K. Tamvakis, "Rare Top-quark Decays to Higgs boson in MSSM," *JHEP*, vol. 11, p. 137, 2014.

[157] E. Arganda, M. J. Herrero, R. Morales, and A. Szynkman, "Analysis of the h, H, A decays induced from SUSY loops within the Mass Insertion Approximation," *JHEP*, vol. 03, p. 055, 2016.

[158] D. Aloni, Y. Nir, and E. Stamou, "Large BR($h \to \tau\mu$) in the MSSM?," *JHEP*, vol. 04, p. 162, 2016.

[159] P. Paradisi, "Constraints on SUSY lepton flavor violation by rare processes," *JHEP*, vol. 10, p. 006, 2005.

[160] R. Kitano, M. Koike, and Y. Okada, "Detailed calculation of lepton flavor violating muon electron conversion rate for various nuclei," *Phys. Rev.*, vol. D66, p. 096002, 2002. [Erratum: Phys. Rev.D76,059902(2007)].

[161] N. Arkani-Hamed and S. Dimopoulos, "Supersymmetric unification without low energy supersymmetry and signatures for fine-tuning at the LHC," *JHEP*, vol. 06, p. 073, 2005.

[162] J. D. Wells, "PeV-scale supersymmetry," *Phys. Rev.*, vol. D71, p. 015013, 2005.

[163] T. Moroi and M. Nagai, "Probing Supersymmetric Model with Heavy Sfermions Using Leptonic Flavor and CP Violations," *Phys. Lett.*, vol. B723, pp. 107–112, 2013.

[164] S. A. R. Ellis and G. L. Kane, "Lepton Flavour Violation via the Kähler Potential in Compactified M-Theory," 2015.

[165] R. Garisto and J. D. Wells, "Constraints on supersymmetric soft phases from renormalization group relations," *Phys. Rev.*, vol. D55, pp. 1611–1622, 1997.

[166] T. Ibrahim and P. Nath, "The Neutron and the electron electric dipole moment in N=1 supergravity unification," *Phys. Rev.*, vol. D57, pp. 478–488, 1998. [Erratum: Phys. Rev.D60,119901(1999)].

[167] D. Chang, W.-Y. Keung, and A. Pilaftsis, "New two loop contribution to electric dipole moment in supersymmetric theories," *Phys. Rev. Lett.*, vol. 82, pp. 900–903, 1999. [Erratum: Phys. Rev. Lett.83,3972(1999)].

[168] T. Falk, K. A. Olive, M. Pospelov, and R. Roiban, "MSSM predictions for the electric dipole moment of the Hg-199 atom," *Nucl. Phys.*, vol. B560, pp. 3–22, 1999.

[169] S. Abel, S. Khalil, and O. Lebedev, "EDM constraints in supersymmetric theories," *Nucl. Phys.*, vol. B606, pp. 151–182, 2001.

[170] J. S. Lee, A. Pilaftsis, M. Carena, S. Y. Choi, M. Drees, J. R. Ellis, and C. E. M. Wagner, "CPsuperH: A Computational tool for Higgs phenomenology in the minimal supersymmetric standard model with explicit CP violation," *Comput. Phys. Commun.*, vol. 156, pp. 283–317, 2004.

[171] K. A. Olive, M. Pospelov, A. Ritz, and Y. Santoso, "CP-odd phase correlations and electric dipole moments," *Phys. Rev.*, vol. D72, p. 075001, 2005.

[172] J. Ellis, J. S. Lee, and A. Pilaftsis, "A Geometric Approach to CP Violation: Applications to the MCPMFV SUSY Model," *JHEP*, vol. 10, p. 049, 2010.

[173] T. Fukuyama, "Searching for New Physics beyond the Standard Model in Electric Dipole Moment," *Int. J. Mod. Phys.*, vol. A27, p. 1230015, 2012.

[174] T. Ibrahim, A. Itani, and P. Nath, "Electron electric dipole moment as a sensitive probe of PeV scale physics," *Phys. Rev.*, vol. D90, no. 5, p. 055006, 2014.

[175] I. Affleck and M. Dine, "A New Mechanism for Baryogenesis," *Nucl. Phys.*, vol. B249, pp. 361–380, 1985.

[176] G. F. Giudice and A. Masiero, "A Natural Solution to the mu Problem in Supergravity Theories," *Phys. Lett.*, vol. B206, pp. 480–484, 1988.

[177] P. Ramond, R. G. Roberts, and G. G. Ross, "Stitching the Yukawa quilt," *Nucl. Phys.*, vol. B406, pp. 19–42, 1993.

[178] S. P. Martin and M. T. Vaughn, "Two loop renormalization group equations for soft supersymmetry breaking couplings," *Phys. Rev.*, vol. D50, p. 2282, 1994. [Erratum: Phys. Rev.D78,039903(2008)].

[179] S. Weinberg, "Larger Higgs Exchange Terms in the Neutron Electric Dipole Moment," *Phys. Rev. Lett.*, vol. 63, p. 2333, 1989.

[180] S. M. Barr, "Measurable T and P odd electron - nucleon interactions from Higgs boson exchange," *Phys. Rev. Lett.*, vol. 68, pp. 1822–1825, 1992.

[181] G. Degrassi, E. Franco, S. Marchetti, and L. Silvestrini, "QCD corrections to the electric dipole moment of the neutron in the MSSM," *JHEP*, vol. 11, p. 044, 2005.

[182] J. Engel, M. J. Ramsey-Musolf, and U. van Kolck, "Electric Dipole Moments of Nucleons, Nuclei, and Atoms: The Standard Model and Beyond," *Prog. Part. Nucl. Phys.*, vol. 71, pp. 21–74, 2013.

[183] J. R. Ellis and M. K. Gaillard, "Strong and Weak CP Violation," *Nucl. Phys.*, vol. B150, pp. 141–162, 1979.

[184] I. B. Khriplovich, "Quark Electric Dipole Moment and Induced θ Term in the Kobayashi-Maskawa Model," *Phys. Lett.*, vol. B173, pp. 193–196, 1986. [Yad. Fiz.44,1019(1986)].

[185] J.-M. Gérard and P. Mertens, "Weakly-induced strong CP-violation," *Phys. Lett.*, vol. B716, pp. 316–321, 2012.

[186] J. R. Ellis, S. Ferrara, and D. V. Nanopoulos, "CP Violation and Supersymmetry," *Phys. Lett.*, vol. B114, pp. 231–234, 1982.

[187] K. Bobkov, V. Braun, P. Kumar, and S. Raby, "Stabilizing All Kahler Moduli in Type IIB Orientifolds," *JHEP*, vol. 12, p. 056, 2010.

[188] P. Svrcek and E. Witten, "Axions In String Theory," *JHEP*, vol. 06, p. 051, 2006.

[189] D. Bowser-Chao, D. Chang, and W.-Y. Keung, "Electron electric dipole moment from CP violation in the charged Higgs sector," *Phys. Rev. Lett.*, vol. 79, pp. 1988–1991, 1997.

[190] A. Pilaftsis, "Higgs boson two loop contributions to electric dipole moments in the MSSM," *Phys. Lett.*, vol. B471, pp. 174–181, 1999.

[191] D. Chang, W.-F. Chang, and W.-Y. Keung, "Additional two loop contributions to electric dipole moments in supersymmetric theories," *Phys. Lett.*, vol. B478, pp. 239–246, 2000.

[192] A. Pilaftsis, "Higgs mediated electric dipole moments in the MSSM: An application to baryogenesis and Higgs searches," *Nucl. Phys.*, vol. B644, pp. 263–289, 2002.

[193] D. Chang, W.-F. Chang, and W.-Y. Keung, "New constraint from electric dipole moments on chargino baryogenesis in MSSM," *Phys. Rev.*, vol. D66, p. 116008, 2002.

[194] D. Chang, W.-F. Chang, and W.-Y. Keung, "Electric dipole moment in the split supersymmetry models," *Phys. Rev.*, vol. D71, p. 076006, 2005.

[195] Y. Li, S. Profumo, and M. Ramsey-Musolf, "Higgs-Higgsino-Gaugino Induced Two Loop Electric Dipole Moments," *Phys. Rev.*, vol. D78, p. 075009, 2008.

[196] M. Pospelov and A. Ritz, "CKM benchmarks for electron electric dipole moment experiments," *Phys. Rev.*, vol. D89, no. 5, p. 056006, 2014.

[197] J. R. Ellis, J. S. Hagelin, D. V. Nanopoulos, K. A. Olive, and M. Srednicki, "Supersymmetric Relics from the Big Bang," *Nucl. Phys.*, vol. B238, pp. 453–476, 1984.

[198] H. Goldberg, "Constraint on the Photino Mass from Cosmology," *Phys. Rev. Lett.*, vol. 50, p. 1419, 1983. [Erratum: Phys. Rev. Lett.103,099905(2009)].

[199] K. R. Dienes, C. F. Kolda, and J. March-Russell, "Kinetic mixing and the supersymmetric gauge hierarchy," *Nucl. Phys.*, vol. B492, pp. 104–118, 1997.

[200] A. Corti, M. Haskins, J. Nordström, and T. Pacini, "G_2-manifolds and associative submanifolds via semi-Fano 3-folds," *Duke Math. J.*, vol. 164, no. 10, pp. 1971–2092, 2015.

[201] B. Batell, M. Pospelov, and A. Ritz, "Exploring Portals to a Hidden Sector Through Fixed Targets," *Phys. Rev.*, vol. D80, p. 095024, 2009.

[202] B. Holdom, "Two U(1)'s and Epsilon Charge Shifts," *Phys. Lett.*, vol. B166, pp. 196–198, 1986.

[203] K. R. Dienes, "Statistics on the heterotic landscape: Gauge groups and cosmological constants of four-dimensional heterotic strings," *Phys. Rev.*, vol. D73, p. 106010, 2006.

[204] K. R. Dienes, M. Lennek, D. Senechal, and V. Wasnik, "Supersymmetry versus Gauge Symmetry on the Heterotic Landscape," *Phys. Rev.*, vol. D75, p. 126005, 2007.

[205] J. Giedt, "Completion of standard model like embeddings," *Annals Phys.*, vol. 289, p. 251, 2001.

[206] O. Lebedev, H.-P. Nilles, S. Raby, S. Ramos-Sanchez, M. Ratz, P. K. S. Vaudrevange, and A. Wingerter, "Low Energy Supersymmetry from the Heterotic Landscape," *Phys. Rev. Lett.*, vol. 98, p. 181602, 2007.

[207] M. Cvetic, T. Li, and T. Liu, "Supersymmetric patiSalam models from intersecting D6-branes: A Road to the standard model," *Nucl. Phys.*, vol. B698, pp. 163–201, 2004.

[208] F. Gmeiner, R. Blumenhagen, G. Honecker, D. Lust, and T. Weigand, "One in a billion: MSSM-like D-brane statistics," *JHEP*, vol. 01, p. 004, 2006.

[209] T. P. T. Dijkstra, L. R. Huiszoon, and A. N. Schellekens, "Supersymmetric standard model spectra from RCFT orientifolds," *Nucl. Phys.*, vol. B710, pp. 3–57, 2005.

[210] W. Taylor and Y.-N. Wang, "A Monte Carlo exploration of threefold base geometries for 4d F-theory vacua," *JHEP*, vol. 01, p. 137, 2016.

[211] D. Joyce, *Compact Manifolds with Special Holonomy*. Oxford University Press, 2000.

[212] W. Taylor and Y.-N. Wang, "The F-theory geometry with most flux vacua," *JHEP*, vol. 12, p. 164, 2015.

[213] J. Halverson and W. Taylor, "$\mathbb{P}^1$-bundle bases and the prevalence of non-Higgsable structure in 4D F-theory models," *JHEP*, vol. 09, p. 086, 2015.

[214] H. Jockers and J. Louis, "The Effective action of D7-branes in N = 1 Calabi-Yau orientifolds," *Nucl. Phys.*, vol. B705, pp. 167–211, 2005.

[215] L. E. Ibanez, R. Rabadan, and A. M. Uranga, "Anomalous U(1)'s in type I and type IIB D = 4, N=1 string vacua," *Nucl. Phys.*, vol. B542, pp. 112–138, 1999.

[216] I. Antoniadis, E. Kiritsis, and J. Rizos, "Anomalous U(1)s in type 1 superstring vacua," *Nucl. Phys.*, vol. B637, pp. 92–118, 2002.

[217] R. Blumenhagen, M. Cvetic, P. Langacker, and G. Shiu, "Toward realistic intersecting D-brane models," *Ann. Rev. Nucl. Part. Sci.*, vol. 55, pp. 71–139, 2005.

[218] M. Cvetic, J. Halverson, and P. Langacker, "Implications of String Constraints for Exotic Matter and Z' s Beyond the Standard Model," *JHEP*, vol. 11, p. 058, 2011.

[219] W.-Z. Feng, G. Shiu, P. Soler, and F. Ye, "Building a Stückelberg portal," *JHEP*, vol. 05, p. 065, 2014.

[220] L. B. Anderson, J. Gray, A. Lukas, and E. Palti, "Two Hundred Heterotic Standard Models on Smooth Calabi-Yau Threefolds," *Phys. Rev.*, vol. D84, p. 106005, 2011.

[221] T. W. Grimm and A. Klemm, "U(1) Mediation of Flux Supersymmetry Breaking," *JHEP*, vol. 10, p. 077, 2008.

[222] S. A. Abel and B. W. Schofield, "Brane anti-brane kinetic mixing, millicharged particles and SUSY breaking," *Nucl. Phys.*, vol. B685, pp. 150–170, 2004.

[223] S. A. Abel, J. Jaeckel, V. V. Khoze, and A. Ringwald, "Illuminating the Hidden Sector of String Theory by Shining Light through a Magnetic Field," *Phys. Lett.*, vol. B666, pp. 66–70, 2008.

[224] S. A. Abel, M. D. Goodsell, J. Jaeckel, V. V. Khoze, and A. Ringwald, "Kinetic Mixing of the Photon with Hidden U(1)s in String Phenomenology," *JHEP*, vol. 07, p. 124, 2008.

[225] M. Goodsell and A. Ringwald, "Light Hidden-Sector U(1)s in String Compactifications," *Fortsch. Phys.*, vol. 58, pp. 716–720, 2010.

[226] M. Bullimore, J. P. Conlon, and L. T. Witkowski, "Kinetic mixing of U(1)s for local string models," *JHEP*, vol. 11, p. 142, 2010.

[227] V. Balasubramanian, P. Berglund, J. P. Conlon, and F. Quevedo, "Systematics of moduli stabilisation in Calabi-Yau flux compactifications," *JHEP*, vol. 03, p. 007, 2005.

[228] M. Goodsell, J. Jaeckel, J. Redondo, and A. Ringwald, "Naturally Light Hidden Photons in LARGE Volume String Compactifications," *JHEP*, vol. 11, p. 027, 2009.

[229] M. Cicoli, M. Goodsell, J. Jaeckel, and A. Ringwald, "Testing String Vacua in the Lab: From a Hidden CMB to Dark Forces in Flux Compactifications," *JHEP*, vol. 07, p. 114, 2011.

[230] A. Lukas and K. S. Stelle, "Heterotic anomaly cancellation in five-dimensions," *JHEP*, vol. 01, p. 010, 2000.

[231] R. Blumenhagen, G. Honecker, and T. Weigand, "Loop-corrected compactifications of the heterotic string with line bundles," *JHEP*, vol. 06, p. 020, 2005.

[232] M. Goodsell, S. Ramos-Sanchez, and A. Ringwald, "Kinetic Mixing of U(1)s in Heterotic Orbifolds," *JHEP*, vol. 01, p. 021, 2012.

[233] A. Arvanitaki, N. Craig, S. Dimopoulos, S. Dubovsky, and J. March-Russell, "String Photini at the LHC," *Phys. Rev.*, vol. D81, p. 075018, 2010.

[234] A. Ibarra, A. Ringwald, and C. Weniger, "Hidden gauginos of an unbroken U(1): Cosmological constraints and phenomenological prospects," *JCAP*, vol. 0901, p. 003, 2009.

[235] H. Georgi and S. L. Glashow, "Unity of All Elementary Particle Forces," *Phys. Rev. Lett.*, vol. 32, pp. 438–441, 1974.

[236] H. Georgi, H. R. Quinn, and S. Weinberg, "Hierarchy of Interactions in Unified Gauge Theories," *Phys. Rev. Lett.*, vol. 33, pp. 451–454, 1974.

[237] H. Fritzsch and P. Minkowski, "Unified Interactions of Leptons and Hadrons," *Annals Phys.*, vol. 93, pp. 193–266, 1975.

[238] H. Georgi. American Institute of Physics, New York, 1975.

[239] S. Dimopoulos and H. Georgi, "Softly Broken Supersymmetry and SU(5)," *Nucl. Phys.*, vol. B193, pp. 150–162, 1981.

[240] S. Dimopoulos, S. Raby, and F. Wilczek, "Supersymmetry and the Scale of Unification," *Phys. Rev.*, vol. D24, pp. 1681–1683, 1981.

[241] L. E. Ibanez and G. G. Ross, "Low-Energy Predictions in Supersymmetric Grand Unified Theories," *Phys. Lett.*, vol. B105, pp. 439–442, 1981.

[242] J. R. Ellis, S. Kelley, and D. V. Nanopoulos, "Precision LEP data, supersymmetric GUTs and string unification," *Phys. Lett.*, vol. B249, pp. 441–448, 1990.

[243] J. R. Ellis, S. Kelley, and D. V. Nanopoulos, "Probing the desert using gauge coupling unification," *Phys. Lett.*, vol. B260, pp. 131–137, 1991.

[244] A. J. Buras, J. R. Ellis, M. K. Gaillard, and D. V. Nanopoulos, "Aspects of the Grand Unification of Strong, Weak and Electromagnetic Interactions," *Nucl. Phys.*, vol. B135, pp. 66–92, 1978.

[245] S. Weinberg, "Effective Gauge Theories," *Phys. Lett.*, vol. B91, pp. 51–55, 1980.

[246] L. J. Hall, "Grand Unification of Effective Gauge Theories," *Nucl. Phys.*, vol. B178, pp. 75–124, 1981.

[247] C. Giunti, C. W. Kim, and U. W. Lee, "Running coupling constants and grand unification models," *Mod. Phys. Lett.*, vol. A6, pp. 1745–1755, 1991.

[248] P. Langacker and N. Polonsky, "Uncertainties in coupling constant unification," *Phys. Rev.*, vol. D47, pp. 4028–4045, 1993.

[249] R. Dermisek, A. Mafi, and S. Raby, "SUSY GUTs under siege: Proton decay," *Phys. Rev.*, vol. D63, p. 035001, 2001.

[250] A. Anandakrishnan, B. C. Bryant, and S. Raby, "LHC Phenomenology of SO(10) Models with Yukawa Unification II," *Phys. Rev.*, vol. D90, no. 1, p. 015030, 2014.

[251] J. Hisano, T. Kuwahara, and N. Nagata, "Grand Unification in High-scale Supersymmetry," *Phys. Lett.*, vol. B723, pp. 324–329, 2013.

[252] J. Hisano, D. Kobayashi, T. Kuwahara, and N. Nagata, "Decoupling Can Revive Minimal Supersymmetric SU(5)," *JHEP*, vol. 07, p. 038, 2013.

[253] L. J. Hall and Y. Nomura, "Grand Unification and Intermediate Scale Supersymmetry," *JHEP*, vol. 02, p. 129, 2014.

[254] A. Hebecker and J. Unwin, "Precision Unification and Proton Decay in F-Theory GUTs with High Scale Supersymmetry," *JHEP*, vol. 09, p. 125, 2014.

[255] F. Wang, W. Wang, and J. M. Yang, "A split SUSY model from SUSY GUT," *JHEP*, vol. 03, p. 050, 2015.

[256] L. Lavoura and L. Wolfenstein, "Resuscitation of minimal SO(10) grand unification," *Phys. Rev.*, vol. D48, pp. 264–269, 1993.

[257] K. Tobe and J. D. Wells, "Gravity assisted exact unification in minimal supersymmetric SU(5) and its gaugino mass spectrum," *Phys. Lett.*, vol. B588, pp. 99–104, 2004.

[258] M. E. Machacek and M. T. Vaughn, "Two Loop Renormalization Group Equations in a General Quantum Field Theory. 1. Wave Function Renormalization," *Nucl. Phys.*, vol. B222, pp. 83–103, 1983.

[259] M. E. Machacek and M. T. Vaughn, "Two Loop Renormalization Group Equations in a General Quantum Field Theory. 2. Yukawa Couplings," *Nucl. Phys.*, vol. B236, pp. 221–232, 1984.

[260] M. E. Machacek and M. T. Vaughn, "Two Loop Renormalization Group Equations in a General Quantum Field Theory. 3. Scalar Quartic Couplings," *Nucl. Phys.*, vol. B249, pp. 70–92, 1985.

[261] R. Slansky, "Group Theory for Unified Model Building," *Phys. Rept.*, vol. 79, pp. 1–128, 1981.

[262] I. Affleck, M. Dine, and N. Seiberg, "Dynamical Supersymmetry Breaking in Four-Dimensions and Its Phenomenological Implications," *Nucl. Phys.*, vol. B256, pp. 557–599, 1985.

[263] C. Beasley and E. Witten, "A Note on fluxes and superpotentials in M theory compactifications on manifolds of G(2) holonomy," *JHEP*, vol. 07, p. 046, 2002.

[264] A. Brignole, L. E. Ibanez, and C. Munoz, "Soft supersymmetry breaking terms from supergravity and superstring models," *Adv. Ser. Direct. High Energy Phys.*, vol. 21, pp. 244–268, 2010.

[265] J. A. Bagger, T. Moroi, and E. Poppitz, "Anomaly mediation in supergravity theories," *JHEP*, vol. 04, p. 009, 2000.

[266] J. P. Conlon and F. Quevedo, "Gaugino and Scalar Masses in the Landscape," *JHEP*, vol. 06, p. 029, 2006.

[267] K. Choi and H. P. Nilles, "The Gaugino code," *JHEP*, vol. 04, p. 006, 2007.

[268] D. M. Pierce, J. A. Bagger, K. T. Matchev, and R.-j. Zhang, "Precision corrections in the minimal supersymmetric standard model," *Nucl. Phys.*, vol. B491, pp. 3–67, 1997.

[269] L. J. Hall, H. Murayama, and Y. Nomura, "Wilson lines and symmetry breaking on orbifolds," *Nucl. Phys.*, vol. B645, pp. 85–104, 2002.

[270] T. Sjostrand, S. Mrenna, and P. Z. Skands, "PYTHIA 6.4 Physics and Manual," *JHEP*, vol. 05, p. 026, 2006.

[271] A. Avetisyan *et al.*, "Methods and Results for Standard Model Event Generation at $\sqrt{s}$ = 14 TeV, 33 TeV and 100 TeV Proton Colliders (A Snowmass Whitepaper)," in *Proceedings, Community Summer Study 2013: Snowmass on the Mississippi (CSS2013): Minneapolis, MN, USA, July 29-August 6, 2013*, 2013.

[272] J. de Favereau, C. Delaere, P. Demin, A. Giammanco, V. Lemaître, A. Mertens, and M. Selvaggi, "DELPHES 3, A modular framework for fast simulation of a generic collider experiment," *JHEP*, vol. 02, p. 057, 2014.

[273] J. Anderson *et al.*, "Snowmass Energy Frontier Simulations," in *Proceedings, Community Summer Study 2013: Snowmass on the Mississippi (CSS2013): Minneapolis, MN, USA, July 29-August 6, 2013*, 2013.

[274] E. Conte, B. Fuks, and G. Serret, "MadAnalysis 5, A User-Friendly Framework for Collider Phenomenology," *Comput. Phys. Commun.*, vol. 184, pp. 222–256, 2013.